Thermal Kinetic Inductance Detectors (TKIDs) for Cosmic Microwave Background (CMB) Polarimetry

Thesis by
Albert Kamau Wandui

In Partial Fulfillment of the Requirements for the
Degree of
Doctor of Philosophy

CALIFORNIA INSTITUTE OF TECHNOLOGY
Pasadena, California

2025
Defended June 3rd, 2024

Albert Kamau Wandui
ORCID: 0000-0002-8232-7343

ACKNOWLEDGEMENTS

I am deeply grateful to my advisor, James Bock, for his mentorship, quiet guidance, and insightful suggestions throughout graduate school. Anything mentioned twice was a strong indication to pay attention, and I have benefited greatly. Thank you for steering me away from unrealistic project timelines while keeping an eye on the prize at the end of every scientific question.

I also owe heartfelt thanks to Jonas Zmuidzinas for his initial ideas on resonator bolometers, which sparked this entire research thread. Your enthusiasm for science and mentorship has left a profound impression on me. Thanks to Sunil Golwala for giving me my initial lessons on noise theory in devices. I had only been at Caltech for about a week when I attended your summer school lecture on detector noise. That one-hour lecture provided a strong foundation for my graduate research. I am also grateful to Michael Roukes for his Physics of Measurement class, which I participated in for two quarters during my first year of graduate school. I have revisited the ideas we discussed in that class at every stage of my graduate career.

It is difficult to imagine graduate school without Roger O'Brient and Bryan Steinbach, who mentored me in the lab. Roger, thank you for fighting to get me access to JPL to conduct my research. You taught me a great deal about detector design, as well as giving engaging talks and writing papers. Bryan, I am grateful for your patient lessons throughout graduate school. You indulged all my questions and trusted me even when I was terrified of messing up in the lab. Fixing plumbing in the lab was one of my favorite moments. This work would not have been possible without the endless effort put in by our fabrication team: Clifford Frez and Anthony Turner. Thank you for your patient feedback on my less-than-workable early designs and for working so closely with me both in and out of the cleanroom.

Thank you, Chao-Lin Kuo, for giving me my first research opportunity. It was serendipity that I attended your talk during my freshman year of college. Thank you for sharing your passionate interest in the Cosmic Microwave Background with me; it set me on an adventure that has now lasted a decade. I am also grateful to Zeeshan Ahmed, Keith Thompson, Jimmy Grayson, Kimmy Wu, and Jae-Hwan Kang, who worked with me during those early years.

I am very thankful for Lorenzo Minutolo, who has been part of this project as long as I have. You always made timely suggestions that got the cryostat working when

I was frustrated. Thank you for the many late nights in the lab, the back-and-forth when analyzing noise data, and all the fun times in the office, at pizza nights, and conferences.

My office mates in graduate school—Richard Feder, Cheng Zhang, Silvia Zhang, Sinan Kefeli, and Ahmed Soliman—you made coming to work a joy. Bagel Tuesdays have been a highlight of my time here. I am also grateful to Howard Hui, Hien Nguyen, Lorenzo Moncelsi, and Alessandro Schillaci for their advice throughout graduate school and for modeling how to treat junior graduate students. To everyone in observational cosmology, it has been a delight to work with and learn from all of you. A special thanks to Nancy Roth-Rappard for fostering warmth and community in ObsCos and for the timely reminders to handle university requirements.

To my friends in graduate school, you made life enjoyable even when it was at its most difficult. Varun, Tom, and Zander, thanks for hunkering down with me during the pandemic. Tom, thank you for indulging my Swahili lessons and for not feeling weird when I suggested we should grow sugarcane. Varun, you have kept all of us in contact with each other. Thanks for suggesting we get together and setting up pizza nights. Andy, thank you for your friendship from college through graduate school and beyond. You invited me into friendship when all my Physics 40 friends were gone, and I needed company to work through upper-level courses. Widi, you perfected pork belly. It was a delight to lead GCF with you and Andy. To the GCF crew, present and graduated, you have been a consistent source of joy and comfort throughout graduate school. Hannah, Nathan, Grace, Rachel, Sami, Raymond, Isaac, George, Saren, Tanner, Voon, Bekah, Jamie, and Mark, your lives have inspired how I live mine. A shout-out to the disaster movie crew, Maria, Grigory, and Caroline for indulging me so generously. Tony, thanks for the fun chats and adventures all the way from SAS. Ben, thank you for all the hikes and fun lunches.

Missio has been my home throughout graduate school. Len, thank you for meeting with me consistently and listening to my joys and frustrations, and for helping me grow. You taught me to care about the community beyond my work. Amy, thank you for sharing your joy of nature and gardening with me and for allowing me to be a part of it. Thank you both for providing the space I needed to heal and recover after my procedure. Mike, the Sunday walks and your wisdom and thoughtfulness are much appreciated. Dylan, Melanie, and Nick, thank you for being so excited to be my friends. Your support was exactly what I needed when I felt I didn't measure

up during the Ph.D. Chris Harper, you sat with me through many appointments and have championed me endlessly. Wayne, Ryan, Tiffany, Juli, Daniel, Aileen, Chris, Chen, Sub, Saharai, Luis, Nico, and Camila, you have been tremendous friends.

To my aunt, Grace, you have shared your life and family with me from the very first moment I came to the United States. Thank you for the check-in phone calls and the Christmas dinners that I always look forward to. Hos, your humor has brought much joy whenever we meet. Thank you for reminding me to take care of not just my studies but also my physical well-being.

Jeremy, my older brother, I am grateful for your keen attention and wisdom. I have felt known and inspired by you. Thank you for spending so much time with me on the phone and in person and for broadening my horizons. Jimmy, my younger brother, I am excited to see your life unfold. Thank you for our discussions and for letting me be your older brother. Angie and Shane, you have brought so much joy and life.

Ma, I love you deeply. Your endurance in difficulty has been an inspiration to me. You hold tightly to your friends and family and pushed me to pursue my goals and dreams. Thank you for holding me in your concern and encouraging me with your prayers.

Dad, it was your love of reading that set me on this path. I am eternally grateful.

Guka, you passed away too soon. I would have loved to celebrate this milestone with you. I bear your name proudly.

ABSTRACT

The modern era of precision cosmology has been driven by advances in detector technology and observing techniques. Observational cosmology is experiencing a rapid growth in detector numbers. New architectures are emerging for low-loading applications such as far-infrared spectroscopy, ultra-sensitive low-threshold sensors for particle astrophysics, and dark matter investigations. Current millimeter-wave observatories use kilo-pixel arrays of detectors to measure the polarization of the Cosmic Microwave Background (CMB). There is a strong push within the CMB community to deploy new experiments with hundreds of thousands of detectors to achieve novel scientific outcomes.

However, for over a decade, CMB detectors have been limited by background noise, where fluctuations in the photon flux incident on the camera overshadow internal detector noise. As a result, improving instrument sensitivity now requires increasing the number of pixels. This focal plane size and detector density increase significantly complicates integration and readout. Thermal Kinetic Inductance Detectors (TKIDs) are an innovative solution for scaling up detector counts, offering high sensitivity and ease of multiplexing. TKIDs are narrow-bandwidth superconducting resonators that can be multiplexed and read out using a single transmission line via microwave frequency division multiplexing.

In this thesis, I present the design, development, and laboratory characterization of a TKID polarimeter for CMB studies at 150 GHz with a 25% bandwidth. I provide a detailed physical model of TKID operation and readout, accurately predicting detector noise and responsivity. Three generations of prototype detectors were developed and tested, leading to the final tile design. The first generation demonstrated the feasibility of fabricating TKIDs with internal noise low enough for background-limited performance given the expected optical loading on our telescope. The second generation validated the scalability of the initial design to larger arrays and was crucial for refining fabrication processes, cosmic ray susceptibility testing, and readout development. The third generation integrated the tested detector design with a polarization-sensitive planar phased-array antenna. This required precise fabrication of sub-micron microstrip lines and an in-depth understanding of both the antenna and detector fabrication processes. We show that antenna-coupled TKIDs achieve end-to-end optical efficiency comparable to existing Transition Edge Sensor (TES) detectors and exhibit smooth Gaussian antenna beams matching the

design spectral response.

Our efforts culminate in the design of a 64-pixel dual-polarization TKID array, intended for CMB observations in a telescope observing from the South Pole. This camera will be the first demonstration of TKIDs in the millimeter-wave regime, advancing the technology for future cosmological and astrophysical applications. I present results from in-lab dark and optical testing of the TKID focal plane, along with design methodologies, electromagnetic simulations, and fabrication procedures for achieving high-yield, uniform TKID arrays.

PUBLISHED CONTENT AND CONTRIBUTIONS

Agrawal, Shubh et al. (2021). "Strong negative electrothermal feedback in thermal kinetic inductance detectors". In: *Journal of Applied Physics* 130.12, p. 124503. DOI: 10.1063/5.0064723. eprint: https://doi.org/10.1063/5.0064723. URL: https://doi.org/10.1063/5.0064723.

A.K.W. hybridized detectors for measurements and contributed to the data acquisition, analysis and writing of this manuscript.

Minutolo, L., C. Frez, et al. (2021). "Thermal Kinetic Inductance Detectors Camera: System Level Design, Strategy and Performance Forecast". In: *IEEE Transactions on Applied Superconductivity* 31.5, pp. 1–4. DOI: 10.1109/TASC.2021.3069732.

A.K.W. instrumented the optics of the cryostat, modelled and designed the detectors. A.K.W. led the detector characterization and contributed to the data analysis software and the writing of this manuscript.

Wandui, Albert et al. (2020). "Thermal kinetic inductance detectors for millimeter-wave detection". In: *Journal of Applied Physics* 128.4, p. 044508. DOI: 10.1063/5.0002413. eprint: https://doi.org/10.1063/5.0002413. URL: https://doi.org/10.1063/5.0002413.

A.K.W. modelled and designed the detectors, contributed to the software base for data acquisition and analysis, and led the authorship of this manuscript.

Wandui, Albert K. et al. (2020). "Antenna-coupled thermal kinetic inductance detectors for ground-based millimeter-wave cosmology". In: *Millimeter, Submillimeter, and Far-Infrared Detectors and Instrumentation for Astronomy X*. Ed. by Jonas Zmuidzinas and Jian-Rong Gao. Vol. 11453. International Society for Optics and Photonics. SPIE, 114531E. DOI: 10.1117/12.2563373. URL: https://doi.org/10.1117/12.2563373.

A.K.W. designed the detectors and housing and led both dark and optical detector characterization. A.K.W. led the writing of the manuscript.

Minutolo, L., B. Steinbach, et al. (2019). "A Flexible GPU-accelerated Radio-frequency Readout for Superconducting Detectors". In: *IEEE Transactions on Applied Superconductivity* 29.5, pp. 1–5. ISSN: 1051-8223. DOI: 10.1109/TASC.2019.2912027.

A.K.W. contributed resonator fitting and diagnostics code to the software base. A.K.W contributed to extensive testing of the software platform on TKIDs.

TABLE OF CONTENTS

LIST OF ILLUSTRATIONS

LIST OF TABLES

Chapter 1

INTRODUCTION AND MOTIVATION

1.1 The Standard Model of Cosmology

Our current knowledge of the composition and evolution of our universe at its largest scales is captured under the ΛCDM standard model of cosmology (Bergström and Goobar, 2006). This work began early in the 1930s after Einstein's Theory of General Relativity was first applied to the understanding the universe at large. Einstein's Field Equations are a set of coupled differential equations that relate the geometry of space-time to its energy and momentum. For a universe with cosmological constant Λ, the field equations can be expressed as

$$R_{\mu\nu} - \frac{1}{2} g_{\mu\nu} R = 8\pi G T_{\mu\nu} - \Lambda g_{\mu\nu}. \tag{1.1}$$

Using the cosmological principle, that is, the basic assumption that the universe is homogeneous (has no special points) and isotropic (all directions are equivalent) at its largest scales, a solution to Einstein's Field Equations was co-discovered by Friedmann, Lemaitre, and Walker (Peebles, 1993). This is the FRW metric which can be parametrized using time t and spherical coordinates $(r,\ \theta,\ \phi)$ as

$$\mathrm{d}s^2 = -\mathrm{d}t^2 + a(t)^2 \left[\frac{\mathrm{d}r^2}{1 - Kr^2} + r^2 \mathrm{d}\Omega^2 \right]. \tag{1.2}$$

The scale factor $a(t)$ captures the relative change in physical scale of spacial slices of the universe with the same spatial coordinates (given by a vector $\vec{r}$). K is the global curvature of the universe which can take on the values [1,0,-1] depending on whether the universe is closed, flat or open, respectively. $\mathrm{d}\Omega^2 = \mathrm{d}\theta^2 + \sin\theta^2 \mathrm{d}\phi^2$ is a surface area element in spherical coordinates. Measurements of the Cosmic Microwave Background (CMB) have shown that the universe is geometrically flat to high precision ($\kappa = 0$). In the FRW model, the evolution of the universe is entirely captured by the scale factor as a function of time. Relativity couples the composition of the universe to its geometry. This motivates defining the Hubble parameter $H(t)$, which is the logarithmic change in the rate of expansion of the universe

$$H(t) = \frac{1}{a(t)}\frac{\mathrm{d}a}{\mathrm{d}t} = \frac{\dot{a}(t)}{a(t)}. \tag{1.3}$$

A related and convenient quantity is the conformal time or comoving horizon, $\eta(t)$ which is the time of travel of a light ray from ($t = 0$) up to the current time

$$\eta(t) = \int_0^t \frac{dt}{a(t)} = \int_0^a \frac{\mathrm{d}a'}{H(a')a'}. \tag{1.4}$$

If at a time t, two locations in the universe separated by a comoving distance greater than the conformal time $\eta(t)$ they could never have been in causal contact. Light propagating from one location to the other as the universe expands would not have had enough time to reach the second location by the time the universe has an age of t. This fact will be important later when we discuss the horizon problem that motivates inflation.

To relate geometry to energy, we will take the universe to be permeated of substance described by an energy density ρ and exerting pressure p. This energy density is the sum of different components, each of which can evolve differently over time. However, our assertion is valid because for an isotropic universe, all cosmological fluids are at rest in comoving coordinates. Einstein's equations reduce to the Friedmann equations:

$$\left(\frac{\dot{a}}{a}\right)^2 = \frac{8\pi G}{3}\rho - \frac{K}{a^2}, \tag{1.5}$$

$$\frac{\ddot{a}}{a} = -\frac{4\pi G}{3}\left(\rho + 3p\right). \tag{1.6}$$

Combining the two Friedmann equations allows us to write out the energy conservation from the stress-energy tensor explicitly as

$$\dot{\rho} = -3H\left(\rho + p\right). \tag{1.7}$$

These equations make explicit the evolution of the scale factor at a time t provided that we can account for the composition of the universe at the same time. We typically parametrize the equation of state that relates the pressure to the energy density as $p = w\rho$. For non-relativistic (cold) matter, $w = 0$, radiation $w = 1/3$

and for dark energy $w = -1$. From equation 1.7, it is clear that $\rho \propto a^{-3(1+w)}$ which shows that the energy density for radiation, matter and dark energy evolve as a^{-4}, a^{-3}, const, respectively. A useful quantity is the critical energy density ρ_c which is the energy density at which the universe becomes flat,

$$\rho_c = \frac{3H^2}{8\pi G}. \tag{1.8}$$

The energy density today ρ_0, relative to the critical energy can be expressed as $\Omega_0 = \rho_0/\rho_c$ which can be decomposed into the contributions from cold matter, radiation, dark energy and curvature as

$$\Omega_0 = \Omega_m + \Omega_\gamma + \Omega_\Lambda + \Omega_K. \tag{1.9}$$

We can recast the first Friedmann equation using the Hubble parameter as measured today H_0 and the energy density parameter. We will use subscript 0 to indicate that the quantities are measured in the present epoch. Additionally, we can make use of the cosmological redshift z defined by $a = 1/(1+z)$ where we take the scale factor today to be unity ($a\,(t_0) = 1$) since the redshift is a direct cosmological observable:

$$H(z)^2 = H_0^2 \left[\Omega_{0,m}\,(1+z)^3 + \Omega_{0,\gamma}\,(1+z)^4 + \Omega_{0,\Lambda} + \Omega_{0,K}\,(1+z)^2\right]. \tag{1.10}$$

The current best measurements of the composition of the universe as reported by the Planck Collaboration, report that the universe is composed of $\sim 70\%$ dark energy, and $\sim 30\,\%$ cold matter including dark matter and with a tiny amount of radiation. We are therefore in the dark energy dominated epoch of the universe. Since dark energy has $w = -1$, the right hand side of the second Friedmann equation is greater than zero(equation 1.6). Therefore in the dark energy dominated epoch, the expansion of the universe accelerates with time. Even though radiation has negliglible influence on the evolution of the universe today since the density of radiation drops off much faster than matter or dark energy, radiation played a critical role early in the history of the universe when it contributed a much greater fraction of the total energy density.

1.2 The Cosmic Microwave Background

The Cosmic Microwave Background (CMB), which was first discovered by Penzias and Wilson in the 1960s, is one of the key observables that have informed the

development of the standard Hot Big Bang model of cosmology. We understand the CMB to be the relic radiation from when the universe was roughly 380,000 years old. During this epoch, called recombination, the universe cooled enough for neutral hydrogen to form. The formation of neutral hydrogen decouples the radiation in the universe from the baryons, making the universe transparent. Since then, these photons have been free-streaming towards us, cooling down as the universe expanded, and now observed as the CMB. Before recombination, the photons, free electrons and protons were strongly coupled together into an opaque plasma. Before recombination, the rate of Compton scattering between the photons and the free electrons was much faster than the expansion rate of the universe and therefore the hot plasma was in thermal equilibrium. This is why the CMB has a blackbody spectrum with a temperature of 2.7525K as measured by the FIRAS instrument on the COBE satellite.

Recombination occurred when the universe, having expanded adiabatically, cooled to reached a temperature of $\sim 4000K$ at a redshift z $\sim$ 1100. At first glance, we would expect recombination to occur once the temperature of the universe is lower than 13.6 eV, the first ionization energy of Hydrogen[1]. However since the number density of photons in our universe is greater than that of baryons by about 10 orders of magnitude, the number density of photons with energy above the ionization energy of hydrogen due to the tail in the Planck distribution of photon energy, remains higher than the baryon number density until the universe is much cooler. At recombination, the free electron density drops rapidly and therefore recombination is a snapshot of the universe in a narrow window in time.

The CMB is not only a blackbody, but it is also very isotropic across the entire sky. The global (monopole) CMB signal is well described by a single temperature $T_{\rm CMB} = 2.7525K$. In addition, there is also a dipole signal of amplitude $\Delta T/T_{\rm CMB} \sim 10^{-2}$ which is believed to be sourced by our motion relative to the last scattering surface. In addition to the dipole, the CMB has smaller fluctuations in temperature less than 1 part in 10^4 at all angular scales as measured from space by both the DMR instrument on COBE and the later Planck satellite and by many ground based experiments. Figure 1.1 shows the full sky map of the CMB temperature anisotropies as measured by *Planck*.

[1] Recombination into the ground state of hydrogen is actually quite inefficient since the ionization cross-section for Ly-α photons is quite high leading to no net recombination. More efficiently, electrons can be captured into the 2s level and then subsequently decay into the 1s state. See the discussion in Peebles, 1993

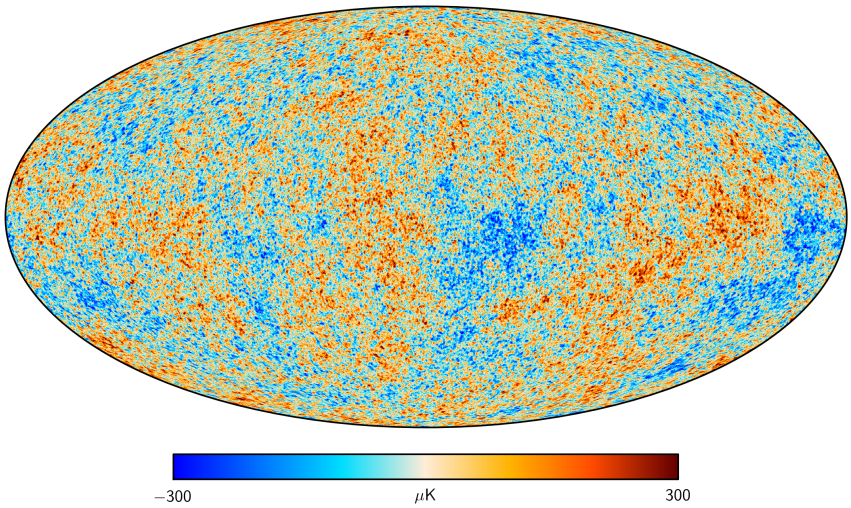

Figure 1.1: Full sky CMB temperature anisotropy as measured by *Planck* from their 2015 data release.

Since the CMB is observationally a sphere on sky, the fluctuations can be naturally described in terms of a spherical harmonics Y_{lm} basis. Let $T(\theta,\phi) = T_{\rm CMB}\left[1+\Theta(\theta,\phi)\right]$, then

$$\Theta(\theta,\phi) = \sum_{l=1}^{l=\infty}\sum_{m=-l}^{m=l} a_{lm}^{T} Y_{lm}(\theta,\phi)\,. \tag{1.11}$$

The superscript T shows that we are considering temperature fluctuations here.

A key goal of modern cosmology is to characterize the distribution of these anisotropies in the CMB in order to make comparisons of theory to observation. Since we expect the fluctuations to be well described by a Gaussian random field[2], $\left\langle a_{lm}^{T}\right\rangle = 0$, and the angular power spectrum C_l^{TT} captures the variance in the distribution of fluctuations as a function of angular scale.

$$C_l^{TT} = \frac{1}{2l+1}\sum_{m=-l}^{m=l}\left(a_{lm}^{T*}a_{lm}^{T}\right) \tag{1.12}$$

Since for a given l, each a_{lm} is drawn from the same distribution, there is only a finite number of modes at a given l. This limit to the amount of statistical information, called *cosmic variance* is quite significant at the largest scales. Quantitatively, the uncertainity ΔC_ℓ is given by

[2]This is motivated by tracing the origins of the fluctuations back to the initial quantum fluctuations during inflation.

$$\Delta C_\ell = \frac{2}{2l+1} C_\ell^2. \tag{1.13}$$

Cosmic variance is a limit to the precision with which the underlying statistical distribution that generates the large scale modes on the sky can be measured.

CMB anisotropies are sensitive to not only the composition of the universe, but also the initial conditions for seeding the perturbations. Figure 1.2 shows the measured full-sky temperature power spectrum and a best fit model to the underlying cosmology that generates the fluctuations. The related quantity $\mathcal{D}_\ell^{TT} = [(l(l+1))/(2\pi)]\, C_\ell^{TT}$ is traditionally plotted since in this quantity, the spectrum for a scale invariant cosmology is expected to be flat at the largest scales. The best fit model is a 6 parameter ΛCDM model. This thesis does not discuss the best fit model to depth, but in order to give a sense of how the underlying cosmology shapes the spectrum, we will highlight a few of the parameters. The location of the first peak constrains the mean spatial curvature Ω_K giving a value of Ω_Λ. The ratio of the 2nd and 3rd peaks constrains both the total matter (dark matter + baryons) fraction Ω_m and the baryon fraction Ω_b. The tilt of the primordial spectrum n_s is measurable at low l. A strong deviation from $n_s = 1$ supports the theory of inflation described in section 1.3. The locations of the acoustic peaks also favors adiabatic modes (perturbations that affect all the cosmological species while keeping their relative number densities unperturbed) over isocurvature modes (perturbations in the entropy) as the initial conditions for inflation.

1.3 Inflation

The Big Bang cosmology framework was remarkably successful in providing a framework for explaining the relative abundance of light elements, the observed expansion of the universe and the existence of the relic microwave radiation. However, it does not naturally predict the observed isotropy of the CMB, the flatness of the universe nor provides a mechanism for generating the initial perturbations that seed the growth of large scale structure.

Inflation is a paradigm that was first proposed by Alan Guth to supplement the hot Big Bang model. Inflation proposes that the universe went through a period of rapid accelerated exponential expansion for $\sim$ 60 e-folds before standard Big Bang expansion commences. However, inflation requires exotic physics because for accelerated expansion of the universe we require matter with $w < -\frac{1}{3}$ in the equation of state.

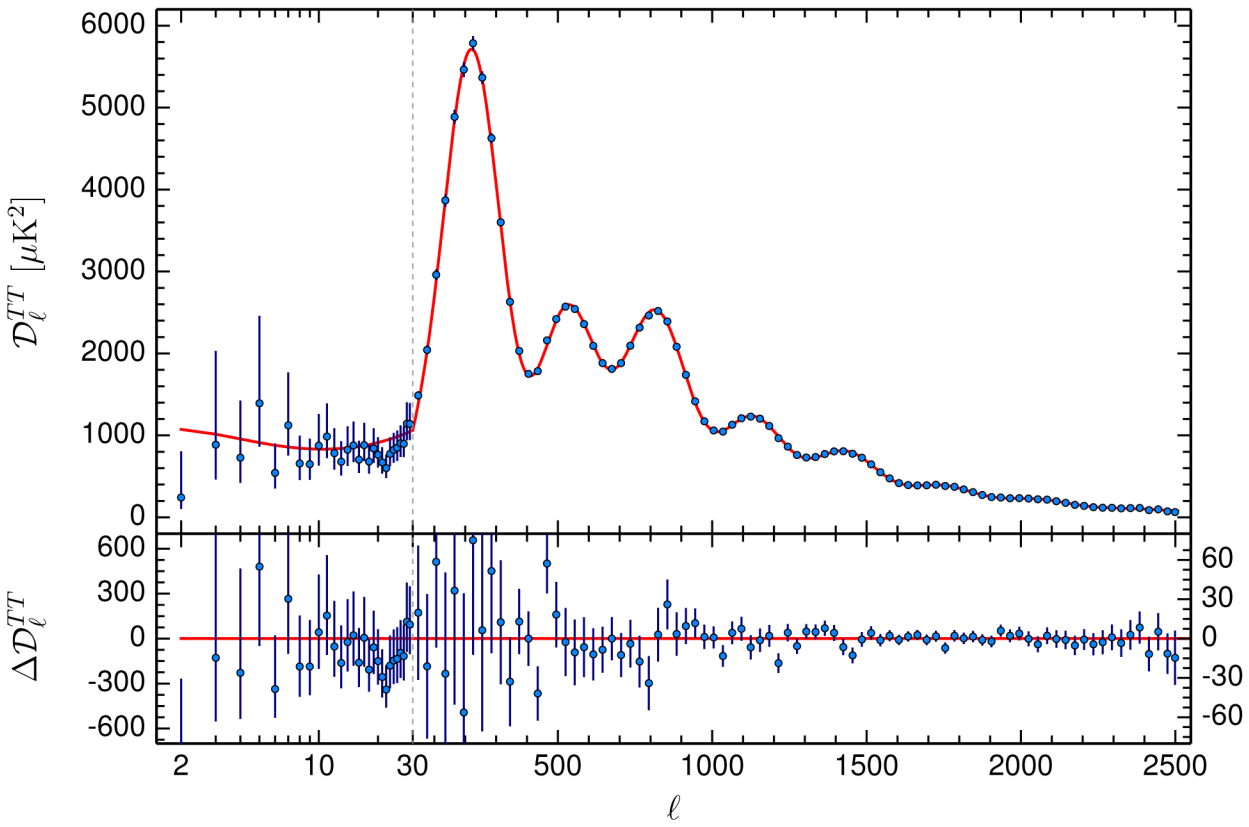

Figure 1.2: The power spectrum of temperature fluctuations of the CMB as measured by *Planck* from their 2015 data release. The red curve is the best fit to a six parameter model that describes the cosmology with the residuals from the fit in the bottom plot. The larger error bars for low l data is due to the cosmic variance limit. $l \sim 80$ corresponds to scales of about 1 ° on sky.

Regardless, inflation naturally addresses a number of key questions in the standard model of cosmology. Two important puzzles are: the Horizon Problem and the Flatness Problem. Since Guth and Linde's early work, the theory of inflation has been further developed and checked observationally against the anisotropy spectrum of the CMB. The observable predictions of inflation such as a background of cosmic gravitational waves or non-gaussianity (depending on the nature of inflation) are the focus of many current and future cosmic observatories.

Horizon Problem

The high level of isotropy of the CMB as measured today is an important puzzle in cosmology called the Horizon problem. In order for the CMB to be so uniform as measured in the present epoch, the entire observable universe as seen today, must have been in thermal equilibrium at some point before recombination. However, given our knowledge of the history of the universe, we know that at recombination,

the comoving horizon corresponds to an angular scale of about 2° on sky today. The observable universe consisted of many causally disconnected patches. It is remarkable that large scale isotropy can be observed in the CMB.

Inflation provides a mechanism to bring regions in the observable universe that we now see to be flat into thermal contact with each other before pushing them out of causal contact.

Flatness Problem

Measurements of the CMB show the universe to be spatially flat. A joint constraint of Planck data with Baryon Acoustic Oscillation (BAO) measurements sets $\Omega_K = 0.0007 \pm 0.00037$. However, in the FRW model, a flat geometry is an unstable equilibrium. To see this, we can recast the first Friedmann equation (equation 1.5) as

$$1 - \Omega = -\frac{K}{(aH)^2}. \tag{1.14}$$

The comoving Hubble radius $(aH)^{-1}$ has increased during the matter and radiation dominated epochs of the universe. However, an increasing Hubble radius drives Ω away from one. Even small deviations in K away from 0 would cause the universe to develop curvature with time. It therefore seems contrived that the universe appears so flat today.

Inflation provides a natural mechanism for decreasing the Hubble radius while stretching out space in the early universe. This removes the fine-tuned requirement need to match the observed geometry of the universe.

Slow-Roll Inflation

A simple but powerful model for inflation is slow-roll scalar inflation which proposes that the universe was permeated by a scalar field ϕ called the inflaton evolving under a potential $V(\phi)$. The stress-energy tensor of the field gives the energy and pressure, respectively, as

$$\rho = \frac{1}{2}\dot{\phi}^2 + V(\phi), \tag{1.15}$$

and

$$p = \frac{1}{2}\dot{\phi}^2 - V(\phi). \tag{1.16}$$

If the dynamics of the field is dominated by the potential ($\frac{1}{2}\dot{\phi}^2 \ll V(\phi)$), then $p \approx -\rho$ and the scalar field has the negative pressure needed to generate accelerated expansion of the universe. This is the first slow-roll condition. The energy conservation equation (1.7) gives the dynamics of the inflation field,

$$\ddot{\phi} + 3H\dot{\phi} - \frac{\mathrm{d}V}{\mathrm{d}\phi} = 0. \tag{1.17}$$

This is the equation of a damped harmonic oscillator where the Hubble expansion generates the friction term that damps the oscillations in the field. The second slow-roll condition is that the kinetic energy term remains small for a sufficiently long enough period of time, i.e., $|\ddot{\phi}| \ll 3H|\dot{\phi}|$. These 2 conditions can be recast by defining 2 variables ϵ, η (not to be confused with the conformal time) that vanish when ϕ is no longer evolving. These variables can be expressed given the Planck mass M_{pl} as

$$\epsilon \equiv \frac{\dot{H}}{H^2} \ll 1, \tag{1.18}$$

$$\eta \equiv -\frac{\dot{\epsilon}}{H\epsilon} \ll 1. \tag{1.19}$$

The number of e-folds N_e in the exponential expansion of the universe is

$$N_e = \int_{a_i}^{a_f} d\ln a = \int_{t_i}^{t_f} dH \simeq \int_{\phi_{end}}^{\phi} \frac{V}{dV/d\phi} d\phi. \tag{1.20}$$

In order to solve the Horizon problem, inflation must last for about 50-60 e-folds. The exact number of e-folds however, depends on the energy density in the field at reheating when the energy in the inflaton field is converted to kinetic energy, breaking the slow-roll condition and ending the inflationary epoch.

Perturbations in Inflation

Inflation predicts that the anisotropies of the CMB and the perturbations that seed the growth of large scale structure in the universe were generated by the zero-point

vacuum quantum fluctuations of the inflaton field. These become the nearly scale-invariant spectrum that we see today. In order to study the initial conditions for structure formation, we need to consider the perturbations in both the inflaton field ϕ and the metric $g_{\mu\nu}$.

To first order, the perturbation in the inflaton is given by

$$\phi(\vec{x}, t) = \bar{\phi}(t) + \delta\phi(\vec{x}, t), \tag{1.21}$$

where $\bar{\phi}$ is the unperturbed field and $\delta\phi$ the perturbation. Similarly the perturbations to the metric can be expressed as

$$g_{\mu\nu}(\vec{x}, t) = \bar{g}_{\mu\nu}(t) + h_{\mu\nu}(\vec{x}, t), \tag{1.22}$$

with $\bar{g}_{\mu\nu}$ the unperturbed FRW metric. Perturbations to the metric can be decomposed into 4 scalar modes, 2 vector components (each with 2 degrees of freedom) and a single transverse traceless tensor (with 2 degrees of freedom). This decomposition totals the 10 degrees of freedom in the original perturbation. Scalar perturbations of the metric couple to the density of matter and radiation. Vector perturbations decay away as the universe expands. The tensor perturbations are gravitational waves which do not couple directly to matter but do induce fluctuations in the polarization of the CMB.

Since the perturbations are small, we can work in a linear approximation. This allows us to switch to Fourier space where the perturbative modes evolve independently. Isotropy requires that each mode is labelled only by its wavenumber $k = |\vec{k}|$ and not its direction. During inflation, quantum mechanical perturbations are induced when all the modes at relevance scales today were in causal contact. These modes were then forced outside the causal horizon by inflation once $k < aH$. At this point, the modes stop evolving and then re-enter much later as the initial conditions for the growth of structure and anisotropy. All modes with the same wavenumber enter the horizon simultaneously and in phase. It is this coherence that leads to the peaks and troughs in the CMB anisotropy spectrum.

The scalar perturbations can be described by a power spectrum $P_s(k)$ parametrized by a power law with amplitude A_s and spectral index n_s as

$$P_s(k) = A_s k^{n_s - 4}. \tag{1.23}$$

A power spectrum with $n_s = 1$ is said to be scale invariant. Inflation predicts that n_s deviates slightly from 1. Expressed in the slow roll parameters, we find that

$$n_s = 1 - 4\epsilon - 2\eta. \tag{1.24}$$

Similarly, the power spectrum of tensor perturbations is:

$$P_t(k) \ = A_t k^{n_t - 3}. \tag{1.25}$$

A scale invariant tensor spectrum therefore has $n_t = 0$. The spectral index of tensor perturbations generated by inflation is

$$n_t = -2\epsilon. \tag{1.26}$$

This is one of the most robust predictions of inflation. For both scalar and tensor perturbations, we can define dimensionless power spectra Δ_s^2, Δ_t^2 close to scale invariant such that

$$\Delta^2 \equiv \frac{k^3}{2\pi^2} P(k). \tag{1.27}$$

The primordial perturbations are usually parametrized by the tensor-to-scalar ration r

$$r \ = \ \frac{\Delta_t^2}{\Delta_s^2} \ = 16\epsilon, \tag{1.28}$$

which is proportional to the potential energy scale of the inflaton field.

$$V^{1/4} \sim \left(\frac{r}{0.01}\right) 10^{16}\text{GeV}. \tag{1.29}$$

A measurably large r allows us to explore physics at the Grand Unified Theory (GUT) scale. Since $r = -8\ n_t$, measuring the spectral tilt of tensor perturbations is a powerful probe their primordial origins. The current best constraint on r is $r_{0.05} < 0.035$, (95% CL), with $\sigma(r) = 0.009$ (Ade, Ahmed, Amiri, Barkats, et al., 2021) at the pivot scale $k_0 = 0.05\ \text{Mpc}^{-1}$. Figure 1.3 shows the

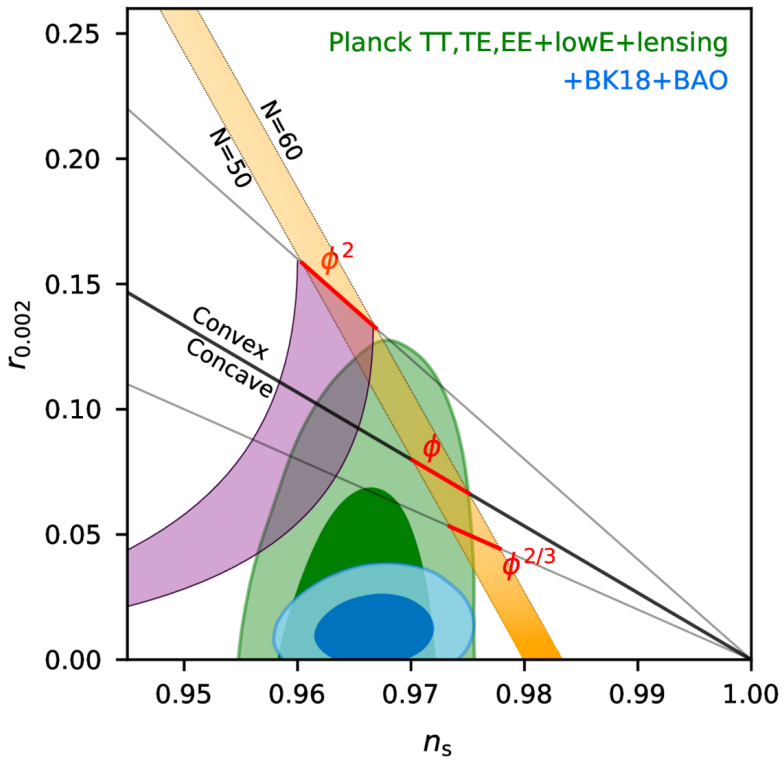

Figure 1.3: Joint constraints in the r (at the pivot scale $k_0 = 0.002$ Mpc^{-1}) vs. n_s plane for the Planck 2018 baseline analysis (Planck Collaboration, Aghanim, N., et al., 2020), with BICEP/Keck data acquired through the end of the 2018 season (Ade, Ahmed, Amiri, Barkats, et al., 2021). Baryon Acoustic Oscillation (BAO) data was also added to improve constraints on n_s. The black lines are the predicted values for a few single field polynomial inflation models along with the $N_e = 50$ and $N_e = 60$ e-fold contour boundaries. The purple band represents natural inflation. Once popular models are now largely ruled out by the BK data at the 2σ level.

From Primordial Fluctuations to CMB anisotropies

Scalar perturbations generated during inflation remain largely constant when they are outside the horizon. As they enter the horizon, they begin to evolve through the epochs of radiation and matter domination. Before recombination, these perturbations couple to both the radiation and matter distributions. The combined effect of gravitational instability and radiation pressure causes the perturbations to evolve as acoustic waves in the baryon-photon plasma. Overdensities in the plasma during recombination result in redshifted photons because the photons must climb out of the potential well to free stream towards us.

Given the primordial scalar power spectrum $P_s(k)$, the temperature angular power spectrum as measured today is given by

$$C_l^{TT} = \frac{2}{\pi} \int_0^\infty \mathrm{d}k k^2 P_s(k) |\Delta_{T,l}(k)|^2, \tag{1.30}$$

where $\Delta_{T,l}(k)$ is a transfer function that accounts for the evolution of a mode from horizon re-entry to recombination and the geometric projection to the CMB sphere.

The largest scale modes have hardly evolved since they were the last to cross the horizon before recombination. Therefore, they preserve the initial perturbation spectrum from inflation. The power spectrum for those modes is given by $l(l+1)C_\ell^{TT} \propto l^{n_s-1}$. To date, n_s has been measured to be less than 1 decisively using data from *Planck's* CMB TT Power Spectrum. However, the measurement using only the temperature data is limited by cosmic variance. Anisotropies in the polarization of the CMB provide us with an additional probe of inflationary cosmology.

1.4 Polarization of the Cosmic Microwave Background

Generation of Polarization

During recombination, the CMB is weakly polarized by the Compton scattering of CMB photons off electrons in the plasma. However, isotropic radiation cannot generate a net polarization through Compton scattering. The contributions from different directions cancel to generate zero polarization in the line of sight. Dipole anisotropies, also do not generate any net polarization. A quadrupolar anisotropy is the simplest incoming radiation pattern required to generate a net polarization. This fact has important consequences for CMB cosmology.

As already discussed, scalar perturbations from inflation source density perturbations in the baryon-photon plasma. These density perturbations generate a velocity gradient field in the plasma under the action of gravitational attraction and radiation pressure. The velocity field is responsible for the quadrupole anisotropy because photons approaching an electron from different directions will be Doppler shifted by different amounts. We therefore expect the polarization generated by scalar perturbations to be correlated to the temperature anisotropies. This polarization is even under parity inversion because the polarization direction is perpendicular to the gradient of the amplitude of the polarization signal. Such even parity modes are commonly referred to as E-modes.

The quadrupole signal is very small because the electrons and photons are tightly coupled to each other and therefore the mean free path of the photons is quite short. After recombination, the electron density is too small for Compton scattering to

occur efficiently. The polarization anisotropy signal can therefore be produced only within a small window around recombination and is therefore much fainter than the temperature anisotropy.

The tensor perturbations that create a stochastic background of primordial gravitational waves also polarize the CMB. The distortion of space by the gravitational waves as they travel also generates quadrupolar anisotropies. However, in this case, the anisotropies are not rotationally invariant around the direction of propagation and have a handedness to them. These modes can again be decomposed into even parity E modes and additionally odd parity B modes. Since the B mode polarization signal is generated only by tensor and not scalar perturbations, the measurement of primordial B mode polarization of the CMB is a clean test for primordial gravitational waves. B modes and E modes are in orthogonal subspaces of the polarization field and therefore the B mode signal is not limited by the cosmic variance of the E mode signal.

Stokes Parameters

The combined temperature and polarization signal on sky can be decomposed into the 4 Stokes' parameters, [I, Q, U, V]. A monochromatic polarized plane electromagnetic wave is specified by its propagation vector $\vec{k}$ and its complex Jones vector (E_1, E_1) in two basis directions $(\hat{\epsilon}_1, \hat{\epsilon}_2)$. For convinience, we will choose the propagation direction as the $\hat{z}$ direction and $\hat{\epsilon}_1 = \hat{x}, \hat{\epsilon}_2 = \hat{y}$. Its the transverse wave vector has a decomposition into its two components as:

$$E_x(z,t) = E_{0x}\cos\left(kz - \omega t + \theta_x\right) \tag{1.31}$$

$$E_y(z,t) = E_{0y}\cos\left(kz - \omega t + \theta_y\right) \tag{1.32}$$

where $E_1 = E_{0x}e^{i\theta_x}$ and $E_2 = E_{0y}e^{i\theta_y}$.

The 4 Stokes parameters are defined as:

$$I = \left\langle E_{0x}^2\right\rangle + \left\langle E_{0y}^2\right\rangle \tag{1.33}$$

$$Q = \left\langle E_{0x}^2\right\rangle - \left\langle E_{0y}^2\right\rangle \tag{1.34}$$

$$U = 2\left\langle E_{0x}E_{0y}\right\rangle\cos\left(\theta_x - \theta_y\right) \tag{1.35}$$

$$V = 2\left\langle E_{0x}E_{0y}\right\rangle\sin\left(\theta_x - \theta_y\right). \tag{1.36}$$

I represents the total intensity of the wave while Q and U are the 2 linear polarizations. The angle brackets represent time averaging. The 4th parameter V is the degree of circular polarization. Compton scattering only generates linear polarization therefore we expect $V = 0$ in the early universe.

Our decomposition of the plane wave is coordinate dependent. When the 2 axes are rotated through an angle ϕ about the propagation axis, Q,U changes by $(Q \pm iU) = e^{\mp i2\phi}(Q \pm iU)$. The polarization field has symmetry under rotations by π and is therefore a spin-2 field and can be decomposed in spin-2 weighted spherical harmonics:

$$(Q \pm iU)(\hat{n}) = \sum_{lm} a_{\pm 2,lm\,\pm 2}Y_{lm}(\hat{n}). \tag{1.37}$$

A more useful parametrization is to use the two coordinate-invariant quantities referred to as E and B modes. The E and B modes are defined as:

$$a^E_{lm} = -\frac{1}{2}\left(a_{2,lm} + a_{-2,lm}\right) \tag{1.38}$$

$$a^B_{lm} = \frac{i}{2}\left(a_{2,lm} - a_{-2,lm}\right), \tag{1.39}$$

so that

$$(Q \pm iU)(\hat{n}) = \sum_{lm}\left(a^E_{lm} \mp i a^B_{lm}\right)\,{}_{\pm 2}Y_{lm}(\hat{n}). \tag{1.40}$$

And the power spectra:

$$C^{EE}_\ell = \frac{1}{2l+1}\sum_{m=-l}^{m=l}\left(a^{E*}_{lm}a^E_{lm}\right) \tag{1.41}$$

$$C^{EB}_\ell = \frac{1}{2l+1}\sum_{m=-l}^{m=l}\left(a^{E*}_{lm}a^B_{lm}\right) \tag{1.42}$$

$$C^{BB}_\ell = \frac{1}{2l+1}\sum_{m=-l}^{m=l}\left(a^{B*}_{lm}a^B_{lm}\right). \tag{1.43}$$

Under this definition, E modes are even under parity inversion while B modes are odd. As discussed, tensor perturbations generate both E and B modes on sky, while

scalar perturbations generate only E modes. Oscillations in the E mode spectrum are out of phase with the temperature spectrum. This is because the E modes are primarily sourced by the dipole at recombination while the temperature anisotropies are sourced by both the monopole and dipole terms. The dipole is proportional to the velocity of the baryon-photon fluid. Since the velocity is maximum for modes halfway between their compression or rarefaction extrema, the dipole is out phase with the monopole which peaks at the extrema. The primordial B mode signal peaks at lower angular scales since B modes are only created by the tensor modes that cross the horizon at recombination. These modes subsequently decay rapidly. The primordial B-mode signal is expected to peak at $l \approx 80$.

1.5 Reionization and Weak Lensing

The polarization signal from recombination is altered by two main processes before it is detected today: weak gravitational lensing and re-ionization. Reionization is the Thomson scattering of the free streaming CMB photons by free electrons along the line of sight once the universe becomes reionized by a redshift $z \sim 6$. Reionization is parametrized by the optical depth to reionization τ, once of the 6 ΛCDM parameters. Reionization damps anisotropies generated at recombination by a factor $e^{-\tau}$. Re-ionization also enhances the polarization signal at the largest scales of $l \leq 30$. The height and position of the polarization bump depends on the mean reionization redshift and the duration of reionization. τ is the least well constrained with an uncertainty of about 10% in comparison with the sub percent precision on the other parameters. A direct measurement of τ on the reionization peak will also break the degeneracy between τ and A_s, the amplitude of the scalar perturbations. The reionization peak has only been directly measured on full sky-polarized observations from space (both EE and TE) by WMAP and *Planck*. Large scales on sky are difficult to access from ground based observatories but are targeted by projects such as CLASS (Essinger-Hileman et al., 2014).

Weak lensing is the distortion of the initial polarization pattern by the gravitational effect of large scale structure between us and the surface of last scattering. The effect is to remap the observed temperature and polarization maps by the gradient of the gravitational potential projected along the line of sight ϕ:

$$\Theta(\hat{n}) = \tilde{\Theta}\left(\hat{n} + \nabla\phi\right) \tag{1.44}$$

$$\left(Q(\hat{n}) \pm iU(\hat{n})\right) = \left(\tilde{Q}(\hat{n}) \pm i\tilde{U}(\hat{n})\right)\left(\hat{n} + \nabla\phi\right). \tag{1.45}$$

The lensing potential ϕ is an integral over the gravitational potential Ψ along the line of sight

$$\phi = -\int_0^{D_s} \mathrm{d}D \frac{D_s - D}{D D_s} \Psi\left(D\hat{n}, D\right) \tag{1.46}$$

where D is the comoving distance along the line of sight and D_s is the distance to the surface of last scattering. By working with sufficiently small sections of sky, we can use the flat sky approximation and work in Fourier space to get a sense of the impact of lensing on the temperature and polarization anisotropies (Hu and Okamoto, 2002). The changes in the anisotropy moments are

$$\delta\Theta(\vec{l}) = \int \frac{\mathrm{d}^2 l'}{(2\pi)^2} \tilde{\theta}(\vec{l'}) W(\vec{l'}, \vec{L}), \tag{1.47}$$

$$\delta E(\vec{l}) = \int \frac{\mathrm{d}^2 l'}{(2\pi)^2} \left[\tilde{E}(\vec{l'}) \cos 2\psi_{\vec{l'},\vec{l}} - \tilde{B}(\vec{l'}) \sin 2\psi_{\vec{l'},\vec{l}}\right] W(\vec{l'}, \vec{L}), \tag{1.48}$$

$$\delta B(\vec{l}) = \int \frac{\mathrm{d}^2 l'}{(2\pi)^2} \left[\tilde{B}(\vec{l'}) \cos 2\psi_{\vec{l'},\vec{l}} + \tilde{E}(\vec{l'}) \sin 2\psi_{\vec{l'},\vec{l}}\right] W(\vec{l'}, \vec{L}), \tag{1.49}$$

where $\psi_{\vec{l'},\vec{l}} = \psi_{\vec{l'}} - \psi_{\vec{l}}$, $\vec{L} = \vec{l} - \vec{l'}$, and $W(\vec{l'}, \vec{L}) = -\left(\vec{l'} \cdot \vec{L}\right) \phi(\vec{L})$. $\cos\psi_{\vec{l}} = \hat{n} \cdot \vec{l}$. Since $\tilde{B}$ is small, the effect of lensing on E modes is similar to that in Θ when $\cos\psi_{\vec{l'},\vec{l}} \approx 1$ for $L \ll l$, when the lens is smooth compared to the deflection. The lensing potential peaks at $L \sim 50$ because the line of sight deflects coherently by a few degrees. Lensing smooths the peaks and troughs of the temperature and E mode power spectra. In contrast, lensing will generate B mode polarization even in the absence of unlensed B mode polarization. Because lensing generates B modes from E modes, the lensing B mode signal peaks at much smaller angular scales. These modes have non-vanishing EB and TB correlation. This is expected because large scale structure formation is a non-linear process and therefore these lensed modes are both anisotropic and non-Gaussian. For $\ell \leq 200$, lensing generates B modes that look like white noise. The lensed contribution to the B mode spectrum dominates over the primordial B mode spectrum for many possible values of r as shown in fig. 1.4. Measurement of the primordial B mode power spectrum requires reconstructing the lensing potential from a suitable tracer such as the small scale E mode anisotropy map. The reconstructed lensing potential can then be used to

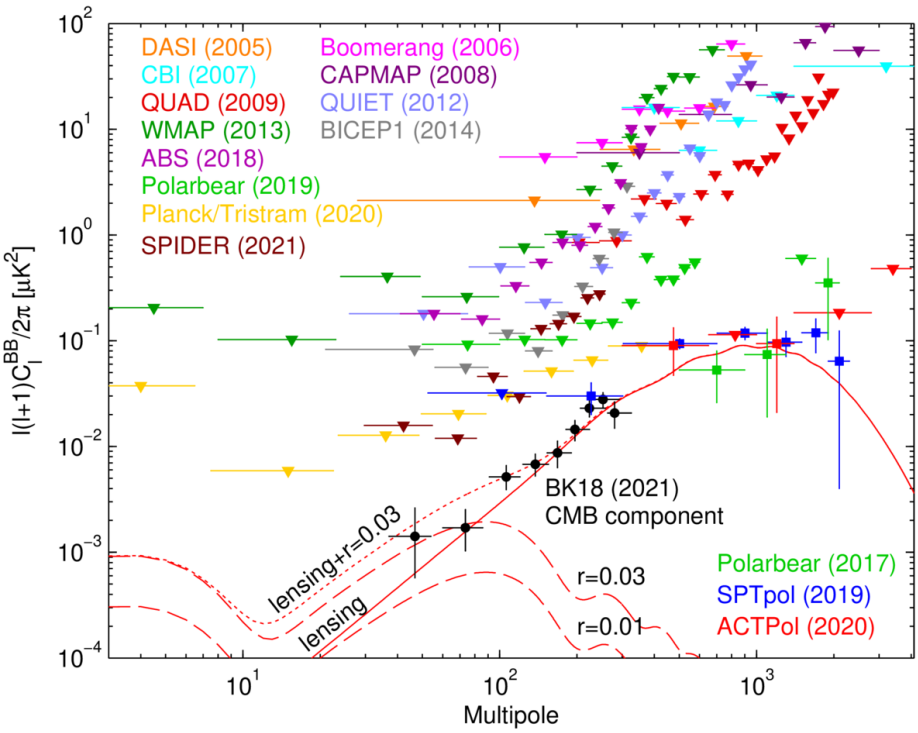

Figure 1.4: A summary of publsihed CMB B-mode polarization upper limits and detections up to 2021. The lensing B-mode signal has been detected by BICEP, SPT, POLARBEAR and ACT collaborations. Also included are theoretical predictions shown for the lensing B-modes signal in solid red. Primordial B-modes are shown in dashed red for two values of r peaking at degree angular scales.

reduce the effective lensing sample variance in the B mode measurements at the scale of interest ($\ell \sim 80$). This subtraction procedure is referred to as delensing and is essential for achieving the targetted uncertainities on r for current and future CMB experiments (Abazajian et al., 2016; Ade, Ahmed, Amiri, Anderson, et al., 2021). The lensing signal is interesting in its own right as a powerful tool for studying the cumulative matter power spectrum. The lensing potential is sensitive to parameters such as the sum of neutrino masses, or the equation of state of dark energy that impact structure formation in the late history of the universe. It is therefore complementary to galaxy surveys and particle experiments as a probe to constraining these quantities.

1.6 Foregrounds

Efforts to detect the cosmic B mode polarization signal are also confounded by the presence of polarized galactic foregrounds with the strongest of these signals being due to galactic synchrotron radiation and the polarized emission from dust

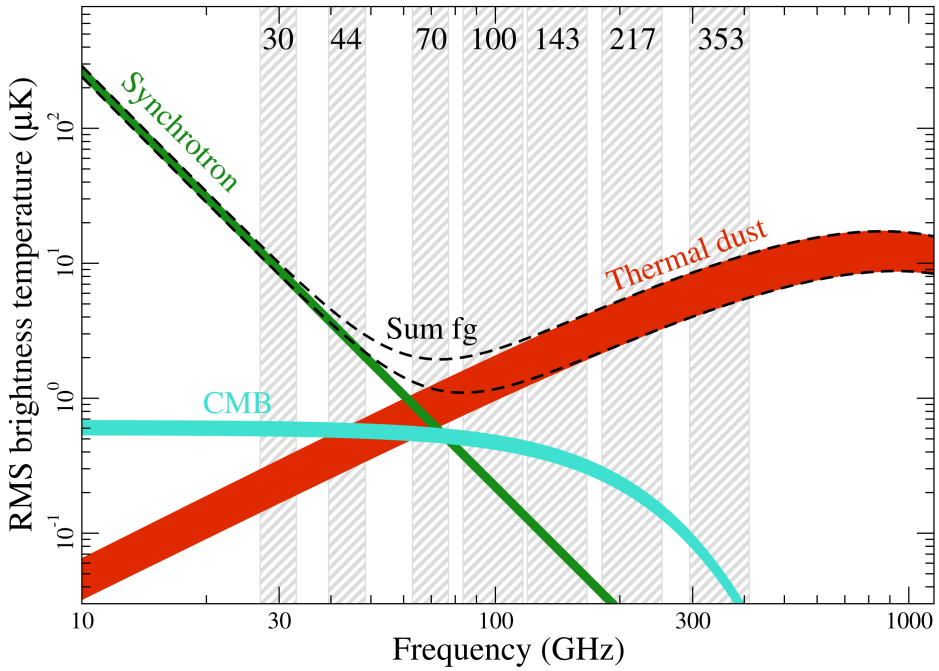

Figure 1.5: Diffuse polarized galactic foregrounds and their spectral dependence as measured by *Planck* from their 2015 data release (Planck Collaboration, Adam, R., Ade, P. A. R., Aghanim, N., Alves, M. I. R., et al., 2016). The amplitude of the foregrounds are presented as the rms brightness temperature

grains. However, since the foreground signal is not distributed uniformly on sky, CMB observers have been able to select patches of sky where the foregrounds are at their lowest. Additionally, as shown in figure 1.5 , the foregrounds have a spectral signature different from that of the CMB's blackbody spectrum. These foregrounds can in principle be characterized and subtracted from CMB maps if the sky is mapped at multiple frequency channels.

Synchrotron Radiation

Diffuse synchrotron emission is generated by relativistic cosmic-ray electrons accelerated by the galactic magnetic field. Synchrotron radiation can have a polarization fraction as high as 75%, but this is typically lower due to line of sight averaging. Theoretical models and observations suggest that synchrotron radiation is well approximated by a power law with index $\beta \approx -3$ at frequencies above 20 GHz. The synchrotron brightness temperature $T(\nu) \propto \nu^{-\beta}$, where the power law index β relates to the power law SED of the electrons, $N(E) \propto E^{-p}$ where $\beta = (p+3)/2$. The negative spectral index makes synchrotron the dominant foreground at lower frequencies.

Dust Emission

Interstellar dust grains are thermally excited by absorbing background starlight. They cool down through thermal emission which can be described as blackbody radiation with a frequency dependent emissivity. Thermal dust typically has a temperature of about 20K and is the dominant foreground in the higher frequency CMB bands. These grains are aspherical and can have large magnetic moments. This causes them to align with their long axis perpendicular to the magnetic field lines of the interstellar media. As a result, they absorb radiation with a partial polarization perpendicular to the fieldlines. Polarized dust emission is typically modelled as

$$I(\nu) \propto \ell^{\alpha_d} \nu^{\beta_d} B\left(\nu, T_d\right), \tag{1.50}$$

where α_d is the spatial index, β_d the power index of the emissivity and T_d the dust temperature.

1.7 Design Requirements for CMB Polarimetry

The goal of any CMB experiment is to make estimates and quantify uncertainities on cosmological parameters by making maps of the CMB temperature and polarization on a part of, or the whole sky. The data analysis pipeline transforms large quantities of time ordered data, often taken across multiple observatories for many years, first into maps of the sky, then one dimensional power spectra and finally a small set of cosmological parameters. At each step, care must be taken to appropriately deal with systematics of the instrument and observing strategy, as well as noise and analysis artifacts in the data. These details are far beyond the scope of this section. Our goal is to instead consider the requirements that observing the CMB imposes on the telescope design.

We consider a fiducial CMB experiment observing a fraction of sky f_{sky} for an observed period t_{obs} seeking to set constraints only on the scalar-to-tensor ratio r. Our goal is to estimate a single power spectrum C_ℓ in bands centered at ℓ and with a bandwidth of $\Delta\ell$. The underlying cosmology makes predictions of C_ℓ through a model with a set of cosmological parameters. We can use a Fisher matrix formalism to study the uncertainties on the model parameters from the measurement.

Since the effect of tensor modes on the temperature and E-mode power spectrum is small, constraints on r are primarily set by the B-mode power spectrum (given

perfect delensing and setting aside the enhancement in the low-ℓ B mode spectrum). In this limit, the Fisher matrix reduces to (Wu, 2015)

$$F_{ij} \;=\; \sum_{\ell} \frac{1}{(\Delta C_\ell)^2} \left(\frac{\partial C_\ell^{B_{\rm tensor}}}{\partial r} \right)^2 , \tag{1.51}$$

where $C_\ell^{B_{\rm tensor}}$ is the tensor contribution to the B mode power spectrum and

$$(\Delta C_\ell)^2 \;=\; \frac{2}{(2\ell+1)\, f_{sky}} \left(C_\ell^{B_{\rm tensor}} + N_\ell^{inst} + N_\ell^{fg} + N_\ell^{res} \right)^2 . \tag{1.52}$$

The error in the measurement of the power spectrum ΔC_ℓ in eq. (1.52) has contributions from both the cosmic variance, the instrument noise N_ℓ^{inst}, the foreground N_ℓ^{fg} and the residuals from delensing N_ℓ^{res} .The instrument noise covariance (Bowden et al., 2004) is given by

$$N_\ell = |B_\ell|^{-2} \cdot \Omega_{pix} \sigma_{pix}^2, \tag{1.53}$$

where Ω_{pix} is the instrument solid angle per pixel and B_ℓ is the azimuthally averaged spherical harmonic transformation of the telescope beam. Typically, the beam is Gaussian with full width at half maximum beam size, $\theta_{\rm FWHM}$ so that

$$|B_\ell|^2 \;=\; \exp\left(-l(l+1) \frac{\theta_{\rm FWHM}^2}{8 \ln 2} \right). \tag{1.54}$$

The pixel noise σ_{pix} for an experiment covering a fraction f_{sky} of the total sky area A_{sky} with N_{det} detectors each of sensitivity, NET is

$$\sigma_{pix}^2 \;=\; \frac{{\rm NET}_{\rm CMB}^2 f_{sky} A_{sky}}{t_{obs} N_{det} \Omega_{pix}}. \tag{1.55}$$

Appendix A details how to calculate the single pixel NET of CMB receiver. The integrated sensitivity of a CMB experiment is given by the map noise achieved at the end of observations. Using eq. (1.53), we can see that the polarization map depth s at a single frequency, is the quantity $s^2 \;=\; 2\sigma_{pix}^2 \cdot \Omega_{pix}$, typically expressed in units of μK·arcmin. The polarization map depth is $\sqrt{2}$ higher than the temperature map depth because pairs of detectors are used to construct the polarized signal.

As an example, a polarimeter with $\theta_{\rm FWHM} = 0.2°$observing at 150 GHz fielding 1024 detectors with single pixel NET of $350\mu{\rm K}\cdot\sqrt{s}$ and observing 1% of the sky continuously for 5 years, will achieve a map depth of about 2 μK $\cdot$ arcmin and $\frac{\ell(\ell+1)}{2\pi}N_\ell \sim 1\times10^{-4}\mu{\rm K}^2$ at $\ell \sim 80$ for a Signal to Noise Ratio (SNR), $C_\ell/\Delta C_\ell \sim 1$ for the $r = 0.03$ scenario shown in fig. 1.4. For a realistic experiment, the observing efficiency, detector yield and NET degradation need to be accounted for in the performance forecast. As the back of the envelope calculations here show, achieving the goal of constraining cosmological parameters using CMB power spectra requires long duration observations with large numbers of sensitive detectors.

1.8 Motivation for TKIDs for CMB Polarimetry

To date, most ongoing (Abitbol et al., 2018; Benson et al., 2014; Henderson et al., 2016; H. Hui et al., 2016; Howard Hui et al., 2018; Kermish et al., 2012) and planned CMB experiments (Abazajian et al., 2016) use bolometers as detectors to measure the optical power from the CMB. Bolometers are incoherent/direct detectors and are sensitive only to the amplitude of the incoming radiation and not its phase. An optical detector is background limited when the greatest source of noise present is that of the incoming radiation itself. In this respect, at frequencies of interest to CMB studies, incoherent bolometric detectors outperform coherent receivers such as interferometers (Zmuidzinas, 2003). In fact, bolometers that are in current use for CMB observations are already background limited and have been so for the last decade.

Since the detectors are background limited, the raw sensitivity of CMB experiments can only be improved by scaling the number of detectors as eqs. (1.53) and (1.55) demonstrate. Stage-3 CMB experiments being fielded currently deploy $\sim 10^4$ detectors. Upcoming stage-4 experiments such as CMB-S4 (Abazajian et al., 2016) require 1 μK $\cdot$ arcmin across over half the sky to achieve their science goals which can only be achieved by fielding $\sim 10^5$ detectors.

Modern bolometric detectors use Transition Edge Sensors (TESes) (Irwin and Hilton, 2005) as their thermometers because TESes can be fabricated using thin-film lithography and thus integrated into monolithic arrays with large detector counts. TESes are superconducting devices and require cryogenic cooling to very low temperatures in order to operate. However, in order to limit the thermal cable load on the cryogenic stages, which have limited cooling capacity, multiple TESes must be read out on a single line using Superconducting Quantum Interference Devices

(SQUIDs) (Clarke and Braginski, 2005). SQUIDs are low noise and have low impedance as well as sufficient bandwidth to multiplex many TESes on a single line with minimal crosstalk. The two main schemes developed to multiplex TES pixels are time-division multiplexing (TDM) (Irwin, Vale, et al., 2002; Korte et al., 2003) and frequency-division multiplexing (FDM) (Dobbs et al., 2012). Currently operating instruments fielding kilo-pixel detector arrays have implemented TDM and FDM readout schemes. However, it is challenging and expensive to integrate and read out arrays with detector counts above ~10,000 using the existing SQUID-based multiplexing schemes.

Kinetic Inductance Detectors (KIDs) (Day et al., 2003; Dober et al., 2014; Doyle et al., 2008; Golwala et al., 2012; Kovács et al., 2012; Mazin et al., 2013; McKenney et al., 2012; Monfardini et al., 2011; Patel et al., 2013) are an alternative detector technology that offer a promising solution to the problem of scaling up to larger detector counts. Like TESes, KIDs can be fabricated on silicon wafers using thin-film lithography. However, each KID pixel, which is a superconducting resonator, has a unique frequency and a narrow bandwidth. This is an advantage of KIDs over TESes because large numbers of KIDs can be read out on a single transmission line using microwave frequency-division multiplexing (mFDM) without requiring complex SQUID-based readout and assembly.

In the place of SQUIDs, KID readout systems typically use fast FPGA-based (Bourrion et al., 2016; Golwala et al., 2012; Gordon et al., 2016; van Rantwijk et al., 2016) or GPU-based (L. Minutolo, B. Steinbach, et al., 2019; Lorenzo Minutolo, 2019) digital electronic systems to generate probe tones that are sent down a coaxial line with filters and attenuators to excite the KID array. The detector responses are then amplified using a cryogenic Low Noise Amplifier (LNA) before passing out of the cryostat where they are demodulated and digitized into detector timestreams (Mauskopf, 2018).

Thermal Kinetic Inductance Detectors (TKIDs) are a variation of Kinetic Inductance Detectors and as such, they offer the same multiplexing benefits. A TKID integrates a superconducting resonator into a bolometer. Rather than tracking the changes in the resistance of the superconductor as TES bolometers do, the temperature variations of the thermally isolated island are measured by the changes in the kinetic inductance of the superconducting resonator circuit. Because all the power is thermalized on the bolometer island, a TKID's absorber can be electrically decoupled from the resonator circuit, unlike in most KID designs. This gives TKIDs an additional degree

of engineering flexibility since the resonator and the absorber can be optimized independently.

TKIDs have been an active area of research since (Sauvageau and McDonald, 1989) early work on kinetic inductance thermometry. TKIDs have been developed as energy detectors for X-ray imaging spectroscopy (Ulbricht et al., 2015) to simultaneously achieve high spatial and energy resolution and for thermal X-ray photon detection (Quaranta et al., 2013). TKIDs have also been used as THz radiation detectors (Arndt et al., 2017; Dabironezare et al., 2018; Timofeev et al., 2013; Wernis, 2013) operating at kelvin-range temperatures.

However, TKIDs have not yet been demonstrated as power detectors for millimeter-wave instruments that operate at sub-kelvin temperatures. The measurement of the polarization anisotropies of the Cosmic Microwave Background (CMB) is one of the most important use cases for bolometric power detectors working in the millimeter-wave regime. CMB observations have strict requirements on detector sensitivity, stability, and scalability, especially for future experiments targeting high detector counts.

This thesis demonstrates the feasibility of using TKIDs for CMB observations. Our TKID design targets the detector performance requirements needed for CMB observations at 150 GHz.

1.9 Thesis Outline

In this thesis, I describe the design, development, and laboratory characterization of a TKID CMB polarimeter. Chapter 2 details a physical model of TKID operation and readout. This model makes robust predictions of the expected detector noise and responsivity.

In Chapter 3, I discuss three successive generations of prototype detectors that were developed and tested before the final tile design. With the first generation, we demonstrated a TKID device design and fabrication procedure that yielded TKIDs with internal detector noise low enough for background limited performance given the expected optical loading on our telescope. The second generation of TKID prototype devices validated the scale-up of the initial design to larger arrays. These devices were indispensable for fabrication refinement as well as cosmic ray susceptibility testing, and readout development. In the third generation, we integrated our tested detector design with a polarization sensitive planar phased-array antenna. The lithographed antenna imposes strict requirements in both fabrication and de-

sign, such as sub-micron line fidelity in the microstrip lines. Coupling an antenna to TKID bolometers required an extensive understanding of the fabrication process in order to smoothly accommodate the fabrication requirements of both the antenna and the detector. We demonstrate that antenna-coupled TKIDs have end-to-end optical efficiency comparable to that of exisiting TES detectors, and match the design spectral response with smooth Gaussian antenna beams.

Chapter 4 presents the design and operation of the TKID demonstration receiver. I present the design principles for a small aperture, compact telescope with cold optics for measuring the polarization of the CMB at 150 GHz from the South Pole. The TKID receiver maintains many features from the earlier *Keck* Array telescopes but adapts the receiver with an RF chain, new DC wire routing and additional modifications for compatibility with TKID readout. We also discuss TKID readout for both lab and on sky measurements.

These efforts culminate with the design of the 64 pixel dual-polarization TKID arrays presented in Chapters 5 and 6. The TKID focal plane is the focus of Chapter 5. In chapter 6, I present the laboratory characterization of the receiver. The focal plane consists of 4, 4-inch TKID tiles. This camera would be the first demonstration of TKIDs operating in the millimeter wave regime, maturing the technology for broader future cosmological and astrophysical applications. I detail design methodologies, electromagnetic simulations, and fabrication procedures for realizing uniform TKID arrays with high yield.

Chapter 2

TKID THEORY

2.1 Introduction

This chapter details the principles of operation of TKID devices. In operation, TKIDs have much in common with TES bolometers. Just like a TES, a TKID is a bolometer; a temperature sensitive impedance that is heated by incoming radiation and that transduces the absorbed power into an electrical signal. Much of AC TES bolometer theory carries over to the TKID bolometer physics discussed here.

In readout and design, TKIDs share many features in common with microwave Kinetic Inductance Detectors (MKIDs). Much like in many MKID designs, electrical readout circuit of a TKID consists of a parallel LC resonator typically built up of lumped element components. A large capacitor C sets the resonance frequency f_r, and with smaller additional capacitors C_c couple the resonator to both the transmission line and to ground. The inductor, is the temperature sensitive impedance and is located on the island. The proportion of the total inductance L that is sensitive to temperature is its kinetic inductance L_k. Kinetic inductance arises from the superconductivity of the inductor film. The remaining inductance is the geometric inductance L_g due to the geometric layout of the inductor wire on the island. Changes in L_k with temperature shift both the resonance frequency and the internal quality factor Q_i of the resonator. A large kinetic inductance fraction, $\alpha_k = L_k/(L_g + L_k)$ therefore creates a large responsivity to thermal fluctuations (Zmuidzinas, 2012). We can achieve this by either minimizing the geometric inductance by design, or alternatively by choosing a material with a large resistivity or a large T_c.

There are some noteworthy distinctions. In TKIDs the absorber element on the island that receives incident radiative is in thermal contact with but electrically isolated from the inductor. The absorber can be modified with no impact on the resonator. In this, TKIDs differ from many MKID designs in which the inductor also doubles as the optical absorber. Optimizing a single design for these two competing goals is difficult in practice. A separate absorber also allows TKIDs to be used as a drop-in replacement for TESes in a bolometer in order to take advantage of already developed radiation-coupling technologies such as planar phased-array antennas, horns or lenslets (Ade, Aikin, Amiri, Barkats, Benton, Bischoff, Bock,

Bonetti, et al., 2015; Henderson et al., 2016; Kermish et al., 2012) even at different observing frequencies with minor changes to the TKID design. Figure 2.1a shows a schematic of the thermal and electrical circuit of a TKID pixel as an aid to the discussion presented here.

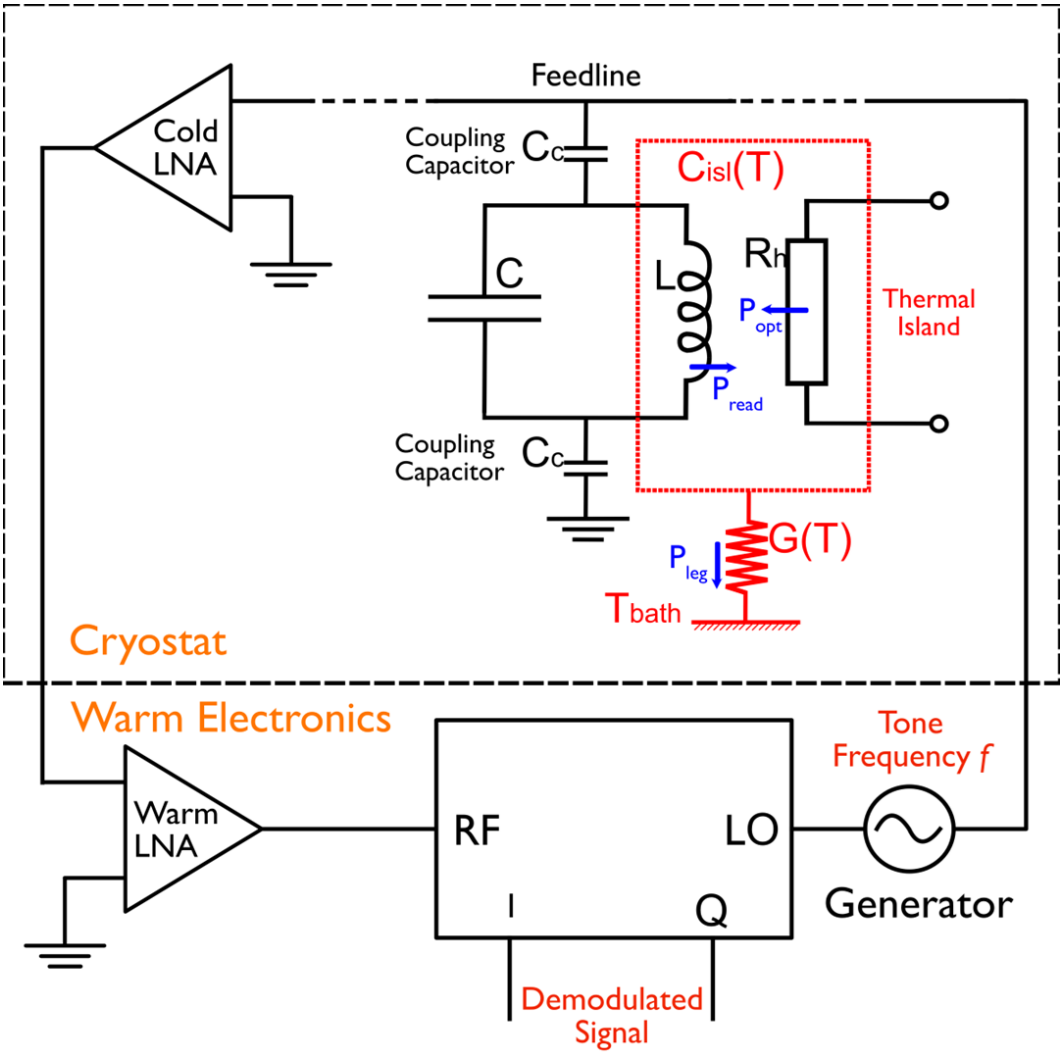

Figure 2.1: Schematic of a TKID bolometer coupled to a readout chain. The thermal circuit is shown in red while the electrical system is depicted in black. R_h represents the absorber which thermalizes optical power on the bolometer membrane. The electrical circuit includes the 2 amplification stages typically used in the TKID readout chain.

TKIDs are a complementary technology to both MKIDs and TESes. As we will discuss in this chapter, TKID design and operation offers a unique window into understanding material properties, non-linear processes, and readout techniques

that are broadly relevant to many superconducting device architectures.

2.2 Modeling Superconducting Resonators

In order to make predictions of the power dissipation in the TKID bolometer as well as its small signal response, a complete model of the scattering parameters of the resonator is needed. In the simplest case of a single-pole, symmetric shunt resonator, the forward scattering parameter S_{21} completely specifies the resonator properties.

In general, however, non-ideal experimental configurations and unaccounted parasitic effects often lead to asymmetry in the resonator line shape. This not only complicates the recovery of the quality factors of the resonator, but also creates additional ambiguity in the determining the amount of power dissipated in the resonator. Predicting the power dissipation in resonators is especially important as superconducting resonators are increasingly used under high excitation, especially for negative electrothermal feedback in TKIDs (Agrawal et al., 2021). Power dissipation in the resonator also determines the dynamic range within which the resonator can be operated. The onset of non-linearity at high readout power levels sets the upper limit of the linear dynamic range, while the readout noise in the resonator often sets the noise floor relative to which any signals mediated by the resonance can be measured. The question of whether resonator asymmetry leads to readout noise penalties remains open.

Close to resonance, microwave resonators can be described using an equivalent lumped element circuits. One such model, depicted in fig. 2.2 representing a notch-type resonator with both capacitive and inductive coupling to a transmission line. Khalil et al., 2012 considers this network and derives the forward scattering parameter S_{21} from the circuit elements by finding the Norton equivalent circuit of the network. On the other hand, Deng et al., 2013, develops an algebraic approach to the same network topology, the Closest Pole and Zero Method (CPZM) to isolate the resonator parameters. Both these approaches show how effects such as resonator asymmetry can arise due to line mismatch, wirebond inductance and other parasitic effects.

However, both the forward scattering parameter S_{21} and the reflected scattering parameter S_{11} are needed in order to compute the power dissipation in the resonator. In more complicated circuits or simulations, the relationship between S_{21} and S_{11} is not trivial. It is not a priori clear that the approximate expression for S_{21} captures all

L_1 [nH]	M [nH]	L [nH]	C_c [pF]	C [pF]	$R[k\Omega]$
0.71	0.9	10.0	0.2	22.5	50

Table 2.1: Circuit parameters for network shown in fig. 2.2.

$\omega_0^{'}$	α	β	γ	ξ	q
$2\pi \times$ 335.5MHz	0.090	0.071	0.0089	0.42	0.00042

Table 2.2: Reduced network parameters matching the circuit elements in section 2.2.

the information needed to correctly predict the resonator properties. Since a circuit can have an arbitrarily large number of elements, we require a general approach that is applicable to different circuit designs beyond the current model. The results of this section are applicable to any passive microwave system with an embedded notch-type resonator. This includes electromagnetic simulations in which the loss in the system is dominated by the dissipation in the resonance.

Lumped Element Model for a Single Pole Resonator

It is informative to first examine the network's impedance parameters, here denoted $\hat{Z}$. For clarity, we reduce the circuit elements to a new set of 6 variables: three dimensionless variables that describe the coupling $[\alpha = M/L, \beta = L_1/L, \gamma = C_c/C]$, the bare resonance frequency, $\omega_0^{'} = 1/\sqrt{L\,C}$, and two additional dimensionless resonator quantities, $q = 1/(\omega_0^{'}RC)$, the inverse quality factor and, $\xi = 1/(\omega_0^{'}Z_0C)$. ξ is the ratio of the capacitive/inductive reactance at the bare resonance frequency, $\sqrt{L/C}$, to the reference impedance and measures the total energy stored in the resonator. Deng et al., 2013 also makes use of the same set of variables. Table section 2.2 lists the values of the parameters used to generate all the plots in this section. The parameter values are chosen to match typical values used in our TKID resonator design (see section 3.1).

By applying Kirchoff's first rule at every node in the network, we can derive the impedance parameters of the model presented in fig. 2.2. For clarity, C and R are combined into the single complex variable $C_p = C + 1/j\omega R$. This gives the impedance parameters:

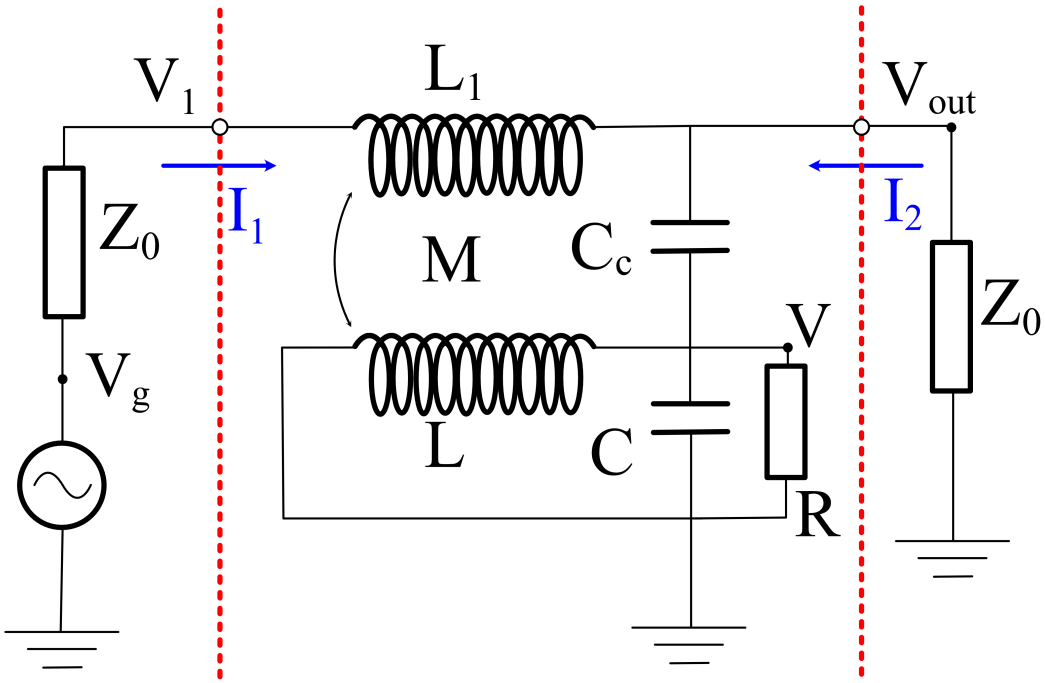

Figure 2.2: Schematic of a lumped element resonator with inductive and capacitive coupling. The red dashed lines are the reference planes at which the ports are defined. The voltage and current at the input port are V_1 and I_1 respectively. $V_2 = V_{\text{out}}$ is the voltage at the output port and I_2 is the current at the output port. V is the voltage across the resonator.

$$Z_{11} = j\omega L_1 + \frac{1}{j\omega C_c} + \frac{j\omega(L-M)}{1-\omega^2 LC_p} - j\omega M \frac{1-\omega^2 MC_p}{1-\omega^2 LC_p}, \tag{2.1}$$

$$Z_{21} = \frac{1}{j\omega C_c} + \frac{j\omega(L-M)}{1-\omega^2 L\, C_p}, \tag{2.2}$$

$$Z_{22} = \frac{1}{j\omega C_c} + \frac{j\omega L}{1-\omega^2 L\, C_p}. \tag{2.3}$$

This is a reciprocal, passive network, and therefore, $Z_{12} = Z_{21}$. The impedance parameters have the factor $\left(1-\omega^2 LC_p\right)^{-1}$ in common. We can isolate this factor dividing the rational functions Z_{11} and Z_{22} by Z_{21} to obtain quotients δ and $1/\delta$. The remainders are Z_A/δ and $Z_B \cdot \delta$, respectively.

$$\frac{Z_A}{\delta} = \frac{1}{j\omega C_c}\frac{M}{L} + j\omega\left(L_1 - M^2/L\right), \tag{2.4}$$

$$\delta \cdot Z_B = \frac{1}{j\omega C_c}\left(1 - \frac{1}{1 - M/L}\right), \tag{2.5}$$

$$\delta = \frac{1}{1 - M/L}. \tag{2.6}$$

The full impedance matrix with no approximations, is succint when captured using this set of 4 network functions: $[Z_A, Z_B, Y, \delta]$. Explicitly,

$$\hat{Z}(\omega) = \begin{bmatrix} \frac{1}{\delta}\left(Z_A(\omega) + \frac{1}{Y(\omega)}\right) & \frac{1}{Y(\omega)} \\ \frac{1}{Y(\omega)} & \delta\left(Z_B(\omega) + \frac{1}{Y(\omega)}\right) \end{bmatrix}. \tag{2.7}$$

The description of the impedance matrix in eq. (2.7) is similar to a T decomposition of a 2 port passive network (Pozar, 2005). This motivates the equivalent network model shown in fig. 2.3, where Z_A, Z_B and Y are the elements of a T decomposition of a 2 port network. The scaling factor $\delta = N^2$ gives the turns ratio N of the 2 identical transformers that couple the source and the load to the resonator network. Therefore, the condition $\delta \neq 1$ signals that the resonator network is mismatched to either the source or the load or both.

In the reduced variable scheme, the network functions are

$$Z_A(j\omega) = j\omega\frac{Z_0\xi\left(\beta - \alpha^2\right)}{\omega_0^{'}(1-\alpha)} + \frac{1}{j\omega}\frac{Z_0\alpha\xi\omega_0^{'}}{\gamma(1-\alpha)}, \tag{2.8}$$

$$Z_B(j\omega) = \frac{1}{j\omega}\frac{Z_0\alpha\xi\omega_0^{'}}{\gamma}, \tag{2.9}$$

$$Y(j\omega) = \bar{Y}(j\omega)\cdot H(j\omega), \tag{2.10}$$

$$\bar{Y}(j\omega) = j\omega\frac{\gamma}{Z_0\xi\omega_0^{'}}, \tag{2.11}$$

$$H(j\omega) = \frac{(j\omega)^2 + j\omega\cdot q\,\omega_0^{'} + (\omega_0^{'})^2}{a_0^{-1}(j\omega)^2 + j\omega\cdot\, q\,\omega_0^{'} + (\omega_0^{'})^2}, \tag{2.12}$$

$$\delta = \frac{1}{1-\alpha}, \tag{2.13}$$

where $a_0 = (1+\gamma(1-\alpha))^{-1}$. a_0 is a measure of the detuning of the resonator due to the coupling to the transmission line. Z_A is a capacitance in series with an

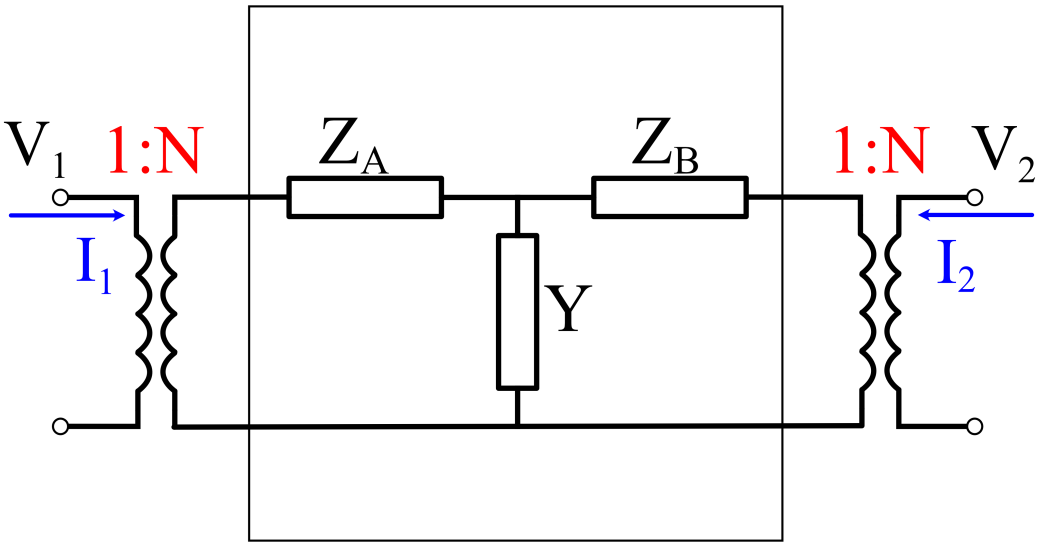

Figure 2.3: An equivalent network description of the impedance matrix given in equation eq. (2.7). The impedance matrix of the Khalil network can be interpreted as a 2 port network with a T decomposition coupled to ideal transformers at the input and output. The turns ratio $N = \sqrt{\delta}$.

inductance while Z_B and $\bar{Y}$ are pure capacitances. Additionally, eqs. (2.8), (2.9) and (2.11) show that $[Z_A, Z_B, \bar{Y}]$ have no poles or zeros close to the bare resonance frequency.

Fig. 2.4 plots the magnitude of the network functions given the parameters specified in table section 2.2. From the set eqs. (2.8) to (2.13), we observe that:

- Y can be decomposed as a product of a rational function H of frequency and a purely imaginary admittance $\bar{Y}$. $\bar{Y}$ carries the global frequency dependence of the shunt admittance.
- Z_A, Z_B and $\bar{Y}$ are purely imaginary. This reflects the fact that the resonator is the only lossy part of the network.
- While Z_A, Z_B and $\bar{Y}$ have non-trivial frequency dependence, they are smooth slowly varying functions of frequency within the frequency range of interest.
- δ is a real constant.
- $H(\omega)$ is a rational function of $j\omega$ and is a second order notch filter. The closer a_0 is to 1, the tighter the notch.
- The single parameter q captures all the loss in the network. The resonance vanishes in the limit $q \to \infty$ since $H \to 1$.

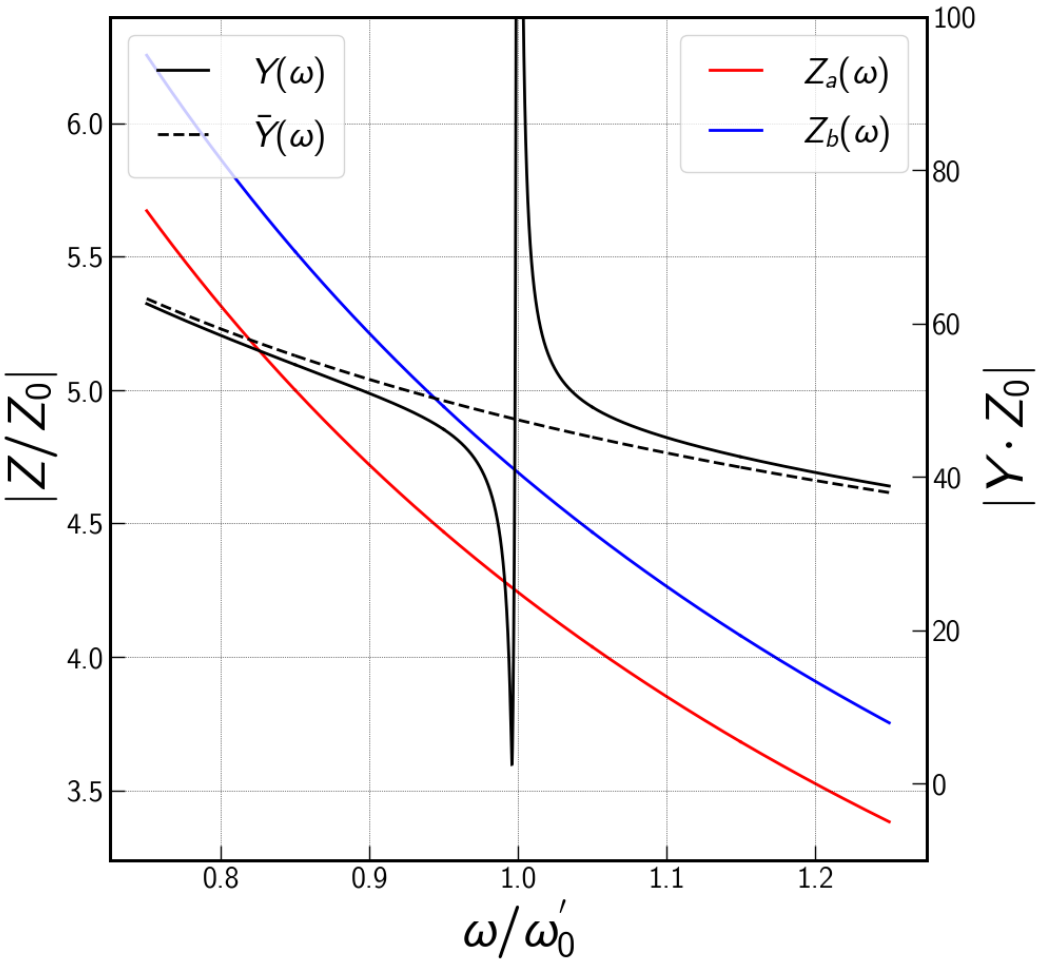

Figure 2.4: Magnitude of the impedance parameters (eq. (2.7)) of the circuit model fig. 2.2 as a function of frequency.

The 3 smoothly varying network functions [Z_A, Z_B and $\bar{Y}$] collectively determine the coupling to resonance and generate the resonator asymmetry. Note that the individual circuit elements (except R) map non trivially onto more than one of the smooth network functions.

Deriving the Scattering Parameters

The scattering matrix $\hat{S}$ referenced to the port impedance Z_0, given an impedance matrix $\hat{Z}$ and I the identity matrix, is defined by $\hat{S}(\omega) = \left[\hat{Z}(\omega) + Z_0 \cdot I\right]^{-1}\left[\hat{Z}(\omega) - Z_0 \cdot I\right]$. We introduce two complex dimensionless functions: $\zeta(\omega) = \delta + Z_A(\omega)/Z_0$ and $\eta(\omega) = 1/\delta + Z_B(\omega)/Z_0$. As we will see, the scattering parameters are concisely expressed in terms of ζ and η. Additionally, let $Z_{\text{tot}} = Z_0\left[1/\zeta + 1/\eta\right]^{-1}$ be the total impedance looking out into the external circuit from the resonator. In closed form and with no approximations, S_{11}, S_{21}, and S_{22} are

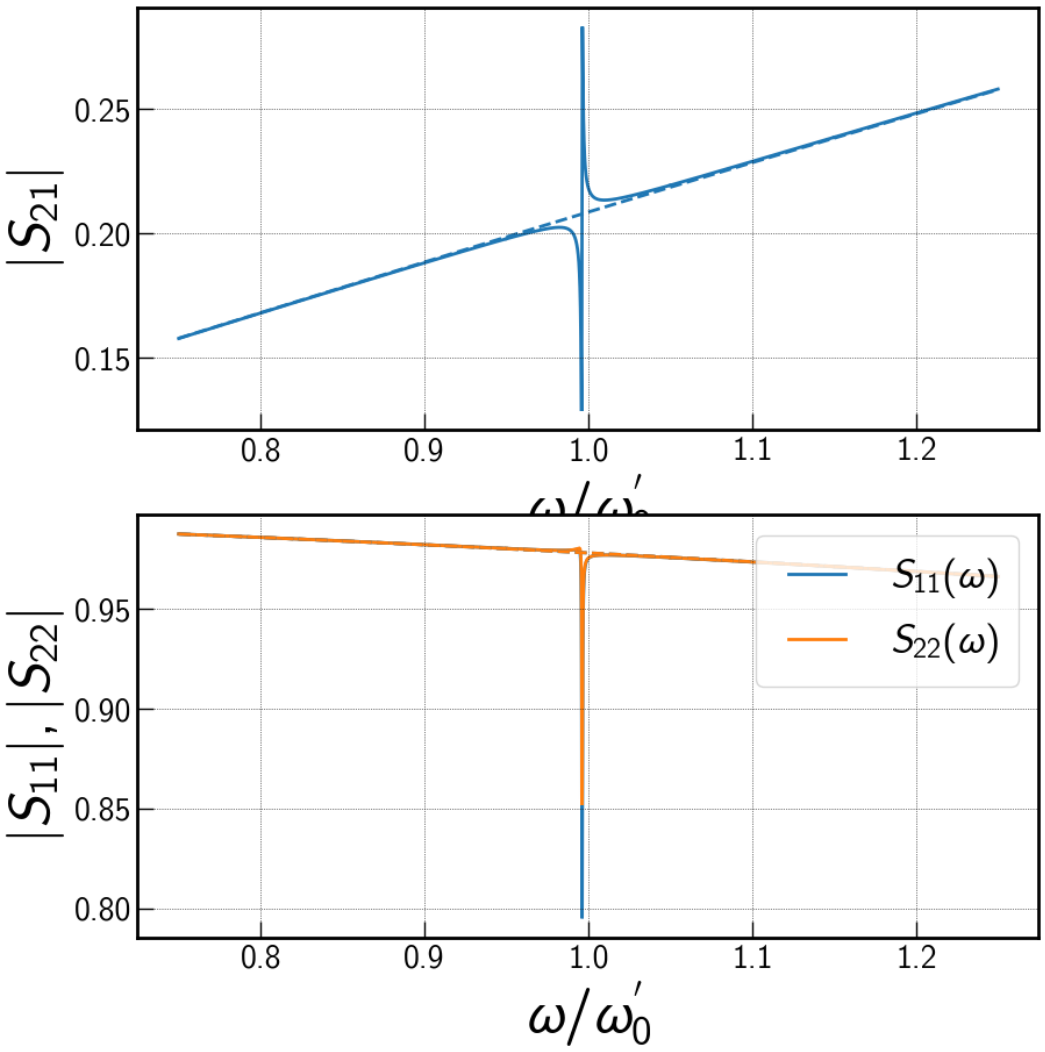

Figure 2.5: Magnitude of the scattering parameters of the circuit in fig. 2.2 as a function of frequency. The dashed curves are the baseline of the scattering parameters.

$$S_{21} = \frac{2}{\zeta+\eta} \cdot \frac{1}{1+Y \cdot Z_{\text{tot}}} \tag{2.14}$$

$$S_{11} = 1 - \frac{2\delta}{\zeta} + \frac{\eta\,\delta}{\zeta}\frac{2}{\zeta+\eta} \cdot \frac{1}{1+Y \cdot Z_{\text{tot}}} \tag{2.15}$$

$$S_{22} = 1 - \frac{2}{\eta\,\delta} + \frac{\zeta}{\eta\,\delta}\frac{2}{\zeta+\eta} \cdot \frac{1}{1+Y \cdot Z_{\text{tot}}}. \tag{2.16}$$

Figure 2.5 shows the magnitude of the scattering parameters matching the impedance parameters shown in figure 2.4. eqs. (2.14) to (2.16) reflect the non-trivial relationship between S_{11} and S_{21} that makes predicting the power dissipation difficult.

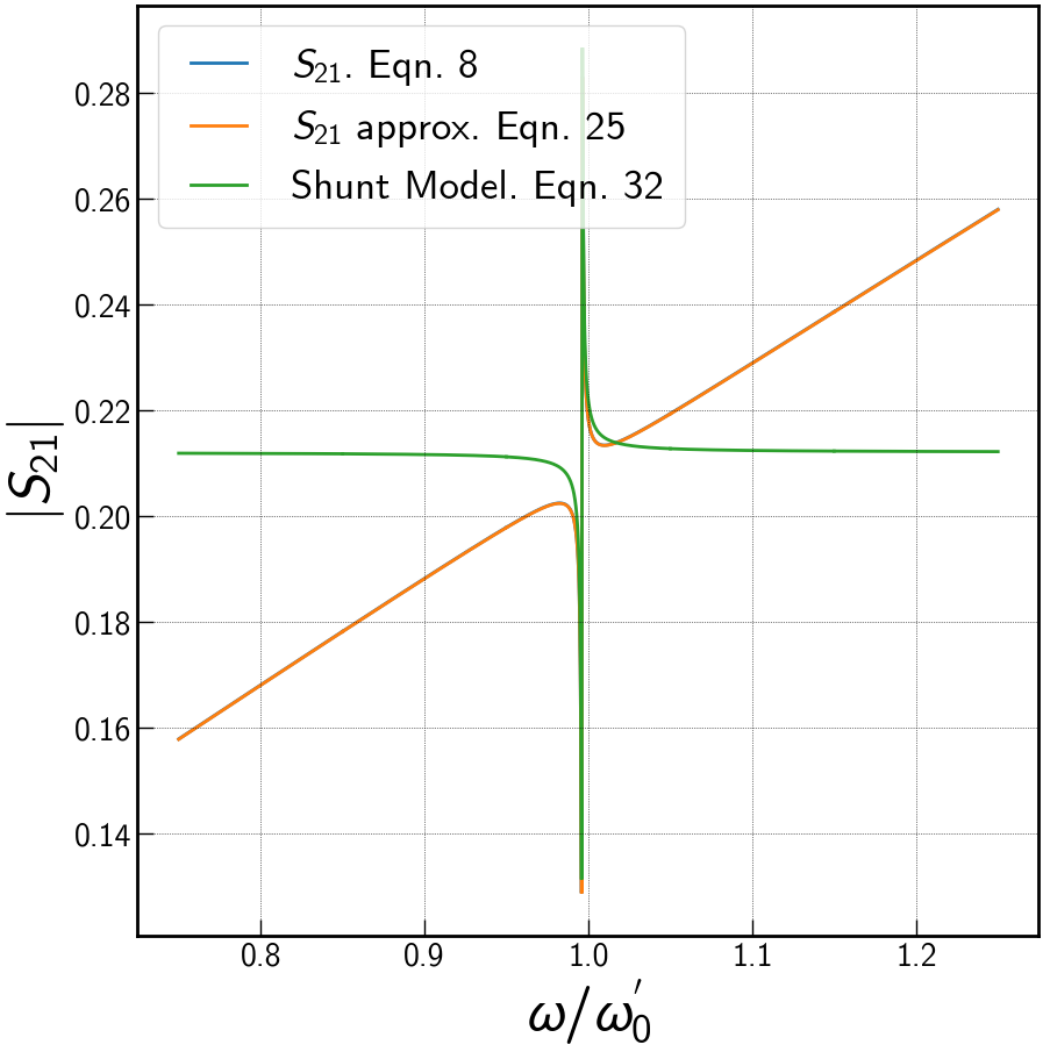

Figure 2.6: A comparison of the full $|S_{21}|$ from eq. (2.15) with its CPZM approximation given in eq. (2.30). The two curves completely overlap across the entire frequency range. The green curve is the shunt S_{21} model given in eq. (2.44) which captures all the resonator parameters but completely ignores the line transmission.

We will first consider S_{21} fully and then consider S_{11} and S_{22} in turn. In equations eqs. (2.10) to (2.12), we showed that Y can be decomposed into a product of $\bar{Y}$, which carries the global behavior of the shunt admittance, and H, a notch filter. Intuitively, for a high quality factor resonator, the response of the network close to resonance will be dominated by the frequency dependence of H.

To proceed, we recognize $\kappa(\omega)$ to be a dimensionless coupling parameter given by

$$\kappa = \frac{j\bar{Y}(\omega) \cdot Z_{\text{tot}}(\omega)}{1 + \bar{Y}(\omega) \cdot Z_{\text{tot}}(\omega)}, \tag{2.17}$$

so that S_{21} from eq. (2.15) can be rewritten as

$$S_{21} = \frac{2\,(1 + j\kappa)}{\zeta + \eta} \cdot \frac{1}{1 + j\kappa - j\kappa \cdot H}. \tag{2.18}$$

From eq. (2.18), when $\kappa \to 0$, the resonance disappears. The complex parameter κ screens the effect of the resonance on S_{21}. Its additional effect is seen far from resonance where $S_{21} \to \frac{2(1+j\kappa)}{\zeta+\eta}$. Therefore, κ captures the perturbation to the line due to the presence of the resonator network. The weak coupling limit corresponds to $|\kappa| \ll 1$ in which case, $S_{21} \approx \frac{2}{\zeta+\eta}$ and is unperturbed even far from resonance. In the ideal case, κ is small and purely real so it only induces a small phase shift on the transmission through the line.

Let ω_z, ω_p be the zero and pole frequencies of H respectively when $R \to \infty$ ($q \to 0$). eq. (2.36) directly shows that $\omega_z = \omega_0^{'}$. ω_p is shifted slightly from the bare resonance by the coupling capacitance and mutual inductance. When the coupling is weak, we expect $\omega_p < \omega_z$.

H has a pair of conjugate zeros at $(z_0, \bar{z}_0)$ and conjugate poles at $(p_0, \bar{p}_0)$. Where $\bar{z}_0$ is the complex conjugate of z_0. We can therefore write $H(j\omega)$ as

$$H(j\omega) = \left(\frac{\omega_p}{\omega_z}\right)^2 \cdot \frac{(j\omega - z_0)}{(j\omega - p_0)} \cdot \frac{(j\omega - \bar{z}_0)}{(j\omega - \bar{p}_0)}. \tag{2.19}$$

The inverse quality factor perturbs the zero and pole frequencies so that $z_0 = j\omega_z(1 + j\frac{q}{2})$ and $p_0 = j\omega_p(1 + j\frac{\omega_p}{\omega_z}\frac{q}{2})$ accurate to second order in q. p_0 and z_0 are the pole and zero closest to the bare resonance frequency. These dominate the resonator response and therefore we can make the approximation

$$H(j\omega) \approx \left(\frac{\omega_p}{\omega_z}\right)^2 \cdot \frac{\left(j\omega_0^{'} - \bar{z}_0\right)}{\left(j\omega_0^{'} - \bar{p}_0\right)} \frac{(j\omega - z_0)}{(j\omega - p_0)}. \tag{2.20}$$

Since $q \ll 1$ and ω_p is close to ω_z, the frequency independent factors in eq. (2.20) are close to 1 and can be dropped. This gives us

$$\boxed{H \approx \frac{j\omega - j\omega_z\left(1 + j\frac{q}{2}\right)}{j\omega - j\omega_p\left(1 + j\frac{q}{2}\right)}}. \tag{2.21}$$

To derive the response the network, we will make one additional approximation. We take $\zeta(\omega) \approx \zeta(\omega_0^{'})$, $\eta(\omega) \approx \eta(\omega_0^{'})$, and $\bar{Y}(\omega) \approx \bar{Y}(\omega_0^{'})$ in all terms multiplying H in eqs. (2.14) to (2.16).

Using our first approximation, we specify $\kappa_0 = \kappa\,(\omega = \omega_z)$ to be the coupling at the bare resonance frequency in the denominator in eq. (2.18). Therefore,

$$S_{21} \approx \frac{2\,(1 + j\kappa)}{\zeta + \eta} \cdot \left[1 - \frac{-j\kappa_0\left(\omega_p - \omega_z\right)\left(\frac{1}{q} + \frac{j}{2}\right)}{\frac{\omega}{q} - \left(\frac{1}{q} + \frac{j}{2}\right)\left(\omega_p + j\kappa_0\left(\omega_p - \omega_z\right)\right)}\right] \tag{2.22}$$

From eq. (2.22), we can define the measured resonance frequency ω_0 which is shifted from the resonance pole at ω_p as

$$\boxed{\omega_0 = \omega_p - \mathrm{Im}(\kappa_0)\left(\omega_p - \omega_z\right)}. \tag{2.23}$$

We can group the remaining terms in eq. (2.22) in a familiar form by defining the resonator parameters as:

$$Q_c^{-1} = -2\frac{\omega_z - \omega_p}{\omega_0}\,\mathrm{Re}(\kappa_0), \tag{2.24}$$

$$Q_i^{-1} = q, \tag{2.25}$$

$$\phi_c = \arg(\kappa_0), \tag{2.26}$$

where Q_c is the coupling quality factor, Q_i the internal quality factor and ϕ_c is the resonator asymmetry angle. For our network, $\mathrm{Re}(\kappa_0) < 0$ and therefore $Q_c > 0$ as expected. The total quality factor $Q_r = \left(Q_i^{-1} + Q_c^{-1}\right)^{-1}$ as expected. Q_c and ϕ_c

combine into a single complex coupling parameter $\hat{Q}_c = Q_c \cdot \cos\phi_c \cdot e^{j\phi_c}$ chosen so that $Q_c = 1/[\mathrm{Re}(\hat{Q}_c^{-1})]$ holds.

To relate S_{21} to S_{11} and S_{22}, we also define the line perturbation parameters

$$\phi = \arg(\kappa) \tag{2.27}$$

$$\varphi = \arg(Z_{\mathrm{tot}}). \tag{2.28}$$

so that $\kappa = \sin(\phi-\varphi)\sec(\varphi)\exp(j\phi)$. This is the equation of a circle on the complex plane with center $(-\frac{1}{2}\tan\varphi, \frac{1}{2})$, radius $\sec\varphi$ and polar angle 2ϕ. κ is purely real when $\phi = 0$. Just as in the Fano picture, we can interpret ϕ as a phase difference between the resonant pathway and the continuum transmission through the line. Note that $\boxed{\phi\,(\omega = \omega_z) = \phi_c}$. With this, S_{21} can be written in the form

$$S_{21} = \frac{2}{\zeta+\eta}\cdot\frac{1-j\tan\varphi}{1-j\tan\phi}\left[1 - \frac{Q_r\hat{Q}_c^{-1}\left(1+j\frac{1}{2Q_i}\right)}{1+j2Q_r\frac{\omega-\omega_0}{\omega_0}+\frac{j}{2}\frac{1}{Q_c+Q_i}}\right] \tag{2.29}$$

$$\approx \frac{2}{\zeta+\eta}\cdot\frac{1-j\tan\varphi}{1-j\tan\phi}\left[1 - \frac{Q_r\hat{Q}_c^{-1}}{1+j2Q_r\frac{\omega-\omega_0}{\omega_0}}\right]. \tag{2.30}$$

The final line of equation 2.30 is valid whenever $Q_i, Q_c \gg 1$, as is true for high quality resonances. This is our final approximation that gives the usual expression for a single pole resonance in the square brackets.

We can reproduce the results of Khalil et al., 2012 and Deng et al., 2013, obtaining S_{21} can be obtained directly from the impedance parameters as

$$S_{21} = \frac{2Z_{21}Z_0}{(Z_{11}+Z_0)(Z_{22}+Z_0)-Z_{21}^2}. \tag{2.31}$$

Let the impedance seen from the input of the 2 port network terminated by the load resistor be Z_{in}. Therefore,

$$Z_{\mathrm{in}} = Z_{11} - \frac{Z_{21}^2}{Z_0+Z_{22}} \tag{2.32}$$

The voltage across the resonator, $V = V_2-(I_1+I_2)/(j\omega C_c) = -((1+j\omega C_c Z_0)\,I_2 + I_1)/(j\omega C_c)$ and $I_2 = (Z_{\mathrm{in}}-Z_{11})/Z_{21}I_1$. With this, we obtain the same expression

for S_{21} given Eqn. 1 in Deng et al., 2013 and Eqn. 1. in Khalil et al., 2012 with $Z_{\text{in}} = Z_{\text{out}} = Z_0$.

$$S_{21} = (1 + \hat{\epsilon}) \cdot \left[1 - \frac{V}{V_g} \frac{\bar{Y} \cdot Z_0 \cdot \delta}{\zeta}\right], \tag{2.33}$$

where

$$(1 + \hat{\epsilon}) = \frac{2}{2 + j\omega C_c Z_0 + j\omega \left(L_1 - M^2/L\right) \cdot (1 + j\omega C_c Z_0) / Z_0}, \tag{2.34}$$

$$\frac{\bar{Y} \cdot Z_0 \cdot \delta}{\zeta} = \frac{M}{L} + j\omega C_c \left(Z_0 + j\omega \left(L_1 - \frac{M^2}{L}\right)\right). \tag{2.35}$$

Comparing eq. (2.33) to eq. (2.18), $(1 + \hat{\epsilon}) = (2\,(1 + j\kappa))\,/(\zeta + \eta)$. This prefactor is typically ignored in derivations of S_{21} for a single pole resonance. Here, we accounted for it in order to correctly relate S_{21} to S_{11} to compute the power dissipation. Additionally, eq. (2.33) gives the voltage across the resonator directly.

We can also examine H in terms of the circuit elements

$$H(j\omega) = \frac{1 + j\frac{\omega L}{R} - \omega^2 LC}{1 + j\frac{\omega L}{R} - \omega^2 \left(L\left(C + C_c\right) - MC_c\right)}. \tag{2.36}$$

We recognize that

$$\bar{Y} \frac{H}{1 - H} = \delta \left[\frac{1}{j\omega L} + \frac{1}{R} + j\omega C\right]. \tag{2.37}$$

This demonstrates that the pole in the resonance is shifted away from the zero at the bare resonance frequency by the coupling to the transmission line.

To complete this analysis, we express eqs. (2.24) to (2.26) using the network parameters defined in eqs. (2.8) to (2.13). This determines the leading order contributions to Q_c, ϕ_c and ω_0.

$$Q_c^{-1} = \frac{C_c^2 Z_0 \omega_0^{'}}{2\,C} + \frac{M^2\,\omega_0^{'}}{2\,L\,Z_0} \tag{2.38}$$

$$\phi_c = -\frac{C_c \omega_0^{'} Z_0}{2} - \left(\frac{M}{L}\right)^2 \frac{1}{2\,C_c\,Z_0 \omega_0^{'}} + \frac{L_1 \omega_0^{'}}{2\,Z_0} \tag{2.39}$$

$$\omega_0 = \omega_0^{'}\left[1 - \frac{C_c}{2\,C}\right] \tag{2.40}$$

To leading order, the capacitive and inductive couplings contribute additively to Q_c^{-1}. Both C_c and M show up as second order terms in Q_c^{-1}. On the other hand the asymmetry angle has contributions from $C_c, M,$ and L_1 to leading order. However, we expect the dominant contributor to the resonator asymmetry to be the line inductance L_1 which can be arbitrarily large. Typically, design constrains both $M \ll L$ and $C_c \ll C$. Again, this matches our expectation that the reactive elements in the network will generate the resonator asymmetry.

Completing S_{11} and S_{22}

There is little additional work needed to derive the frequency dependence of S_{11} and S_{22} since the relevant resonator term are shared with S_{21}.

One helpful observation, is that in the limit that the resonator vanishes (say $Q_r \to 0$), this network is now lossless and therefore the scattering matrix must be unitary. We can make this explicit in our notation by taking $\zeta = \delta\,(1 + j\tan\theta_{\text{in}})$ and $\eta = (1 + j\tan\theta_{\text{out}})\,/\delta$, where θ_{in} and θ_{out} are the input and output port phase delays. This definition also gives the rotation matrix that shifts the reference plane of our network, $R_z = \text{diag}\left(e^{-j\theta_{\text{in}}}, e^{-j\theta_{\text{out}}}\right)$.

φ (derived in equation 2.28) and δ are not independent parameters and can be combined into a single angle ψ using the relation $\tan(\psi/2)\cdot\delta = \cos\theta_{\text{in}}/\cos\theta_{\text{out}}$. As we will show in 2.41, the angle ψ gives the magnitude of S_{21} far from resonance.

Our 3 original functions: $[Z_A, Z_B, \delta]$ now correspond to 3 angles $[\theta_{\text{in}}, \theta_{\text{out}}, \psi]$ that relate to the measured scattering parameters. In general, these angles are functions of frequency. The scattering matrix is a sum of 3 terms:

$$\hat{S} \;=\; \hat{S}_0(\omega) \;-\; j\sin\phi\; e^{j\phi}\hat{K}(\omega) \;+\; \hat{K}(\omega_0^{'})e^{j2\phi_c}\cdot\frac{Q_r}{Q_c}\frac{1}{1 + j2Q_r\frac{\omega-\omega_0}{\omega_0}}. \tag{2.41}$$

Intuitively, we have decomposed the full scattering parameters into the continuum and the resonant modes. The presence of the resonator perturbs the continuum mode

from its initial configuration. The scattering matrix therefore comprises into 3 terms: the unperturbed continuum transmission (the unitary matrix $\hat{S}_0$), the perturbation to the continuum and the resonant term. The resonator asymmetry angle ϕ sets the magnitude of the perturbation and the resonant terms. Equation 2.41 quantifies the perturbation to the transmitting continuum mode due to the presence of the resonator network. The resonator network has a back-reaction on the embedding network. The strength of this perturbation unsurprisingly, also gives the coupling of the resonator to the network.

Expressed in ψ, $\hat{S}_0$ is

$$R_z \cdot \hat{S}_0 \cdot R_z = \begin{pmatrix} -\cos\psi & \sin\psi \\ \sin\psi & \cos\psi \end{pmatrix}, \tag{2.42}$$

while the coupling matrix $\hat{K}$ given by

$$R_z \cdot \hat{K} \cdot R_z = \begin{pmatrix} -1+\cos\psi & -\sin\psi \\ -\sin\psi & -(1+\cos\psi) \end{pmatrix}. \tag{2.43}$$

Close to resonance, can simplify the scattering matrix by shifting the reference planes to remove the input and output phases, θ_{in} and θ_{out}, respectively. Additionally, $\phi = \phi_c$. When $\psi = \pi/2$, we recover the familiar relation between S_{11} and S_{21} for a purely shunt network, i.e., $\boxed{S_{21}^{\text{shunt}} = 1 + S_{11}^{\text{shunt}}}$. However, the form of S_{21} is modified to

$$\boxed{S_{21}^{\text{shunt}} = \cos\phi_c \cdot e^{j\phi_c}\left(1 - \frac{Q_r}{Q_c}\frac{1 + j\tan\phi_c}{1 + j2Q_r\left(\frac{\omega-\omega_0}{\omega_0}\right)}\right)}. \tag{2.44}$$

Whereas, we typically consider S_{21} to be fully determined modulo any scale factors, eq. (2.44) shows that this isn't true for asymmetric resonators. The asymmetry angle also scales the overall transmission through the resonator. To see this further, consider $|S_{21}^{\text{shunt}}|^2$, with $\delta = 2Q_r x$ (not to be confused with our previous use of δ),

$$|S_{21}^{\text{shunt}}|^2 = \left[\cos^2\phi_c + \frac{Q_r^2}{Q_c^2}\frac{1}{1+\delta^2} - 2\frac{Q_r}{Q_c}\cos\phi_c\frac{\cos\phi_c + \sin\phi_c\delta}{1+\delta^2}\right]. \tag{2.45}$$

$|S_{21}^{\text{shunt}}|^2$ is exactly the Fano transmission in Yoon and Magnusson, 2013. The key distinction is that, for superconducting resonators, we preserve both the magnitude

and the phase information in the measurement. We conclude that an asymmetric resonator is a Fano-type resonator with non-resonant transmission $\cos^2\phi_c$, and ϕ_c as the phase difference between the resonant and non-resonant transmission paths. The time reversibility from Maxwell's Equations requires that given $\hat{S}$ relating the incoming and outgoing modes of the network, the time-reversed outgoing waves must also scatter to the time-reversed incoming waves (Yoon, Jung, et al., 2012). This constraints the form of the scattering matrix such that $\hat{S}^{\dagger}\left(Q_i- > -Q_i\right) = \hat{S}^{-1}\left(Q_i- > -Q_i\right)$. As a result, the phase difference the resonant and continuum pathways and amplitude of the continuum pathway are not independent parameters and are both given by ϕ_c.

The coupling matrix satisfies the relations: $\hat{K}\cdot\hat{K}^{\dagger} = -2\hat{S}_0\cdot\hat{K}^{\dagger}$ and $\hat{S}_0\cdot\hat{K}^{\dagger} = \hat{K}\cdot\hat{S}_0^{\dagger}$. The perturbed continuum transmission through the network, $\hat{S}_0 + j\sin\phi e^{j\phi}\hat{K}$, is therefore unitary for all possible values of the asymmetry angle ϕ.

Far from resonance, $\boxed{S_{21} \rightarrow S_{21}^0 = \sin\psi\cdot\cos\phi\cdot e^{j\phi}e^{j(\theta_{\text{in}}+\theta_{\text{out}})}}$. In the weak coupling limit, $\cos\phi \approx 1$ and therefore $\boxed{|S_{21}^0(\omega)| = \sin[\psi(\omega)] + O(\phi^2)}$. Weak coupling induces a small phase shift to the transmission in the line to leading order.

Computing the Power Dissipation

Given the full scattering matrix, we can immediately compute the fraction of power available from the source that is dissipated by the resonator, $\chi = 1 - |S_{11}|^2 - |S_{21}|^2$. This is the 1,1 component of the matrix $\left(I - \hat{S}\hat{S}^{\dagger}\right)$ (Zmuidzinas, 2003). Using eq. (2.41),

$$\begin{aligned}\chi &= \left(-\hat{S}_0\hat{K}^{\dagger}\right)_{1,1}\chi_c\cdot\chi_g,\\ &= \sin^2\left(\frac{\psi}{2}\right)\cdot\chi_c\cdot\chi_g.\end{aligned} \tag{2.46}$$

The coupling efficiency $\chi_c = \frac{4Q_r^2}{Q_iQ_c}$ and the detuning efficiency $\chi_g = \left[1+4Q_r^2x^2\right]^{-1}$ for $x = (\omega-\omega_0)/\omega_0$ are well discussed in Zmuidzinas, 2012. Equation 2.46 is a modified version of the well-known expression for power dissipation in single pole resonators, $\chi = \frac{1}{2}\cdot\chi_c\cdot\chi_g$ (ibid.). **Importantly, the power dissipation in the resonator is independent of ϕ_c.** Figure 2.7 compares the computed dissipation in the network using the full network solution and the approximation given in eq. (2.46).

In the weak coupling limit, we find that

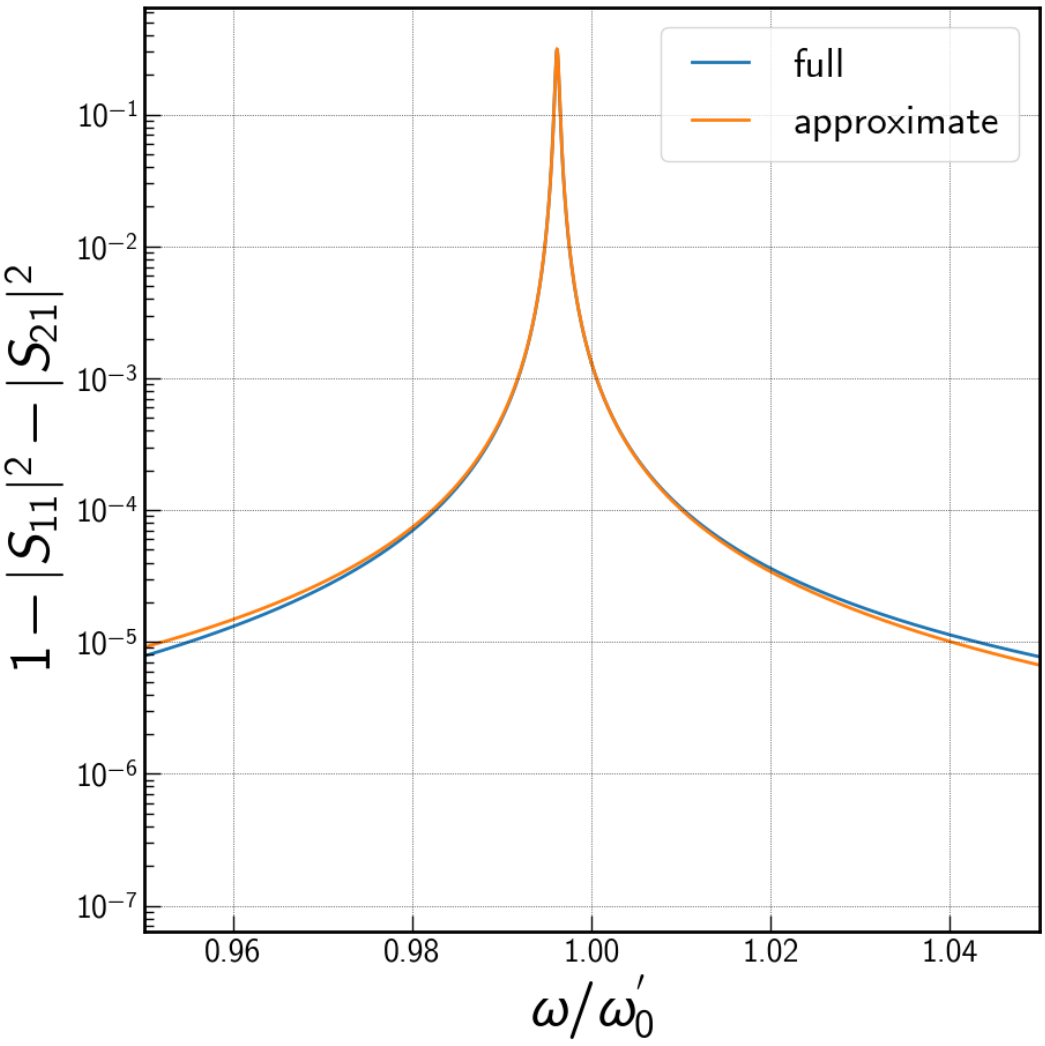

Figure 2.7: Power dissipation in the resonator computed using the full circuit model compared to the prediction from the model in eq. (2.46).

$$\sin^2\left(\frac{\psi}{2}\right) \approx \frac{1}{2}\cdot\left[1-\sqrt{1-|S_{21}^0(\omega)|^2}\right]. \tag{2.47}$$

This is what we intuitively expect if we consider for example, a resonator coupled to a mismatched line so that $|S_{21}^0| \sim 0$ in which case we should obtain $\chi \sim 0$.

In our circuit variables, to lowest order

$$\sin^2\left(\frac{\psi}{2}\right) \approx \frac{1}{2}\left[1-\frac{M}{L}+\frac{L_1 M}{LC_c Z_0^2}\right]. \tag{2.48}$$

In conclusion, the network analysis presented in this section, details a systematic approach for extracting resonator parameters from general circuit models while

capturing all the necessary aspects of the circuit that are important in determining the power dissipation of the resonator. Furthermore, the decomposition of the scattering parameters into transmission and resonant contributions can be more generally applied even to lossy networks. As a result, we have determined that the resonator asymmetry does not affect the power dissipation in the resonator.

2.3 Bolometer Physics

A bolometer consists of a radiation absorber and thermometer on a thermally isolated island at a temperature T_{bath}, that is weakly linked to a thermal bath held at a fixed temperature T_0. Let $k(T^{'})$ be the thermal conductivity at temperature $T^{'}$ of a point x of the thermal link of area A and length l. For simplicity, we assume that material is homogeneous so that the thermal conductivity has no dependence on the position along the thermal link. The temperature gradient across the thermal link induces power $P(x)$ to flow from the island to the bath.

$$P(x) \;=\; A \cdot k(T^{'}) \cdot \frac{\mathrm{d}T^{'}}{dx}. \tag{2.49}$$

The net power flowing across the thermal link P_{leg} is obtained by integrating over the total length and temperature difference

$$P_{\text{leg}} = \frac{A}{l} \int_{T_0}^{T_b} k(T^{'})\mathrm{d}T^{'}. \tag{2.50}$$

In our TKID design, a narrow dielectric bridge between a suspended membrane and the silicon wafer substrate provides the weak thermal link. At the low temperatures of interest, the thermal conductivity typically has a power law form $k(T) = k_0 \cdot T^{\beta}$. The total power through the legs is therefore given by

$$P_{\text{leg}} \;=\; \frac{k_0 \cdot A}{l} \left(T^{\beta+1} - T_b^{\beta+1} \right). \tag{2.51}$$

The conductivity index β is indicative of the type of heat carriers in the material. $\beta = 1$ for electron thermal transport while $\beta = 3$ corresponds to phonons in a 3D material (Ade, Aikin, Amiri, Barkats, Benton, Bischoff, Bock, Bonetti, et al., 2015).

The incident sources of power on the bolometer are the optical power being measured P_{opt}, and the readout power dissipated by the inductor P_{read}. Let C_b be the heat

capacity of the island. The thermal response of the bolometer is governed by the heat balance differential equation

$$C_b \frac{\mathrm{d}T_b}{\mathrm{d}t} = -P_{\mathrm{leg}} + P_{\mathrm{read}} + P_{\mathrm{opt}}. \tag{2.52}$$

The bolometer steady-state operating condition is satisfied when the left hand side of eq. (2.52) vanishes. Of interest, is the small-signal response δT_b of the bolometer to small fluctuations in the optical power δP_{opt}. The fluctuation in the power flowing down the leg is given by the thermal conductance $G(T)$ which is the derivative of the net heat flow through the leg with respect to temperature. $\delta P_{\mathrm{leg}} = G(T_b)\delta T_b$. In Fourier space,

$$j\omega C_b \cdot \delta T_b = \delta P_{\mathrm{opt}} - G(T_b) \cdot \delta T_b. \tag{2.53}$$

For now, we assume that there is negligible readout power dissipation on the bolometer island. This is the operating condition for the devices discussed in chapters 3 and 5. We will revisit this assumption when we consider electrothermal feedback in section 2.9. Rearranging eq. (2.53), gives the single pole thermal response of the bolometer with a time constant $\tau_{\mathrm{bolo}} = C_b(T_b)/G(T_b)$.

$$\delta T_b(\omega) = \frac{\delta P_{\mathrm{opt}}(\omega)}{G(T_b)} \frac{1}{1 + j\omega\tau_{\mathrm{bolo}}} \tag{2.54}$$

The bolometer time constant sets the usable bandwidth of the device. We require that the device bandwidth $\nu_{BW} = 1/(2\pi\tau_{\mathrm{bolo}})$ be much larger than the frequency band of the CMB signal on sky, i.e., $\nu_{BW} > \dot{\theta}/\theta_{\mathrm{FWHM}}$ where $\dot{\theta}$ is the scan rate of the telescope and θ_{FWHM} is the detector beam size on sky. For ground based telescopes mapping degree scale features on sky, the science band is between 0.01-1 Hz whereas the thermal bandwidth is on the order of tens of Hz. For space applications which have tighter bandwidth requirements, the detector bandwidth must be modified either by reducing the heat capacity of the island or taking advantage of negative electrothermal feedback to speed up the bolometer response.

The discrete nature of the phonon quanta that transport heat down the bolometer legs to the thermal bath sets a limit to the fundamental sensitivity of a bolometer. We can derive this noise threshold by first taking the thermal island to be in thermal equilibrium with the bath. In thermal equilibrium there is no net heat flow between the island and the bath.

Phonon Noise

To derive the phonon noise, we consider the mean square fluctuations $\left\langle \delta U^2 \right\rangle$ in the internal energy U of the thermal island. A standard result from statistical mechanics is that $\left\langle \delta u^2 \right\rangle = k_B T^2 \cdot C_b$ (Kittel and Kroemer, 1980). In a bolometer, $\delta U = C_b \cdot \delta T_b$, and therefore, $\left\langle \delta T_b^2 \right\rangle = k_B T_b^2 / C_b$. The variance of the temperature fluctuations relates to integral of the power spectrum $S_{\rm ph} = \mathrm{NEP}_{\rm ph}^2 / \left(1 + \omega^2 \tau_{\rm bolo}^2\right)$ of thermal fluctuations across the bolometer thermal link through eq. (2.54)

$$\left\langle \delta T_b^2 \right\rangle = \frac{k_B T_b^2}{C_b} = \frac{S_{\rm ph}}{G^2} \int_0^\infty \frac{\mathrm{d}\omega}{2\pi} \cdot \frac{1}{1 + \omega^2 \tau_{\rm bolo}^2}. \tag{2.55}$$

Completing the integral gives

$$\mathrm{NEP}_{\rm ph}^2 = 4 k_B T_b^2 G(T_b).. \tag{2.56}$$

Impact of the Thermal Gradient Across the Thermal Link

The phonon NEP we have derived is only strictly true when the weak link is in thermal equilibrium. Since the island is typically at a higher temperature than the thermal bath, we need to generalize the result to account for the temperature gradient across the bolometer leg.

The approach is to divide the bolometer link into a series of nearly isothermal sections for each of which eq. (2.56) holds. The total noise is a weighted sum of the contributions of each section accounting for the relative thermal conductivity of each section of the link. This derivation is well discussed in literature (Mather, 1982, 1984; Richards, 1994). The cumulative effect is to modify the phonon NEP to

$$\mathrm{NEP}_{\rm ph}^2 = 4 k_B T_b^2 G(T_b) F\left(T_b, T_0\right), \tag{2.57}$$

where the bolometer F link factor is typically between 0.5-1. The F link factor, depends not only on the island and bath temperatures, but additionally on whether the phonon reflection from the surface is specular or diffusive. As has been noted in Hoevers et al., 2005, depending on the leg geometry, the thermal conductivity can be dominated by radiative ballistic transport over diffusive conductivity in which case $F = 1$.

To directly compare phonon noise to photon noise defined in eq. (A.7), we rewrite the phonon NEP by taking advantage of the fact that $P_{\rm leg} = P_{\rm opt}$ to eliminate $G(T_b)$ in favor of $P_{\rm opt}$. We find that $\mathrm{NEP}^2_{\rm ph} = 4\tilde{F}(T_b, T_0) k_B T_b P_{\rm opt}$, where $\tilde{F}(T_b, T_0) = F(T_b, T_0) \cdot n/(1 - (T_0/T_b)^n)$ and $n = \beta + 1$. For our device parameters, $F(T_b, T_0) = 0.57$ and $\tilde{F}(T_b, T_0) = 2.4$, giving $\mathrm{NEP}_{\rm ph} = 16\ \mathrm{aW}/\sqrt{\mathrm{Hz}}$, which is much smaller than the expected photon NEP, $\mathrm{NEP}_{\rm photon} = 45\ \mathrm{aW}/\sqrt{\mathrm{Hz}}$ at $\nu_{\rm opt} = 150$ GHz, $\Delta\nu_{\rm opt}/\nu_{\rm opt} = 0.25$. Bolometers are optimized so that the phonon noise is the dominant contributor to the internal detector noise at the operating temperature. This is a key distinction between TKIDs and other MKID designs (Zmuidzinas, 2012).

2.4 Electrodynamics of a Superconductor

Kinetic Inductance

Many properties of a superconductor can be understood under a 2-fluid model as discussed in Tinkham, 1996. The superconducting electrodynamics are due to the combined effects of both the superconducting and normal electron fluid in the material. We will distinguish these 2 contributions using subscripts s and n to label quantities relating to the superconducting and normal contributions, respectively. q, n and m are the charge, volume charge density and mass of given charge carriers in the superconductor.

The 2 London equations govern the relationship between the superconducting current and the applied electric and magnetic fields. These are

$$\frac{\partial \vec{J}_s}{\partial t} = \frac{n_s q_s}{m_s}\vec{E}, \tag{2.58}$$

$$\vec{\nabla} \times \vec{J}_s = -\frac{n_s q_s}{m_s}\vec{B}. \tag{2.59}$$

According to the first London equation, an AC superconducting current must be sustained by a non-zero electric field within the superconductor. This electric field also acts on the small population of normal electrons in the superconductor generating a small but non zero dissipation. This is in contrast to the DC case where the resistance vanishes entirely.

The inertia of the superconducting charge carriers under the effect of the changing electric field creates reactance. To see this, we consider a superconductor with a time varying electric field $\vec{E}$ applied across it. This causes an AC supercurrent I_s

to flow through the conductor of length, width and thickness l, w, t, respectively. The conductor has cross-sectional area $A = w \cdot t$. We can use the Drude model to describe the motion of the charge carriers in the material as a drift with velocity $\vec{v}_d$ and a scattering relaxation time τ. The normal and superconducting fluids have different densities, drift velocities and relaxation times. The drift velocity of the charge carriers satisfies the differential equation

$$-q\vec{E} - m\frac{\vec{v}_d}{\tau} = m\frac{\mathrm{d}}{\mathrm{d}t}\vec{v}_d. \tag{2.60}$$

Crudely, for the superconducting carriers, the scattering time is long $\tau \to \infty$ and the Drude equation reduces to the first London equation. Considering a single mode in Fourier space at frequency ω, the current density $\vec{J}_s = n_s q_s \vec{v}_s$. This gives the relation

$$V = j\omega \left[\frac{m_s}{n_s q_s^2 t} \cdot \frac{l}{w}\right] I_s. \tag{2.61}$$

The quantity in square brackets is the kinetic inductance L_k of the superconductor. We can also similarly define the kinetic inductance of the normal charge carriers, but since their drift velocity is small, their contribution to the total kinetic inductance of the superconductor is negliglible.

The kinetic inductance relates to the density of kinetic energy in the charge carriers

$$\frac{L_k I^2/2}{A \cdot l} = n_s \frac{1}{2} m_s v_s^2. \tag{2.62}$$

Looking ahead, we know from BCS theory that the superconducting charge carriers are pairs of electrons bound together over a distance roughly set by the coherence length ξ_0. Therefore $q_s = 2e$ and $m_s = 2m_e$ where e, m_e are the charge and mass of a single electron, respectively. The surface kinetic inductance, $\mathcal{L}_s = L_k/(l/w)$, is therefore

$$\mathcal{L}_s = \frac{m_e}{2n_s e^2 t}. \tag{2.63}$$

The calculation presented here is not rigorous but gives some intuition. We can expect that the conductivity in a superconductor is a complex function of frequency $\sigma(\omega) = \sigma_1(\omega) - j\sigma_2(\omega)$. $\sigma_2 \to 0$ as $\omega \to 0$. However, our model does not

predict the density of normal charge carriers in the superconductor. It also fails to account for the loss in superconducting properties for frequencies above $\Delta/\hbar$ and the temperature dependence of the superconducting state. A full treatment of the electrodynamics of a superconductor requires BCS theory which we will now consider.

BCS Theory

The full details of BCS theory are beyond the scope of this thesis. The interest reader can consult Bardeen et al., 1957. We will reproduce only the key results required in order to model TKID performance. Through laboratory and on-sky measurements, TKIDs are operated over a broad temperature range from $0.1 - 0.8\ T_c$. Modeling the device response across this entire regime requires a careful consideration of the BCS model beyond the asymptotic expressions for the complex conductivity in common use since these are typically only accurate below $0.2T_c$.

In BCS theory, pairs of electrons form bound states called Cooper pairs due to weak attraction from electron-phonon interactions in the superconductor. The details of the electron-phonon interaction are not required; it suffices that the relevant matrix element in the Hamiltonian is approximately $-V_{\mathrm{BCS}}$ for energies close to the Fermi level E_F.

A key prediction of BCS theory is that there exists a gap energy $\Delta(T)$ that sets the minimum excitation energy $E_{\mathrm{min}} = 2\Delta(T)$ that is required to break a Cooper pair generating 2 quasiparticle excitations. At $T = 0$, all the electron states up to the Fermi energy are occupied. We will denote the gap energy at $T = 0$ as Δ_0. At finite temperatures, taking $\beta = k_B T$, quasiparticles are excited into energy states with $E \geq \Delta$ with a probability given by the Fermi-Dirac distribution $f(E) = \left[e^{\beta E} + 1\right]^{-1}$. At higher microwave excitation powers, the quasiparticle distribution is modified on account of quasiparticle injection. The quasiparticle density of states relative to the Fermi level $\rho(E)$ is given by

$$\rho(E) = \frac{E}{\sqrt{E^2 - \Delta^2}}. \tag{2.64}$$

The quasiparticle excitation spectrum cuts off at high energies of the order of the Debye energy $\Omega_D = \hbar\omega_D$ where ω_D is the Debye frequency. This is not surprising since the electron-electron attraction in a Cooper pair is phonon mediated. Given

the single spin electron density at the Fermi level N_0, the gap energy satisfies the relation

$$\frac{1}{N_0 V_{\mathrm{BCS}}} = \int_{\Delta(T)}^{\Omega_D} \frac{\mathrm{d}E}{\sqrt{E^2 - \Delta^2}} \cdot (1 - 2f(E)) \,. \tag{2.65}$$

As we will see, this equation can be numerically inverted to obtain the gap energy as a function of temperature. The critical temperature T_c is the temperature at which $\Delta(T) \to 0$. By comparing eq. (2.65) in the 2 limits: $T = 0$ and $T = T_c$ we can show that $\Delta_0 = 1.764 k_B T_c$.

In materials with strong electron-phonon coupling, Δ can no longer be taken to be real. The imaginary part of the gap energy, Γ, gives the damping of quasiparticle excitations by decay through the generation of real phonons (Eliashberg, 1960). Such materials are better described by a density of states given by

$$\rho(E, \Gamma) = \mathrm{Re}\left\{ \frac{E}{\sqrt{E^2 - (\Delta - j\Gamma)^2}} \right\}. \tag{2.66}$$

Regardless, given the density of states, the quasiparticle density n_{qp} is given by

$$n_{qp} = 4N_0 \int_{\Delta}^{\infty} \mathrm{d}E \; \rho(E) f(E). \tag{2.67}$$

Superconductor length scales

Using Ampere's Law $\vec{\nabla} \cdot \vec{B} = \mu_0 \vec{J}$ and the second London equation eq. (2.59), we can define a characteristic length scale $\lambda = \sqrt{m_e / \mu_0 n_s e}$, over which an external magnetic field is suppressed exponentially. This is the London penetration depth.

A second length scale can be obtained by considering the long range coherence of the superconducting state. This scale is the superconducting coherence length $\xi_0 = h v_F / \pi \Delta_0$, where v_F is the Fermi velocity. For BCS superconductors, the coherence length is the length scale over which n_s varies and gives the typical size of a Cooper pair.

The final length scale, l is the mean free path over which electrons in the material are scattered. The mean free path relates to the quality of the film since the presence

of impurities or defects act as scattering centers. The mean free path also limits the range over which the superconducting field coheres giving an effective length scale ξ,

$$\frac{1}{\xi} = \frac{1}{\xi_0} + \frac{1}{l}. \tag{2.68}$$

With 3 length scales there are several limiting cases we could take. A full consideration is presented by Jiansong Gao, 2008. In our case, we are interested in the local (dirty) limit which holds when $l \ll \xi_0$ or $l \ll \lambda_{local}$. The penetration depth is now modified to $\lambda_{local}(T) = \sqrt{\hbar/\pi\Delta(T)\mu_0\sigma_n}$. For superconducting thin films, the film thickness t also plays a role. When $t < l$, then the thickness is the limiting length scale. The penetration depth is modified to

$$\lambda_{thin} = \lambda_{local}^2/t. \tag{2.69}$$

The Mattis Bardeen Equations

When BCS Theory is applied to the electrodynamics of the superconductor, we obtain the 2 Mattis Bardeen (MB) equations for the conductivity $\sigma = \sigma_1 - j\sigma_2$, relative to the normal state conductivity σ_n (Mattis and Bardeen, 1958). The conductivity is only reasonably defined in the local(dirty) limit, where the electron mean free path in the superconductor is much shorter than both the coherence length and the London penetration depth. In this case, Ohm's law $\vec{J} = \sigma\vec{E}$ holds. Restricting our analysis to frequencies lower than the gap frequency, $\hbar\omega < 2\Delta$, the real part of the conductivity is given by

$$\frac{\sigma_1(\omega,T)}{\sigma_n} = \frac{2}{\hbar\omega}\int_{\Delta}^{\infty} \mathrm{d}E\,[f(E) - f(E+\hbar\omega)]\,\rho(E)\rho(E+\hbar\omega)h(E,E+\hbar\omega). \tag{2.70}$$

The coherence factor $h(E,E') = \left(1 + \Delta^2/EE'\right)$ accounts for the phase coherent superposition of occupied one-electron states in the superconducting phase. The constructive interference of these states enhances the transition probabilities with the largest effect for states within about Δ away from the Fermi Level. The factor $\rho(E)\rho(E+\hbar\omega)\,[f(E) - f(E+\hbar\omega)]$ is worth closer consideration. $\rho(E)f(E)$ is the number of occupied states at energy E while $\rho(E)(1 - f(E))$ is the number of available states at energy E. The transition probability from an initial state at energy

E to a final state at energy $E+\hbar\omega$ is given by $\rho(E)f(E)\rho(E+\hbar\omega)\,[1-f(E+\hbar\omega)]$. The reverse process also occurs where quasiparticles fall from the higher energy state $E+\hbar\omega$ down to E with probability $\rho(E+\hbar\omega)f(E+\hbar\omega)\rho(E)\,[1-f(E)]$. The difference between these two terms is exactly the factor in the integral.

Plugging in our expressions for the density of states (eq. (2.64)) gives

$$\frac{\sigma_1(\omega,T)}{\sigma_n} = \frac{2}{\hbar\omega}\int_{\Delta}^{\infty} \mathrm{d}E \frac{E^2+\Delta^2+\hbar\omega E}{\sqrt{E^2-\Delta^2}\sqrt{(E+\hbar\omega)^2-\Delta^2}}\left[f(E)-f(E+\hbar\omega)\right]. \tag{2.71}$$

The imaginary part of the conductivity has a similar form but is less amenable to the previous breakdown

$$\frac{\sigma_2(\omega,T)}{\sigma_n} = \frac{1}{\hbar\omega}\int_{\Delta}^{\Delta+\hbar\omega} \mathrm{d}E\,[1-2f(E)]\,\frac{E^2+\Delta^2-\hbar\omega E}{\sqrt{E^2-\Delta^2}\sqrt{\Delta^2-(E-\hbar\omega)^2}}. \tag{2.72}$$

At $T=0$, σ_1 vanishes and we have the following closed form expression for σ_2 in terms of elliptic integrals E and K,

$$\sigma_2(\omega,0) = \frac{\sigma_n}{2}\left[\left(\frac{2\Delta_0}{\hbar\omega}+1\right)E(k')+\left(\frac{2\Delta_0}{\hbar\omega}-1\right)K(k')\right]. \tag{2.73}$$

In eq. (2.73), $k = |2\Delta_0-\hbar\omega|\,/|2\Delta_0+\hbar\omega|$ and $k' = \sqrt{1-k^2}$.

Surface Impedance

Using the BCS framework, we can now refine our prior discussion of the kinetic inductance. Consider the surface impedance of a thin superconducting film $Z_s(\omega,T) = R_s(\omega,T) + jX_s(\omega,T)$. Given the conductivity, the surface impedance is

$$Z_s(\omega,T) = \mu_0\omega\lambda_{thin}(T)\frac{\sigma_2(\omega,0)}{\sigma(\omega,T)}. \tag{2.74}$$

The surface inductance defined by $X_s(T) = j\omega\mathcal{L}_s(T)$ can be expressed approximately as

$$\mathcal{L}_s \approx \frac{1}{\sigma_n t}\frac{\hbar}{\pi\Delta(T)}\frac{\sigma_2(\omega,0)}{\sigma_2(\omega,T)}. \tag{2.75}$$

This generalizes our earlier expression in eq. (2.63) incorporating the temperature and microwave frequency dependence of the superconducting state.

2.5 Responsivity at Low Readout Powers

We can now consider the response of the TKID resonator to the thermal fluctuations of the bolometer island. The small signal changes in the island temperature are read out by monitoring the forward transmission S_{21} of the TKID resonator given in eq. (2.44). At the operating temperature T_b, the resonance frequency and internal quality factor are f_r, and Q_i, respectively. Given the resonance frequency at absolute zero $f_{r,0}$, $f_r = f_{r,0}\,(1 + x_{\rm MB})$ and Q_i directly arise from the full MB conductivity as

$$x_{\rm MB} \;=\; -\frac{\alpha_k}{2}\left(\frac{\sigma_2(\omega,T_b)-\sigma_2(\omega,0)}{\sigma_2(\omega,0)}\right), \tag{2.76}$$

and

$$Q_i^{-1} \;=\; \alpha_k\left(\frac{\sigma_1(\omega,T_b)}{\sigma_2(\omega,0)}\right). \tag{2.77}$$

In the equations above,

Fluctuations over time t in the island temperature $\delta T_b(t)$, induce fractional changes in the resonance frequency, $\delta x(t) = (f_r(t) - f_r)/f_r$ as well as in the resonator dissipation, $\delta_i = Q_i^{-1}(t) - Q_i^{-1}$. In the adiabatic limit, these fluctuations are slower than the resonator bandwidth $\Delta f_r = f_r/2Q_r$, and the response of the resonator $\delta S_{21}(\nu)$ in Fourier space is given by

$$\delta S_{21}(\nu) = \frac{Q_i}{4}\chi_c\chi_g e^{-2j\left(\phi_g-\phi_c\right)}\left[\delta_i(\nu) - j2\delta x(\nu)\right]. \tag{2.78}$$

Expressed in our conductivity integrals, with $\delta\sigma_2(\omega,T_b) = \sigma_2(\omega,T_b) - \sigma_2(\omega,0)$, we find

$$\delta x(t) \;=\; x_{\rm MB}(T_b)\frac{{\rm d}\ln\delta\sigma_2(\omega,T_b)}{{\rm d}\ln T_b}\frac{\delta T_b(t)}{T_b}, \tag{2.79}$$

and

$$\delta_i(t) \;=\; Q_i^{-1}(T_b)\frac{{\rm d}\ln\sigma_1(\omega,T_b)}{{\rm d}\ln T_b}\frac{\delta T_b(t)}{T_b}. \tag{2.80}$$

At lower temperatures, we can make the approximation that the superconductor state is fully specified once the quasiparticle density $n_{\rm qp}$ is known. The quasiparticle generation mechanism is a key distinction between standard KIDs and TKIDs. In KIDs, energy is injected into the quasiparticle system directly via photons or

athermal phonons. On the other hand, in TKIDs, thermal phonons are the main quasiparticle generators.

For aluminum TKIDs, the expected quasiparticle lifetime τ_{qp} is in the tens to hundreds of microseconds range; much smaller than the thermal time constant. Since we take the thermal quasiparticle generation to be the dominant mechanism, the total quasiparticle density reduces to the thermal quasiparticle density n_{th} given by BCS theory as in (Tinkham, 1996):

$$n_{th} = 2N_0\sqrt{2\pi k_B T\Delta}\cdot\exp\left[-\frac{\Delta}{k_B T}\right]. \tag{2.81}$$

As expected, n_{th} depends on the temperature T, the gap energy Δ and the single-spin density of states at the Fermi level N_0. Changes in the quasiparticle density with temperature can be directly related to changes in the resonant frequency and dissipation using the Mattis-Bardeen equations by introducing β; the ratio of the frequency response to the dissipation response. β is a function of the probe frequency f and temperature T and for a thermal quasiparticle distribution, it is asymptotically given by the equation

$$\beta(f,T) = \frac{1+\sqrt{\frac{2\Delta}{\pi k_B T}}\exp\left[-\frac{hf}{2k_B T}\right] I_0\left[\frac{hf}{2k_B T}\right]}{\frac{2}{\pi}\sqrt{\frac{2\Delta}{\pi k_B T}}\sinh\left[\frac{hf}{2k_B T}\right] K_0\left[\frac{hf}{2k_B T}\right]}. \tag{2.82}$$

K_0 and I_0 are the zeroth-order modified Bessel functions of the first and second order, respectively. At our targeted $T_b = 380$mK and $f \sim 300$MHz, $\beta >> 1$. The frequency shift provides a larger signal than the dissipation channel. Given β, $Q_i\cdot\delta_i = \left(\delta n_{qp}/n_{qp}\right)$ and $Q_i\cdot\delta x = \frac{1}{2}\beta(f,T)\left(\delta n_{qp}/n_{qp}\right)$.

Therefore, the power-to-frequency responsivity S of a TKID bolometer in the low readout power limit is

$$S \equiv \frac{\delta f_r}{\delta P_{opt}} = \frac{\partial f_r}{\partial x}\frac{\partial x}{\partial n_{qp}}\frac{\partial n_{qp}}{\partial T}\frac{\partial T}{\partial P_{opt}} = f_{r,0}\frac{\kappa(T)\beta(f,T)}{2\,Q_i\,G(T)\,T}, \tag{2.83}$$

where

$$\kappa(T) \equiv \frac{\mathrm{d}\ln n_{qp}}{\mathrm{d}\ln T} = \left(\frac{1}{2}+\frac{\Delta}{k_B T}\right).$$

Fig. 2.8 shows the predicted responsivity of a TKID bolometer designed to achieve an operating temperature of 380 mK under a 5 pW optical load with no electrothermal

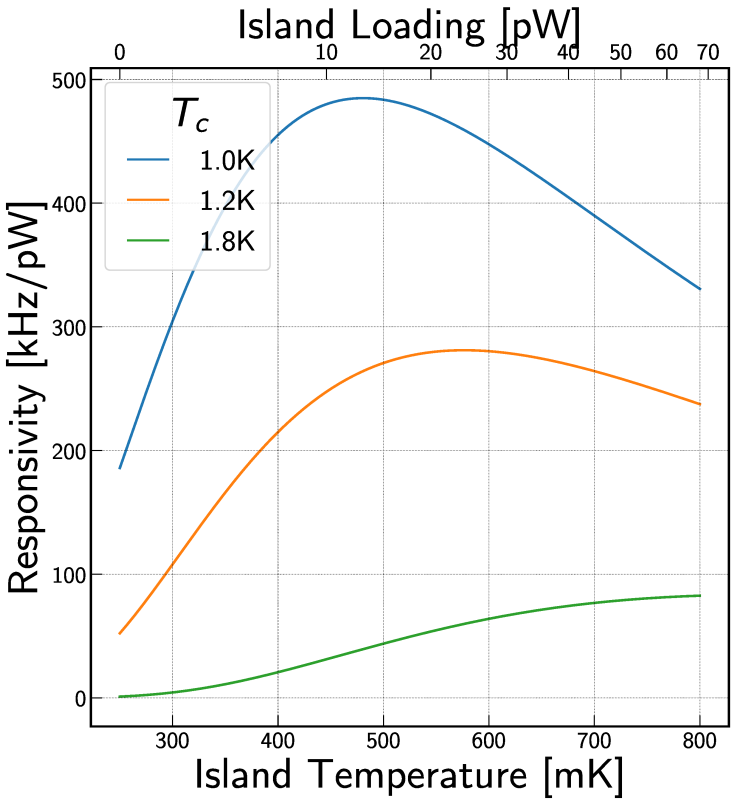

Figure 2.8: Predicted responsivity for three TKID bolometers for 3 different choices of superconducting temperature T_c. The bolometer properties were chosen to match those of the 337 MHz resonator in table 3.2 and the resonator was taken to be optimally coupled at 380 mK.

feedback. Over a large range in loading, the responsivity is non-linear. However, in typical operation, where a telescope only measures small variations over a slowly varying background, the non-linearity is comparable to that of Planck for the case where $T_c = 1.2$ K.

2.6 Numerical Evaluation of the Mattis Bardeen Equations

The initial step in numerically evaluating the conductivity integrals is to determine $\Delta(T)$. We take N_0, Ω_D, and Δ_0 to be known through direct measurements material properties or from reported literature. $1/N_0V_{\mathrm{BCS}} = \log(2\Omega_D/\Delta_0)$. To do so, we define two strictly positive dimensionless variables, $\gamma = \beta\Omega_D/4$, and $\xi = \Delta/\Omega_D$. To make use of Gauss-Jacobi quadrature (suitable for integrals defined over the range [-1,1]), we change the integration variable to $x = (\xi + 1 - 2(E/\Omega_D))/(\xi - 1)$. We can re-express the consistency relation as a function

$$g(\xi;\gamma) = \int_{-1}^{1} \mathrm{d}x\,(1+x)^{-1/2}\cdot f(x;\gamma,\xi) - \frac{1}{N_0 V_{\mathrm{BCS}}}, \tag{2.84}$$

so that when $g(\xi=\xi^*;\gamma)=0$, $\Delta(T)=\xi^*\Omega_D$.

The kernel of the integral,

$$f(x;\gamma,\xi) = 2\,(1-\xi)^{-1/2}\cdot\frac{\tanh\left[\gamma\,(1+\xi+x(1-\xi))\right]}{\sqrt{1+3\xi+x(1-\xi)}}, \tag{2.85}$$

is a smooth function on the interval [-1,1]. This integral can be evaluated using Gauss-Jacobi quadrature and weight indices $\alpha=0,\beta=-1/2$.

The derivative of the kernel, $\mathrm{d}f/\mathrm{d}\xi$, is also required in order to evaluate the root of the consistency equation using Newton's method.

$$\begin{aligned}\frac{\mathrm{d}f(x;\gamma,\xi)}{\mathrm{d}\xi} = 2\gamma\,(1-\xi)^{-1/2}\cdot\frac{(1-x)\,\mathrm{sech}^2\left[\gamma\,(1+\xi+x(1-\xi))\right]}{(1+3\xi+x(1-\xi))^{1/2}} \\ +4\,(1-\xi)^{-3/2}\cdot\frac{\tanh\left[\gamma\,(1+\xi+x(1-\xi))\right]}{(1+3\xi+x(1-\xi))^{3/2}}.\end{aligned} \tag{2.86}$$

ξ converges rapidly to ξ^* within a few iterations of the Newton-Raphson algorithm.

In a similar procedure, to evaluate eqs. (2.71) to (2.72), we define new dimensionless variables: $\gamma = \beta\Delta/2$ and $\eta = \hbar\omega/\Delta$. Our conductivity integrals are now of the form

$$\frac{\sigma_1(\omega,T)}{\sigma_n} = \int_0^{\infty}\mathrm{d}x\;e^{-x}\;f_1(x;\gamma,\eta), \tag{2.87}$$

and

$$\frac{\sigma_2(\omega,T)}{\sigma_n} = \int_{-1}^{1}\mathrm{d}x\;\frac{f_2(x;\gamma,\eta)}{\sqrt{1-x^2}}. \tag{2.88}$$

Gauss-Laguerre and Chebyshev-Gauss quadrature are appropriate for the σ_1 and σ_2 integrals, respectively.

The integration kernels are

$$f_1(x;\gamma,\eta) = \frac{e^x}{\sqrt{1+x^2}}\cdot\frac{\sinh(\gamma\,\eta)}{\gamma\eta}\frac{1+x^2+\eta\left(\sqrt{1+x^2}+\eta\right)}{\sqrt{x^2+\eta\left(2\sqrt{1+x^2}+\eta\right)}}, \tag{2.89}$$

and

$$f_2(x;\gamma,\eta) \;=\; \frac{\tanh\left[\gamma\,(1+\eta(1+x)/2)\right]}{4\eta}\,\frac{8+4\eta x-\eta^2(1-x^2)}{\sqrt{4+\eta(x+1)}\sqrt{4+\eta(x-1)}}. \qquad (2.90)$$

These two kernels are obtained from the change of variables, $E = \Delta\sqrt{1+x^2}$ and $E = \Delta + \frac{\hbar\omega}{2}(x+1)$, respectively. Fig. 2.9 compares the results of the numerical routine presented here and the asymptotic analytical expressions valid at small fractions of the transition temperature. This is especially important when assessing the resonator response under high loading conditions.

2.7 The Quasiparticle and Phonon Systems in TKID Devices

The fluctuations in the quasiparticle density of the superconductor due to the random nature of the pair-breaking and recombination processes determines not only the noise in the superconductor but also the responsivity of the TKID device. In fact, as we will discuss, the electron-phonon link in the superconductor can be modelled in much in the same way as the bolometer link. The physics of electron-phonon coupling give an effective generation-recombination (gr) conductance. We can therefore expect an additional noise term of the form $4k_BT^2G_{\rm gr}(T)$. In addition to the noise, the 'heat capacity' of the quasiparticle system sets the generation-recombination time constant of the superconductor. For a TKID, unlike in many KID applications, TKID responsivity is maximized when the quasiparticle time constant is short to ensure that the superconductor is always in thermal equilibrium with the bolometer.

One approach, is to construct a set of kinetic equations for the dynamics of the superconductor and phonon systems. This effort was inspired by the work done by Wilson and Prober, 2004 and maintains their notation. The approach taken by Rostem et al., 2018 was also instructive. Let N be the number of quasiparticle in the superconductor of total volume V_{sc}. Only phonons with energy $E_\Omega > 2\Delta$ can break Cooper pairs to generate quasiparticles. We will therefore only consider the phonon spectra of the superconductor, bolometer island and bath at frequencies above twice the gap energy. Let the density of phonons in the superconductor with energy greater than 2Δ be N_Ω. Similarly, the superconductor is in thermal contact with a substrate with a phonon density $N_{\Omega,s}$ and the bath has a phonon density $N_{\Omega,b}$. Again, we are only interested in pair breaking phonons. The TKID is a 4 level dynamical system as shown in fig. 2.10. In the general case, we include a term for

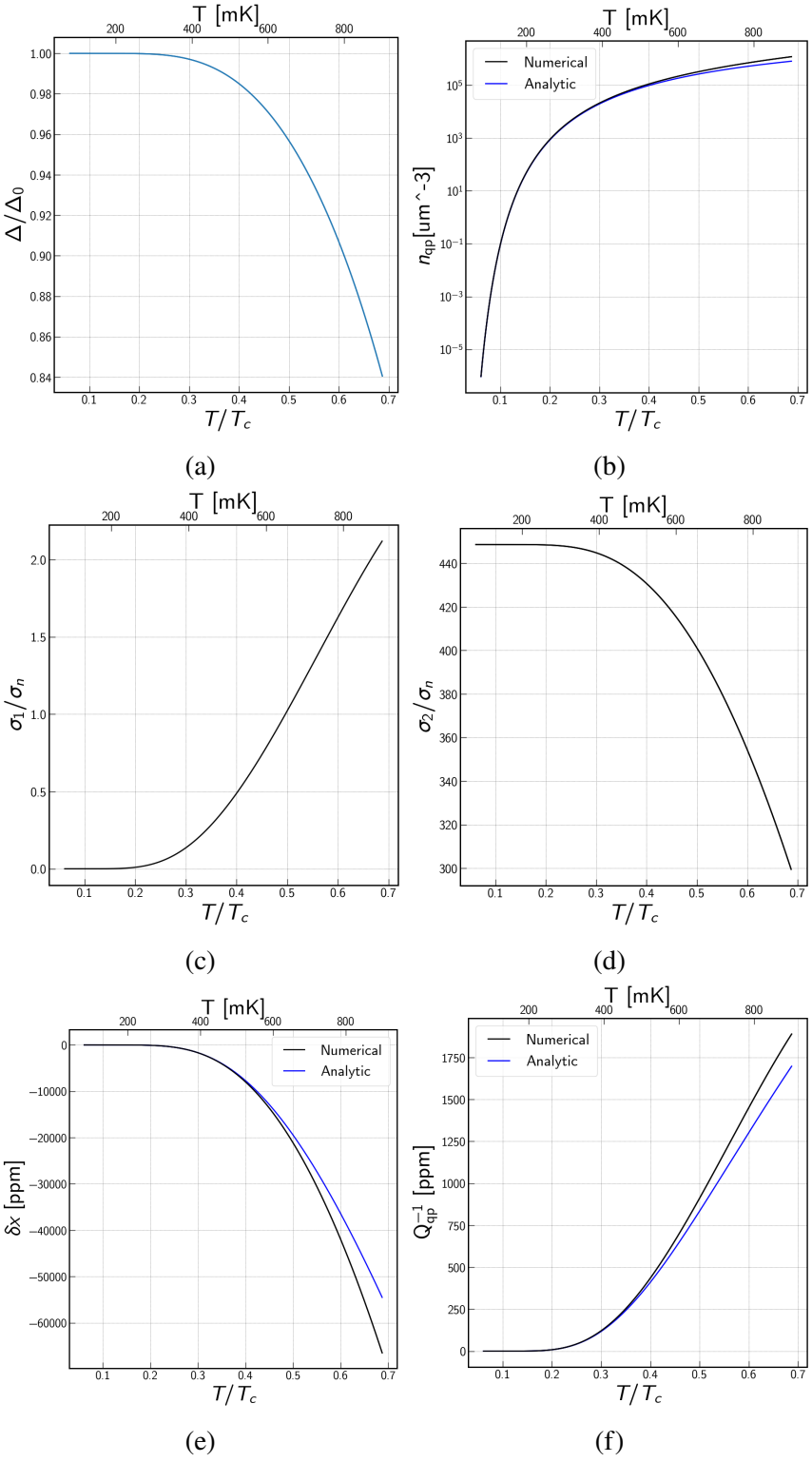

Figure 2.9: A comparison of the full numerically integrated superconductor electrodynamics to the low temperature asymptotic analytic expressions for a 50 nm thick Al film with $T_c = 1.2$K and surface resistance $R_s = 0.25\Omega/\text{sq}$ with $\omega = 2\pi\times300$MHz. Figure 2.9a. The suppression in the gap energy as a function of temperature. Figure 2.9b compares the quasiparticle density from eq. (3.2) to eq. (2.81). Figures 2.9c and 2.9d are the numerically evaluated Mattis Bardeen conductivity integrals. Figures 2.9e and 2.9f show that for $T/T_c > 0.5$, the asymptotic expressions underestimate the fractional frequency shift x_{MB} and Q_i^{-1}.

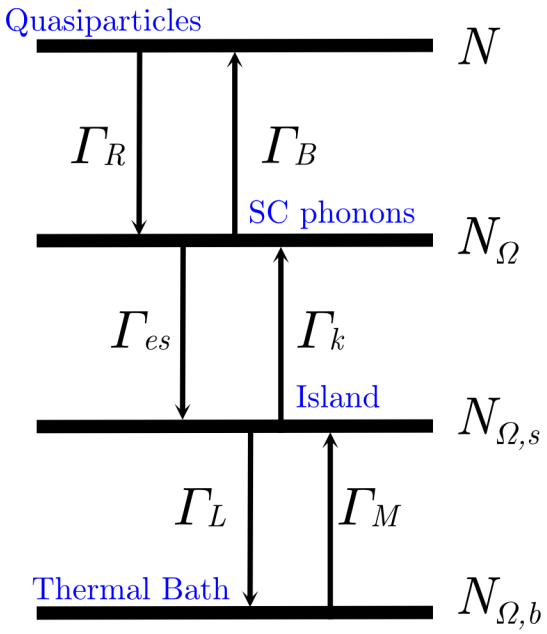

Figure 2.10: The 4 level quasiparticle and phonon system of a TKID.

quasiparticle injection I_{qp} into the SC but we will ignore it in this discussion. The dynamics of the combined quasiparticle and phonon systems is given by

$$\frac{dN}{dt} = 2\left[-\frac{1}{2}\frac{R}{V_{sc}}N^2 + \Gamma_B N_\Omega\right] \tag{2.91}$$

$$\frac{dN_\Omega}{dt} = \frac{1}{2}\frac{R}{V_{sc}}N^2 - \Gamma_B N_\Omega - \Gamma_{es}N_\Omega + \Gamma_k N_{\Omega,s} \tag{2.92}$$

$$\frac{dN_{\Omega,s}}{dt} = \Gamma_{es}N_\Omega + \Gamma_M N_{\Omega,b} - \Gamma_\ell N_{\Omega,s} - \Gamma_k N_{\Omega,s} \tag{2.93}$$

$$\frac{dN_{\Omega,b}}{dt} = \Gamma_L N_{\Omega,s} - \Gamma_M N_{\Omega,b} \tag{2.94}$$

The quasiparticle recombination constant R is a material property. Given the electron-phonon time constant τ_0,

$$\frac{1}{R} = \tau_0 \cdot 2N_0 k_B T_c \cdot \left(\frac{2\Delta}{k_B T_c}\right)^2. \tag{2.95}$$

We account for phonon generation in the thermal island due to absorbed optical power by raising the temperature of the island to T above that of the bath T_{bath}. The equilibrium phonon spectrum in the thermal island is therefore given by

$$N^0_{\Omega,s} \;=\; N_{ion,s} \int_{2\Delta}^{\hbar\Omega_{D,s}} F(\Omega) n(\Omega, T), \tag{2.96}$$

where $N_{ions,s}$ is the number of ions in the substrate, $\Omega_{D,s}$ is the Debye frequency of the substrate, $F(\Omega)$ is the phonon density of states. This is typically taken to be quadratic at low excitations $F(\Omega) \;=\; a\Omega^2$ with a a material dependent constant. Finally, $n(\Omega) \;=\; [\exp(\hbar\Omega/k_B T) - 1]^{-1}$ is the Bose-Einstein distribution.

Since the thermal bath is large, we can assume its phonon density to be constant and set only by its temperature, T_{bath}. We take $\mathrm{d}N_{\Omega,b}/\mathrm{d}t \;=\; 0$ so that $\Gamma_L N^0_{\Omega,s} \;=\; \Gamma_M N^0_{\Omega,b}$. The superscript denotes that we are taking the steady state values. Our system reduces to the effective 3 level system given by

$$\frac{\mathrm{d}N}{\mathrm{d}t} \;=\; -\frac{R}{V_{sc}} N^2 \;+\; 2\Gamma_B N_\Omega \tag{2.97}$$

$$\frac{\mathrm{d}N_\Omega}{\mathrm{d}t} \;=\; \frac{1}{2}\frac{R}{V_{sc}} N^2 \;-\; \Gamma_B N_\Omega - \Gamma_{es} N_\Omega + \Gamma_k N_{\Omega,B} \tag{2.98}$$

$$\frac{\mathrm{d}N_{\Omega,s}}{\mathrm{d}t} \;=\; \Gamma_{es} N_\Omega - (\Gamma_L + \Gamma_k)\, N_{\Omega,B} + \Gamma_L N^0_{\Omega,B}. \tag{2.99}$$

We can linearize the equations above by expanding about the steady state condition where the left hand side of each equation vanishes. In the steady state, we will also take the thermal island is at the same temperature as the superconductor. The following three relations must be satisfied:

$$\Gamma_B N^0_\Omega \;=\; \frac{R}{2V_{sc}} \left(N^0\right)^2 \tag{2.100}$$

$$\Gamma_k N^0_{\Omega,s} \;=\; \Gamma_{es} N^0_\Omega \tag{2.101}$$

$$\Gamma_M N^0_{\Omega,b} \;=\; \Gamma_L N^0_{\Omega,B} \tag{2.102}$$

that allow us to determine $[\Gamma_B, \Gamma_k, \Gamma_M]$ since the equilibrium phonon and quasiparticle densities are known. The dynamics of the phonon-quasiparticle system is therefore dependent on 3 parameters: $[R, \Gamma_{es}, \Gamma_L]$.Γ_{es} is a function of the acoustic mismatch between the SC and the substrate as well as the relative geometry of the SC and the thermal island. Similarly, Γ_L is the rate of phonon escape from the thermal island to the bath and depends on the geometry of the bolometer legs and the volume of the thermal island.

$N = N^0 + \Delta N$. Let $\Gamma_R = RN^0/V_{sc}$, $\Gamma_\Omega = \Gamma_B + \Gamma_{es}, \Gamma_{\Omega,s} = \Gamma_L + \Gamma_k$. We can combine the perturbations to the quasiparticle, SC phonon and bolometer phonon densities into a single vector $\Delta\vec{a} = \left(\Delta N, \Delta N_\Omega, \Delta N_{\Omega,s}\right)$. The linearized equations is concisely the matrix equation

$$\frac{\mathrm{d}\Delta\vec{a}}{\mathrm{d}t} = -\hat{\Gamma}\cdot\Delta\vec{a}, \tag{2.103}$$

where

$$\hat{\Gamma} = \begin{bmatrix} 2\Gamma_R & -2\Gamma_B & 0 \\ -\Gamma_R & \Gamma_\Omega & -\Gamma_k \\ 0 & -\Gamma_{es} & \Gamma_{\Omega,B} \end{bmatrix}. \tag{2.104}$$

The eigenvalues of the $\hat{\Gamma}$ matrix give the time constants of the response of the system to small perturbations. An ideal TKID operates in the regime where $\Gamma_R \to \infty$ so that the quasiparticle system responds near instantaneously to changes in the phonon density. In practice, the effect of the phonon system is to give an effective recombination constant $\Gamma_R^* = 2\Gamma_R \cdot F^{-1}(\Gamma_B, \Gamma_{es}, \Gamma_k, \Gamma_{\Omega,B})$ where F is the phonon trapping factor. The factor of 2 accounts for the fact that quasiparticles recombine in pairs.

The characteristic polynomial χ of $\hat{\Gamma}$ is a cubic polynomial of the variable λ

$$\chi = \Gamma_{es}\left(\lambda\Gamma_k - 2\Gamma_k\Gamma_R\right) + \left(\Gamma_{\Omega,s} - \lambda\right)\cdot\left(\lambda^2 - 2\lambda\Gamma_R - 2\Gamma_B\Gamma_R - \lambda\Gamma_\Omega + 2\Gamma_R\Gamma_\Omega\right). \tag{2.105}$$

We can solve $\chi(\lambda) = 0$ directly to obtain the 3 eigenvalues but this is not instructive in general. One useful limit is when $\Gamma_{\Omega,B} \to \infty$. In this limit, there is no distinction between the bolometer island and the bath and we obtain the superconductor on substrate limit already tackled in literature (Wilson and Prober, 2004). We can find a perturbative solution to the full equations in powers of $\tau_{\Omega,s} = 1/\Gamma_{\Omega,s}$. To first order, the i^{th} eigenvalue can be written as $\lambda_i = \lambda_i^0 + \alpha_i \cdot \tau_{\Omega,s}$ where α_i is a yet undetermined coefficient.

The zeroth order eigenvalues, $\left[\lambda_1^0, \lambda_2^0\right]$ are given by

$$\lambda_{1,2}^0 = \Gamma_R + \frac{\Gamma_\Omega}{2} \mp \frac{1}{2}\sqrt{8\Gamma_B\Gamma_R + \left(\Gamma_\Omega - 2\Gamma_R\right)^2}. \tag{2.106}$$

With some algebra, we can show that to first order, the perturbed eigenvalues are

$$\lambda_1 \;=\; \Gamma_R + \frac{\Gamma_\Omega}{2} - \frac{1}{2}\sqrt{8\Gamma_B\Gamma_R + (\Gamma_\Omega - 2\Gamma_R)^2} - \frac{\Gamma_{es}\Gamma_k}{\Gamma_{\Omega,B}}\left[1 - \frac{\Gamma_\Omega - 2\Gamma_R}{8\Gamma_B\Gamma_R + (\Gamma_\Omega - 2\Gamma_R)^2}\right], \tag{2.107}$$

$$\lambda_2 \;=\; \Gamma_R + \frac{\Gamma_\Omega}{2} + \frac{1}{2}\sqrt{8\Gamma_B\Gamma_R + (\Gamma_\Omega - 2\Gamma_R)^2} - \frac{\Gamma_{es}\Gamma_k}{\Gamma_{\Omega,B}}\left[1 + \frac{\Gamma_\Omega - 2\Gamma_R}{8\Gamma_B\Gamma_R + (\Gamma_\Omega - 2\Gamma_R)^2}\right], \tag{2.108}$$

$$\lambda_3 \;=\; \Gamma_{\Omega,s} + \frac{\Gamma_{es}\Gamma_k}{\Gamma_{\Omega,B}}\left(1 + \frac{\Gamma_\Omega}{\Gamma_{\Omega,B}}\right). \tag{2.109}$$

At the low temperatures of interest, $\Gamma_R \ll \Gamma_\Omega$. Taking advantage of this limit, we define $F_\Omega = 1 + \Gamma_B/\Gamma_{es}$ and $F_{\Omega,s} = 1 + \Gamma_k/\Gamma_L$. The eigenvalues $\lambda = 1/\tau$,

$$\frac{1}{\tau_1} \;=\; 2\Gamma_R \frac{F_{\Omega,s} + F_\Omega - 1}{F_\Omega^2 F_{\Omega,s}}, \tag{2.110}$$

$$\frac{1}{\tau_2} \;=\; 2\Gamma_R \frac{(F_\Omega - 1)\left(F_\Omega F_{\Omega,s} + F_{\Omega,s} - 1\right)}{F_\Omega^2 F_{\Omega,s}} + \Gamma_{es}\frac{F_\Omega F_{\Omega,s} - F_{\Omega,s} + 1}{F_{\Omega,s}}, \tag{2.111}$$

$$\frac{1}{\tau_3} \;=\; \Gamma_L\left(F_{\Omega,s} + 1\right) + \Gamma_{es}\frac{F_{\Omega,s} - 1}{F_{\Omega,s} + 1}. \tag{2.112}$$

In a general multivariable master equation approach (Wilson and Prober, 2004), the covariance matrix $\sigma^2 = \left\langle \Delta\vec{a} \cdot \Delta\vec{a}^T \right\rangle$ is given by the matrix equation

$$\sigma^2 \cdot \hat{\Gamma}^T + \hat{\Gamma} \cdot \sigma^2 \;=\; \hat{B}, \tag{2.113}$$

where

$$\hat{B} \;=\; N^0 \cdot \Gamma_R \begin{bmatrix} 4 & -2 & 0 \\ -2 & 1 + \frac{\Gamma_{es}}{\Gamma_B} & -\frac{\Gamma_{es}}{\Gamma_B} \\ 0 & -\frac{\Gamma_{es}}{\Gamma_B} & \frac{\Gamma_{es}}{\Gamma_B}\left(1 + \frac{\Gamma_L}{\Gamma_k}\right) \end{bmatrix}. \tag{2.114}$$

The cross power spectrum matrix is given by

$$\hat{G}(\omega) \;=\; 2\,\mathrm{Re}\left[\left(\hat{\Gamma} + j\omega\hat{I}\right)^{-1} \cdot \hat{B} \cdot \left(\hat{\Gamma}^T - j\omega\hat{I}\right)^{-1}\right]. \tag{2.115}$$

where $\hat{I}$ is the identity matrix.

The power spectra are therefore sums of Lorentzians with characteristic frequencies determined by the eigenvalues of $\hat{\Gamma}$ which we have already computed approximately.

The quasiparticle power spectrum $S = \hat{G}_{1,1}$ is of the form

$$S(\omega) = \frac{4\alpha_1\tau_1 N^0}{1+(\omega\tau_1)^2} + \frac{4\alpha_2\tau_2 N^0}{1+(\omega\tau_2)^2} + \frac{4\alpha_3\tau_3 N^0}{1+(\omega\tau_3)^2}, \tag{2.116}$$

where

$$\alpha_1 = \frac{a\tau_1^4 - b\tau_1^2 + c}{\tau_1\left(\tau_1^2-\tau_2^2\right)\left(\tau_1^2-\tau_3^2\right)}, \tag{2.117}$$

$$\alpha_2 = \frac{a\tau_2^4 - b\tau_2^2 + c}{\tau_2\left(\tau_2^2-\tau_1^2\right)\left(\tau_2^2-\tau_3^2\right)}, \tag{2.118}$$

$$\alpha_3 = \frac{a\tau_3^4 - b\tau_3^2 + c}{\tau_3\left(\tau_3^2-\tau_1^2\right)\left(\tau_3^2-\tau_2^2\right)}. \tag{2.119}$$

and

$$a = \frac{1+F_{\Omega,B}\left(F_\Omega-1\right)}{2\Gamma_R}, \tag{2.120}$$

$$b = \frac{1}{2\Gamma_R}\left(\frac{F_\Omega^2}{\Gamma_L^2} + \frac{F_{\Omega,s}^2}{\Gamma_{es}^2} + 2\frac{F_{\Omega,s}-1}{\Gamma_L\Gamma_{es}}\right), \tag{2.121}$$

$$c = \frac{1}{2\Gamma_R}\frac{1}{\Gamma_{es}^2}\frac{1}{\Gamma_L}. \tag{2.122}$$

The quasiparticle statistics are Poissonian and therefore the variance of the fluctuation in quasiparticles is given by

$$\int_0^\infty \frac{\mathrm{d}\omega}{2\pi} S(\omega) = N^0, \tag{2.123}$$

and $\alpha_1 + \alpha_2 + \alpha_3 = 1$.

In the limit, $\Gamma_{\Omega,B} \ll \Gamma_R \ll \Gamma_\Omega$, we $\tau_1 \gg \tau_2, \tau_3$, and therefore $4\alpha_1\tau_1 \approx 4a = \tau_1\left[1 + O\left((F_{\Omega,s} - 1)^2\right)\right]$. Therefore,

$$S(\omega) \approx \frac{4\tau_1 N^0}{1 + (\omega\tau_1)^2}, \tag{2.124}$$

accurate up to second order in the perturbative expansion.

Our expression for the quasiparticle time constant in eq. (2.110) is particularly illuminating. Given $N^0 = n_{\mathrm{qp}} \cdot V_{\mathrm{sc}}$ can rewrite $\tau_1 = \tau_{\mathrm{qp}}$ as

$$\tau_{\mathrm{qp}} = \frac{1}{R^* n_{\mathrm{qp}}}, \tag{2.125}$$

where the recombination constant is now modified by a phonon trapping factor $F_{\mathrm{trap}} = \frac{F_{\Omega,s}+F_\Omega-1}{F_\Omega^2 F_{\Omega,s}}$ so that $R^* = R \cdot F_{\mathrm{trap}}^{-1}$. F_{trap}^{-1} is the probability of a phonon escaping out into the thermal bath. The time constant also picks up a factor of 2 since quasiparticles always recombine in pairs.

We do not currently have a physical model that can predict the phonon trapping factor. To do so would require accounting for the geometry of the bolometer island and legs, the phonon pair-breaking length in the superconductor, total internal reflection at dielectric and metal boundaries as well as phonon scattering due to impurities. Even so, measured GR noise (see section 3.3) in TKIDs shows evidence of a large trapping factor leading to gr noise in excess of the prediction from the material recombination constant. This is certainly of interest in KID applications such as photon counting where phonon recycling leads to gains in the responsivity and improved energy resolution (Pieter J. de Visser et al., 2021).

The generation-recombination NEP is the square root of the power spectrum divided by $V_{\mathrm{sc}}^2 \cdot \left(\partial n_{\mathrm{qp}}/\partial P_{\mathrm{opt}}\right)^2$,

$$\mathrm{NEP}_{\mathrm{gr}} = \frac{2G(T)T}{n_{\mathrm{qp}}(T)\ \kappa(T)} \cdot \frac{1}{\sqrt{R^* V_{\mathrm{sc}}}}. \tag{2.126}$$

Equation 2.126 shows that at high temperatures, gr noise is suppressed because the quasiparticle density increases exponentially with temperature. In addition, the responsivity, given in equation 2.83, is independent of the superconductor volume. As a result, we are free to make the inductor volume large to further suppress the gr noise. This is an additional degree of flexibility for TKIDs, unlike many

KID designs in which the inductor volume must be kept small to keep the optical responsivity high (McCarrick et al., 2014; Zmuidzinas, 2012). The freedom to use a large inductor also allows us to use lower readout frequencies at a fixed capacitor size or alternatively, use smaller capacitors to achieve the same readout frequency.

The form of the GR noise in eq. (2.126) is very similar to the phonon NEP given in eq. (2.57). In fact, favoring $\tau_{\rm qp}$ over R^* and defining the quasiparticle heat capacity $C_{\rm qp} = \kappa N_{qp}\Delta_0/T$ gives

$$\mathrm{NEP}^2_{\rm gr} = 4Gk_BT^2\left[\frac{\kappa-1}{\kappa}\frac{G}{G_{qp}}\right]. \tag{2.127}$$

In eq. (2.127), $G_{\rm qp} = C_{\rm qp}/\tau_{\rm qp}$ is the effective thermal conductance between the quasiparticles in the superconductor and the substrate. In defining the heat capacity, we assumed that the quasiparticles have energy close to the gap energy, i.e., $E_{qp} = N_{qp}\Delta_0$ so that $C_{qp} = \partial E/\partial T \approx \kappa N_{qp}\Delta_0/T$. The term in square brackets therefore resembles the bolometer Flink factor discussed previously in section 2.3. In an ideal TKID device, $G_{qp} \to \infty$ so that the dynamics of the device are dominated only by the bolometer weak link. This is an important point where operating space for TKIDs is quite orthogonal to that of KIDs.

In summary, we have derived an expression for the phonon trapping factor for a TKID in thermal equilibrium at a temperature T and connected to a bath at a fixed temperature $T_{\rm bath}$. The phonon trapping factor accounts for both thermal links: the island to the bath, and the substrate to the superconductor. We can separate the 2 contributions from noise measurements of TKIDs before and after bolometer island release. Further modeling work is also needed to estimate the rates, $[\Gamma_{es}, \Gamma_L]$ given the island and SC geometries. We also need to account for the effect of normal metal on the island.

2.8 Additional Detector Noise Terms

The two remaining noise terms are: Two-Level System (TLS), and amplifier noise, sourced from the first amplifier in thereadout chain. All the noise terms add in quadrature: $\mathrm{NEP}^2_{\rm total} = \mathrm{NEP}^2_{\rm photon} + \mathrm{NEP}^2_{\rm ph} + \mathrm{NEP}^2_{\rm gr} + \mathrm{NEP}^2_{\rm amp} + \mathrm{NEP}^2_{\rm TLS}$. We consider each of these terms in turn and describe the conditions under which each of them remains sub-dominant to the phonon noise level.

Two-Level System Noise

TLS noise in resonators is sourced by fluctuations in the permittivity of amorphous dielectric in the resonator (W. A. Phillips, 1987). These fluctuations couple to the electric field of the resonator. Unlike the noise terms already considered, there is no microscopic theory of TLS noise. Instead, we apply the semi-empirical TLS noise model which is extensively covered in Gao's thesis (Jiansong Gao, 2008). TLS effects in the resonator also modify the internal quality factor and also introduce an additional temperature-dependent frequency shift. These two effects are given by

$$Q_{\mathrm{TLS}}^{-1} = F\delta_{\mathrm{TLS}} = F\delta_0 \tanh\left(\frac{hf}{2k_BT}\right) \cdot \frac{1}{\sqrt{1 + P_g/P_c}}, \tag{2.128}$$

$$x_{\mathrm{TLS}} = \frac{F\delta_0}{\pi}\left[\mathbb{R}\mathrm{e}\left[\Psi\left(\frac{1}{2} + \frac{hf}{2j\pi k_BT}\right)\right] - \ln\left(\frac{hf}{k_BT}\right)\right]. \tag{2.129}$$

Here, δ_{TLS} is the TLS contribution to the dielectric loss tangent, F is a filling factor that accounts for the fraction of the total electrical energy of the resonator that is stored in the TLS hosting material, δ_0 is the loss tangent constant and Ψ is the digamma function (Jiansong Gao et al., 2008). At a probe tone power P_g and tone frequency f, TLS effects introduce a power dependence to the quality factor characterized by a critical power P_c. The fractional frequency shift is expected to be only weakly power dependent and positive with temperature increase. In the limit that $k_BT \ll hf$, the TLS loss drops off as $1/T$. Our target operating temperature is high enough to allow us to ignore the TLS effects on the resonator frequency and quality factor and only use the Mattis Bardeen relations.

The TLS noise power spectrum S_{TLS} in Hz^{-1} in the limit of strong electric fields is given as (Jiansong Gao, 2008; Zmuidzinas, 2012)

$$S_{\mathrm{TLS}}\left[\mathrm{Hz}^{-1}\right] = \kappa_{\mathrm{TLS}}(\nu, f, T)\,\frac{\int_{V_{\mathrm{TLS}}} |\vec{E}(\vec{r})|^3\,\mathrm{d}^3r}{4\left[\int_V |\epsilon(\vec{r})\,\vec{E}(\vec{r})|^2\,\mathrm{d}^3r\right]^2}, \tag{2.130}$$

where $\kappa_{\mathrm{TLS}}(\nu, f, T)$ captures the dependence on temperature and readout frequency, $\vec{E}(\vec{r})$ is the electric field, $\epsilon(\vec{r})$ is the dielectric constant, V_{TLS} is the volume of the

TLS hosting media and V is the total volume. The electric field terms exhibit the measured $P_g^{-1/2}$ dependence on the readout power.

In order to compare TLS noise in devices with different geometry and operating conditions, it is more useful to use the microwave photon number N instead of the electric field. $N = E/(hf_r)$, where the E is the energy stored in the resonator. $E = \frac{1}{2} \cdot Q_i \cdot \chi_c \chi_g \cdot P_g/(2\pi f_r)$, from the definition of the internal quality factor. We must also account for the known saturation of the power dependence of TLS effects at low electric fields (Jiansong Gao et al., 2008). We can include this saturation factor and make the temperature and readout frequency dependence of κ_{TLS} explicit by rewriting S_{TLS} as

$$S_{\mathrm{TLS}}\left[\mathrm{Hz}^{-1}\right] = \kappa_{\mathrm{TLS},0}\left(\frac{\nu}{300\mathrm{MHz}}\right)^{-\alpha}\left(\frac{T}{380\mathrm{mK}}\right)^{-\beta}(1+N/N_c)^{-\gamma}, \tag{2.131}$$

where $\kappa_{\mathrm{TLS},0}$ is a constant that sets the overall TLS noise level. The exponents typically have measured values (Zmuidzinas, 2012) $\alpha = 1/2, \beta = 1.5-2$ and $\gamma = 1/2$ although other values for the exponents α and β, have been suggested (Burin et al., 2015; Burnett et al., 2016; Frossati et al., 1977; Ramanayaka et al., 2015). N_c captures TLS saturation at $N \ll N_c$ with the correct limit when $N \gg N_c$. We estimate $N_c \sim 7 \times 10^6$ from measured TLS critical powers of our devices, $P_c \sim -95$ dBm. A few simple scaling relations between measured δ_{TLS} and $\kappa_{\mathrm{TLS},0}$, which are useful for predicting TLS behavior, have been reported in literature (Burin et al., 2015; Burnett et al., 2016; Ramanayaka et al., 2015). We do not refer to these but we instead consider measured noise levels for similarly designed devices presented in Figure 14 of Zmuidzinas, 2012 to estimate $\kappa_{\mathrm{TLS},0} \sim 8 \times 10^{-23}$ Hz^{-1}. We specify $T = T_o$ and $f = 300$MHz, to obtain an upper limit of $S_{\mathrm{TLS}}(1\mathrm{Hz},\ T_o,\ -90\mathrm{dBm}) \sim 4 \times 10^{-19}$ Hz^{-1}.

We can obtain the TLS NEP by dividing the TLS power spectrum by the power-to-fractional-frequency-shift responsivity

$$\mathrm{NEP}^2_{\mathrm{TLS}} = \frac{1}{\left(\partial x/\partial P_{\mathrm{opt}}\right)^2} S_{\mathrm{TLS}}. \tag{2.132}$$

In order to satisfy $\mathrm{NEP}^2_{\mathrm{TLS}} \ll \mathrm{NEP}^2_{\mathrm{ph}}$, the following condition must hold:

$$S_{\mathrm{TLS}} \ll 4\chi k_B T_o^2 G(T_o)\left(\frac{\partial x}{\partial P_{\mathrm{opt}}}\right)^2. \tag{2.133}$$

When we specify our design parameters, the condition reduces to $S_{\mathrm{TLS}} \ll 2.7 \times 10^{-17}$ Hz^{-1}. The condition is satisfied because of the high responsivity $\partial x/\partial P_{\mathrm{opt}} = 331$ ppm/pW^{-1} at T_o. The two orders of magnitude gap between the expected TLS noise level and the upper tolerable limit gives us confidence that TLS noise will have negligible impact on our devices during normal operation.

Amplifier Noise

The last noise contribution to consider is the additive noise of the amplifier. For an amplifier with noise temperature T_N and and at readout power P_g, the NEP contribution is given by (Zmuidzinas, 2012)

$$\mathrm{NEP}_{\mathrm{amp}} = \frac{1}{\left(\partial x/\partial P_{\mathrm{opt}}\right)} \cdot \frac{Q_c}{2\,Q_r^2} \cdot \frac{1}{\chi_g} \sqrt{\frac{k_B T_N}{P_g}}. \tag{2.134}$$

The amplifier noise contribution can be made small by using an amplifier with a low enough noise temperature or by biasing the resonators with a large readout power. Cryogenic low noise amplifiers with $T_N < 10$ K are readily available commercially. However, we deliberately limit the bias power to operate the resonators in the linear kinetic inductance regime.

An optimized TKID bolometer has detector noise contributions, $\mathrm{NEP}_{\mathrm{gr}}$, $\mathrm{NEP}_{\mathrm{TLS}}$ and $\mathrm{NEP}_{\mathrm{amp}}$ below the phonon noise. Figure 2.11 shows the noise model of an aluminum TKID as a function of the island temperature. The figure shows the limits under which generation-recombination vs. phonon noise dominates in the resonator. The bolometer parameters were chosen to be suitable for 150 GHz ground-based observations of the CMB. The resonator was taken to be optimally coupled at 380 mK and the readout power was set at –90 dBm with a 5 K amplifier noise temperature.

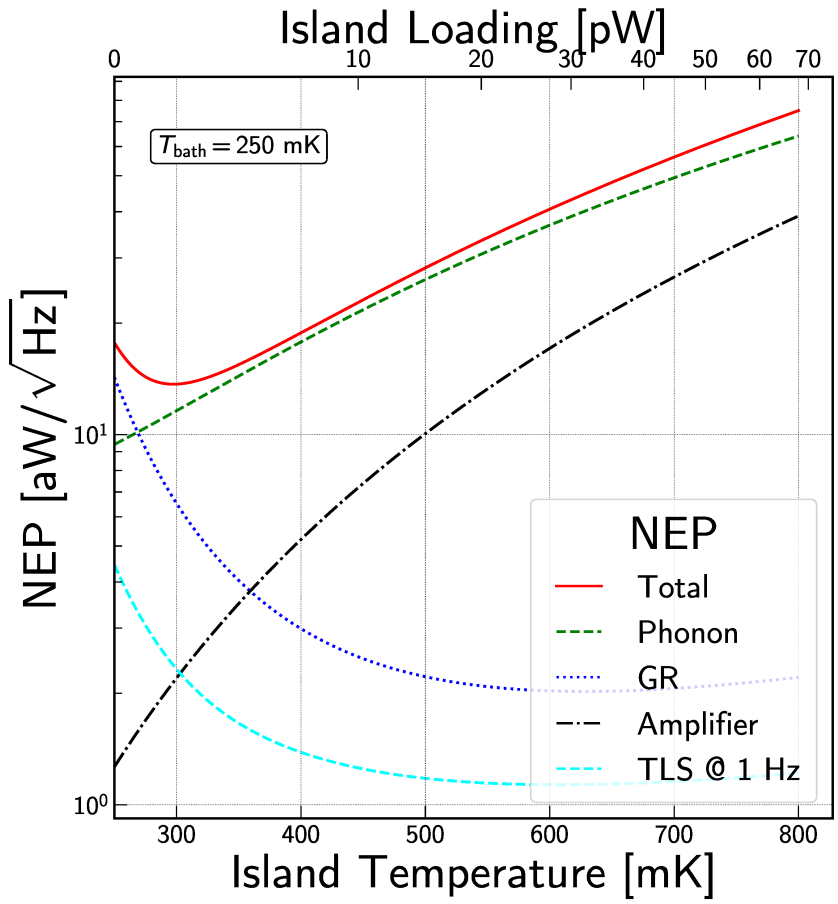

Figure 2.11: Detector noise model of an aluminum TKID as a function of the island temperature showing each noise term. TLS noise was modeled using $\kappa_{\mathrm{TLS},0} = 8 \times 10^{-23}$ Hz^{-1} and the amplifier noise was calculated at a 5 K noise temperature and –90dBm readout power. The bolometer properties were chosen to match those of the 337 MHz resonator in table 3.2 and the resonator was taken to be optimally coupled at 380 mK.

2.9 Electrothermal Feedback

As shown in eq. (2.75), the surface impedance of a TKID is strongly dependent on the temperature $Z_s = Z_s(T)$. At high excitation, the power dissipation in the resonator P_{read} is a function of the temperature. This introduces coupling between the resonator state and the bolometer thermal differential equation eq. (2.52).

The readout power dissipation given in eq. (2.47) is dependent on the detuning of the probe tone away from the resonance. At a fixed probe tone location, the steady state temperature T_0 of the bolometer is set by the balance equation $P_{\mathrm{leg}}(T_b) = P_{\mathrm{read}}(T_b) + P_{\mathrm{opt}}(T_b)$. Stable solutions also require $\partial P_{\mathrm{read}}/\partial T < \partial P_{\mathrm{leg}}/\partial T$. Similar to the Duffing oscillator behavior seen in resonators with non-linear kinetic inductance

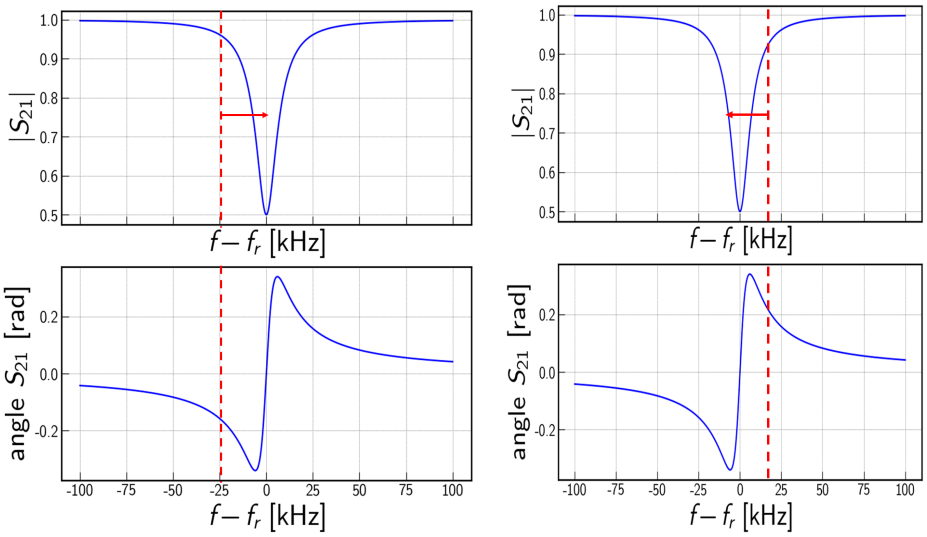

(a) (b)

Figure 2.12: An illustrative example of positive and negative electrothermal feedback in TKIDs. In fig. 2.12a, the probe tone denoted by the red dashed line is to the left of the resonance. When the optical power is slightly increased, the resonator shifts towards the probe tone further increasing the readout power dissipated. This creates a runaway positive feedback loop where small perturbations rapidly increase away from equilibrium. On the other hand in fig. 2.12b, a slight increase in the optical loading shifts the resonator away from the probe tone. The resulting decrease in readout power dissipation relaxes the resonator back into its original state. This negative-electrothermal feedback effect can be used to increase the thermal response of TKIDs just as in TES bolometers.

(Swenson et al., 2013), at high readout powers, there are 2 stable branches of the resonance frequency.

The first is a cold branch with weak positive electrothermal feedback. This branch can be accessed by sweeping the probe tone up in frequency and corresponds to the case shown in fig. 2.12a. Of more interest is the hot branch with strong negative electrothermal feedback as in fig. 2.12b. A third unstable branch also exists but is experimentally inaccessible. Figs. fig. 2.13 show measurements of S_{21} demonstrating both positive and negative feedback under upsweeps and downsweeps, respectively.

Other non-linear mechanisms in superconducting resonators are worth considering. Rigorous calculations (Semenov et al., 2020) show that the surface impedance also has a non-trivial dependence on the applied current. However, kinetic inductance non-linearity is significant as the current in the resonator approaches the critical current at resonator energies of the order $E_* \propto L_k I_c^2$ when the non-linear parameter

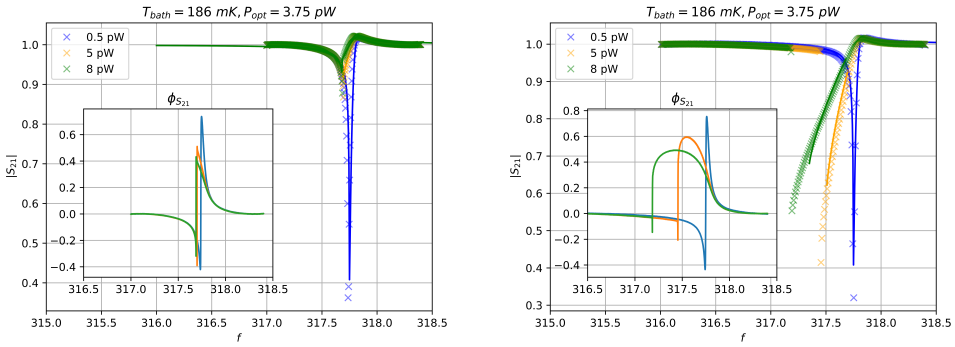

(a) (b)

Figure 2.13: Measured S21 magnitude plotted against frequency for (a) upsweeps and (b) downsweeps. Model predictions are given by lines. Insets show measured S_{21} phase. Strong hysteresis is seen for downsweeps at probe powers of the order of a few pW, when P_g is comparable to P_{opt}.

$a = \left(2Q_r^3/Q_c\right) \cdot P_g/E_* \geq 0.8$ (Swenson et al., 2013; Zmuidzinas, 2012). However, at the relatively high temperatures at which TKIDs are operated, $Q_i \sim Q_c \sim 10^4$. The current in the TKID $I \propto Q_i/(Q_i + Q_c)\sqrt{P_g}$, therefore the current densities are low. Quasiparticle heating (Thomas et al., 2015) due to the decoupling of the quasiparticle and phonon systems can also be an important effect. However, as discussed under generation-recombination noise, by design TKIDs have a large volume to minimize the GR noise eq. (2.126). The high quasiparticle density, the short quasiparticle lifetime at high temperatures coupled with the large inductor volume all minimize quasiparticle heating in the TKID.

Similar to TES bolometers and as derived by Lindeman (Lindeman, 2014; Thomas et al., 2015), given the TKID inductor impedance $Z = R + j\omega L$ at temperature T_b, the sensitivity to temperature is parametrized by the complex valued parameter $\alpha = T_b/R(T_b) \cdot \partial Z/\partial T$. We can express the real and imaginary part of α using the resonator parameters as

$$\alpha_\phi = \operatorname{Im}\alpha = -2Q_i \frac{T}{f_r}\frac{\partial f_r}{\partial T} = \beta\kappa \tag{2.135}$$

and

$$\alpha_A = \operatorname{Re}\alpha = -\left(\frac{T}{Q_i}\frac{\partial Q}{\partial T} + \frac{T}{Q_i}\frac{\partial Q}{\partial T}\right) = -\kappa\left(1 + \frac{\beta}{2Q_i}\right). \tag{2.136}$$

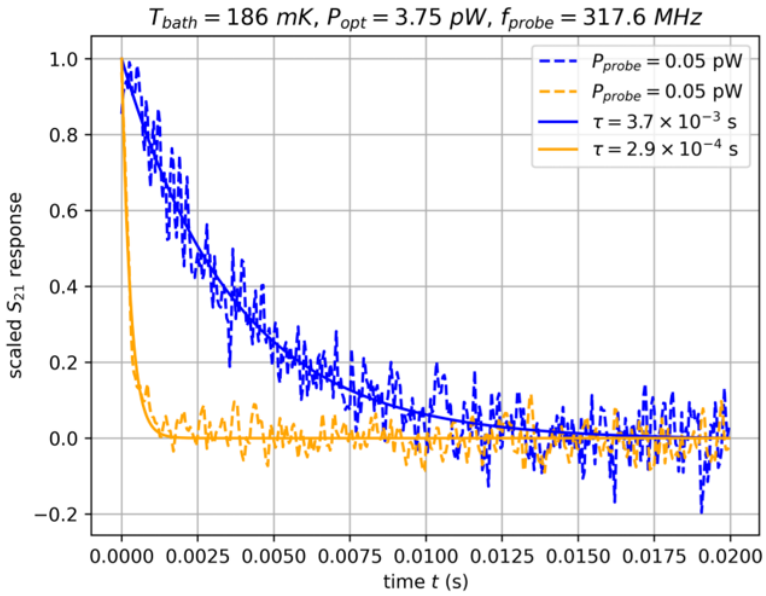

Figure 2.14: Resonator response to a small step change in incident power at low (blue) and high (orange) probe power. Solid lines show the fit to the exponential decay at this edge of the applied Popt square wave. For clarity, the data are scaled and shifted to the range (0, 1]. At high probe power, the thermal response is reduced dramatically due to strong negative electrothermal feedback.

From eqs. (2.135) and (2.136), it is clear that $\alpha_\phi \gg \alpha_A$ since β is large. Electrothermal feedback has a much larger effect on the resonance frequency than the quality factor. Up to some numerical factors, $\partial P_{\rm read}/\partial T = -\alpha_\phi P_{\rm read}/T_b$. We can therefore re-express the linearized bolometer thermal differential equation as

$$C_b \frac{\mathrm{d}\delta T}{\mathrm{d}t} = -\left(G + \alpha_\phi P_{\rm read}/T_b\right)\delta T + \delta P_{\rm opt}. \tag{2.137}$$

Defining the loop gain $\mathcal{L} = \alpha_\phi P_{\rm read}/G(T_b)T_b$ gives

$$\delta T(\omega) = \frac{\delta P_{\rm opt}(\omega)}{G(T_b)\,(1+\mathcal{L})}\frac{1}{1+j\omega\tau_{\rm ETF}} \tag{2.138}$$

where the bolometer time constant $\tau_{\rm ETF} = \tau_{\rm bolo}/(1+\mathcal{L})$. Comparing eq. (2.138) to eq. (2.54), the time constant of the bolometer is sped up since $\mathcal{L} \gg 1$. Similarly, the responsivity is suppressed by a factor of $(1+\mathcal{L})$. Experimentally, we have demonstrated TKIDs with loop gains of about 10-20 using small prototype devices (Agrawal et al., 2021).

2.10 Constructing the Frequency and Inverse Quality Factor Timestreams

For reference, we reconstruct our noise data using the general resonator model given in eq. (2.139) that describes a resonator with resonance frequency f_r, total quality factor $Q_r = 1/\delta_r$ and a complex coupling quality factor $\hat{Q}_c$ defined by $\hat{Q}_c^{-1} = Q_c/(1 + j\tan\phi_c)$. The line properties are described by a complex amplitude $\bar{A}$, line delay D and phase offset ϕ_0. The forward transmission through the resonator is given by

$$S_{21} = \bar{A}\exp\left[-j\left(2\pi(f - f_r)D + \phi_0\right)\right]\left[1 - \frac{\hat{Q}_c^{-1}}{\delta_r + j2x}\right]. \tag{2.139}$$

The fractional fluctuations in the resonance frequency $\delta x(t) = (f_r(t) - f_r)/f_r$ and internal quality factor $Q_i^{-1}(t) = Q_i^{-1} + \delta_i(t)$ generate fluctuations in the measured S_{21} which are converted by the readout system with a probe tone at the frequency f generates a complex timestream $Z(t) = \mathrm{I}(t) + j\mathrm{Q}(t)$. We invert eq. (2.139) to obtain a frequency and quality factor timestream

$$\delta_r(t) + j2x(t) = \frac{\hat{Q}_c^{-1}}{1 - \bar{A}^{-1}\exp\left[j\left(2\pi(f - f_r)D + \phi_0\right)\right]\cdot Z(t)}. \tag{2.140}$$

Finally,

$$\delta_x(t) = x(t) - \langle x(t)\rangle \tag{2.141}$$

$$\delta_i(t) = \delta_r(t) - \langle\delta_r(t)\rangle, \tag{2.142}$$

where the angle brackets represent the time average.

2.11 Line Crosstalk and Limits on Multiplexing

Crosstalk is a key consideration of any readout scheme. In bolometric detectors, crosstalk can create spurious correlations between measurement channels. The crosstalk level set by the design of KID or TKID array limits the multiplexing factor that can be achieved in practice. Many crosstalk mechanisms can arise in readout as detailed in (Mates et al., 2019). Coupled harmonic oscillator physics between physically adjacent resonators, broadband non-linearity in the amplifiers, and line crosstalk are particularly relevant to TKID arrays. This section focuses on line crosstalk; an unavoidable coupling between resonators sharing the same feedline.

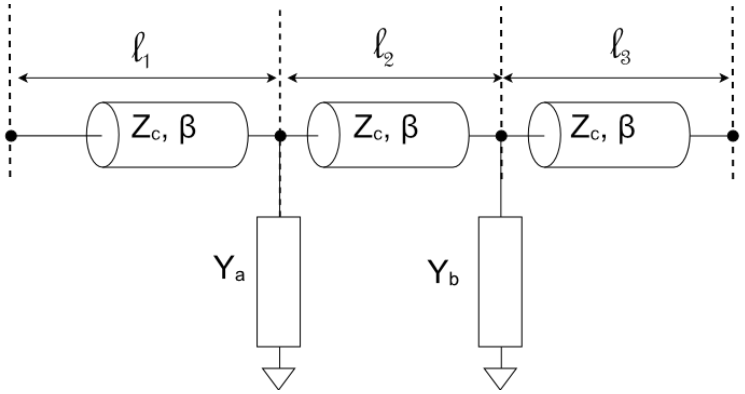

Figure 2.15: A simple model of two resonators on a single line to demonstrate line crosstalk. The resonator admittances Y_a and Y_b, respectively, include the coupling to the feedline. The feedline has characteristic impedance Z_c and propagation constant β.

The off-resonance transmission of a resonator on a line affects the transmission through all the other resonators on the same feedline. Consider two shunt resonators with admittances Y_a, Y_b, respectively, coupled to a single transmission line with line impedance Z_c, propagation constant β, and total length ℓ_t as shown in fig. 2.15. The two resonators split the line into three sections of lengths: ℓ_1, ℓ_2, and ℓ_3, respectively. By cascading the ABCD parameters of each of the sections, we can show that the total transmission through the line is given by

$$S_{21} = S_{21}^{\ell_T} \cdot \frac{S_{21}^a \cdot S_{21}^b}{1 - \zeta S_{11}^a \cdot S_{11}^b}. \tag{2.143}$$

$S_{21}^{\ell_T}$ is the transmission through the entire line ($\ell_T = \ell_1 + \ell_2 + \ell_3$) with no resonators attached. ζ is a product of two factors $\zeta = \zeta_{1;2,3} \cdot \zeta_{1,2;3}$ each of which can be expressed as

$$\zeta_{1;2,3} = \frac{S_{11}^{\ell_1} + 1}{S_{21}^{\ell_1}} \cdot \frac{S_{21}^{\ell_2+\ell_3}}{S_{11}^{\ell_2+\ell_3} + 1}, \tag{2.144}$$

$$\zeta_{1,2;3} = \frac{S_{11}^{\ell_1+\ell_2} + 1}{S_{21}^{\ell_1+\ell_2}} \cdot \frac{S_{21}^{\ell_3}}{S_{11}^{\ell_3} + 1}. \tag{2.145}$$

For a perfectly matched line, $Z_c = Z0$, $\zeta_{1;2,3} \cdot \zeta_{1,2;3} = e^{-j2\theta_2}$, where $\theta_2 = \beta\ell_2$. The total phase accumulated in a round-trip reflection between the 2 resonators is therefore $2\theta_2$. Note that the scattering parameters (S_{11}^a, S_{21}^a) of resonator a are

independent of Y_b but sensitive to the total transmission through the line. The same holds true for resonator b. This is true because we are only considering line crosstalk; other crosstalk mechanisms such as oscillator coupling involve direct interaction between the two resonators.

The impact of crosstalk on this system is evident when we consider a detector signal in one of the resonators (say resonance frequency of resonator b), generating fluctuations $\delta S_{21}^b(t)$ which modulate the total transmission through the line. We only consider the case of adiabatic fluctuations. The general case is difficult to consider analytically. Instead, a much simpler limit is where the two resonators are identical (except for their resonance frequency), and optimally coupled ($Q_r = Q_c/2$). We also assume that the line is matched to 50 Ω. Let $\Delta f_a = f_a/2Q_r, \Delta f_b = f_b/2Q_r$ be the resonator bandwidths for resonators a and b respectively. In this case

$$\frac{\partial S_{21}}{\partial f_b} = -2j\frac{S_{21}^2}{\Delta f_b}\frac{1}{\left(1+2j\frac{f-f_b}{\Delta f_b}\right)^2}\cdot\left[1+2j\frac{e^{j\theta}\sin\theta}{\left(1-2j\frac{f-f_a}{\Delta f_a}\right)}\right]. \tag{2.146}$$

From this equation, a victim tone at $f = f_a$ sees a response proportional to the number of linewidths $n = (f_a - f_b)/\Delta f_b$ between the 2 resonators. This case illustrates the $1/n^2$ dependence of line crosstalk that is typically used as a rule of thumb in design. In practice, the crosstalk has a non-trivial dependence on the phase delay between resonators on the line.

For CMB experiments, the maximum allowable crosstalk level is typically chosen to be $\chi_{\max} = 10^{-3}$. Eq. 2.146 then sets the minimal separation between adjacent resonators on a line. In order to readout N total resonators over m octaves of bandwidth, the total quality factor Q_r of a single resonator at operating temperature must satisfy the inequality

$$Q_r > N \cdot 2^{-(m+1)} \cdot \chi_{\max}^{-1/2}. \tag{2.147}$$

This sets the limit on the multiplexing factor available for a TKID array. As an example, Aluminum TKIDs operating at 380 mK achieve $Q_i \sim 12,000$. For optimal coupling, $Q_r \sim 6,000$. In this case, the maximum number of TKIDs that can be multiplexed over a single octave of bandwidth ~ 760. More resonators can be fit with under-coupling to improve Q_r at the cost of a readout noise penalty. For fixed readout bandwidth, a judicious choice of superconductor is the most robust

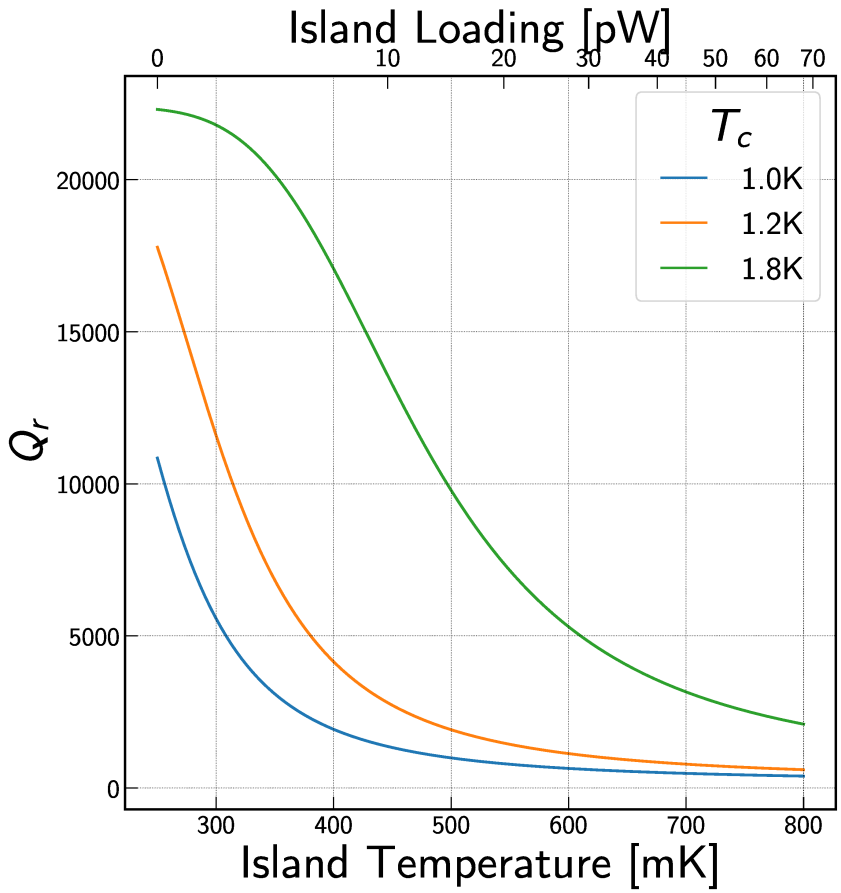

Figure 2.16: Predicted Q_r for three TKID bolometers for 3 different choices of superconducting temperature T_c. The bolometer properties were chosen to match those of the 337 MHz resonator in table 3.2. Q_c was chosen so that the resonator is optimally coupled at 380 mK.

way to improve the multiplexing factor for fixed operating conditions as shown in fig. 2.16.

Chapter 3

TKID DEVICES

The gap between the theoretical detector modeling work presented in chapter 2 and a working TKID camera observing the CMB as motivated in chapter 1 is insurmountable as a monolithic single step. This challenge is more feasible when broken down into successive quasi-independent steps each of which is detailed in this chapter.

The first set of TKID devices (B. A. Steinbach et al., 2018) were designed by Bryan Steinbach and tested by Bryan Steinbach, Hien Nguyen and myself (briefly) are not detailed here. The 3 prototype devices discussed in this chapter were designed by with the help of Bryan Steinbach, Roger O'Brient and Anthony Turner. Bryan Steinbach and Lorenzo Minutolo were instrumental in the testing. Fabrication was done at JPL by Anthony Turner, Roger O'Brient, and Clifford Frez. I performed most of the device hybridization with initial guidance from Anthony Turner. Lorenzo Minutolo and Bryan Steinbach also developed the readout system used for the lab measurements. In addition, amazing summer SURF students did significant measurements: Katie Hughes, who worked on cosmic ray susceptibility and Shubh Agrawal, who worked on electrothermal feedback in TKIDs. A number of publications summarize the work presented in this chapter (Agrawal et al., 2021; L. Minutolo, Frez, et al., 2021; L. Minutolo, B. Steinbach, et al., 2019; A. Wandui et al., 2020; A. K. Wandui et al., 2020).

3.1 Waffle TKIDs

The Waffle TKID devices represent the 2nd generation of TKID devices developed at Caltech/JPL. The devices are so-called because of the dense pattern of XeF_2 release holes present on the bolometer membrane as shown in fig. 3.1. Our primary goal in this design was to demonstrate TKIDs with internal detector noise low enough for background limited performance with an expected 45 $\mathrm{aW}/\sqrt{\mathrm{Hz}}$ photon NEP. This photon NEP level matches the measured noise levels for a *Keck*-style receiver observing from the South Pole at 150 GHz with an expected 5 pW of total optical loading. The waffle TKIDs also introduced a niobium ground plane, a necessary step for compatibility with a planar, lithographed phased-array antenna as is typically used within the BICEP/*Keck* collaboration (Ade, Aikin, Amiri, Barkats, Benton,

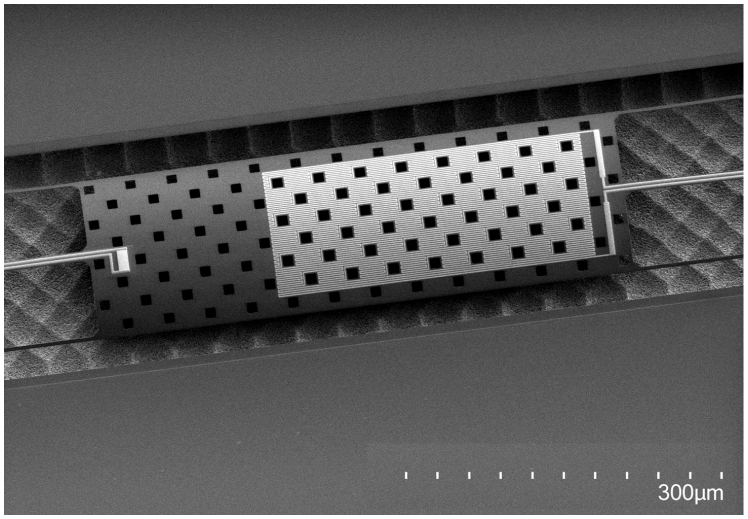

Figure 3.1: An SEM of the waffle TKID inductor taken by Clifford Frez. The aluminum inductor, niobium leads to the capacitor and gold calibration resistor are in clear view. The dense pattern of XeF_2 holes for the bolometer island release led to the moniker, 'waffle'. Waffle TKID devices consistently demonstrated higher quality factors than the previous generation of TKID devices. This was attributed to the degradation of the superconducting film under the action of XeF_2 during the island release process. The imprint of the XeF_2 gas bubbles onto the silicon wafer underneath the island is clearly visible.

Bischoff, Bock, Bonetti, et al., 2015; Kuo et al., 2008).

Device Design

We can apply the results from chapter 2 to determine an optimal design for TKID bolometers. First, since the phonon noise term dominates the internal noise, then the internal noise at the operating temperature is only a weak function of T_c. This means that a wide range of materials with T_c in the range $0.8 - 2$ K can be used as background-limited detectors. We chose aluminum with $T_c \sim 1.2$K as our superconductor for ease of fabrication. Using higher T_c materials could offer a multiplexing advantage because Q_r at the operating temperature increases with T_c.

We designed devices with relatively low resonance frequencies around 300 MHz. We designed each test chip with 10 resonators in 2 frequency bands. The lower frequency band has 5 resonators with a 15 MHz frequency spacing between resonators. The IDC capacitors for the 2 bands have 2 micron wide fingers with 2 micron spacing. The upper band has the remaining 5 resonators with a 20 MHz spacing between resonators. The IDCs for the upper band had 4 micron wide fingers with 4 micron spacing. The resonator circuits are built out of lithographed, lumped element in-

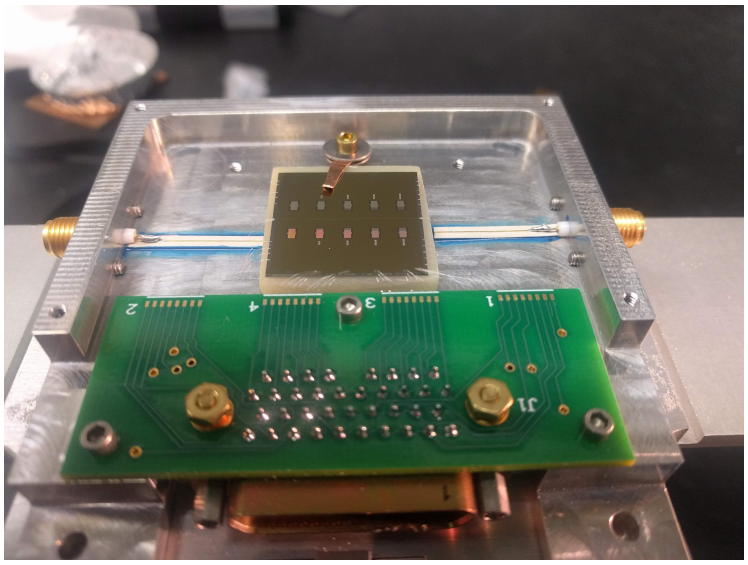

Figure 3.2: A single waffle TKID test chip mounted in a dark holder. The PCB board in the foreground of the photograph distributes power to the calibration heaters. Only 4 out of 8 bolometer heaters can be biased at a time.

ductors and capacitors. A fixed inductor geometry was used for all the devices and each resonator has a unique main capacitor that sets the resonant frequency. Smaller coupling capacitors are used to set the coupling of the resonator to the readout line. The design parameters are detailed in table 3.1. Niobium with $T_c \sim 9$ K was used for all the capacitors and feedline structures so that the thermal response is solely attributable to the aluminum inductor. Figure 2.1 shows a simplified schematic of a TKID as fig. 3.1 is a scanning electron microscope image of the bolometer island with the inductor and heater in view.

Index	f_r [MHz]	C [pF]	C_c [pF]	Q_c
1	306.2	27.0	0.4322	20048
2	321.6	24.5	0.3984	20352
3	336.7	22.4	0.3731	20236
4	352.1	20.4	0.3478	20364
5	367.0	18.8	0.3225	20907
6	433.5	13.5	0.3398	11432
7	454.8	12.3	0.3138	11606
8	477.1	11.1	0.2878	11945
9	497.6	10.2	0.2705	11922
10	521.0	9.3	0.2532	11858

Table 3.1: Summary of the resonator design parameters for a Waffle TKID test device. All the resonator share the exact same inductor design with a total inductance of 10 nH.

Detector Fabrication

We fabricated the detectors at the Microdevices Laboratory at the Jet Propulsion Laboratory (JPL) on 500 μm thick, high resistivity Si wafers (Ade, Aikin, Amiri, Barkats, Benton, Bischoff, Bock, Bonetti, et al., 2015). A low stress silicon nitride (LSN) layer, a niobium ground plane (GP) and a SiO_2 inter-layer dielectric (ILD) layer are deposited over the silicon. The LSN layer is then patterned to form the thermal island which is released using a XeF_2 etch process. The island is mechanically anchored to the main wafer via six LSN legs each about 10 μm wide. These legs make the weak thermal link from island to wafer. By selecting the length of the bolometer legs, we can also tune the thermal conductance. On each test chip, one device was fabricated with no island and the other 4 with bolometer leg lengths 100 μm, 200 μm, 300 μm and 400 μm. The island size was fixed to ~100 μm by ~500 μm for all the devices. This gives an expected heat capacity of 0.06 pJ/K, after accounting for both the dielectric (LSN and ILD) and metal (Nb and Al) layers (Corruccini and Gniewek, 1960; W. A. (Phillips, 1981; Wang et al., 2010). The heat capacity is set by island volume of about 30,000 μm^3, which is much larger than the combined volume of the bolometer legs of about 5,000 μm^3 for the longest leg bolometer. As a result, we expect that all the devices would have the same the heat capacity. A small gold resistor added on the island is used for calibration and noise measurements(see Figure 3.1 (b)).

The aluminum layer of the inductor is deposited and patterned on the LSN. The meandered inductor traces are 50 nm thick and 1 μm wide with 1 μm spacing between the lines for a total volume of 810 μm^3. Sonnet [1] simulations done assuming a surface inductance L_s = 0.27 pH/sq , give a predicted geometric inductance, L_g of about 5 nH and a kinetic inductance fraction, α_k = 0.42. The low film resistivity of aluminum limits the achievable kinetic inductance fraction.

The inter-digitated capacitors (IDC) are deposited directly on the crystalline Silicon wafer. The bare silicon is exposed by etching a large via through the ground plane (GP) and LSN layers. We did this to reduce the presence of amorphous dielectric that hosts two-level system (Jiansong Gao et al., 2008) (TLS) effects from the capacitors. The via is large to minimize stray capacitive coupling between the ground plane and the edges of the capacitor, as determined by Sonnet simulations. An etch-back process was used to pattern the capacitors because liftoff often leaves flags that can potentially host TLS states.

[1] `https://www.sonnetsoftware.com/`

Experimental Setup

We tested the devices in a Model 103 Rainier Adiabatic Demagnetization Refrigerator (ADR) cryostat from High Precision Devices (HPD) [2] with a Cryomech PT407 Pulse Tube Cryocooler[3]. We used an external linear stepper drive motor to run the Pulse Tube in order to avoid RF pulses from a switching power supply. For mechanical stiffness, the ultra cold (UC) and intra cold (IC) stages of the cryostat are supported using long diameter Vespel tubes between the 4K stage and the IC and stiff titanium 15-3 alloy X-shaped crossbars between the IC and UC stages. Copper heat straps make the thermal contacts between the stages and the cold heads. The ADR reached a base temperature of 80 mK on the UC stage when the test chip was installed.

The RF connections between the UC and IC stages are through niobium-titanium (NbTi) coaxial cables with 10dB, 20dB and 30dB attenuators installed at the UC, IC and 4K stages, respectively, on the transmit side. At each thermal stage, the coaxial connections are heat sunk to the stage. A cold Low Noise Amplifier (LNA) is mounted at the 4K stage. The cold LNA is a SiGe HBT cryogenic amplifier from Caltech (CITLF2) [4] with a measured noise temperature of 5.2 K with a 1.5 V bias. We also use a second amplifier with a noise temperature of 35 K at 5.0 V bias at room temperature.

For our data acquisition, we used the JPL-designed GPU accelerated system built on the Ettus Research USRP software defined radio (SDR) platform (L. Minutolo, B. Steinbach, et al., 2019; Lorenzo Minutolo, 2019). 10 Gbit Ethernet connects the SDR to an Nvidia GPU, which handles the computationally heavy demodulation and analysis tasks in place of an FPGA. The SDR platform uses a 14 bit ADC and a 16 bit DAC and provides 120 MHz RF bandwidth.

The chip holder was sealed up with aluminum tape to make it light tight (Barends, Wenner, et al., 2011). A TKID test chip wirebonded and mounted in an aluminum holder is shown in fig. 3.2.

[2] Now part of FormFactor.https://www.formfactor.com/download/hpd-rainier-103-adr-cryostat-datasheet/

[3] Now part of BlueFors. https://bluefors.com/products/cryomech-products/

[4] https://cosmicmicrowavetechnology.com/index.php/cryogenic-low-noise-amplifiers/citlf2-low-noise-amplifier-low-noise-cryogenic-applications/

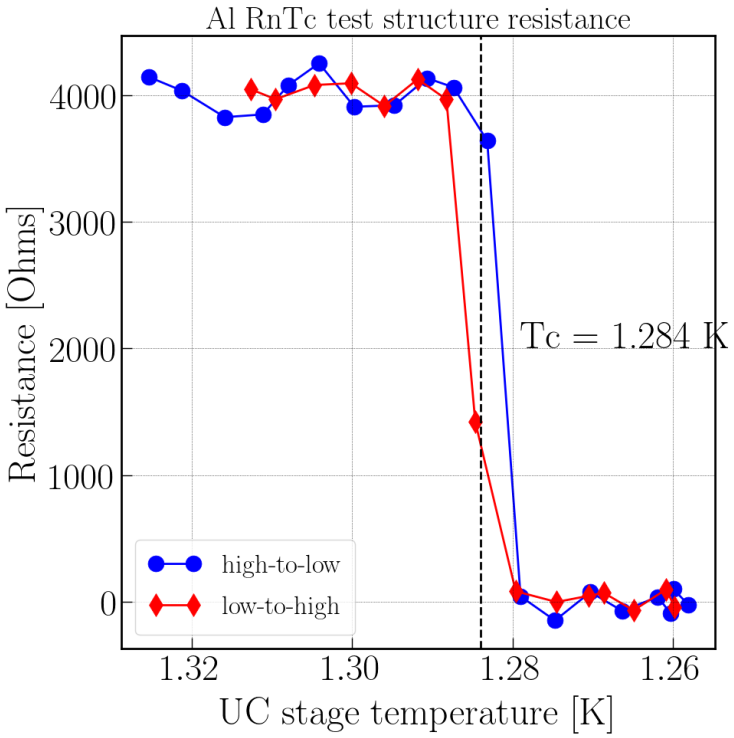

Figure 3.3: 4 point measurements of a test structure on the chip to measure the film resistivity and transition temperature. The reported T_c is the average of two sets of measurements: the first taken slowly ramping the temperature up and the second while lowering the stage temperature past the transition temperature.

Results

For the device discussed here, we achieved a yield of 4/5 resonators in the lower frequency band. All the resonances were found in the frequency range 300-360 MHz and with close to the 15 MHz design spacing. The heaters of the 300, 200 and 100 μm leg bolometers were wired up to make calibrated noise and responsivity measurements.

Film Properties

Using four-point measurements of a test structure on chip, we measured $T_c = 1.284\,K$ as shown in fig. 3.3, implying a superconducting gap energy, $\Delta = 1.95 \times 10^{-4}$ eV. The measured sheet resistance was $R_s = 0.25\ \Omega/\text{sq}$. R_s and Δ together give a surface inductance, $L_s = 0.27$ pH/sq. Taking this value of L_s and accounting for the geometric inductance from simulations, gives an expected kinetic inductance fraction, $\alpha_k = 0.42$.

Resonator Properties and Modeling

We initially characterized the resonators using readout power sweeps at a fixed bath temperature of 80 mK and varying the power in the range, –110 dBm to –80 dBm. A key goal of this measurement was to determine the power level at the onset of the kinetic inductance non-linearity. In addition, changes in the quality factor with readout power probe two-level system effects.

We fit S_{21} using Swenson's nonlinear resonator model (Swenson et al., 2013). However, we found that our resonators could not be described adequately using the ideal S_{21}. In general, parasitic inductance and capacitance, wirebond inductances, line mismatch and other effects modify the resonator line shape. In our experimental setup, these effects show up as an asymmetry in the resonator.

Our resonators have a large ϕ_c in the range $0.4 - 0.7$ radians. As tested by further simulations, we traced the asymmetry to about 7 pF of capacitive loading from short lengths of transmission line that branch from the readout line to the coupling capacitors.

Even up to –80 dBm we found that the bifurcation parameter defined by Swenson $a < 0.8$, implying that the resonators were always below the threshold for the bifurcation (ibid.). Informed by this, we chose a readout power of –90 dBm for all the other measurements that were done at a fixed readout power. At –90 dBm, the amplifier noise is sufficiently suppressed while keeping the readout power smaller than the heater loading on the TKID.

Q_i varies as a function of both the readout power P_g and the temperature T. We chose the following model to describe Q_i:

$$Q_i^{-1}(T, P_g) = Q_{\mathrm{TLS}}^{-1}(T, P_g) + Q_{\mathrm{MB}}^{-1}(T) + Q_{i,0}^{-1}, \tag{3.1}$$

where $Q_{\mathrm{TLS}}^{-1}(T, P_g)$, is given in equation 2.128 and $Q_{\mathrm{MB}}^{-1}(T)$ is the Mattis-Bardeen (MB) prediction (Zmuidzinas, 2012) and the third parameter $Q_{i,0}$ captures the saturation of Q_i at high power.

At 80 mK, the MB term is negligible and can be ignored for the power sweep measurements. Figure 3.4 shows Q_i as a function of the readout power for 4 yielded resonators. All four resonators have the product $F\delta_0 \approx 4.6 \times 10^{-5}$. Three of the resonators have $P_c \approx -95.7$ dBm and $Q_{i,0} \approx 4.4 \times 10^5$. The lower Q_i measured for the 305.9 MHz resonator implied a lower $Q_{i,0}$. Consistent with the TLS prediction, we found the fractional frequency shift with power to be negligibly small, peaking

at about 5 ppm. Even so, TLS effects by themselves do not fully explain the power dependence because we found that $Q_{i,0}$ was needed in order to obtain good fits even though it is not physically motivated. $Q_{i,0}$ may possibly come from a power dependence that is complicated by non-equilibrium quasiparticle distribution effects. This is still being actively investigated (Goldie and Withington, 2012; P. J. de Visser et al., 2014).

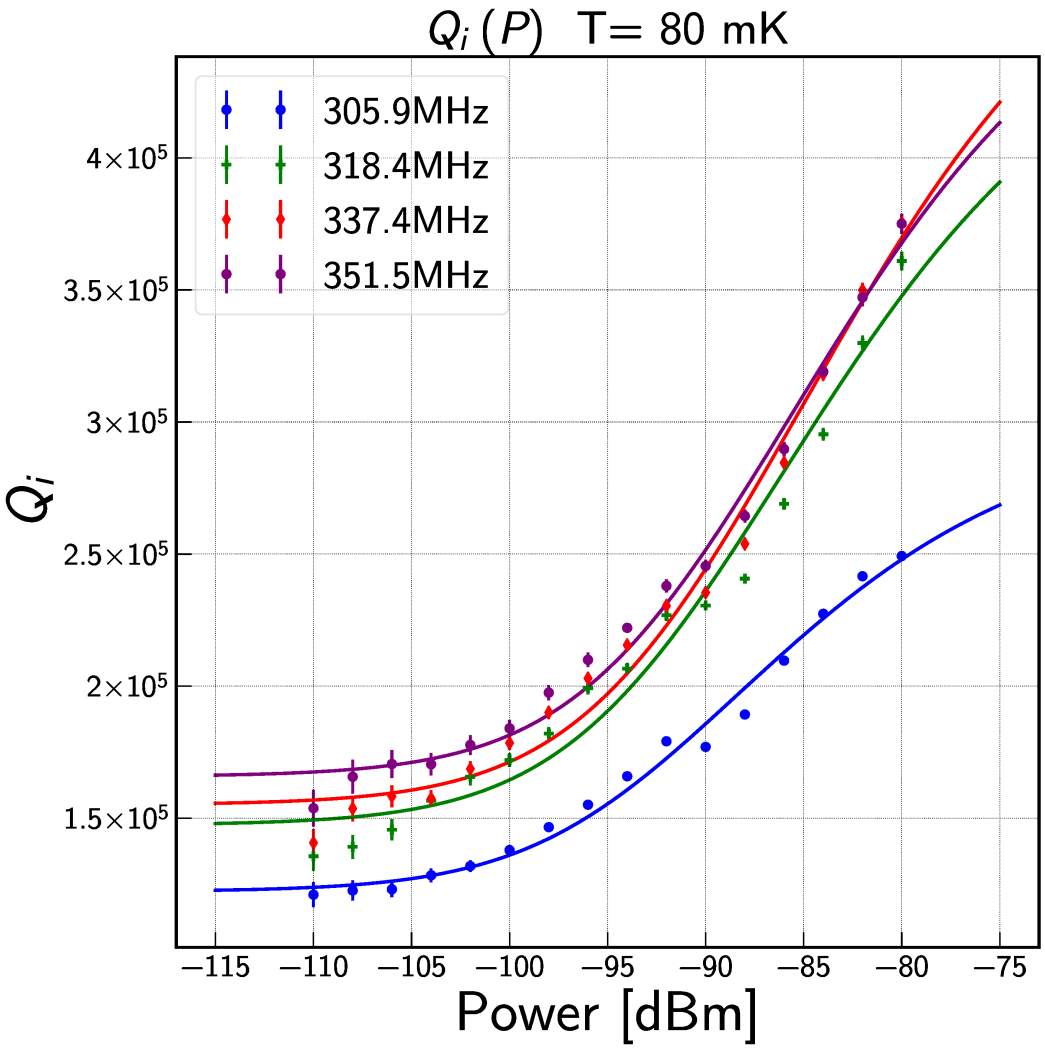

Figure 3.4: Internal quality factor Q_i as a function of the readout power at 80 mK. The dots are the data and the solid lines are the fits to the data using the model described in equation 3.1.

S_{21} for each of the resonators was also measured as a function of the bath temperature. The readout power was fixed at –90 dBm and the temperature was swept up to 460 mK. This maximum temperature is high enough to break the degeneracy between the two MB parameters, α_k and T_c. At our operating temperature, these two parameters

sufficiently describe our data as shown in figures 3.5 and 3.6 which summarize the fit results for the 337.4 MHz resonator.

At lower temperatures, however, the MB prediction fails because the quality factor levels off instead of increasing with a decrease in temperature. We compared three different models to describe this low temperature behavior: a pure MB prediction, a MB + TLS model and lastly, a model assuming a background quasiparticle population but no TLS. All three models were fit to only the frequency shift data and the best fit parameters were then used to make predictions of Q_i. The MB + TLS model best fit product $F\delta_0 \approx 3.4 \times 10^{-5}$ for all 4 resonators. However, this value of $F\delta_0$ gives a Q_{TLS}^{-1} that is too small for the data. In addition, if TLS effects were present, we would expect Q_i^{-1} to increase with decreasing temperature below about 200 mK. Such an increase is not consistent with the data.

A better fit was found using the background quasiparticle population n_{bg} model. In this case, total quasiparticle density is not simply the thermal quasiparticle density but rather it must be obtained by considering the balance between the quasiparticle generation and recombination rates (Wilson and Prober, 2004). In addition, at low temperatures, empirical measurements show that quasiparticle lifetimes in Al resonators are described by the relation $\tau_{\mathrm{qp}} = \tau_{\mathrm{max}} / \left(1 + n_{\mathrm{qp}}/n_{\mathrm{qp}}^*\right)$. The two constants in the equation are n_{qp}^*, which is the crossover density and τ_{max}, which is the observed maximum lifetime (Barends, Baselmans, et al., 2008; Zmuidzinas, 2012). This new form of the quasiparticle lifetime has the expected inverse dependence on quasiparticle density in the limit of high n_{qp}. Because of this, we can relate the two new constants to the recombination constant as $R = 1/\left(\tau_{\mathrm{max}}\, n_{\mathrm{qp}}^*\right)$. The quasiparticle density is now modified to

$$n_{\mathrm{qp}}(T,\ n_{\mathrm{bg}}) = \sqrt{\left(n_{\mathrm{th}}(T) + n_{\mathrm{qp}}^*\right)^2 + n_{\mathrm{bg}}^2} - n_{\mathrm{qp}}^*. \tag{3.2}$$

Thermal and excess quasiparticles are equivalent in their effect on the electrodynamics of the superconductor (J. Gao et al., 2008). As a result, we can describe combined the effect of having both by defining an effective temperature T_{eff} using the relation $n_{\mathrm{qp}}\left(T,\ n_{\mathrm{bg}}\right) = n_{\mathrm{th}}\left(T_{\mathrm{eff}}\right)$. The effective temperature was then used in place of T for all temperature dependent terms that determine the frequency shift and loss with n_{bg} as an additional parameter in the fitting. We have no measurements of n_{qp}^* for these devices, but we fixed its value based on later quasiparticle lifetime

measurements done on similar TKIDs for which we found $n^*_{\rm qp} = 518$ um^{-3} and $R = 5.3$ um^{3}s^{-1}.

When comparing the best fit parameters from each of the three models, we found that the pure MB and the MB + TLS models give $T_c \approx 1.38$K and $\alpha_k \approx 0.55$, which are much higher values than we obtained from the film measurements. The background quasiparticle model gave $T_c \approx 1.32$K and $\alpha_k \approx 0.45$. On average over the 4 resonators, we found that $n_{\rm bg} \approx 700$ um^{-3}, corresponding to an effective temperature of about 150 mK. We estimate the recombination power, $P_{\rm recomb}$ from this population of quasiparticles as $P_{\rm recomb} = \frac{1}{2} \cdot \Delta \cdot R \cdot n^2_{\rm qp} \cdot V_{\rm sc} = 9$ fW which is about 1% of the readout power. The recombination power suggests that only a little additional loading on the bolometer is needed to account for the saturation of Q_i. A complete accounting of the low temperature quasiparticle dynamics in TKIDs as in many other KIDs has not been achieved. Even so, this does not affect TKID performance since our target operating temperature, $T_o = 380$ mK is well in the regime where our devices are fully characterized.

f_r [MHz]	Q_c	ϕ_c [rad]	T_c[K]	α_k	$n_{\rm bg}$[um^{-3}]	K [pW/K^n]	n	C_0 [pJ/K$^{\eta+1}$]	η
305.9	15164 ± 72	0.6455 ± 0.0035	1.33 ± 0.01	0.46 ± 0.01	708 ± 10	352 ± 2	2.962 ± 0.009	1.943 ± 0.213	1.920 ± 0.115
318.4	17675 ± 104	0.7601 ± 0.0034	1.32 ± 0.09	0.45 ± 0.01	711 ± 10	165 ± 1	2.754 ± 0.012	1.839 ± 0.325	1.945 ± 0.184
337.4	22556 ± 129	0.7526 ± 0.0037	1.32 ± 0.01	0.45 ± 0.01	627 ± 9	122 ± 1	2.862 ± 0.011	1.742 ± 0.380	1.914 ± 0.219

Table 3.2: Summary of the measured parameters of 3 TKID bolometers. The error bars on Q_c and ϕ_c were obtained from the spread in Q_e over power sweeps. α_k, T_c, were obtained from the bath temperature sweep data fit with a MB + background quasiparticle model. The K and n values reported here are from measurements done at a 250 mK bath temperature.

Thermal Conductivity and Bolometer Time Constants

By fixing the bath temperature and changing the power deposited by the heaters on the island, we can directly measure the thermal conductance and time constant.

The bath temperature, $T_{\rm bath}$ was fixed at 97 mK and S_{21} was measured at each heater bias power P. The island temperature T was then inferred from the resonance frequency shift using the best fit Mattis-Bardeen parameters α_k and Δ given in table 3.2, assuming that $T = T_{\rm bath}$ when the applied heater power is zero. The island temperature and bias power data are then fit to obtain the thermal conductivity coefficient K and power law index n.

Consistent with other similar bolometers used in BICEP/Keck (Ade, Aikin, Amiri, Barkats, Benton, Bischoff, Bock, Bonetti, et al., 2015), we measured $n \sim 3$. An index $n < 4$ indicates that phonon system has reduced dimensionality. We can motivate

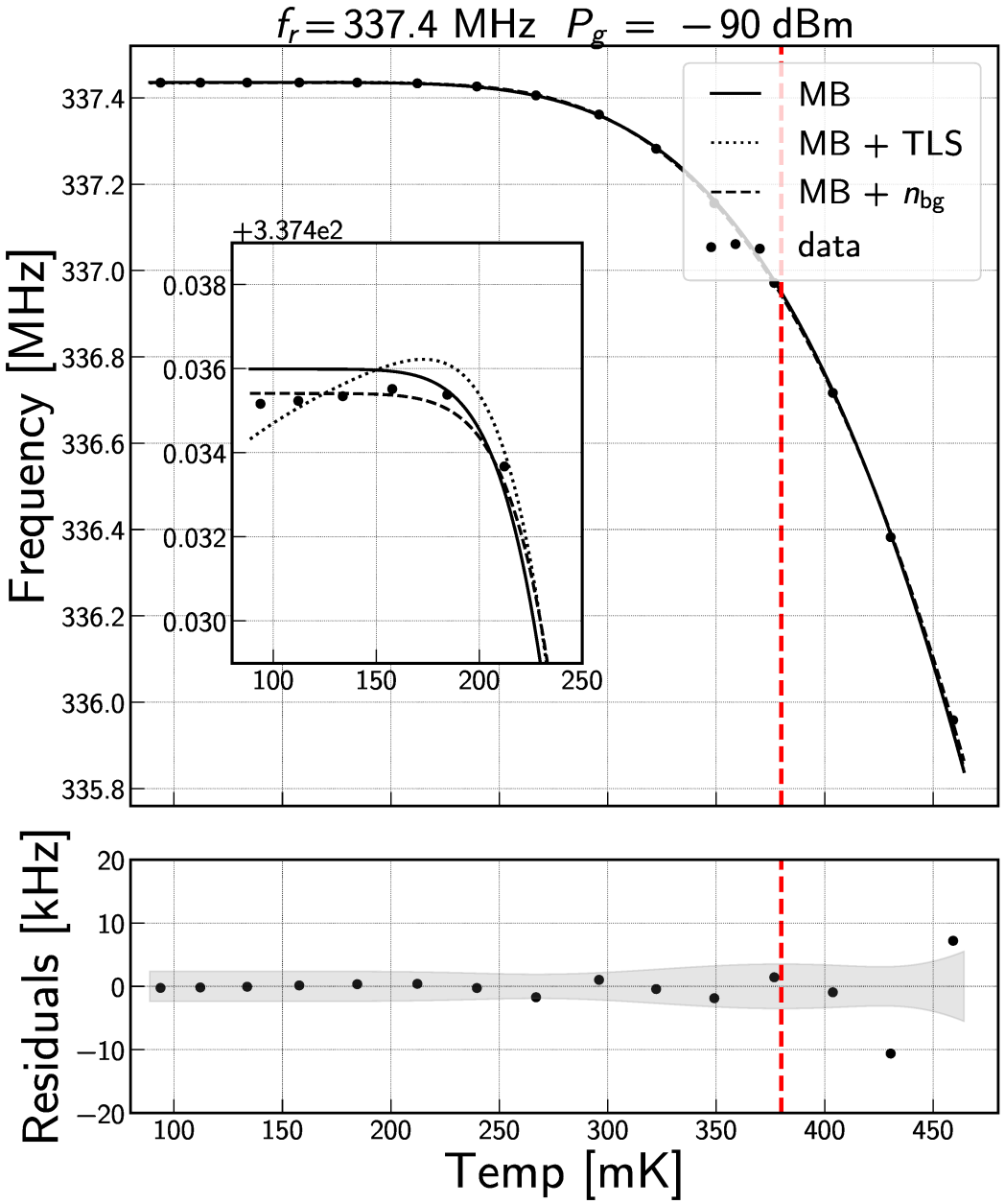

Figure 3.5: Fits of the frequency shift data for the 337.4 MHz resonator to three different models: only MB, MB + TLS and MB + a background quasiparticle density. The inset plot has a much smaller x-axis range to better show the differences in the fits at low temperatures. The lower plot gives the fit residuals (black dots) and the one-sigma error obtained from the covariance of the fit parameters for the MB + background quasiparticle model (gray). The red dashed line is our target operating temperature of 380 mK.

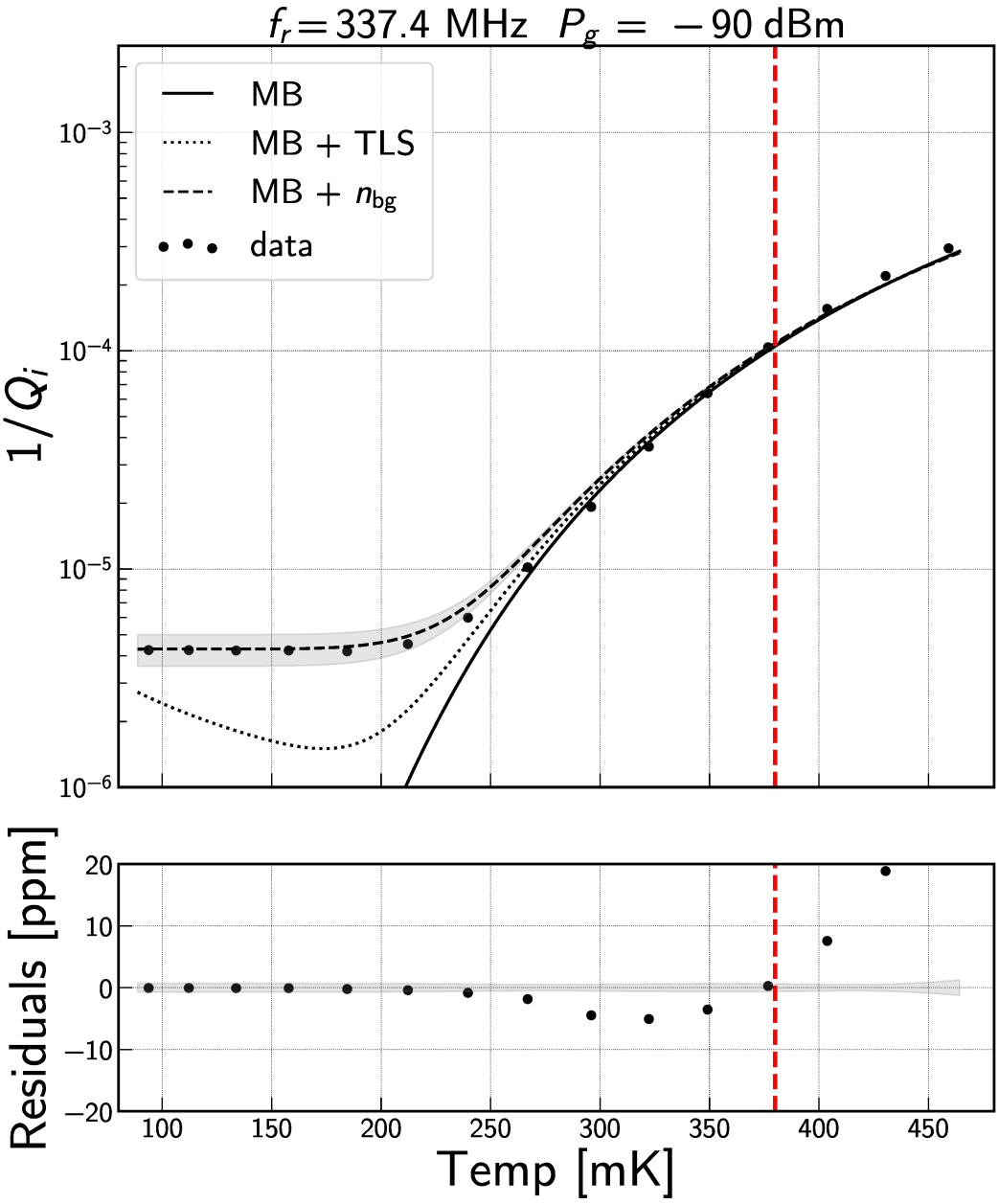

Figure 3.6: A comparison of the measured Q_i to the best fit prediction for Q_i^{-1} obtained from fitting the frequency shift data as shown in figure 3.5. The best agreement between the data and the fit is with a MB + background quasiparticle density model. The lower plot gives the fit residuals (black dots) and the one-sigma error obtained from the covariance of the fit parameters for the MB + background quasiparticle model (gray). The red dashed line is our target operating temperature of 380 mK.

this physically, under the assumption that ballistic phonon propagation dominates over scattering in thermal transport. In this limit, the thermal phonon wavelength is given by $\lambda_{\rm ph} = hc_s/k_BT$ where c_s is the speed of sound (Ade, Aikin, Amiri, Barkats, Benton, Bischoff, Bock, Bonetti, et al., 2015). We expect $\lambda_{\rm ph}$ to vary from 3.5 μm at the 90 mK cold end to about 0.5 μm at the 450 mK hot end for a speed of sound, $c_s \sim 6500$ ms^{-1} in silicon nitride. The nitride layer is only 0.3 μm thick but the legs are 10 μm wide and 300 - 500 μm long. Consequently, we expect thermal behavior consistent with a 2 dimensional phonon gas. The longitudinal sound velocity in silicon dioxide is comparable to that of silicon nitride so the same argument holds for thermal conduction through the similarly thick ILD layer. With the different bolometer leg lengths on the chip, we verified that the coefficient K, scales inversely with the bolometer leg length as shown in Table 3.2. These observations are also supported by measurements of other silicon nitride bolometers that have reported similar values of n for bolometers with leg lengths $<$ 400 μm and width $>$ 2 μm (S. Withington et al., 2017). As an additional step, we repeated the thermal conductivity measurements at a second bath temperature, 249 mK as shown in figure 3.8. The extracted parameters were consistent with each other to about 10 %.

We define the optimal power $P_{\rm optimal}$ as the power needed to achieve the target island operating temperature, T_o = 380 mK. $P_{\rm optimal}$ is dependent on the bath temperature and is chosen so that the saturation power equals the expected loading seen during actual observations. At a 250 mK bath temperature, the 300 μm bolometer with a resonant frequency of 337.4 MHz has $P_{\rm optimal}$ appropriate for the expected loading at the South Pole at 150 GHz as shown in figures 3.7. The 100 μm and 200 μm designs are suitable for operating at 270 GHz and 220 GHz, respectively, under the same sky conditions.

We measured the bolometer time constants using a DC bias voltage plus an additional sine wave excitation was applied across the heater. The amplitude of the sine wave was about 1 % of the DC bias voltage. In addition, we synchronized the start of the data acquisition to the start of the sine wave excitation so that the phase of the input wave was always known. At each bias power, we stepped the excitation frequency of the input sine wave, $f_{\rm exc}$, from 1 Hz to 1000 Hz in 30 logarithmically spaced steps.

We convert from the raw I/Q timestreams to resonance frequency and quality factor timestreams using the measured S_{21} parameters. By fitted the amplitude and phase of the change in resonance frequency with time, we obtained the complex bolometer transfer function, $H(f_{\rm exc})$ which we model as a single-pole low-pass filter with

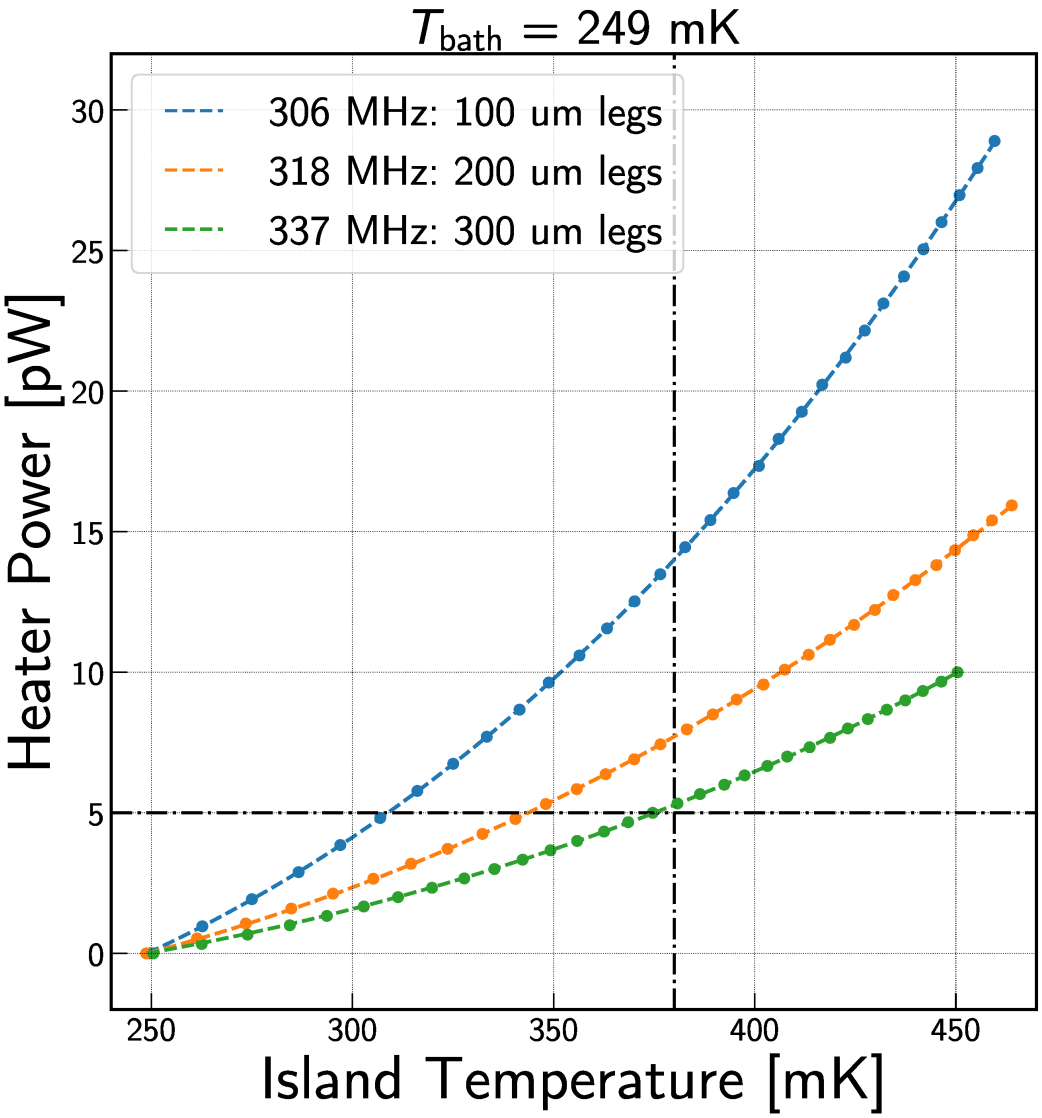

Figure 3.7: Heater power plotted against the island temperature for 3 TKIDs showing agreement between the data (points) and best fit model (lines). The data was taken at a 250 mK bath temperature. The difference in slopes between the 3 curves is due to the difference in thermal conductivity of the three bolometers. The horizontal and vertical lines are the target loading and operating temperature, respectively. These are well matched by the 300um leg bolometer.

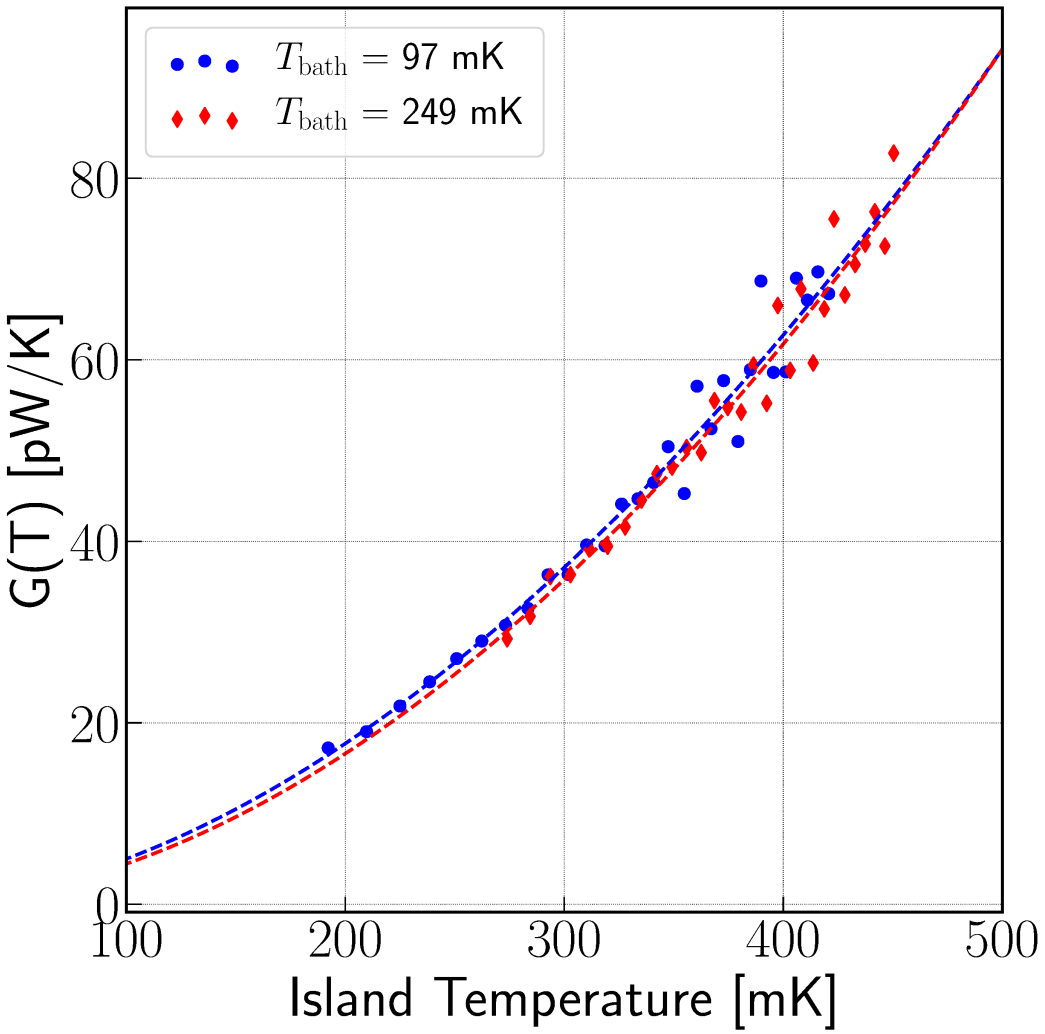

Figure 3.8: The thermal conductance of the 337 MHz bolometer extracted at 2 bath temperatures. The data are given as the filled blue circles and red diamonds while the dotted lines are the best fit to a power law model. The fits show that the parameter K is independent of the bath temperature as expected.

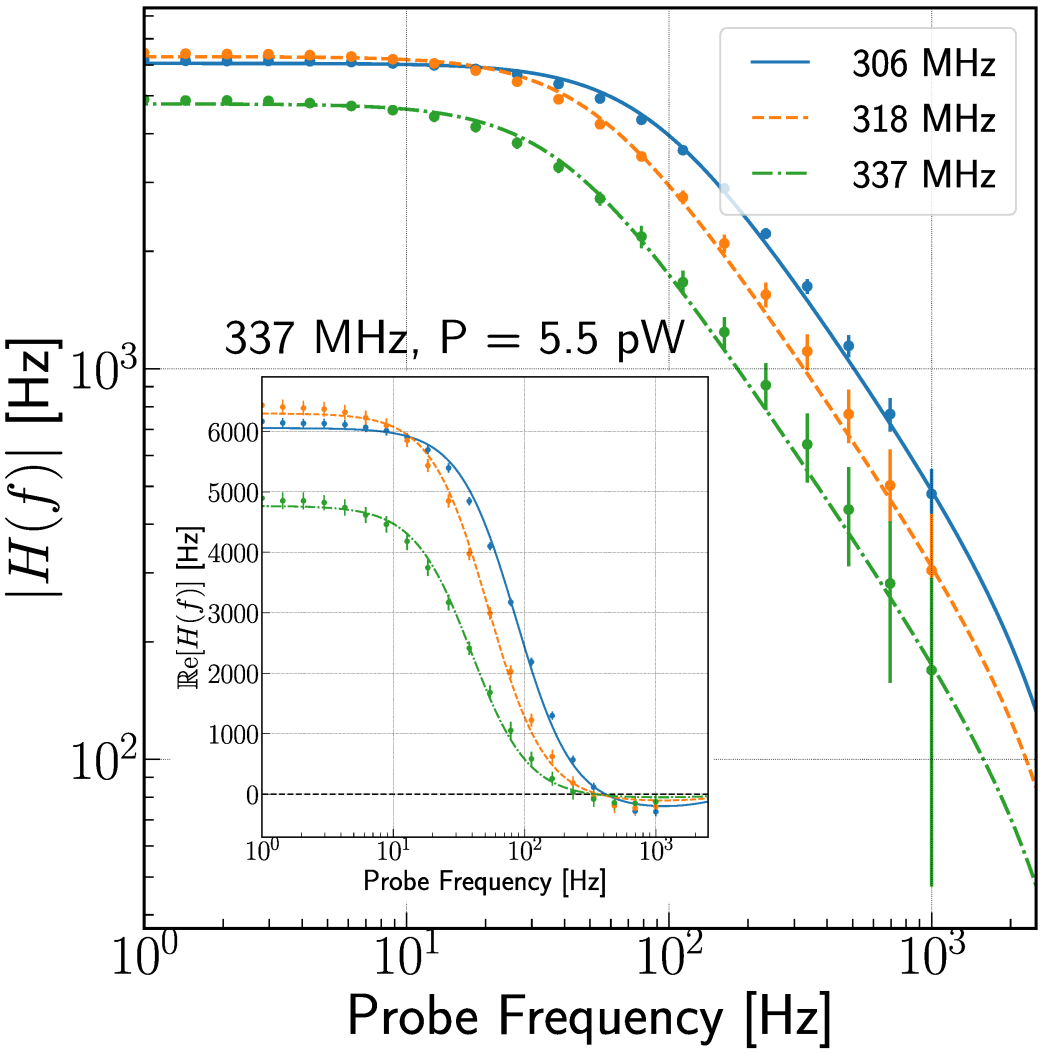

Figure 3.9: A comparison between the magnitude and the real part of the bolometer transfer function measured at an 85 mK bath temperature and heater power of 5.5 pW for the 337 MHz bolometer. The data points have error bars enlarged by a factor of 10. The solid lines show the best fit to the model in equation 2.83. Inset is the real part of the bolometer response showing that response is modulated by the data filtering and additional time delays.

rolloff frequency $f_{3dB} = 1/2\pi\tau_{\rm bolo}$. The measured transfer function also includes the effect of the anti-aliasing filter used to decimate the data as well as unknown time delays in the trigger signal from the USRP to the function generator. Figure 3.9 show the magnitude of the bolometer response with the single pole rolloff.

From these measurements, we conclude that the time constant for the 337 MHz TKID, $\tau \sim 4.5$ms is fast enough for ground-based degree scale CMB observations. Interestingly, the time constants are weakly dependent on the island temperature.

We expect the heat capacity to follow a simple power law $C = C_0 T^{\eta}$ and given that $\tau = C/G$, then this implies that $C \sim T^2$ as summarized in table 3.2. Figure 3.10 confirms that the bulk of the heat capacity is from the island itself and not the bolometer legs. Additionally, the thermal island is almost entirely dielectric so we expect $\eta = 3$. The measured heat capacity is about a factor of 3 larger than predicted (see section 3.1). Even without electrothermal feedback, TKIDs are still fast enough for our targeted science band. There are indications that our dry release process using XeF_2 contributes to the excess heat capacity and that using a wet release process could lead to faster bolometers for space-based applications (Beyer et al., 2010).

Responsivity

Over large ranges of the optical power, the responsivity of a TKID bolometer as given in equation 2.83 is not constant. However, during normal CMB observations, the optical power is typically stable to a few percent. In this case, the responsivity can be approximated as being constant with a small non-linearity correction. The non-linearity level is similar to that of semiconducting NTD Ge bolometers that operate with small correction factors (Pajot, F. et al., 2010; Planck Collaboration, Adam, R., Ade, P. A. R., Aghanim, N., Arnaud, M., et al., 2016).

Noise Performance

The noise measurements were made by recording 10 minute long timestreams of the complex transmission at a 100 MHz native sample rate and then flat-averaging in 1000 sample blocks to a 100 kHz rate. A low noise, highly stable, Lakeshore 121 current source was used to DC bias the heater resistors. The power spectra of the resonance frequency timestream were estimated using the Welch method with a Hann window and a 50% overlap. In order to convert from power spectra in frequency units to NEP, we directly measured the responsivity in short calibration noise acquisitions by modulating the DC bias with a 1% 1 Hz square wave for 10 seconds. The responsivity is then estimated as the ratio of the change in frequency to the change in power dissipated.

The data were taken at a 80 mK bath temperature because the UC stage was less stable at 250 mK. At the same island temperature, the phonon noise with a 250 mK bath temperature is 30% higher than with a 80 mK bath. The measurement results presented here are focused on the 337 MHz resonator.

To simulate pair differencing, which is usually done when making on-sky polariza-

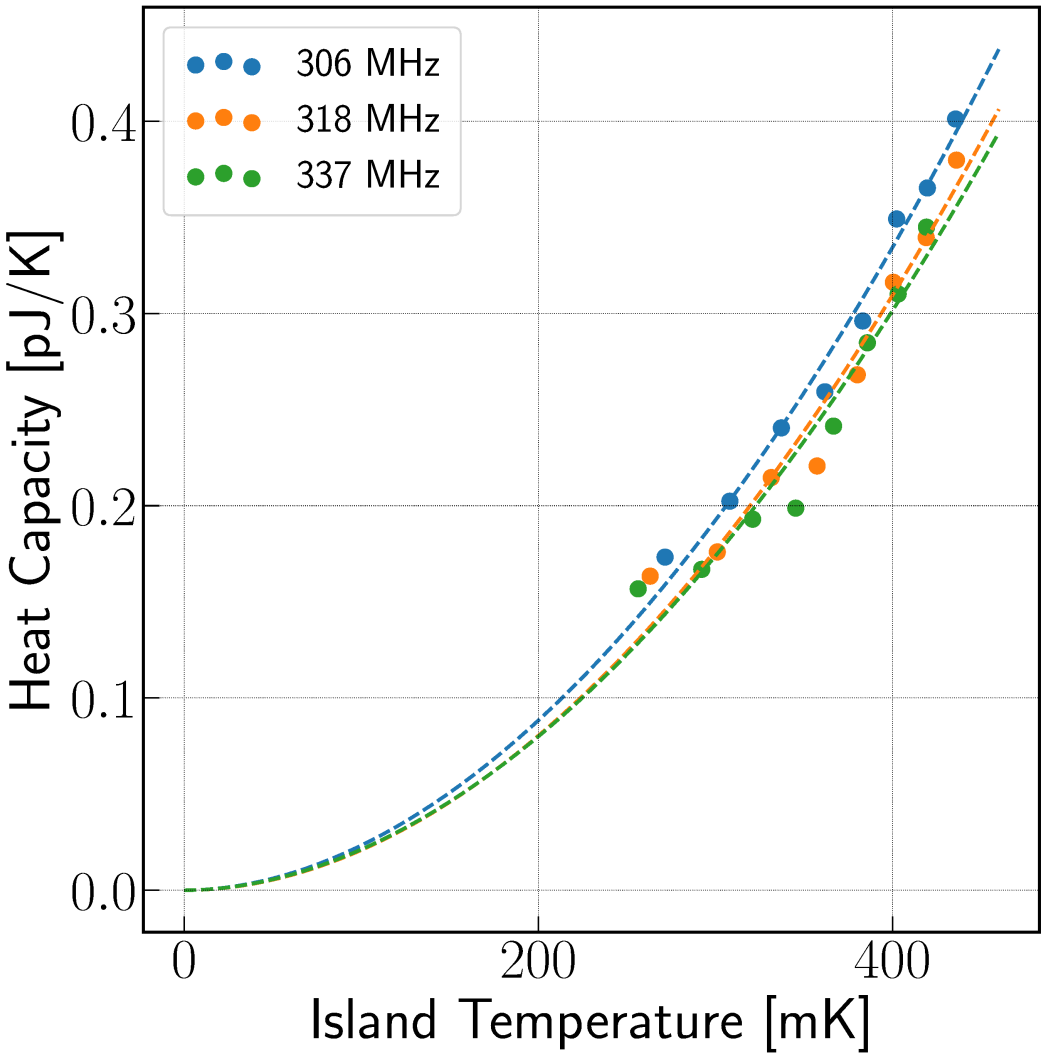

Figure 3.10: Heat capacity for 3 TKID bolometers as a function of the island temperature. All three bolometers have similar heat capacities despite having different leg lengths showing that the island volume is the dominant contribution to the total heat capacity of the bolometer. The dashed lines are power law fits to the heat capacity as a function of the island temperature. The best fit parameters from each bolometer are consistent with each other to within a 1 sigma uncertainty as reported in table 3.2.

tion measurements, we subtracted out all the noise in the 337 MHz resonator that was common-mode with the other resonators as shown in figure 3.11. The origin of the common-mode signal is still under investigation but is likely from either the thermal fluctuations of the stage or RFI susceptibility. From the filtered timestream we computed the NEP at a 4 pW heater bias level. Given the lower bath temperature, the island temperature is 320 mK.

In the 4 pW noise dataset, the expected roll-off in the thermal responsivity at around 35 Hz is not visible. This indicates that at this loading, the device is the regime where the gr noise dominates, giving the single roll-off seen at around 1 kHz as shown in figure 3.12. This figure also shows the comparison of the measured NEP to the noise model described in section 2.8. However, our noise modeling is limited by our knowledge of the quasiparticle recombination constant R, which has not been directly measured for these devices. We instead modelled the noise by setting $R = 0.9\ \mu\mathrm{m}^3\mathrm{s}^{-1}$ in order to match the gr noise roll-off seen at 4 pW loading with good agreement between the total noise from the model and the measured NEP.

A second set of noise data was taken at a 10 pW heater bias that corresponds to an island temperature of 422 mK; much higher than the operating temperature. Figure 3.13 shows a comparison of the measured noise at the two loading levels after common-mode subtraction. Even at the elevated island temperature, the measured NEP is still below the expected photon NEP. However, the NEP measured at the 10 pW level is about 2 times greater than expected from the noise model. This discrepancy is still under investigation. Also of note is that at the 10 pW loading level we see a roll-off in the noise where the thermal response is expected to fall off.

At both loading levels, total detector noise is lower than the expected photon NEP of 45 aW/$\sqrt{\mathrm{Hz}}$ at the 4.7 pW loading for a ground-based CMB telescope observing in the 150 GHz band from the South Pole (Ade, Aikin, Amiri, Barkats, Benton, Bischoff, Bock, Brevik, et al., 2014). We conclude that the device noise is low enough that a similar device coupled to an appropriate antenna (Ade, Aikin, Barkats, et al., 2015; Kuo et al., 2008) would be background noise limited. Future work will focus on further understanding the gr noise and quasiparticle lifetimes in our devices.

Cold Blackbody Response

We also measured the direct stimulation of the waffle chip using a cold blackbody source installed on the 4K shell of the ADR cryostat at JPL. The cold load uses a 650 ohm resistor as a heater and achieves a minimum temperature of cold load of

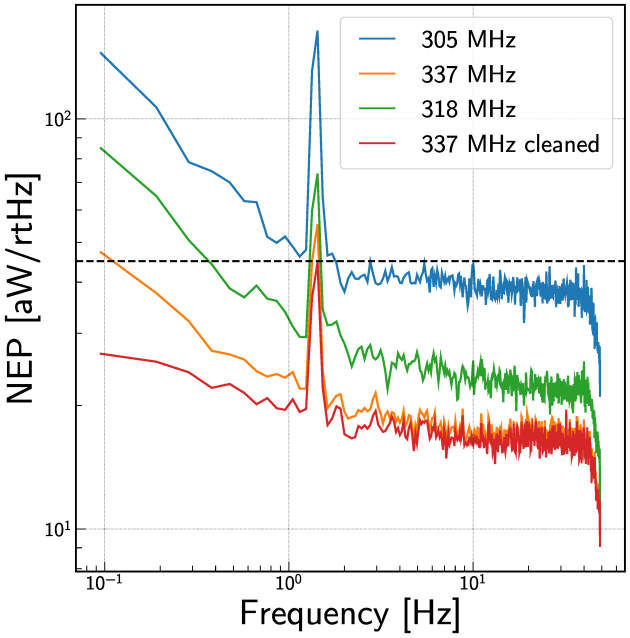

Figure 3.11: NEP spectra for 3 TKID resonators with 4pW loading on the 337 MHz resonator. The red line shows the spectrum of the 337 MHz resonator with common mode noise subtraction applied to suppress the noise at low frequencies. The large spike is the 1.4 Hz pulse tube line. The black dotted line shows the expected photon noise level for a single-mode detector at the South Pole observing in a band centered at 150 GHz with $\Delta\nu/\nu = 0.25$.

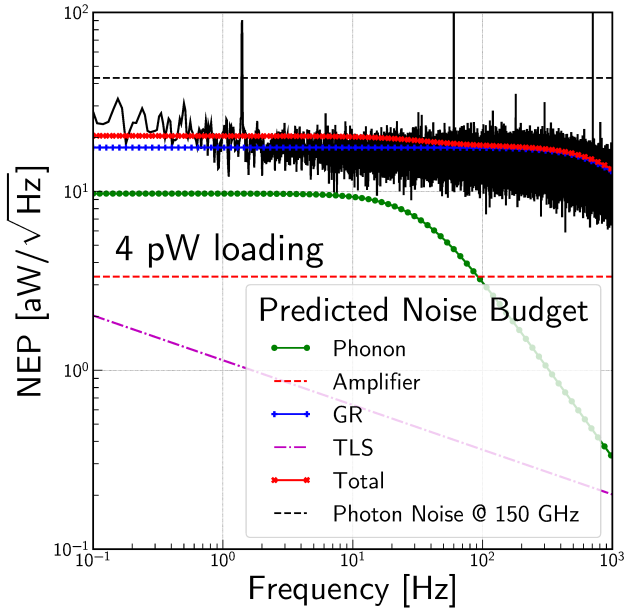

Figure 3.12: NEP of the 337 MHz resonator with a 4pW loading. Over-plotted are the estimated phonon, generation-recombination and amplifier noise contributions to the total noise based on the measured device parameters.

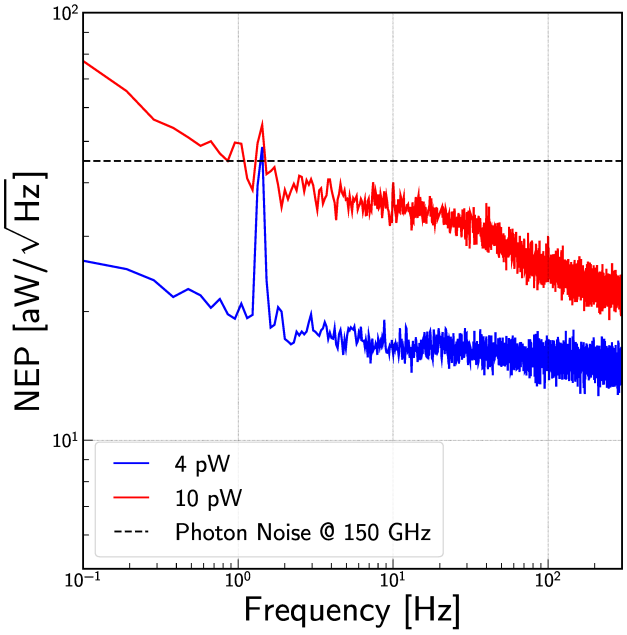

Figure 3.13: A comparison of the measured NEP for the 337 MHz resonator at the 4 and 10 pW loading levels after common mode noise subtraction. The large spike at 1.4 Hz is the pulse tube line. At 10 pW, there is a clear roll-off in the noise at around 35 Hz. This is consistent with the predicted thermal noise roll-off from the thermal conductivity and heat capacity measurements. At 4 pW, this roll-off is not visible suggesting that the gr noise is dominant detector noise term since the island temperature is much lower.

about 7K with a measured thermal conductance of 4.6mW/K as shown in fig. 3.14. There is evidence of some optical load on the cold load from 50K stage and the cold load performance can be improved with better thermalization of the 50K and 4K shells. Figure 3.15 shows the response of a single bolometer to the blackbody load as a function of the cold load temperature. This measurement confirmed that our initial waffle TKID resonator-bolometer design has significant direct stimulation and informed changes to the design discussed under section 3.3.

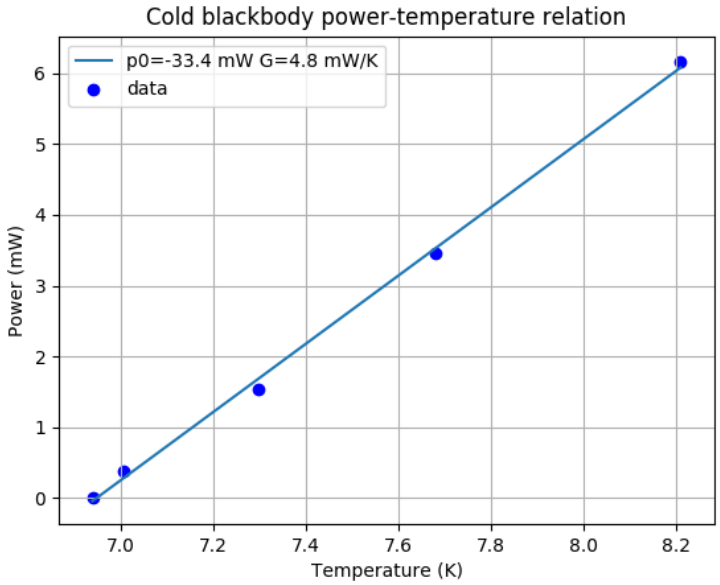

Figure 3.14: Calibration curve of the cold blackbody source.

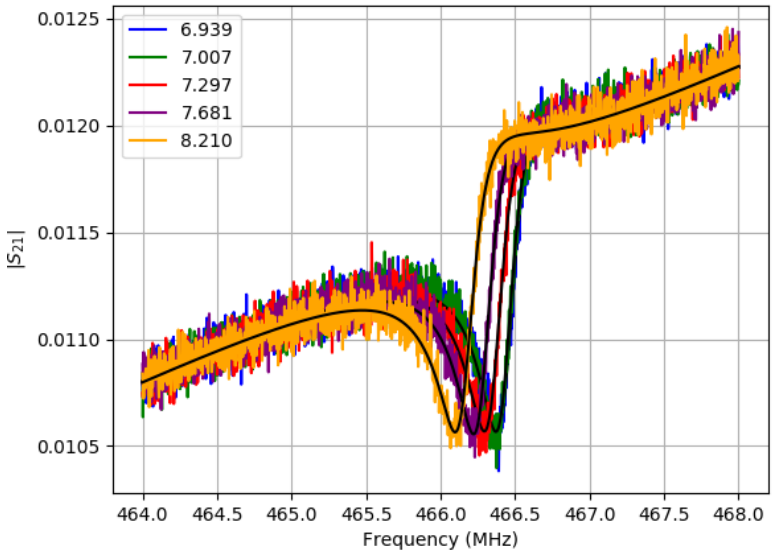

Figure 3.15: Shift in the resonance frequency with the cold load temperature. W that significant direct stimulation of the TKID resonator.

3.2 Dark Resonator Arrays

Scaling up a detector design from a few pixels on a chip to a full wafer scale is fraught with unanticipated risks. The design and testing of the dark resonator arrays represents the intermediate step in pixel density between the waffle TKID chips and the full focal plane. The frequency schedule of a single dark resonator array is shown in fig. 3.16.

Feedline Design

In the smaller waffle TKID chips described in section 3.1, we used a mismtatched 4 μm wide microstrip line as the feedline on the chip. With a 300 nm thick silicon dioxide dielectric layer, this microstrip line has an impedance of about 30 Ω. This had a significant effect on the asymmetry of the resonator but was acceptable due to the short length of the feedline and the generous spacing between adjacent resonators. On a 4" tile, the feedline is significantly longer and line mismatch with the amplifier can greatly degrade the performance of the wafer. However, to achieve 50 Ω using only microstrip requires a narrow 1 micron wide feedline, highly susceptible to defects during the fabrication process. Narrow lines also have

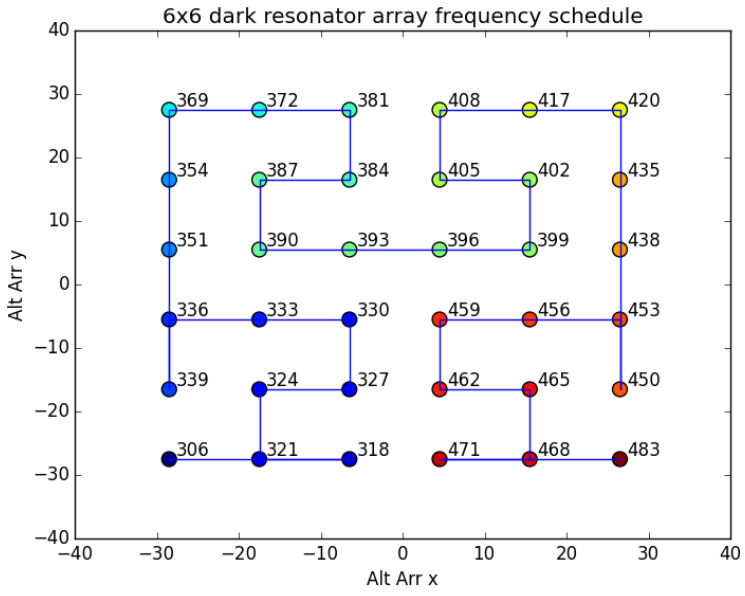

Figure 3.16: Design frequency schedule of the dark resonator array. Frequencies are given in MHz. The resonators are laid out in a 6x6 grid. The original grid was 8x8 and the resonators laid out along a Hilbert curve starting from the bottom left corner. We truncated the outermost pixels in the design to simplify the layout for initial testing.

limited critical current which can be a concern for our resonator readout strategy. A coplanar wave guide (CPW) design would be a good alternative since it has a suitably wide central feedline that is robust to defects during fabrication. However, in a CPW feedline geometry, the ground plane is broken up into disjointed sections with connections to ground only along the edge of the wafer where wirebonds are placed between the ground plane and the metal wafer holder. The ground plane dimensions are comparable to the wavelengths being considered and therefore we can expect that the ground plane properties will no longer be uniform across the wafer.

Our solution was to design and implement a hybrid CPW/microstrip feedline. The CPW geometry allows for a wider central feed that can be reliably fabricated across an entire wafer. The microstrip sections ensure that the ground plane remains continuous and held at the same potential everywhere on the wafer. Periodic microwave structures are well covered in literature (Pozar, 2005; Seki and Hasegawa, 1981).

Following Pozar's approach, we define the periodic length as d. The CPW occupies a fraction η of the periodic length and has impedance $Z_x = xZ_0$ with refractive index n_x. The MS line occupies a fraction $1-\eta$ of the line with impedance $Z_y = yZ_0$ where $Z_0 = 50\Omega$ is our target line impedance. Let $K = y/x$, $u = n_x\eta$, $v = n_y(1-\eta)$. The feedline structure has a propagating constant β and line impedance Z_c at free space wavenumber $k = 2\pi\nu/c$ that satisfies the consistency relations:

$$\cos\beta d = \frac{(1+K)^2}{4K}\cos\left[kd\,(u+v)\right] - \frac{(1-K)^2}{4K}\cos\left[kd\,(u-v)\right] \tag{3.3}$$

and

$$Z_c \sin\beta d = -Z_x\left\{\frac{(1-K)^2}{4K}\sin\left[kd\,(u-v)\right] + \frac{1-K^2}{2K}\sin\left[kdv\right] - \frac{(1+K)^2}{4K}\sin\left[kd\,(u+v)\right]\right\}. \tag{3.4}$$

We chose $d = 100\mu$m, short enough to have minimal radiative loss even at millimeter wavelengths. Once the central feedline width and spacing to ground plane are fixed (say by fabrication constraints), there is only one free parameter, η. The periodic structure imposes passbands so there is a cutoff wavenumber k_c beyond which the wave is attenuated. However, we can expect that the first passband extends down to $k = 0$ since eq. (3.3) has a solution in this limit. We can therefore derive a

closed-form expression for η_*, the fraction of CPW line that gives $Z_c = Z_0$ in the low frequency limit $k \to 0$. We find that

$$\eta_* = \frac{n_y \left(K^2 x^2 - 1\right)}{n_x K \left(1 - x^2\right) + n_y \left(K^2 x^2 - 1\right)}, \tag{3.5}$$

and the propagating constant of the line is

$$\beta_* = k \frac{x n_x n_y \left(K^2 - 1\right)}{n_x K \left(1 - x^2\right) + n_y \left(K^2 x^2 - 1\right)}. \tag{3.6}$$

In our design, we chose a central line width of 8μm and a CPW gap of 20 μm. This gives a CPW line of impedance $Z_x = 60\Omega$ and $n_x = 2.47$. A microstrip line of width 8μm has a small impedance of $Z_y = 8.8\Omega$ and $n_y = 2.60$. Plugging these values gives $\eta_* = 0.94$ and $n_* = 2.82$.

In Sonnet[5], we simulated a 5600 μm long section of the feedline. As per the model, the CPW sections are 94 μm long with 6 μm long microstrip bridges. The simulation includes the ground plane and microstrip layer kinetic inductances of 0.158 pH/sq and 0.138 pH/sq, respectively. The line impedance from the simulation is $Z_c = 53.5\Omega$ with $n = 2.95$. The simulated S parameters are given in fig. 3.17. We have maintained a similar feedline design for all subsequent arrays. Figure 3.18 shows the dispersion relation for the hybrid feedline from eq. (3.3). The dispersion is linear up until the cutoff for the first passband at above 500 GHz.

Because the microstrip and CPW line sections have vastly different line impedances, the electric field will be concentrated in the microstrip sections and the magnetic field in the CPW sections of the line. This spatial separation of regions where the electric and magnetic energy is stored causes the feedline to act as a slow wave structure with a large effective dielectric constant.

[5] https://www.sonnetsoftware.com/

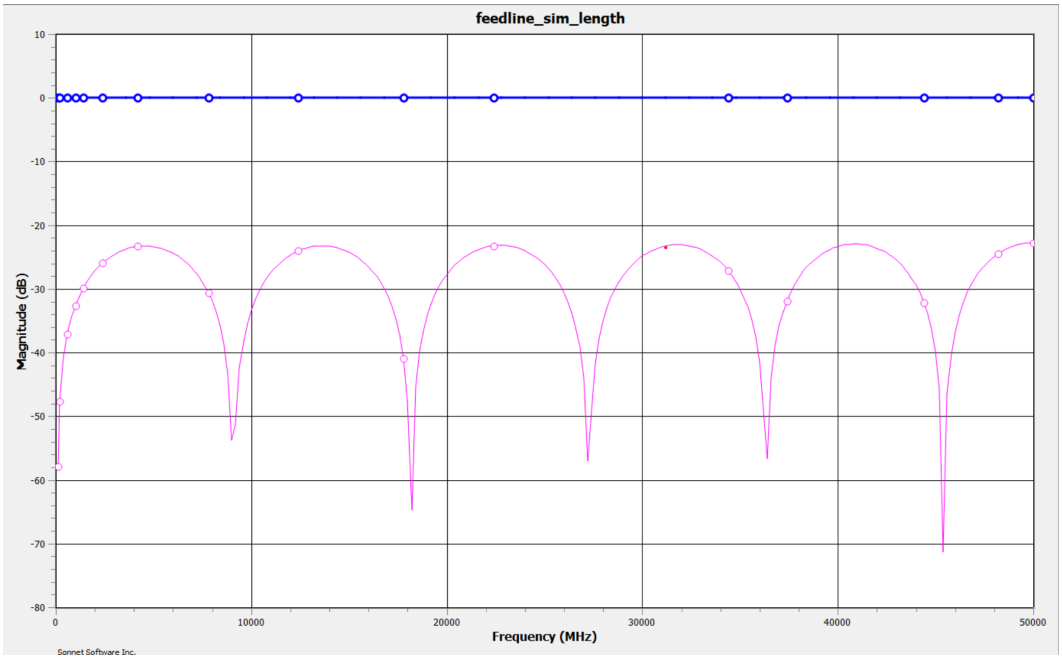

Figure 3.17: Scattering parameters simulated using Sonnet for a 5600 μm long section of the hybrid feedline. The feedline is well matched to 50 Ω well above the frequency range of interest for TKID resonators (< 1 GHz).

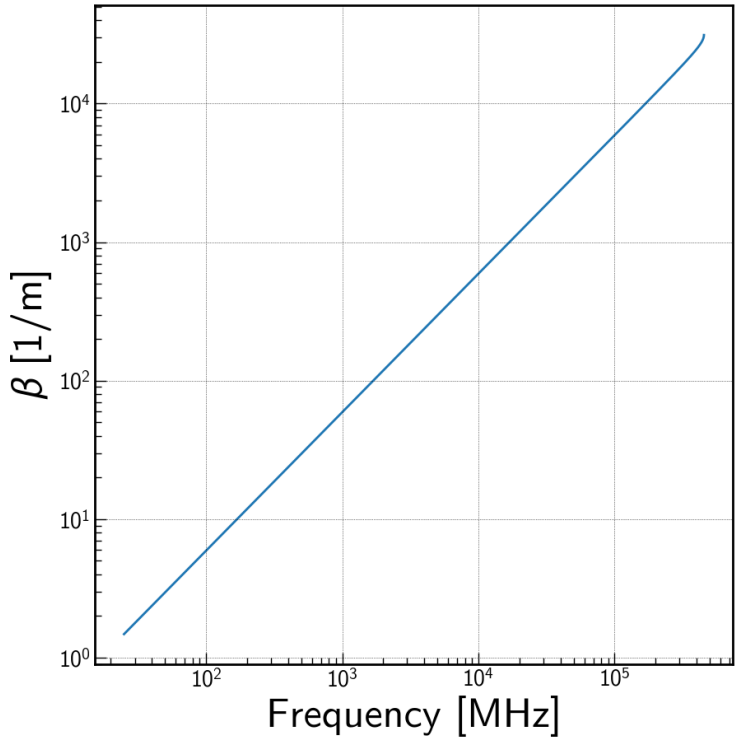

Figure 3.18: A numerical solution to the dispersion relation for a hybrid CPW/microstrip feedline with a periodic length of 100 μm. Linear dispersion is maintained until the cutoff frequency for the first passband at around 500 GHz.

LED Mapping

Directly measuring the frequency-to-pixel mapping is a priority for reliable testing and deployment of resonator arrays. With increasing detector counts, resonators have to be tightly spaced within the frequency band to maximize the multiplexing factor. Often, fabrication non-uniformities or imperfections in the array can cause the resonator frequencies to shift away from their design values. It is therefore difficult to ascertain the physical location of a resonator on the wafer simply from its resonance frequency and relative position in the measured frequency schedule. A number of approaches have been used to break this degeneracy. In the BK-μMUX deployment (Cukierman et al., 2020), individual pointing of detectors relative to the boresight was reconstructed by cross-correlating the known CMB anisotropies as measured by *Planck* to individual detector maps. Shu et al., 2018 use a cryogenic beam mapping system to illuminate individual resonators in the array. Our approach borrows from the cryogenic LED mapper approach developed by NIST (Liu et al., 2017) initially for BLAST-TNG (Dober et al., 2014). A cryogenic LED mapper (christened LiteBrite) is useful for measuring material properties such as quasiparticle time constants.

We designed a 6x6 LED array in a common row cathode configuration. Only 12 wires needed to control all the LEDs - a row is grounded and then a current bias is placed on the column corresponding to the LED of interest. For denser resonator arrays, charlieplexing (Horowitz and Hill, 2015) is the preferred approach to minimize the total number of wires needed to bias each LED. Column 1, Row 1 on the PCB corresponds to the resonator on the lower left corner of the wafer as shown in fig. 3.19. Column Numbers increase going to the right and Row Numbers increase going up along the wafer. The LED coordinates are chosen to position the LED directly above the center of the inductor when cold. We install an aluminum collimator plate to limit stray light exciting more than one resonator at a time. We set the height of the collimator to 2.5 mm above the wafer using spacers.

In our initial attempt, we baselined the HSMD-C190 GaP LEDs shown to work by the NIST team down to 40 mK. In their approach, the LEDs can be operated in a weakly turn-on condition using low ($\sim$ 1 μA) current to bias the LEDs. However, we saw the carriers freeze-out below 40 K as shown in fig. 3.20. This is expected in a non-degenerate semiconductor, since at low enough temperatures, the thermal free electron/hole density drops to zero. However, we routinely found carrier freeze out even in LEDs made from degenerate semiconductors where we expect a residual population of charge carriers even at very low temperatures (Kittel and Kroemer,

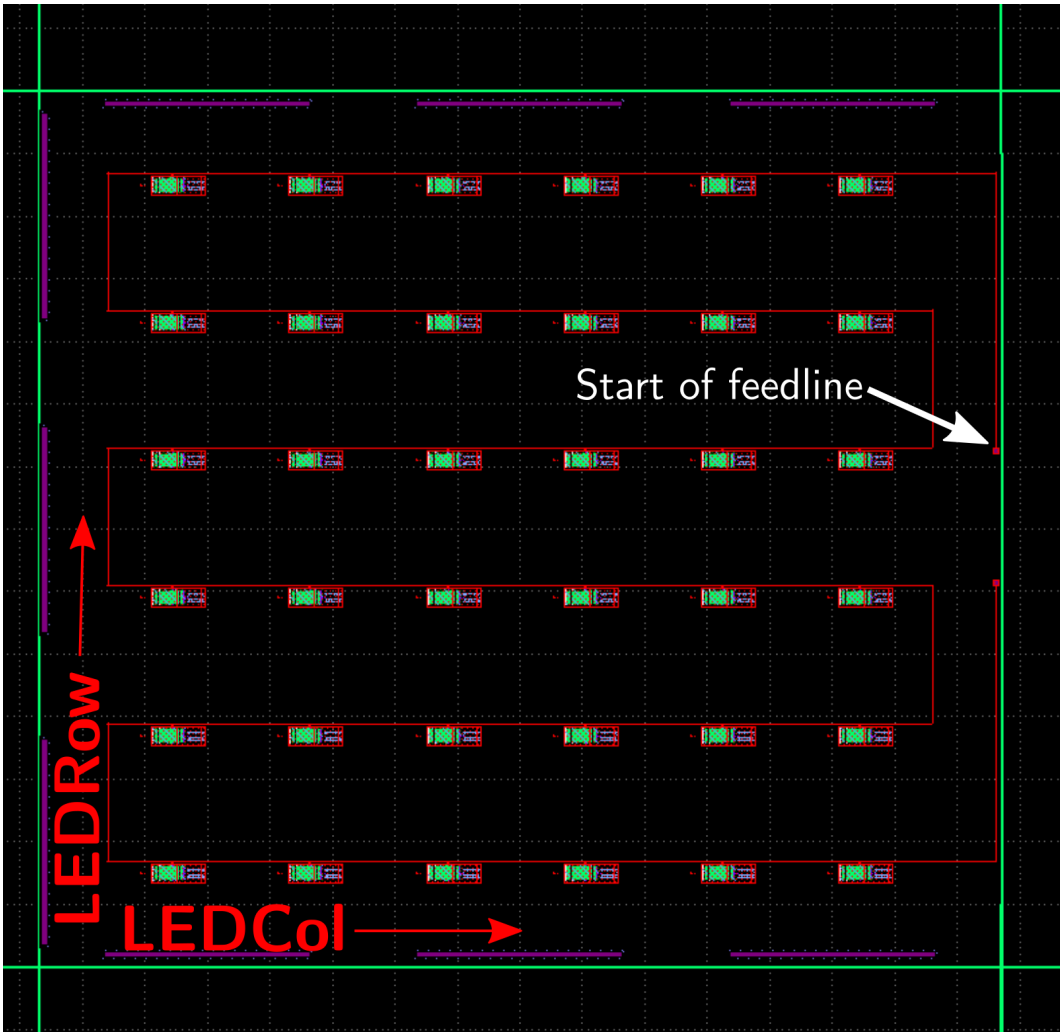

Figure 3.19: Correspondence between the LED Array coordinate system and the resonator array on the tile.

1980). We concluded that it is likely that batch-to-batch variations in LED properties can be significant. The cryogenic performance of the LEDs is not well controlled for in LED fabrication and therefore existing literature provides a useful starting point but cannot be blindly relied on. We therefore decided to cast a wider net and test a variety of different LED types to see if we will find any that works.

We tested 8 different 0603 surface mount LEDs with different semiconductor material purchased in large batches. The LED properties are summarized in table 3.3. We designed an 8 channel dip probe to screen LEDs in liquid He at 4K. Figure 3.21 summarizes the measured LED IV curves. Of the 8 LED types screened initially, 3 were found to work at cryogenic temperatures.

The LTST-C191KGKT green LEDs which worked well down to 93 mK were in-

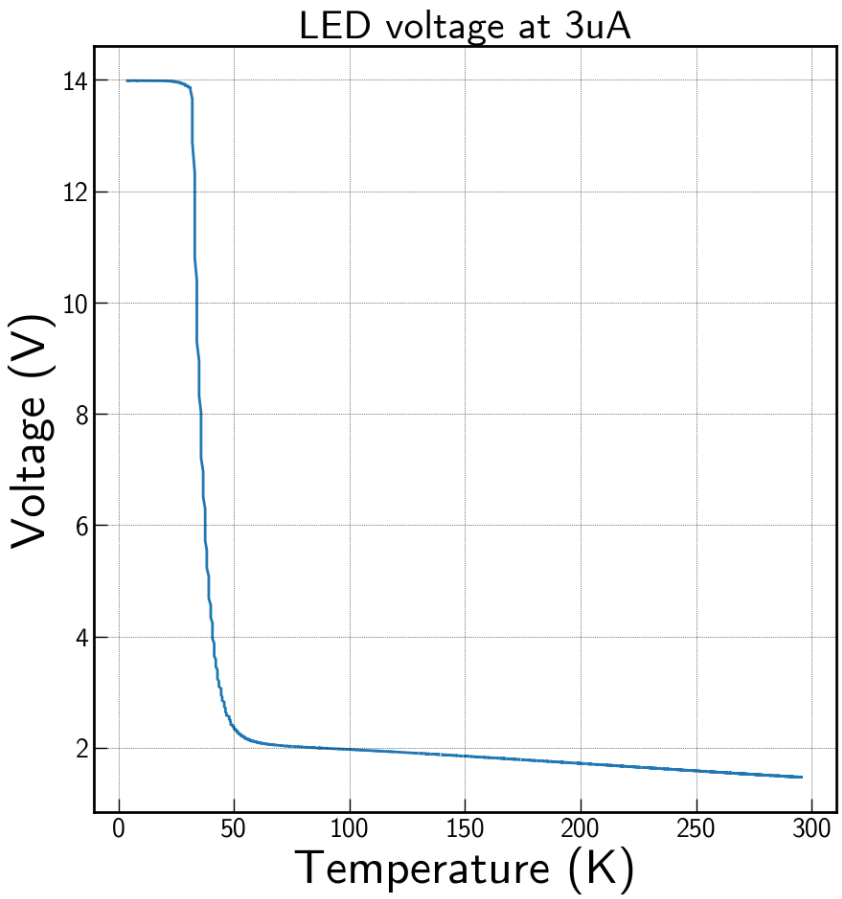

Figure 3.20: Change in the voltage across a HSMD-C190 GaP LED at a fixed current bias of 3 μA as a function of the stage temperature. Below 40 mK, the voltage rapidly rises to the compliance voltage of our current source. This indicates that all the charge carriers have frozen out and the semiconductor has become fully insulating.

Dip Probe Channel	LED type	LED color	material
1	LTST-C193TBKT-5A	Blue	InGaN
2	LTST-C191KSKT	Yellow	AlInGaP
3	HSMS-C190	High Efficiency Red (HER)	GaP
4	LTST-C191KGKT	Green	InGaN
5	HSMY-C190	Yellow	GaP
6	APT1608EC	High Efficiency Red (HER)	GaAsP/GaP
7	HSMG-C190	Green	GaP
8	LTST-C190-KFKT	Orange	AlInGaP

Table 3.3: Properties of LEDs screened for cryogenic LED mapping. LED types 2,4 and 8 were found to be good candidates for cryogenic LED mapping.

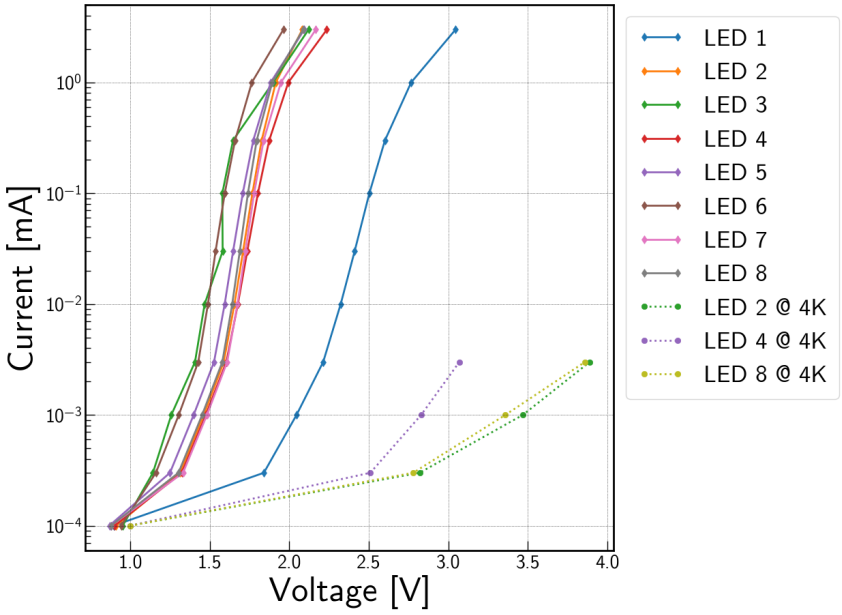

Figure 3.21: Measured IV curves of the 8 LED types screened using the dip probe. We identified LED batches 2, 4 and 8 detailed in table 3.3 as suitable for cryogenic LED mapping.

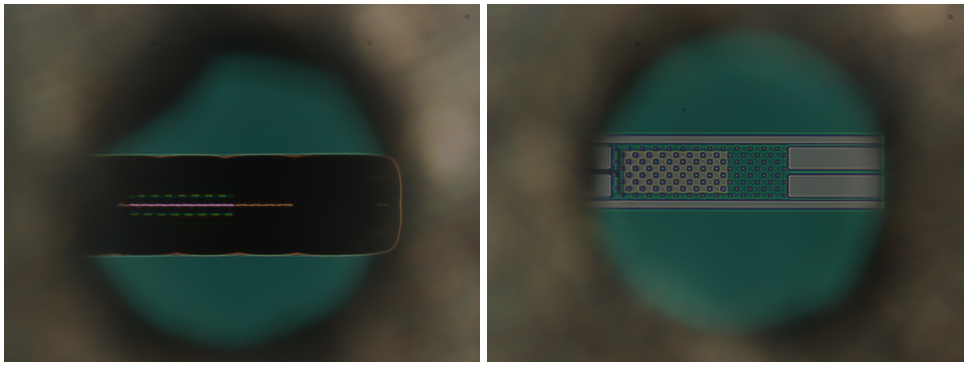

(a) (b)

Figure 3.22: Microscope view of the LED inductors through the collimator plate confirming good alignment before cooldown. The resonators on the dark array are checkerboard released for cosmic ray testing. Figures 3.22a and 3.22b correspond to the row 3 column 3 and row 3 column 4 resonators, respectively.

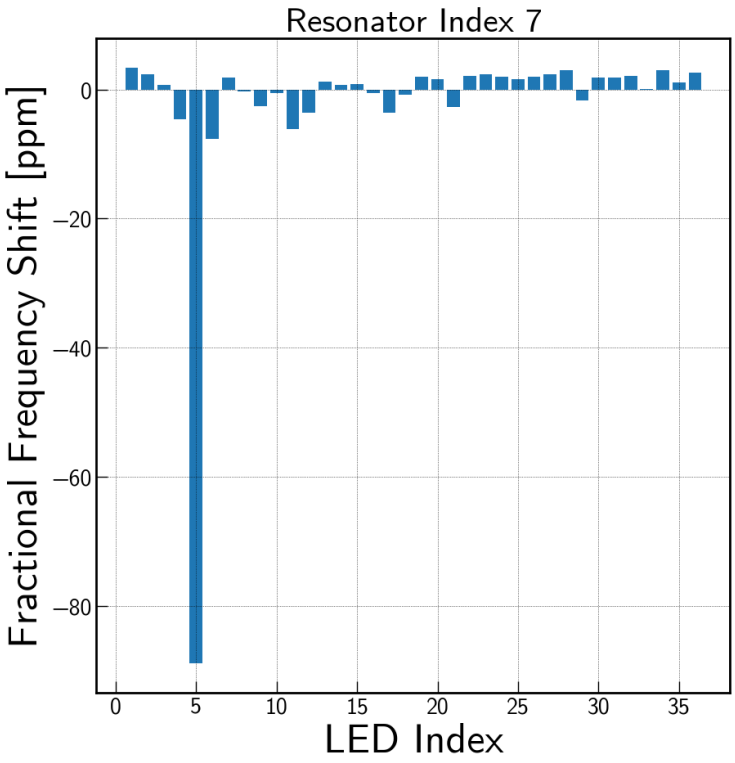

Figure 3.23: A measurement of the response of the resonator at index 7 to the LED pulses. The resonator is unambiguously mapped to the 5th LED. The systematic variation in the frequency shift with LED index is evidence of light leakage from one LED across multiple resonators.

stalled on the LiteBrite and used to map the resonator array. We took data with a 475 nA input current which sets the bias voltage to 4.0-4.2 V.For most of the resonators, the frequency shift when the LED is on is sufficient to unambiguously locate the resonator on the wafer. However, for poorly coupled resonators, the Qi shift information was also useful.

Quasiparticle Lifetime Measurements

Using the litebrite, we measured the quasiparticle time constants by pulsing the LED and sweeping the stage temperature from 100-400 mK by regulating the UC Fridge temperature and recording the UC stage temperature. At each temperature, the LED was pulsed at 20Hz and 4.8V with a 20us pulse width. Data was recorded for 10 seconds and the first second is discarded. All the remaining pulses are averaged, and the relaxation back to equilibrium is fit with a decaying exponential. The first 50us of the data is cut to eliminate the duration when the LED is actually on, and only data below 10ppm frequency shift is used to avoid out of equilibrium effects.

At the highest temperatures, the resonator response was too fast to get a good fit.

The saturation in the time constant shown in fig. 3.24 has been reported in many other aluminum superconducting resonators (Zmuidzinas, 2012). We model the lifetime as a function of temperature using a 2 parameter model

$$\tau = \frac{\tau_{\max}}{1 + n_{qp}/n^*_{\rm qp}}. \tag{3.7}$$

The best fit parameters were found to be $\tau_{\max} = 0.1809 \pm 0.0025$ms and $n^*_{\rm qp} = 517.9 \pm 40.0\ \mu\text{m}^{-3}$.

Cosmic Ray Testing

Dead-time and data loss from cosmic ray hits are a significant concern when designing space-borne observatories, especially envisioned future CMB and far-IR space observatories. These high energy particles can penetrate the instrument and deposit energy in proximity to the detectors through atomic excitation and ionization. Such collisions generate showers of ballistic (athermal) phonons that trigger the detectors as a "glitch" and ultimately necessitate data-cuts (D'Addabbo et al., 2014).

When cosmic rays collide with the upper atmosphere, they generate showers of muons with a sea level flux of 1 particle/cm^2/minute (Tanabashi et al., 2018). Across the wafer area of 50 cm^2, we expect about 0.8 hits/s whereas each TKID bolometer island will be affected about 0.03 hits per hour.

As a muon traverses through a silicon wafer, it deposits energy in the form of athermal ballistic phonons, which can break Cooper pairs and generate extra quasiparticles. This causes large frequency excursions and produce spurious signals. The bulk of cosmic ray muons have energies of a few GeV, near the minimally ionizing, where energy is deposited by ionization at a rate of 2 MeVcm^2/g and specifically will deposit 460 eV/μm into silicon, whose density is 2.32 g/cm^3. Muons normally incident to the tile will therefore deposit 230 keV which, if spread across the wafer, will deposit 0.6 eV into each inductor. In contrast, muons directly hitting the bolometer islands will deposit 280 eV into the island. All the unreleased resonators on the island are affected by the athermal phonons.

The energy E deposited in the inductor for each glitch can be obtained using the already discussed Mattis Bardeen theory. Given a glitch of amplitude $x_{\rm MB}$, the energy is given by

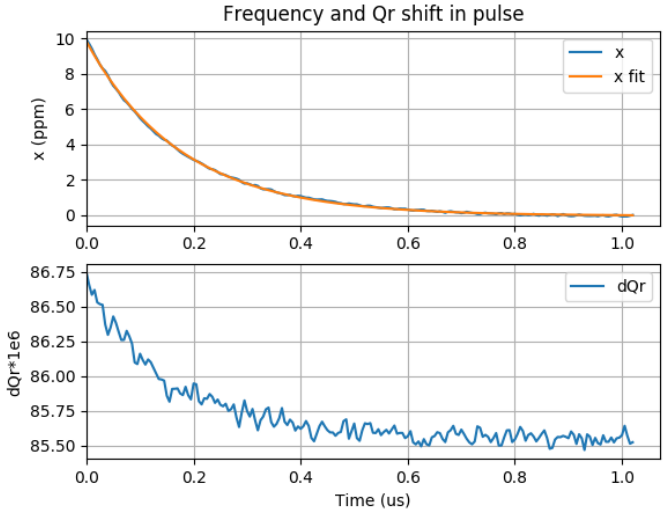

(a)

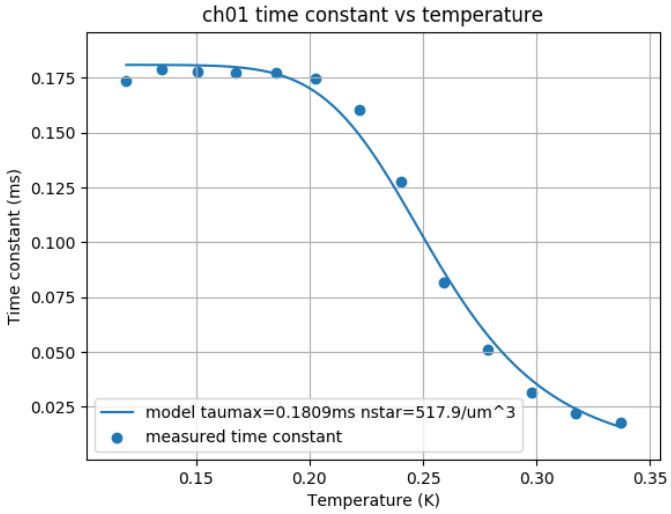

(b)

Figure 3.24: Figure 3.24a shows the measured response of a single resonator to an LED pulse at a bath temperature of 167 mK. The quasiparticle lifetime as measured for the 337 MHz resonator shown in fig. 3.24b saturates below 200 mK.

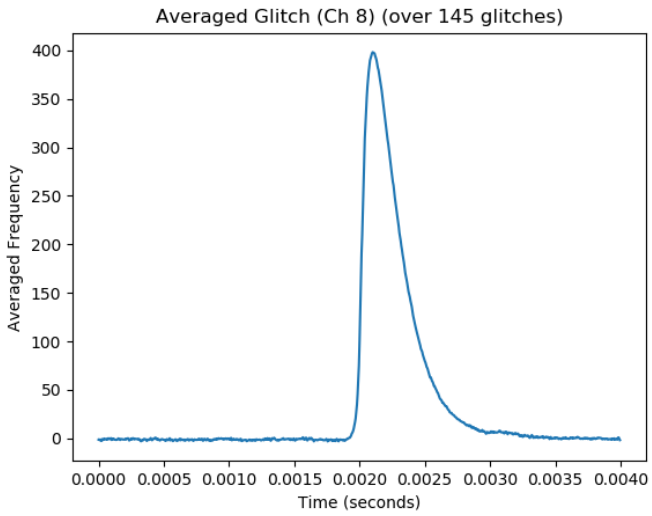

Figure 3.25: Averaged glitch for a single unreleased resonator channel measured at 70 mK.

$$E = n_{\mathrm{qp}} V_{\mathrm{sc}} \Delta = \frac{4 N_0 \Delta^2}{\alpha_k S_2} V_{\mathrm{sc}} \cdot x_{\mathrm{MB}}. \tag{3.8}$$

On the checker-board released dark resonator arrays, we measured frequency timestreams from all detectors from two 8-minute sessions at 70 mK and 320 mK. Our GPU based readout system (L. Minutolo, B. Steinbach, et al., 2019) allows us to record all the data for all the resonators for 10 ms after a triggering event defined by a resonator shift of greater than 6σ. Fig. 3.25 shows the averaged cosmic ray signal for a single unreleased resonator. We additionally scanned the detectors over a 3 hour period at 70 mK to capture direct hit events to the TKID islands. We detected only two candidate events and none in the other unreleased devices. This is an effective rate of 1×10^{-5} events/s and corresponds to the ratio of cross-sectional areas between the wafer and a single inductor.

Fabrication Improvements

We began developing strategies to fix feedline defects on the dark resonator arrays. These approaches were further refined for the 150 GHz science tiles. We identified a defect on the CF190420 wafer that resulted in a short to GND. The deformity on the line is visible on a microscope as shown in fig. 3.26. Luckily the short was on the microstrip section of the line. We could therefore isolate the short by cutting through the microstrip and GP layers to isolate the defect as shown in fig. 3.27.

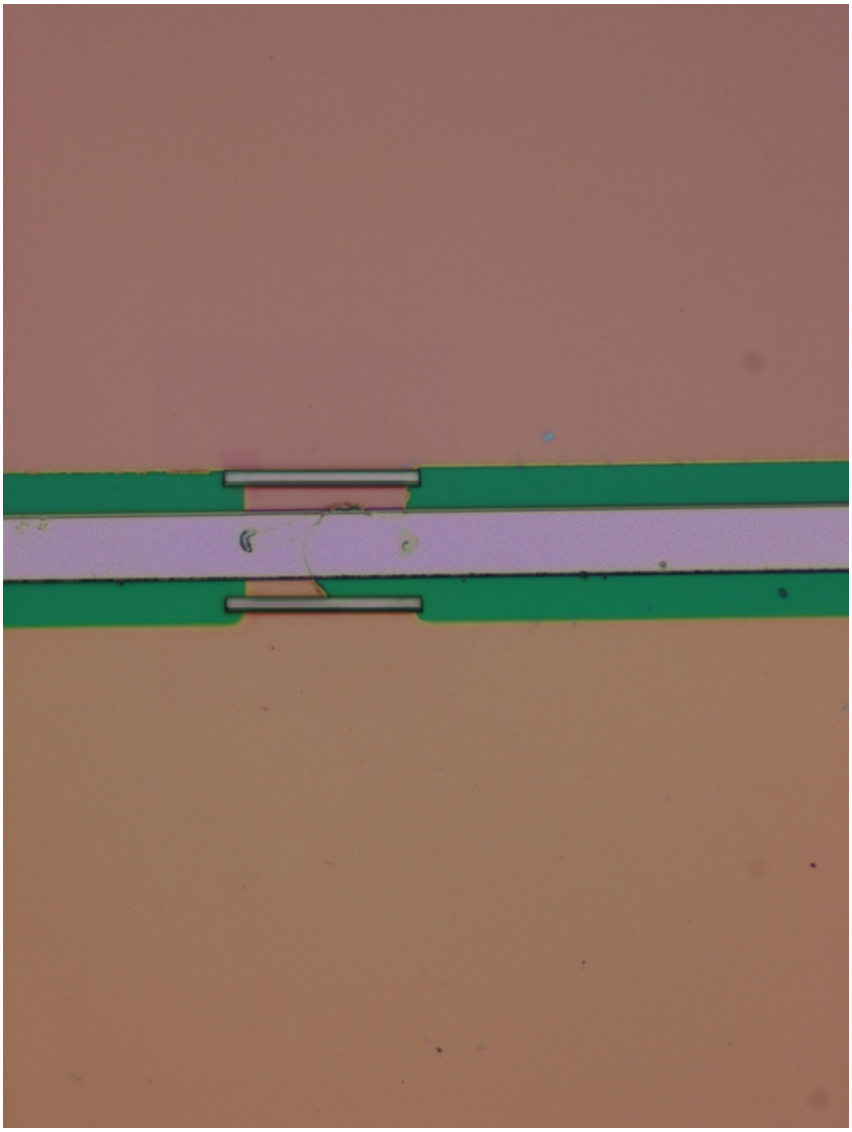

Figure 3.26: Line defect affecting the microstrip section of the feedline leading to a short to GND. The horizontal bars are cuts through the dielectric and into the ground plane. The cuts isolate the defect from the rest of the ground plane restoring conductivity through the feedline. This was done using the Nova 600 gallium Focused Ion Beam (FIB) at KNI.

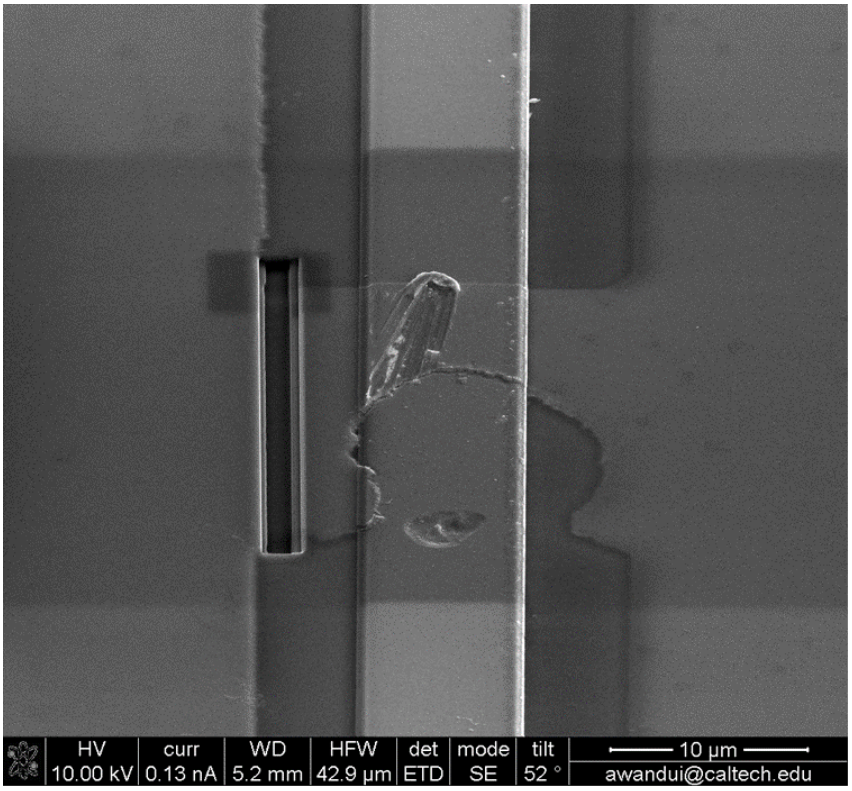

Figure 3.27: SEM taken after the initial step of fixing the defect using the FIB system at KNI. The effect of a probe tip on the feedline is also visible.

We used the NOVA 600 Ga Focused Ion Beam (FIB) at KNI to etch down a 1.5 um by 20 um cavity through the layers. I used a 30 kV beam with a 0.5 nA bias current which should give a 25 nm beam diameter. The ion beam has much less contrast than the electron beam – does not see topography well but distinguishes between conducting and insulating materials well. This arises because the positive ions implanted in the material during the FIB trap the secondary electrons that are the main signal being detected. On conducting surfaces, a fresh supply of electrons can flow to neutralize the excess charge. This was useful in figuring out the stop point of the etch since it was clear when I hit the GP vs dielectric layers.

This wafer was subsequently cooled down and tested showing a 20/36 yield. As shown in fig. 3.28, there is a radial dependence of the fractional frequency shift between the design and measured resonance frequency. This is likely due to variation in the aluminum film thickness across the wafer. More concerning is the systematic loss of the 2 rightmost columns of resonators. In fact, many of the dark resonator arrays exhibited similar behavior where the resonators closest to the wafer edge would fail to yield. By inspecting the unyielded devices, we were able to identify

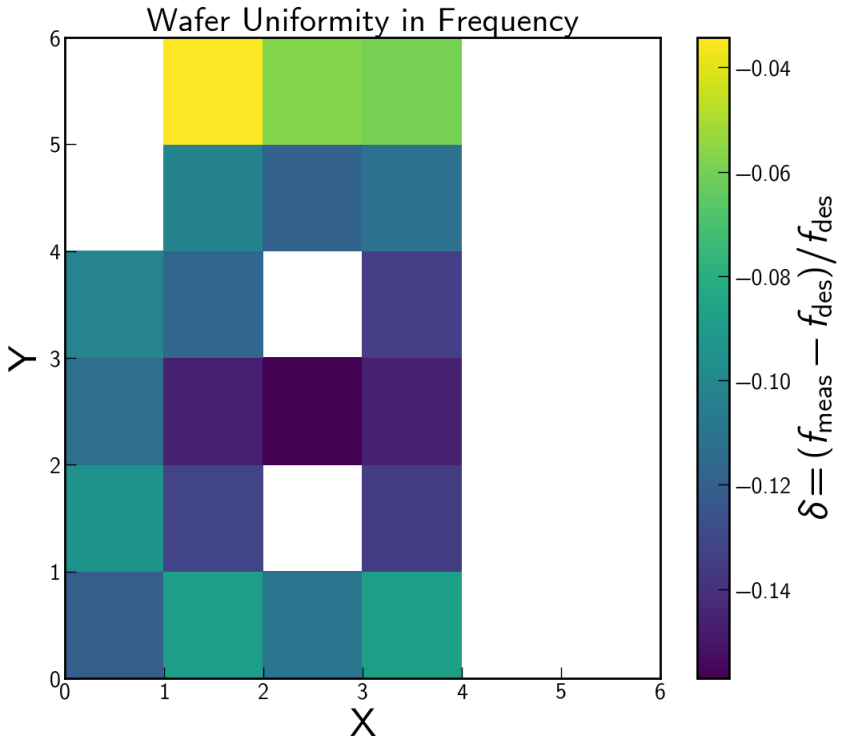

Figure 3.28: Wafer mapping of the fractional frequency shift from design as measured using the LiteBrite. The two rightmost columns of resonators did not yield. We determined that defects in the capacitor via to ground were responsible. Subsequently, these vias were completely eliminated from the design.

the vias between the coupling capacitor and ground through the ILD were the likely culprit. Eliminating the vias from the design in favor of a large parallel plate coupling to ground completely eliminated the edge effect in our design.

3.3 2x3 Antenna-Coupled TKIDs

Direct Stimulation of the Inductor

For our thin Al films, $T_c \sim 1.4$K. This gives a gap frequency $\nu_g = 2\Delta/h \sim 100$ GHz. In our observing band centered at 150 GHz, our Al is normal. It can therefore directly absorb and dissipate optical power. Direct absorption in the inductor is undesirable. This is important because optical power absorbed can break cooper pairs creating additional quasiparticle excitations in the superconductor. As pointed out in appendix A, a single mode detector has the property that $A\Omega = \lambda^2$ where A is the effective area of the detector and Ω is the solid angle subtended by the beam at the detector. From this equation we can define a figure of merit for how well the inductor couples to optical power as $N_{modes} = A\Omega\epsilon/\lambda^2$ where ϵ is the emissivity of the inductor. If $N_{modes} \ll 1$ then we can safely ignore the optical power contribution

to the quasiparticle generation rate.

We model the inductor as having an anisotropic surface resistance. Along the short axis of the inductor, the surface resistance is zero since the 2 um width of the inductor meander is too short to couple effectively to radiation at 150 GHz. Along the long axis, the surface resistance is twice the surface resistance of Aluminum due to the 50% filling factor. Given the thickness of the wire t and the resistivity of Aluminum ρ the surface resistance of the inductor is $R_s = 2\rho/t$.

Our Aluminum films are thin $t = 50\mu$m for high kinetic inductance. In comparison, the skin depth in Aluminum, $\delta = \sqrt{2\rho/\omega\mu_0} = 2.8t$ at 150 GHz. To calculate how much of the incident optical power is absorbed in the inductor, we can use a transmission line equivalent circuit. We back illuminate our antenna through the silicon wafer, therefore an incident plane wave traverses first through the quarter wavelength thick anti-reflection tile, then the silicon wafer before impinging on the inductor. We place a metal backshort at a distance of a quarter wavelength away from the detector. The backshort is designed to act as a short circuit load to the incoming signal, perfectly reflecting the incoming signal back to the antenna improving efficiency.

Our reference impedance is the impedance of free space, $Z_0 = 377\Omega$. Each transmission line section has a characteristic impedance determined by the refractive index of the material. For Si, $Z_{Si} = Z_0/n_{Si}$. We use quarter wavelength thick quartz with a refractive index $n_{\rm AR} = \sqrt{n_{Si}}$ for the anti-reflection coating. The transmission line is shunted by an impedance equal to the surface resistance of the inductor along the long axis.

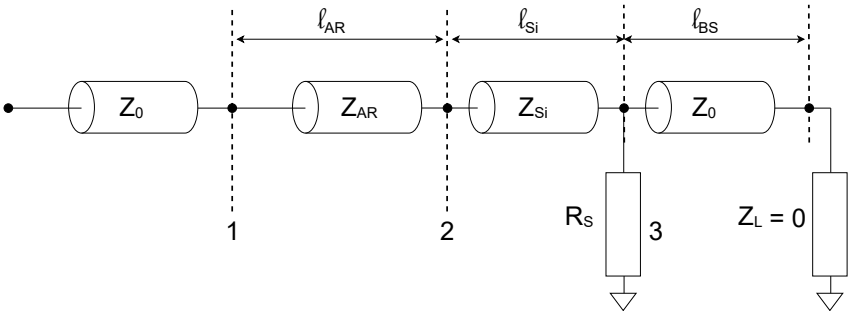

Figure 3.29: Transmission Line Model used to compute the coupling of the inductor to optical power.

The quarter wave condition transforms the backshort to an open at the inductor. This is exact only at the bandcenter ν_0. Taking the frequency $\nu = \nu_0 + \delta\nu$ into account,

we find

$$Z_3\left(\delta\nu\right) \;=\; \frac{R_s Z_0}{Z_0 + jR_s \tan\left(\frac{\pi}{2}\frac{\delta\nu}{\nu_0}\right)}. \tag{3.9}$$

Given the input impedance seen at the reference plane 1, $Z_{\rm in}$, the reflection coefficient is $\Gamma = \frac{(Z_{in}-Z_0)}{(Z_{in}+Z_0)}$. The emissivity ϵ is then the fraction of the incident power that is absorbed in the detector which is given by 1 minus the fraction of incident power that is reflected away. Thus, $\epsilon = 1 - |\Gamma|^2$.

To lowest order in $\delta\nu/\nu_0$, $\epsilon = \epsilon_0$

where

$$\epsilon_0 \;=\; \frac{4n_{Si}R_s Z_0}{\left(Z_0 + n_{Si}R_s\right)^2}. \tag{3.10}$$

Using measured material properties, $\rho = 1.15\mu\Omega\cdot$cm , $t = 0.05$ μm , $n_{Si}^2 = 11.7$, $\epsilon_0 \;=\; 1.7\times10^{-2}$. The low resistivity of Aluminum couples it poorly to incoming radiation in our observing band. We can therefore ignore the direct stimulation contribution of the Al inductor.

Direct Stimulation of the Capacitor

Unlike the Al inductor, the niobium capacitor remains superconducting well above the observing band. However, as has been noted by other experiments such as MUSIC (Golwala et al., 2012), the interdigitated capacitor (IDC) acts as an antenna. The long parallel features of the are many wavelengths long in our band and can couple to multiple radiation modes on sky. The stray radiation from the antenna can travel from the capacitor to the inductor breaking additional quasiparticles. To prevent this, Bryan Steinbach designed a niobium stepped impedance low pass filter that I incorporated into the resonator between the capacitor and inductor but off the bolometer island. The filter was designed to provide -30 dB suppression above 125 GHz, with minimal additional capacitance to minimize two-level system (TLS) noise. The filter was designed using Sonnet [6] and consists of short co-planar wave guide (CPW) and microstrip sections between the capacitor and the inductor. Figure 3.31 shows the simulated transmission through the low pass filter shown in fig. 3.30

[6] https://www.sonnetsoftware.com/

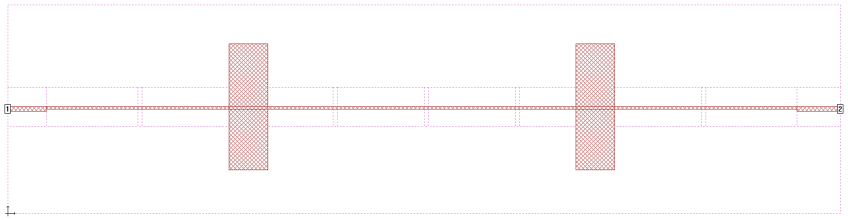

Figure 3.30: A 2-layer stepped impedance low pass filter to suppress direct stimulation from the IDC structure. The high impedance sections are made from 1 μm wide niobium lines and the parallel plate capacitors use the SiO_2 ILD as the dielectric.

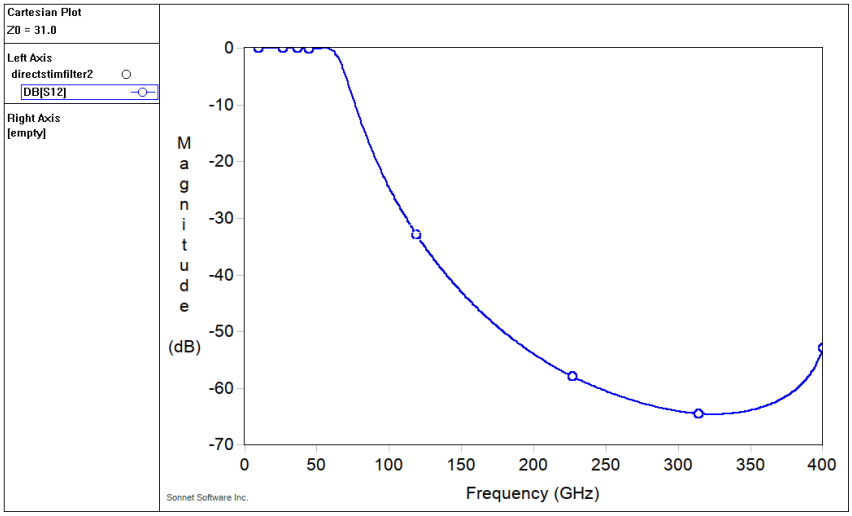

Figure 3.31: Magnitude of the forward transmission through an RF choke designed to suppress direct pickup from the capacitor. Our observing band is from 125 – 175 GHz within which there is more than 30 dB suppression of power.

With the RF choke, we saw less than 2% direct stimulation in the 2x3 optically coupled chips. This is in sharp contrast to the significant response to a cold blackbody measured on the waffle TKID devices discussed in section 3.1.

Device design

We designed test chips with 12 TKID devices each: 8 optically active and 4 dark devices. The resonators were defined in a frequency band starting at 250 MHz and with a 5 MHz frequency spacing. Adjacent pairs of resonators were coupled to a single dual-polarization antenna such that each optically active resonator bolometer measures the optical power from a single polarization mode of the antenna. The chip layout is detailed in fig. 3.32

The antenna itself consists of a two dimensional array of closely-spaced slots in the ground plane. There are two sets of orthogonally oriented and co-located slots

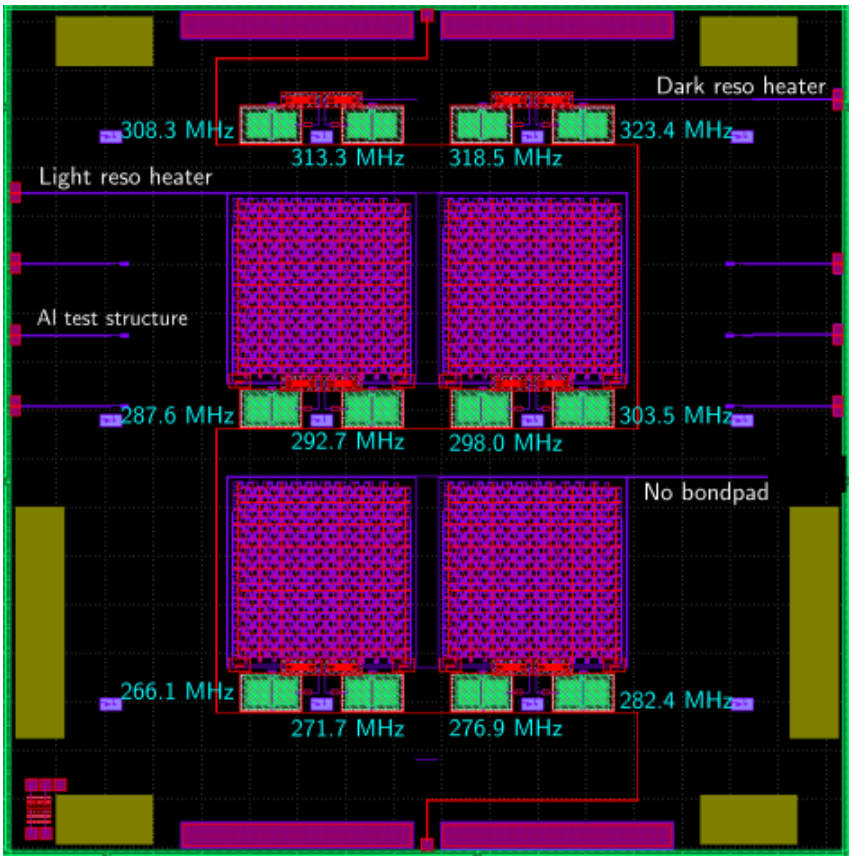

Figure 3.32: Design layout of a single 2x3 chip. The frequency schedule across the chip is given. Along the edge, a series of niobium and aluminum test structures are included to measure the film resistivities and transition temperatures.

corresponding to the two polarization modes. This antenna design is the same as has been used in BICEP2/ *Keck* Array (Ade, Aikin, Amiri, Barkats, Benton, Bischoff, Bock, Bonetti, et al., 2015; Kuo et al., 2008). The optical power from the antenna passes through an on-chip band defining filter before being dissipated in a Au meander strip on the bolometer island. From numerical simulations and measured in-field performance, our antenna design provides spectral bands with 20% - 30% bandwidth, symmetric co-aligned beams and a low 0.5% cross-polar response. The *Keck* Array camera has $f/2.2$ refractive optics (Ade, Aikin, Barkats, et al., 2015). To match the antenna beam to the camera optics, the antenna is 7.8mm long on each side in a 12x12 array of slots. The beam is constructed by a uniform illumination of the slot array and the detector beam terminates at –15 dB on the cold stop of the camera at 4K

The bolometer island is fabricated from a patterned low stress silicon nitride (LSN) layer. The released island is mechanically supported on 300 μm long legs. The

leg length sets the thermal conductance of the bolometer and therefore the island temperature. Our TKID design targets operation from a 250 mK bath temperature in order to achieve a 380 mK operating temperature T_o with the expected 5 pW loading from observing the millimeter wave sky in a 150 GHz band with a 25% bandwidth from the South Pole (Ade, Aikin, Barkats, et al., 2015). The niobium ground plane of the antenna layer extends onto the thermal island through the bolometer legs and is placed underneath the resistive meander to isolate it from the aluminum resonator inductor which is situated at the opposite end of the bolometer island. We maintain a small Au heater on the thermal island to measure thermal conductances, thermal time constants, responsivity and noise. Figure 3.33 shows an Scanning Electron Microscope (SEM) micrograph of the resonator bolometer with the inductor, calibration heater and resistive meander visible.

The resonator is built out of lithographed, lumped-element inductors and capacitors. In our design, the aluminum inductor and niobium main capacitor are identical for all the resonators on the chip. The resonance frequency is set during fabrication by using a pair of knife cells to blade off sections of the fingers of the inter-digitated capacitor. Smaller coupling capacitors were also used to set the coupling of the resonator to the readout line. We chose the coupling capacitors to ensure that the coupling quality factor Q_c of our devices matches the internal quality factor Q_i at the operating temperature. The thermal response of the resonator is limited to the aluminum inductor ($T_c \sim 1.2$K) on the bolometer island since the bulk of the resonator circuit is fabricated out of niobium with a much higher superconducting transition temperature, $T_c \sim 9$K. Figure 3.34 is an SEM micrograph of the resonator capacitor and shows a section of the feedline on chip. The 50 Ω hybrid feedline discussed in section 3.2 was used in this array.

Experimental Setup

We initially characterized our devices in a dark configuration in a Model 103 Rainier Adiabatic Demagnetization Refrigerator (ADR) at the Jet Propulsion Lab (JPL). With the test chip installed, the cryostat achieves an ultra-cold (UC) stage temperature of 80 mK. For the optical testing, we installed our devices in a new focal plane installed in a *Keck* Array camera at Caltech that has been fitted with RF hardware. The optical system consists of a pair of low-loss high-density polyethylene (HDPE) lenses with a refractive index $n = 1.5$ that are cooled to 4K. Unfortunately, the lenses we had available were anti-reflection (AR) coated for the 220 GHz band rather than at 150 GHz. In our target band, the optics are in effect uncoated, causing reflection

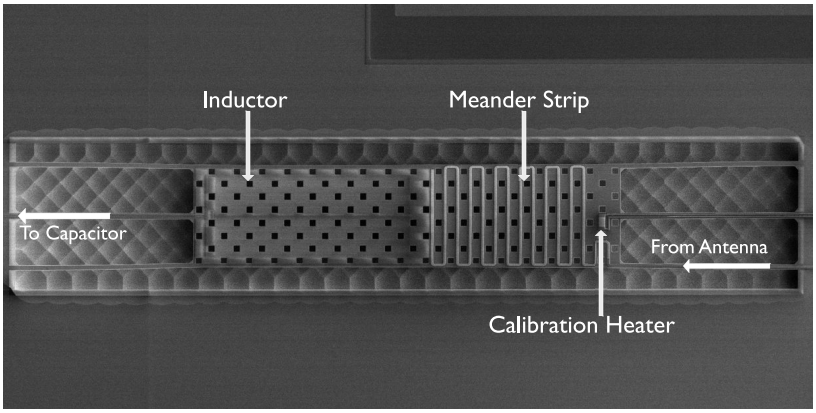

Figure 3.33: SEM micrograph of the TKID bolometer. The inductor and the microstrip lines that run off the island to the capacitor are visible on the left. To the right is the meander strip that terminates the microstrip line from the antenna as well as a Au heater for calibrating the bolometer response. The dense network of square holes on the island are for the XeF_2 release process that forms the island.

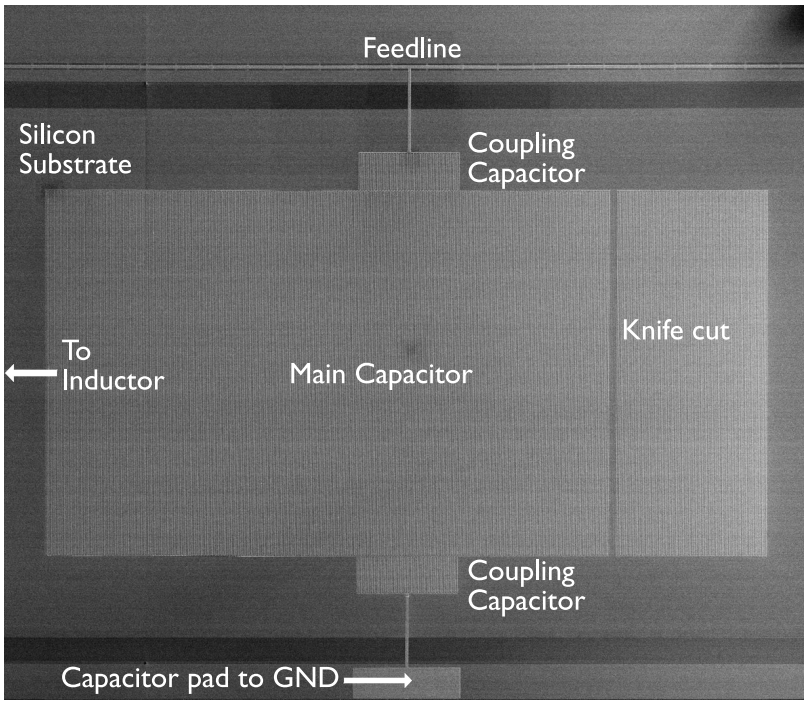

Figure 3.34: SEM micrograph of the TKID capacitors and feedline. The capacitors are deposited directly on the silicon substrate which is exposed in a large via through the dielectric stack of the wafer. The smaller capacitors on each side of the capacitor set the coupling of the resonator to the feedline seen at the top. The large niobium pad at the bottom of the image makes a parallel plate capacitor contact to the ground plane in place of a direct via.

loss at each of the air to dielectric interfaces. For normally incident rays, the reflectance at the air-dielectric interface is given by, $R = \left(\frac{n-1}{n+1}\right)^2 = 4\%$. Accounting for the 2 lenses, we expect the transmission to degrade by about 15%, averaged across the detectors' optical band . The implementation of the RF chain and the system level design requirements for fielding a TKID camera are given in Minutolo et al (L. Minutolo, Frez, et al., 2021).

The test chip was mounted in an aluminum holder installed on the focal plane. The optical window of the holder is 28.6 mm on each side. The chip was held down using copper clips and a quartz microscope slide of thickness .25 mm was glued to the backside of the chip exposed by the optical window as an anti-reflection coating for the air-silicon interface. On the front side of the chip, a 0.5mm gap between the chip and the chip cover provides a $\lambda/4$ backshort for the antenna.

Detector Yield

Of the 12 resonators on chip, we identified 6 resonators within our design band; with 2 dark devices and 4 light devices. 2 of the optically active resonators have calibration heaters wired up for biasing externally. We also identified 5 higher frequency resonators within the 700-850 MHz band. This frequency range matches the expected location of the self resonances of the main capacitor tank found using numerical simulations. These resonators are visible even above 4K, and we have identified them as niobium resonators which arise due to shorts between the capacitor fingers. In the time since the devices discussed here were fabricated, we have further improved our fabrication process to reduce the incidence of shorts between the capacitor fingers. In addition, we have also tested the use of a focused ion beam (FIB) to clear out small shorted capacitor sections to recover devices.

Resonator Properties

We characterize our resonators by measuring the forward transmission S_{21} as a function of the readout frequency for each of the resonators. S_{21} is then fit using a single pole Lorentzian model that accounts for kinetic inductance non-linearity and resonator asymmetry (Khalil et al., 2012; Swenson et al., 2013). In a dark cryostat configuration and starting from a 95 mK bath temperature, we measured the resonator quality factor as a function of the readout power in the range –110 dBm to –70 dBm. Above –80 dBm the kinetic inductance bifurcation parameter $a > 0.8$ marking the onset of the non-linearity. We also characterized our resonators under bath temperature sweeps at a –90 dBm single tone readout power level.

Using the bath temperature sweep data, we fit the frequency as a function of the bath temperature to a Mattis-Bardeen (MB) plus two-level system (TLS) model (Zmuidzinas, 2012). Figure 3.35 shows that the model describes the data well across the entire temperature range measured. As an additional step, we took the best fit parameters and used them to predict the resonator quality factors. Above 300 mK, which is the regime of interest, and where the Mattis-Bardeen dependence dominates, the best fit MB parameters predict the quality factor well. Below 250 mK, we see TLS-like behavior in Q_i. However, the loss tangent, $F\delta_0$ that is obtained from the frequency shift data is too small to match the measured Q_i. This indicates that there is an additional effect that modifies Q_i at lower temperature but that does not affect the frequency shift data. This is currently being investigated. The best fit parameters summarized in table 3.2 show that the resonator parameters are largely consistent from resonator to resonator.

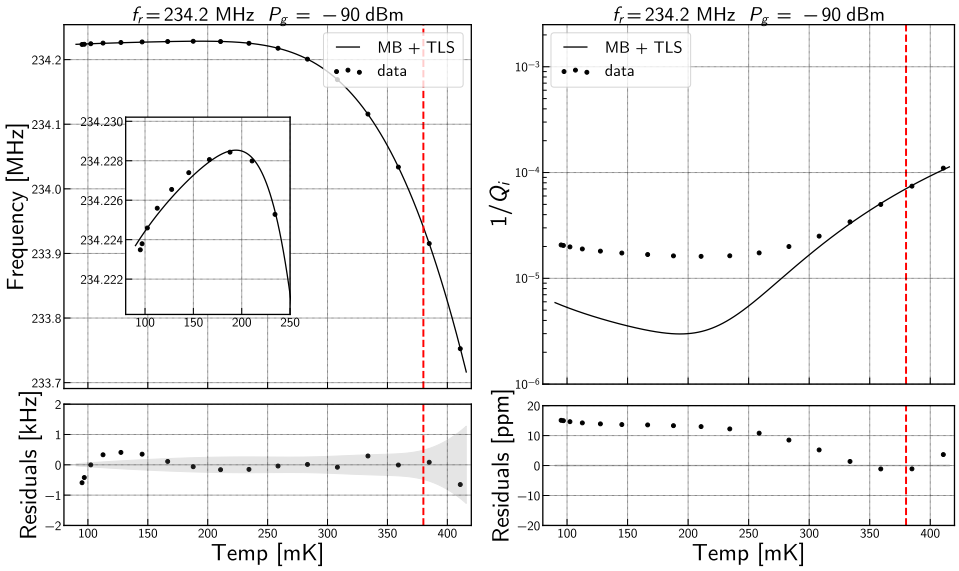

Figure 3.35: Fits to the frequency shift data (section 3.3) for the 234.2 MHz resonator under a MB + TLS model. The inset plot has a smaller x axis range to better show the agreement between the data and the fit. The lower plot gives the residuals to the fit. The shaded region is the 1 sigma error obtained from the covariance of the best fit. The best fit parameters are summarized in table 3.2. In section 3.3, the best fit parameters obtained from fitting the frequency shift data are used to predict the quality factor. Above 300 mK, where the MB dependence dominates, the agreement between the data (black dots) and prediction (solid line) is strong.

Optical Performance

The optical efficiency is the fraction of the total incident optical power that is absorbed by the detectors on the focal plane. Losses due to reflections in the

f_r [MHz]	α_k	T_c[K]	$F\delta_0$ $\left[\times 10^{-5}\right]$
234.2	0.52 ± 0.01	1.388 ± 0.004	9.5 ± 0.4
243.1	0.54 ± 0.01	1.396 ± 0.002	8.6 ± 0.4
258.5	0.53 ± 0.01	1.397 ± 0.005	9.1 ± 0.4
264.7	0.55 ± 0.01	1.396 ± 0.005	9.6 ± 0.3
268.8	0.53 ± 0.01	1.390 ± 0.007	9.9 ± 0.5
279.6	0.53 ± 0.01	1.390 ± 0.006	9.9 ± 0.4

Table 3.4: Best fit Mattis-Bardeen (MB) and two-level system (TLS) parameters of the 6 TKID bolometers measured at -90 dBm. The kinetic inductance fraction, α_k and the superconducting transition temperature T_c are the 2 MB parameters while the loss tangent constant $F\delta_0$ sets the TLS effect.

optical chain, antenna network and detectors contribute to the end-to-end optical efficiency. can measure the end-to-end optical efficiency of the optical system directly. We measured the resonator response in resonance frequency and quality factor to aperture filling blackbody sources at 77K and 300 K. The difference in the optical power ΔP from the temperature difference ΔT = (300K − 77K) needed in order to infer the efficiency can be directly measured by biasing the resonators under a 77K load using the calibration heaters until the resonator response matches the response seen at a 300K load as shown in figure 3.36. The end to end efficiency can be calculated given the measured band center ν_0 and bandwidth $\Delta\nu$ of the device using the relation

$$\Delta P \approx \eta \cdot k_B \cdot \Delta T \cdot \left(\frac{\Delta\nu}{\nu_0}\right) \cdot \nu_0. \tag{3.11}$$

The total camera efficiency is 29% on average as given in table 3.5. We measured a lower $\mathrm{d}P/\mathrm{d}T$ = 0.15 pW/K on average than is expected for our antenna design (0.17 pW/K). This difference can be accounted for by the 15% drop in transmission through the optics chain due to reflections off the uncoated optics. In addition, the microstrip lines of the antenna were fabricated using a liftoff recipe. In early antenna designs for BICEP2 and *Keck* (Ade, Aikin, Amiri, Barkats, Benton, Bischoff, Bock, Bonetti, et al., 2015), it was empirically observed that liftoff recipes contributed to loss in the microstrip lines, presumably by leaching organic materials from the resist. This degrades the antenna performance, and the optical efficiency in particular. Etched microstrip was not observed to have these deficiencies (ibid.). We have switched to an etchback recipe for microstrip lines in devices currently under fabrication. We are also currently working on making direct measurements of the detector efficiency

using an in-cryostat cold load.

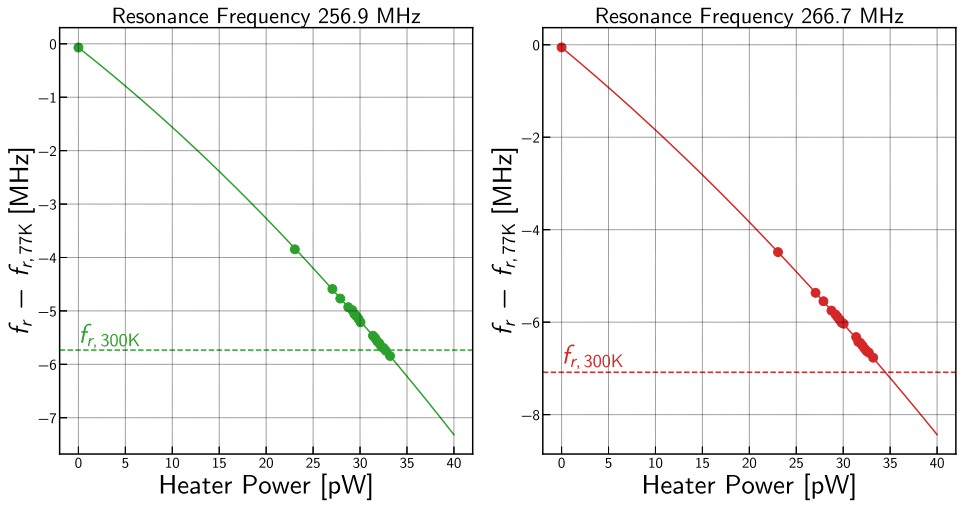

Figure 3.36: Heater calibrated measurements of the optical efficiency of the 258.5 MHz (left) and 268.8 MHz (right) resonators. The y-axis shows the shift in resonance frequency from the measured frequency under a 77 K optical load. The horizontal dashed line shows the position of the resonance under room temperature loading. The points are discrete measurements of the frequency shift with the heater biased. The solid line is a quadratic fit to the measured frequency versus heater power data that is used to predict ΔP.

f_r [MHz]	dP/dT [pW/K]	η	ν_0 [GHz]	$\Delta\nu/\nu_0$
258.5	0.15	0.28	150.4	0.26
268.8	0.15	0.30	148.5	0.29
234.2	-	0.26	148.1	0.28
243.1	-	0.35	146.8	0.29

Table 3.5: Measured optical parameters of the 4 antenna-coupled TKIDs. For the 258.5 MHz and the 268.8 MHz resonators, the optical efficiency was directly measured using the heaters on the bolometer island. For the 234.2 MHz and the 243.1 MHz resonator, the efficiency was computed from the measured spectra assuming that the devices had the same dP/dT as measured on average. The band center ν_0 and bandwidth ν_0 were obtained from the measured spectra of each of the resonators.

Spectra

Understanding the spectral response of the detectors is crucial in order to constrain potential sources of systematic effects. Such measurements are also required to facilitate component separation of the CMB polarized signal from the dust and synchrotron foreground components which have a different spectral signature (H.

Hui et al., 2016). The spectra are primarily determined by the band-defining filter between the antenna and bolometers, but also include roll-off of the antenna, transmission spectra of optics above the focal plane, and any fringing associated with pairs of impedance mismatched interfaces.

To measure the device bandpass, we used a Martin-Pupplet Fourier Transform Spectrometer (FTS) that was mounted on top of the cryostat. In a time reversed sense, the detector beam is split into two beams at the input polarizing beam splitter; with one beam terminating at a 77 K blackbody source made of liquid nitrogen soaked Eccosorb HR-10 and the second beam terminating on an Eccosorb HR-10 blackbody at room temperature. The interference pattern generated as the position of the movable mirror is changed and the interferogram encodes the spectral response of the detectors. The FTS is on a movable x-y stage and is adjusted to find the point of maximum illumination of the detectors. We orient the FTS at a 45° angle to the polarization axes so detectors measuring both polarizations can be simultaneously illuminated. The test chip centered on the focal plane is small enough to illuminate all the detectors at without changing the FTS position on the x-y stage.

All the interferograms are filtered using a moving average filter and aligned at the point of zero path difference before being stacked and averaged. The real part of the Fourier Transform of the averaged interferogram then gives the spectral response of the detector. Figure 3.37 shows the averaged interferogram and resulting spectrum for the 234.2 MHz resonator. The band center and bandwidth of the detectors are then estimated from the spectra $S(\nu)$ using the relations

$$\nu_0 = \int \nu S(\nu) \mathrm{d}\nu, \tag{3.12}$$

$$\Delta\nu = \frac{\left(\int S(\nu)\mathrm{d}\nu\right)^2}{\int S^2(\nu)\mathrm{d}\nu}. \tag{3.13}$$

Table 3.5 shows the measured band center and bandwidth for all 4 resonators. Averaged over the 4 detectors, the band center is 148.5 ± 1.3 GHz and the fractional bandwidth is 28% ± 1%. As designed, the resonator band avoids the atmospheric oxygen line at 118 GHz and the water line at 183 GHz (K. S. Karkare et al., 2014). There are fringes present in the band with an average standing wave ratio (SWR) of 1.26 ± 0.06 averaged over all the detectors and the 140-160 GHz range. Using this SWR with a Fabry Perot reflection model predicts a reflectance $R = 0.058 \pm 0.025$,

consistent with the expected 4% reflectance from each of the lens surfaces. With new optics coated for the 150 GHz band, we therefore anticipate that the spectra will improve.

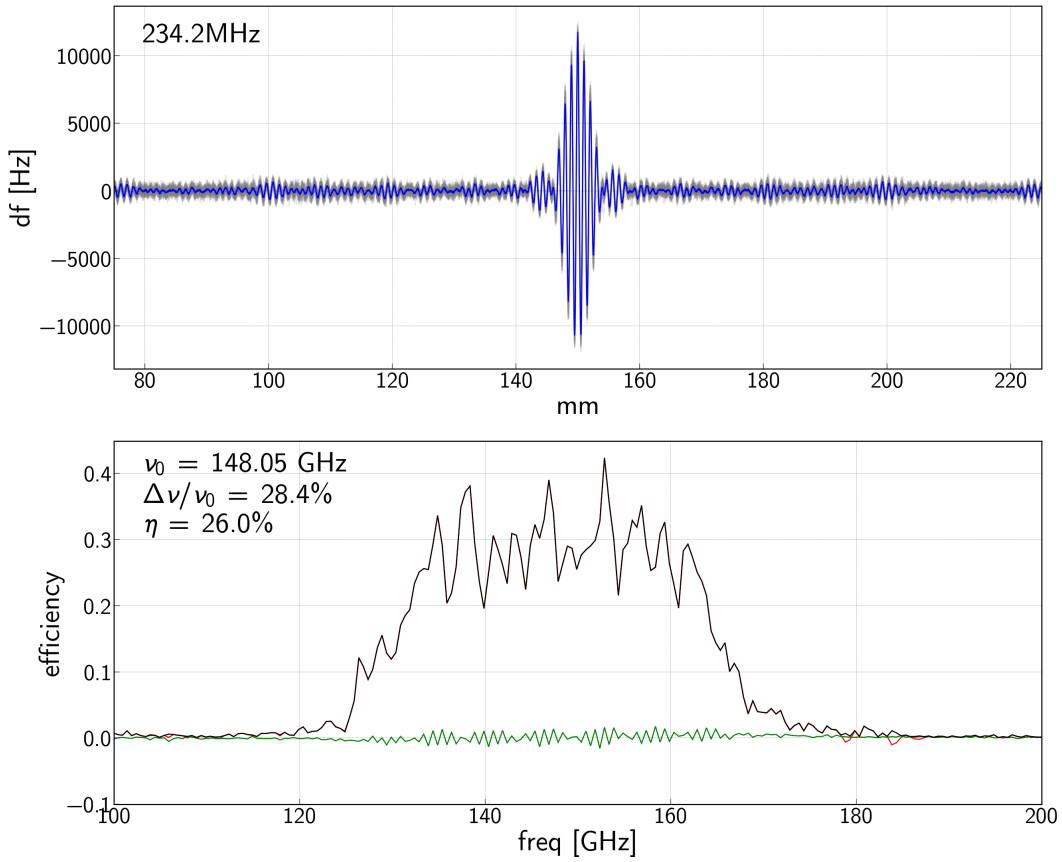

Figure 3.37: The averaged interferogram (top) and spectrum of the 234.2 MHz resonator (bottom). The blue interferogram is the averaged detector response with the individual interferograms in grey. In the lower plot, the magnitude of the spectrum is shown black with the real part in red and the imaginary part in green.

Dark Noise Measurements

Our best detector noise measurements to date were taken on the 2x3 optical chips in a dark configuration. Lorenzo Minutolo developed a battery operated fully analog 'battery box' that provided a stable supply to the cryogenic low noise amplifiers, as well as generate the heater bias and calibration signals for the bolometers. With the battery box, the cryostat can maintain the fridge cycle while disconnected from the noisy housekeeping rack. The design of the battery box is detailed in L. Minutolo, 2024. The battery box has excellent stability and low noise as shown in fig. 3.38 ideal for making noise measurements.

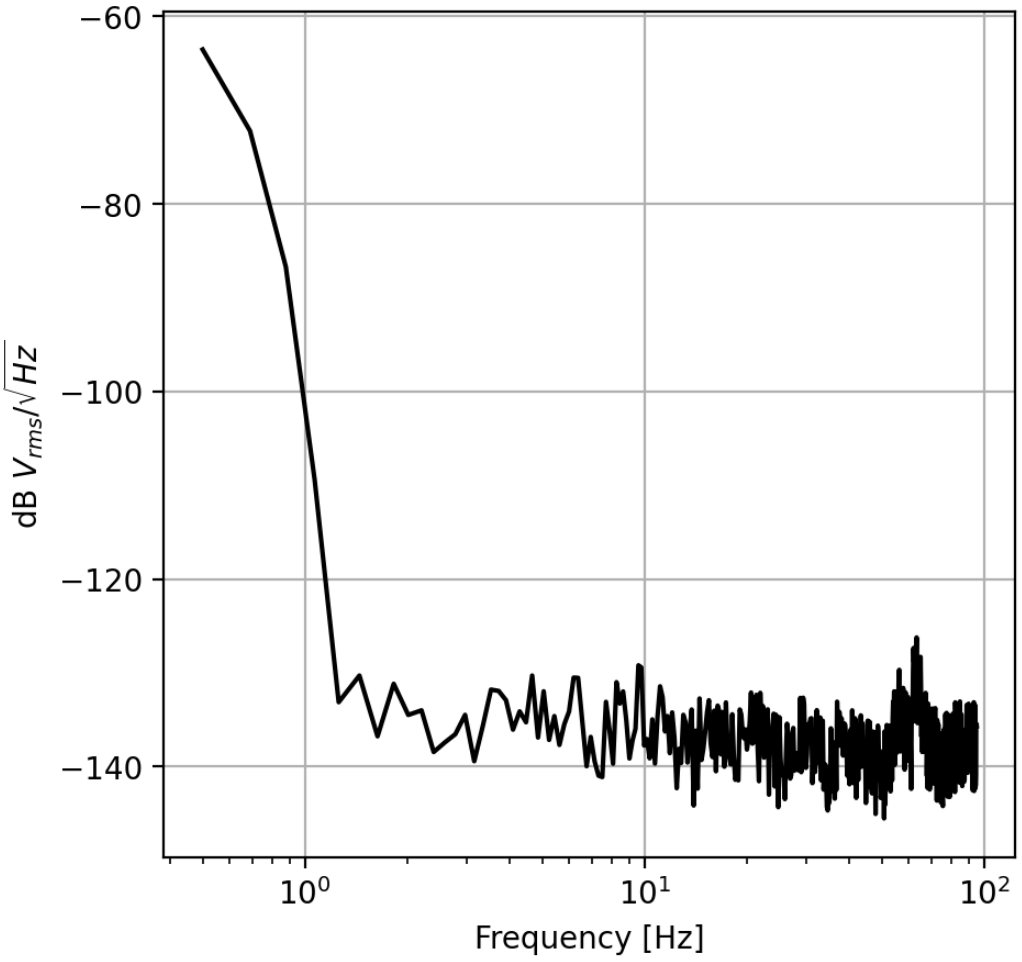

Figure 3.38: Voltage noise spectrum of the calibration battery box in static signal output mode. The data has been acquired using a HP 3563A signal analyzer. The noise is given in decibels referred to a 1Vrms. A single calibration heater has a resistance of about 0.1 Ω and is biased through a 100 $k\Omega$ resistor. At a -140 dB Vrms/$\sqrt{\text{Hz}}$, this corresponds to $\sim$ 1.4aW/$\sqrt{\text{Hz}}$, significantly lower than expected detector noise.

We acquired data at a number of heater bias powers and readout powers. For this analysis, we focused on 2 biased resonators at 258.2 and 268.5 MHz at the 350 mK bath temperature and with no loading. We additionally measured the dark noise for a 3rd unbiased resonator and included 2 guard tones for phase noise subtraction. For calibration, each noise data set was 30s long and was taken at every gain step of our readout system. The noise data sets were longer 300s data acquisitions at a sampling rate of $10^5 s^{-1}$.

Heater Bias [pW]	Square wave amplitude [fW]
5.966	2.366
7.212	2.860
7.567	3.001
8.773	3.479
9.770	3.875
10.205	4.047
11.189	4.438

Table 3.6: Heater bias powers and calibration amplitudes for the noise analysis.

The calibration dataset at a fixed heater bias applied a 1 Hz square wave signal to the heaters. The responsivity S was estimated by fitting the mean-subtracted frequency timestream to a 2 parameter model of a rounded square wave

$$S \;=\; \delta P \cdot S \tanh\left(s \cos(2\pi f t + \phi)\right), \tag{3.14}$$

where ϕ is a phase offset, δP is the amplitude of the square wave as given in table 3.6, the frequency f was fixed to 1 Hz and $s = 20$ is a smoothing parameter applied to the square wave. The results of the fit as applied to a single dataset are given in fig. 3.39. The first second of data was discarded before the responsivity was fitted.

The extracted responsivities were used to calibrate the noise data. The frequency timestreams are generated as discussed in section 2.10. To account for slow drifts in the noise data, we generated timestreams decimated to 100 Hz sampling frequency. The first 10 seconds of data show stronger transient behavior and were clipped from the analysis. These timestreams were fitted to a linear fit and the fit parameters were used to subtract the mean and drift from the full noise datasets as detailed in fig. 3.41. Each drift corrected frequency timestream was then scaled by its responsivity. The two resulting timestreams were then combined into pair sum and pair difference timestreams before computing the noise spectra.

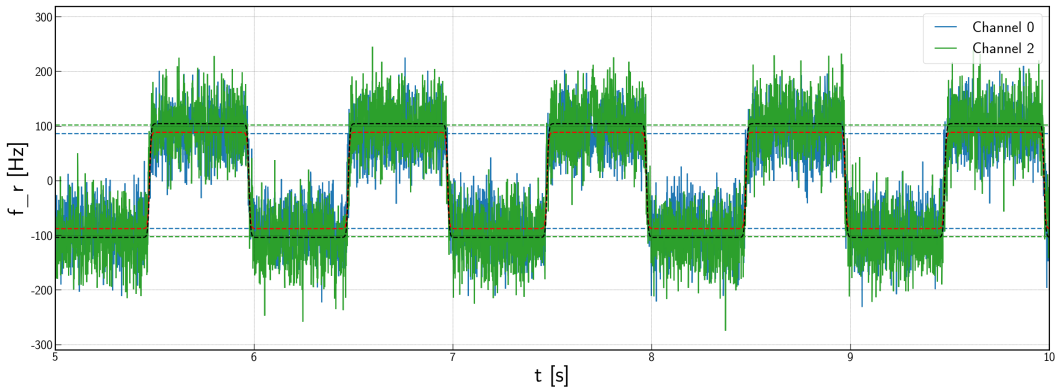

Figure 3.39: Calibration timestreams of a two biased resonators at 5.966 pW heater loading. The timestreams are mean subtracted and fit to extract the responsivity. The dashed red and black lines are the best fits to the 258.2 MHz and the 268.5 MHz resonators, respectively. A first estimate of the responsivity can also be estimated from the difference in the mean positive and negative levels as denoted by the dashed blue and green lines. This estimate is sensitive to the noise level especially at lower amplitudes.

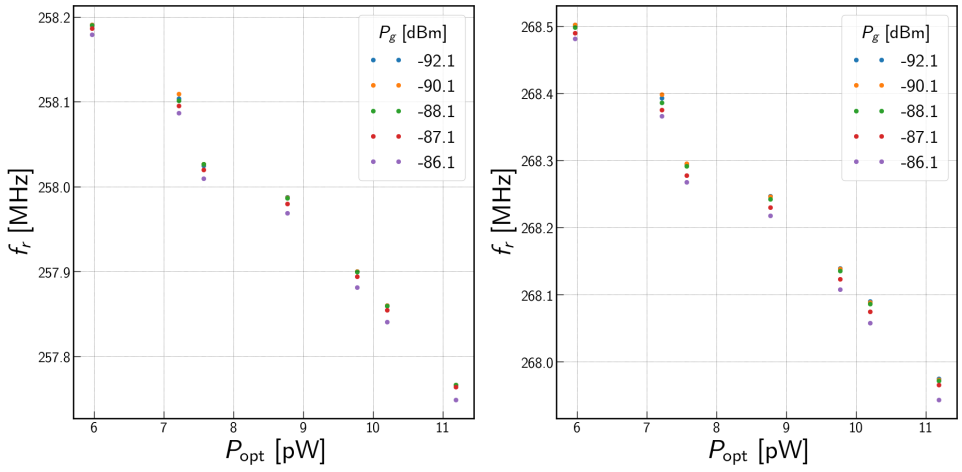

(a) (b)

Figure 3.40: Resonance frequency for 258.2 MHz (left) and the 268.5 MHz (right) resonators as a function of the heater bias and the readout power.

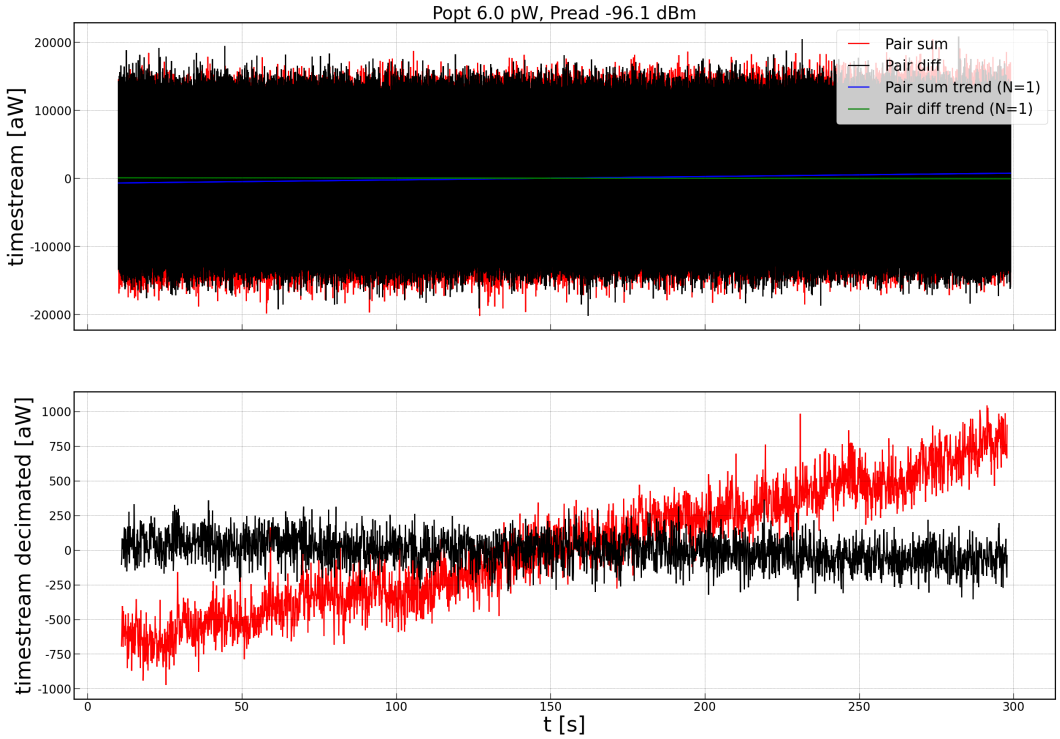

Figure 3.41: Calibrated timestreams for the 258.2 MHz and 268.5 MHz resonators. Above: Pair sum and pair differenced timestreams constructed by applying the responsivity gain to the raw frequency timestreams. The mean level and drift are estimated from the decimated timestreams (below).

We generate the noise spectra using scipy.welch [7] with a Hann window and 2^{23} points per segment. The NEPs are scaled by $\sqrt{2}$ to account for the quadrature noise of 2 detectors. The noise has been logarithmically binned for visual clarity. As shown in figs. 3.42 and 3.43, pair differencing is a robust strategy for rejecting common mode noise. The expected photon noise on sky is about 45 aW/$\sqrt{\text{Hz}}$ for about 5 pW of loading. TKIDs show excellent noise stability across our entire science band down to 0.1 Hz.

[7] `https://docs.scipy.org/doc/scipy/reference/generated/scipy.signal.welch.html`

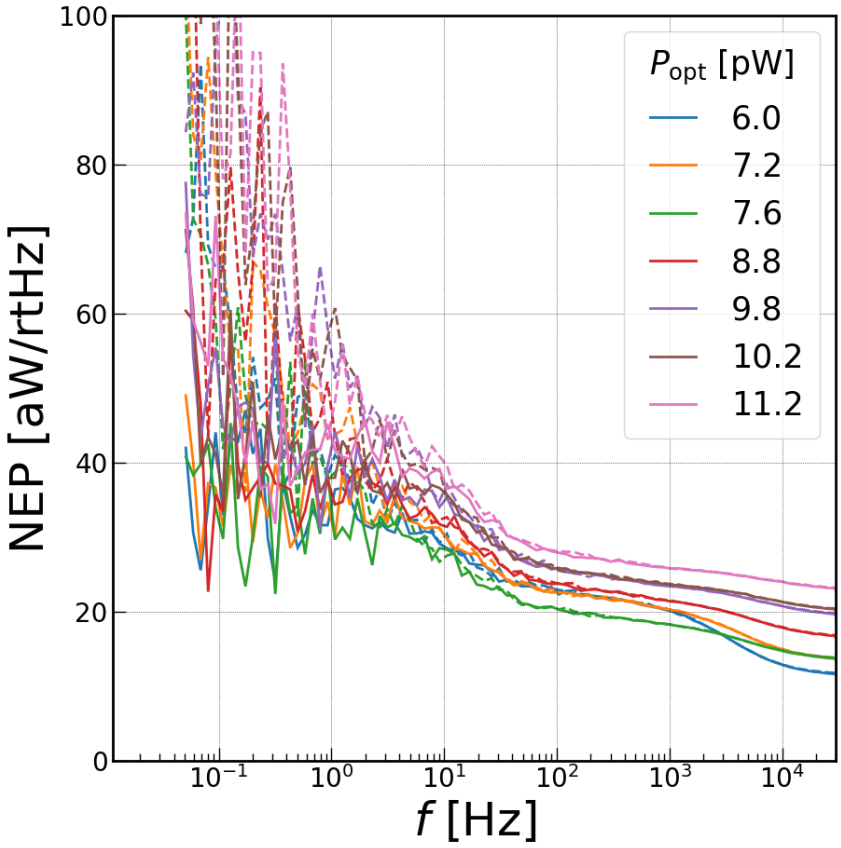

Figure 3.42: Measured TKID NEP in pair sum (dashed) and pair difference (solid) lines as a function of frequency measured with -96 dBm of readout power. The bolometer thermal roll off is visible at a few 10s of Hz. At much higher frequencies, the generation recombination rolloff is visible especially at the lowest heater bias levels.

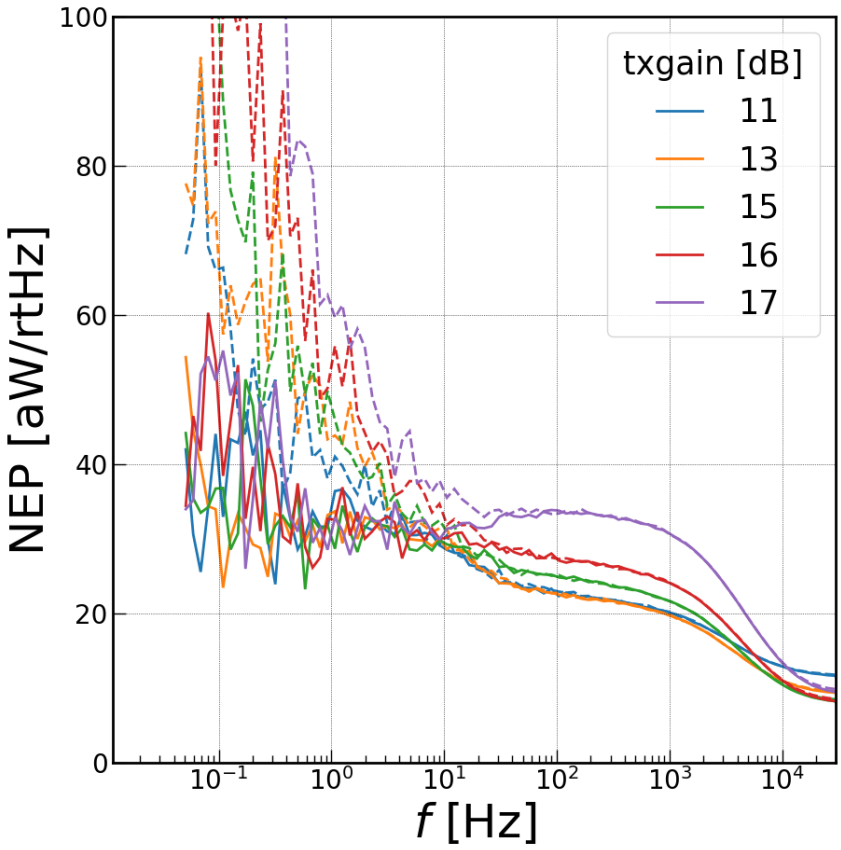

Figure 3.43: Measured TKID NEP in pair sum (dashed) and pair difference (solid) lines as a function of frequency. The noise data was acquired at 5.966 pW and the variation with readout power gain is shown here. The noise spectra show two rolloffs as expected: a thermal and a quasiparticle response. The measured phonon noise level seen below 10 Hz is stable against readout power variation. The generation recombination rolloff set by the quasiparticle lifetime is very evident at above 1000 Hz. A TX gain of 11 dB corresponds to -96 dBm on chip in our readout system.

Chapter 4

THE TKID DEMONSTRATION RECEIVER

The TKID demo camera receiver adapts a pre-existing *Keck* 150 GHz receiver for compatibility with a TKID focal plane. The goal of this experiment is to demonstrate maturity of TKIDs at NASA's technology readiness level 6: deployment in a representative ground environment. TKIDs are an attractive detector across the electromagnetic spectrum and even in particle physics.

Within the context of CMB, our goal is to target degree scale polarization. To mitigate systematics, the telescope is a small aperture refractor, with cold optics. The entire telescope can rotate along its boresight, both to reconstruct Q and U from polarized maps of the sky and to mitigate ground synchronous polarized signals. The TKID Demo Camera targets deployment at the South Pole in the BICEP Array mount, co-observing the sky with the already deployed TES receivers: BA1 (at 30/40 GHz), BA2 (at 150 GHz) and BA4 (to be deployed to observe at 220/270 GHz). Each receiver is independent but observes the same patch of sky. All the receivers will be located on a single mount and rotated together.

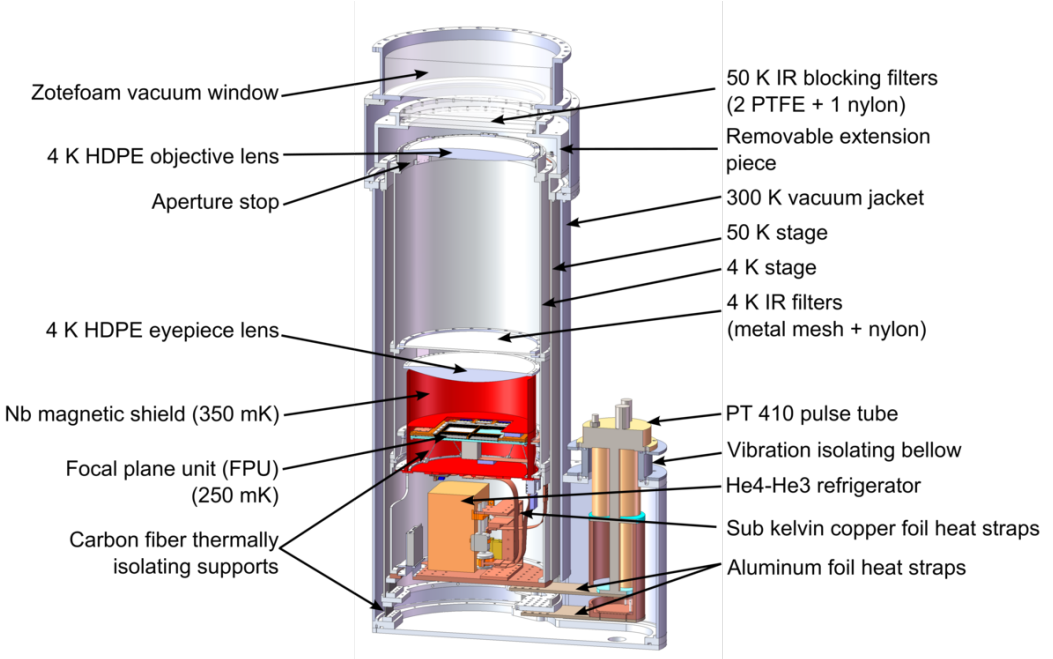

Figure 4.1: A breakdown of a single Keck receiver.

This chapter focuses on the design of the TKID receiver. Special emphasis will be on the modifications to the receiver for compatibility with the RF architecture used for TKID readout. This chapter will also detail the readout platform that was targeted for deployment, SMURF.

The two key advantages of our small-aperture telescope design are:

- **Low Internal Loading**: The photon noise loading the detectors as derived in eq. (A.1) has a significant contribution from the instrument (eq. (A.4)). In our telescope design, all the optics are cooled down to 4K, lowering the contribution to the loading due to the emissivity of the optical system.
- **Axial Symmetry**: The on-axis design of the receiver, allows for rotations around the optical axis. These are typically referred to as 'Deck' rotations. This symmetry also allows the side lobes of the main beam to be intercepted by black absorptive forebaffles.

Optical Design

Window

The cryostat window is constructed from Zotefoam PPA30. Stycast 2850 epoxy is used to attach the foam to the Aluminum vacuum jacket. The surface of the Zotefoam is roughened to promote adhesion to the vacuum jacket. The Zotefoam window is strong enough to withstand pressure under vacuum although must be carefully monitored over long time scales ($\sim$ 2-3 years) for tears in the foam that can lead to catastrophic cryostat failures.

The inside of the vacuum jacket is lined with Multi-Layer Insulation (MLI) to reduce radiative loading of the inner cryostat shells by the warmer 300K vacuum jacket.

50K Insert

The 50K insert is rather simple. The only optical components at 50K are 2 PTFE IR filters and a single Nylon filter. In order from upper to lower, the PTFE filters are 1.35" and 0.5" thick while the Nylon filter is 3mm thick. These materials are transparent at millimeter waves while very absorptive in the Far Infrared. They reduce the total loading on the 4K stage since the Pulse Tube cryocooler only has a limited cooling capacity at 4K.

The filters are secured onto Aluminum rings that are then mounted onto the 50K filter holder. The filters are therefore only cooled through thermal contact along their edges. We expect that the center of the filter is slightly warmer than 50K due to the poor conductivity of Teflon and Nylon. Here however, the low emissivity of PFTE ($\sim$ 2 %) comes to the rescue. We estimate that the total loading in band due to the filter stack is less than 1 pW.

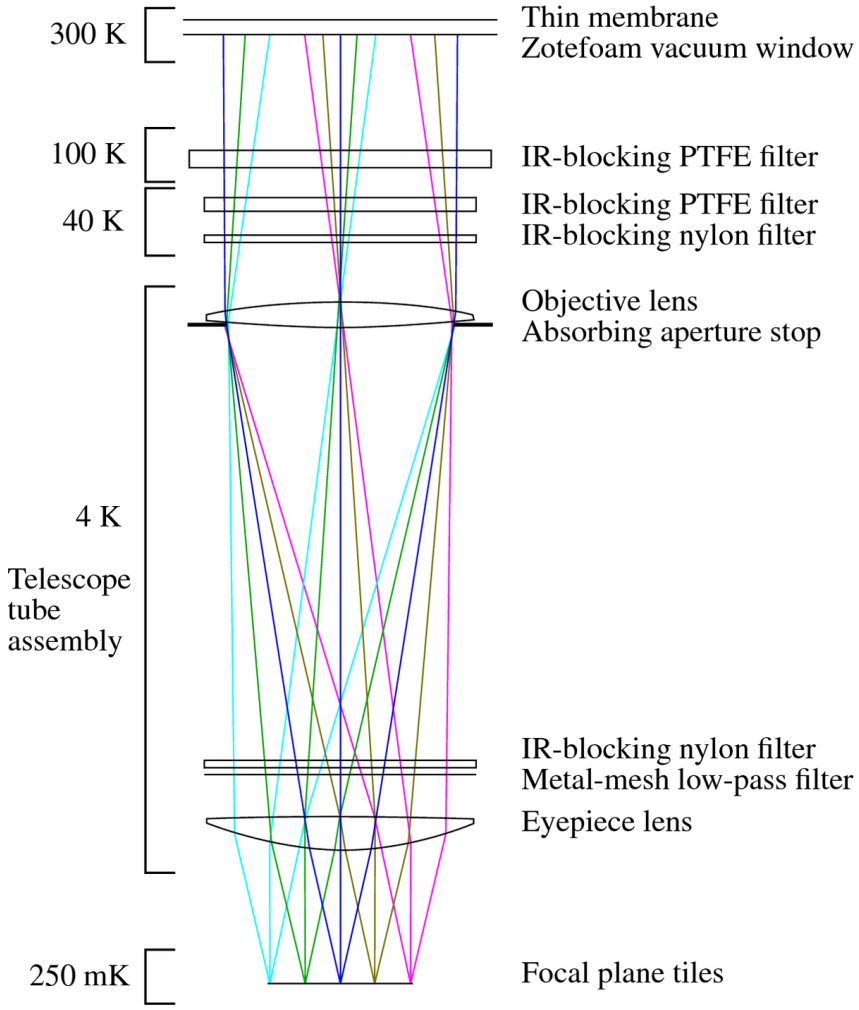

Figure 4.2: Cryostat optics chain

4K Insert

The 2 refractive lenses and an additional set of IR blockers are heat sunk onto the 4K insert. These lenses are each about 30 cm in diameter and are made from anti-reflection coated High Density PolyEthylene (HDPE). An aperture stop intercepts the main beam near the first null of the Airy disk. The aperture stop is made from

a ring of tapered Eccosorb AN73 located directly behind the objective lens. The diameter of the aperture $D = 26$ cm.

The focal ratio f/# of the receiver was chosen to match the 2Fλ criterion. That is, for observations at the wavelength λ, given the pixel spacing Δx, the incoming focal ratio $F = f/D$ for f the focal length of the telescope, the relation

$$2F\lambda = \Delta x \tag{4.1}$$

holds. For $2f\lambda$ pixel spacing, most of the beam couples to the telescope with a spillover fraction of about 13%. The receiver has a focal length of 587mm, giving a focal ratio f/2.2. For $\lambda = 2$mm at 150 GHz, the criterion is satisfied with a pixel spacing of 8.8mm. As we will detail later, the actual pixel spacing on the focal plane is 8.7mm. The final Nylon IR filter and a 8.5 icm low-pass metal mesh filter are located between the objective and eyepiece lenses.

The 4K optics are contained within 2 optics tubes made of Al 6061. The upper tube holds the objective lens and the aperture stop. The lower tube holds the eyepiece lens and the IR filters. The separation between the eyepiece lens and the detectors is 151mm when cold. Copper bars span the outside of the 4K tube to reduce the thermal gradient between the top and bottom of the 4K insert and minimize the subsequent loading on the IC stage of the telescope. The inside of the 4K tube is also line with absorptive Eccosorb HR10 coated with a mixture of Stycast 2850 and carbon lampblack. The specific recipe known as Bock black. The absorptive walls of the 4K tube terminate any stray light rays onto a cold 4K surface minimizing loading on the detectors. HR 10 coated Baffle rings are also mounted on the inside of the 4K tube to minimize low incident angle scattering from the smooth walls of the inside of the 4K tube.

Mechanical Support Structures

The internal stages of the cryostat are both thermally separated and mechanically supported using a series of trusses. These trusses must be strong enough to support the weight of all components of the telescope even when the telescope is in motion or rotated fully upside down during telescope assembly or disassembly.

The 50K shell is isolated from the 300K shell using Carbon fiber trusses at the bottom of the cryostat and titanium boomerang-shaped supports at the top of the cryostat. 20 layers of multi-layer insulation (MLI) are installed between the 300K

and 50K shells and held in place using Kevlar string. The reflective layers in the MLI are thermally isolated from each other and reduce the radiative loading on the 50K stage due to the 300K shell.

Similar carbon trusses and titanium supports are used to isolate the 4K shell from the 50K shell. The 4K insert holds much of the internal thermometry of the cryostat as well as the readout electronics. Specifically for TKIDs, the 4 Low Noise Amplifiers (LNAs) needed to readout each of the 4 tiles on the focal plane are housed in an aluminum box mounted onto the 4K base plate.

The sub-K stage is supported on a set of carbon trusses above the 4K fridge volume. The truss structure contains progressively lower temperature stages: 2K, 1K and a final 250 mK stage that holds the focal plane.

Cryogenic Design

Pulse Tube Cryocooler

The receiver is cooled to 4K using a pulse tube cryocooler. Similar to the other *Keck* telescopes, we use a PT-410 cryocooler from CryoMech[1]. The pulsetube system is aligned with the optical axis of the telescope. The PT-410 supplies roughly 1W of cooling power at the first (4K) stage stage and 50W of cooling power at the second (50K) stage. The frequency of the pulse tube is nominally set to 1.2 Hz but can be tuned to optimize performance.

Heatstraps made of high purity aluminum and copper foil electrically welded onto copper blocks connect the head of the 50K/4K stage to the base of the 50K/4K plate. The heatstraps are made of thin foil to mitigate the transmission of vibrations from the pulsetube head to the rest of the cryostat. Microphonic noise can couple into bolometers causing additional noise.

Sub-K stages

A 3 stage (He^4 – He^3 – He^3) sorption fridge is attached to the base of the 4K stage. This fridge provides all the cooling power necessary to reach the operating temperature of the TKID focal plane. The sorption fridge was designed and provided by Duband.

The sorption fridge consists of pressurized chambers holding He^4, He^3 gas connected to active charcoal sorption pumps. Heating the sorption pumps drives gas out of

[1]Now part of BlueFors. `https://bluefors.com/products/cryomech-products/`

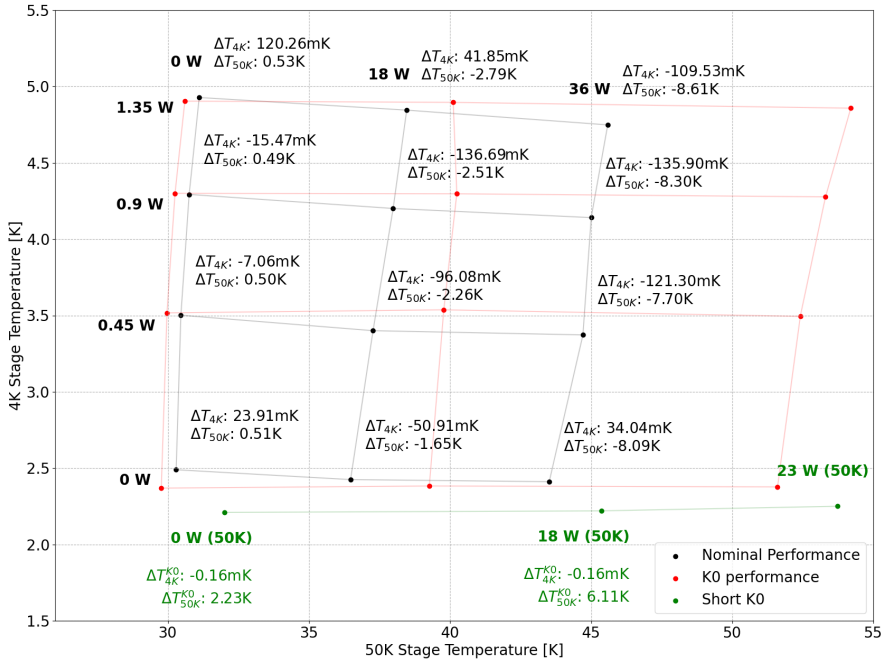

Figure 4.3: Measured Load curves of the PT-410 receiver.

the pumps raising the gas pressure. When the gas reaches thermal equilibrium at the higher pressure, it is then possible to condense liquid Helium in the evaporation chambers of the fridge. Once a sufficient amount of liquid is collected, the pumps are then cooled. The cooling of the pumps lowers the gas pressure causing the liquified He to evaporate. The latent heat of vaporization of the He provides the cooling power of the fridge.

The first stage of the fridge contains only He^4 gas. The fridge bracket thermally sunk to the 4K stage of the cryostat sets the condensation point. Typically, the fridge bracket sits between 3-4K. The evaporator of the first stage provides the condensation point for the second He^3 stage. This is usually referred to as the Inter-Cooler (IC) stage. The IC evaporator can reach down to 350mK during the fridge cycle and provides the condensation set point for the final Ultra-Cooler (UC) stage which can achieve much lower pressures of He^3 allowing it to reach down to 250 mK. Closed system cryocoolers have limited enthalpy and therefore the thermal load on the cooler must be carefully controlled. Additionally, the fridge must be thermal cycled in order to achieve operating temperatures. In lab settings, we perform 3 successive fridge cycles to maximize the hold times of our fridge. The fridge cycle

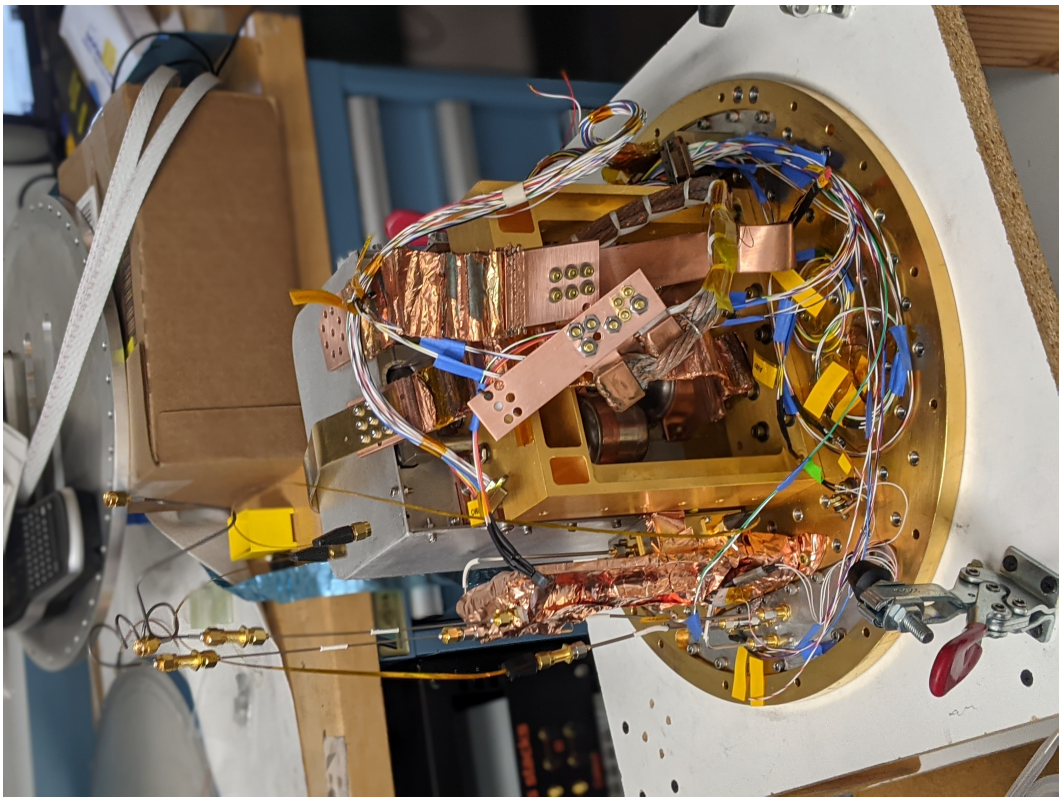

Figure 4.4: The TKID receiver fridge attached to the 4K baseplate with all the thermometry and heatstraps attached.

takes about 8 hours in total and can be run remotely overnight. The hold time is dependent on the thermal load on the cryostat, and we have achieved a maximum hold time of about 2.5 days when the focal plane is unloaded.

All the thermal straps used to connect the UC and IC stages of the sub-K insert to the fridge are made of high thermal conductivity oxygen free (OFHC) copper foil e-beam welded to solid copper blocks. The welded blocks allow for mounting of the heat straps using a set of predetermined washers and screws. The thermal conductivity of the joints is limited by the thermal resistance of the contact between the 2 metal surfaces. In closeup procedure, all mating thermal surfaces are cleaned using isopropanol and scotchbrite. Aluminum screws are used to ensure that the preload during initial mounting is maintained through the thermal contraction of the joint at base temperatures. Kevlar string is used to restrain the positions of the thermal straps to prevent thermal shorts during close up and operation.

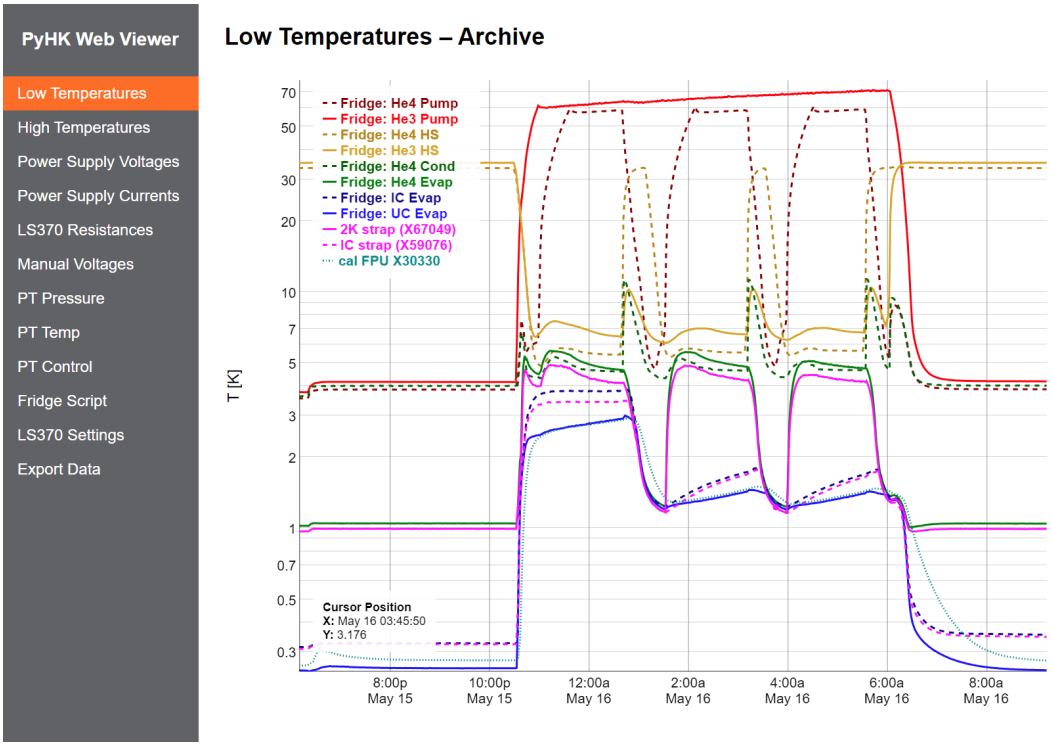

Figure 4.5: An example of a fridge cycle taken in short K0.

HouseKeeping and Thermometry

Lakeshore[2] Diode and Cernox thermometers are used to monitor the cryostat temperatures at key locations on the Focal Plane Unit (FPU), fridge and 4K stages. Reliable and accurate thermometry is necessary for cycling the fridge during receiver operation.

In the TKID receiver, we do not maintain the Neutron Transmutation-Doped (NTD) thermometers for low noise measurements of the tile and focal plane that are present in existing FPU units. For the demonstration camera, the requirements on focal plane temperature stability are much less stringent. In future iterations, we plan to instead use a Two-Level System (TLS) thermometer for monitoring the temperature on each tile. The advantage of this approach is that the thermometer will be integrated into the fabrication of the tile and will not require any additional hybridization and integration. Additionally, the frequency of the TLS thermometer can be set to be within or close to the resonator readout band, allowing the temperature of each tile to be monitored through the same system as the resonator readout without any additional wiring or electronics.

[2] `https://www.lakeshore.com/home`

We also maintain heaters in the cryostat for temperature regulation, fridge cycling and diagnosing cryogenic issues. In the initial cooldowns, we maintained heaters on the 50K and 4K heatstraps to measure the pulse tube performance (see fig. 4.3). Fridge operation also requires heaters specifically for controlling the He^4 and He^3 pumps and heat switches. We use two HP 3632A bench-top power supplies which provide enough channels and bandwidth to run all the heaters.

RF System

The RF system represents the biggest modification to the *Keck* receiver. Our RF system was first tested end-to-end in a modified *Keck* cryostat called short K0 that was used for both optical and dark characterization of TKID devices. The full *Keck* cryostat requires about 3 person-days of work in order to completely open up, make changes and close back up before cooling down. The short K0 cryostat remedies this, reducing the turn-around time to about 6 person-hours.

Short K0

Short K0 entirely modifies the 300K and 50K shells so that the focal plane can be accessed entirely from the top without needing to rotate the cryostat to extract the shells. The 4K optics tube was completely eliminated and we transferred the set of optics onto new adapter pieces. The 4K fridge volume space was also enlarged slightly in short K0. We worked with Precision Cryogenics[3] for the fabrication to meet the tight tolerances and surface finish needed on all the vacuum interfaces. The shells were made from aluminum 6061 since aluminum 1100 was difficult to procure. We commissioned the new testbed complete with a set of thermal and bandpass filters at 50K and 4K and with new thermal straps for the 2K and 1K stages. Our first successful cooldown in the short K0 configuration was in March 2023. All the subsequent optical and dark testing work has been performed in this new testbed.

RF Chain

The readout system is optimized for continuous fixed tone comb readout and is designed to be readily transferable from short K0 into any other *Keck* receiver. Our science tile design band is 450- 900 MHz. A signal generated from the readout system is filtered and attenuated by 30 dB before entering the cryostat.

[3] `https://precisioncryo.com/`

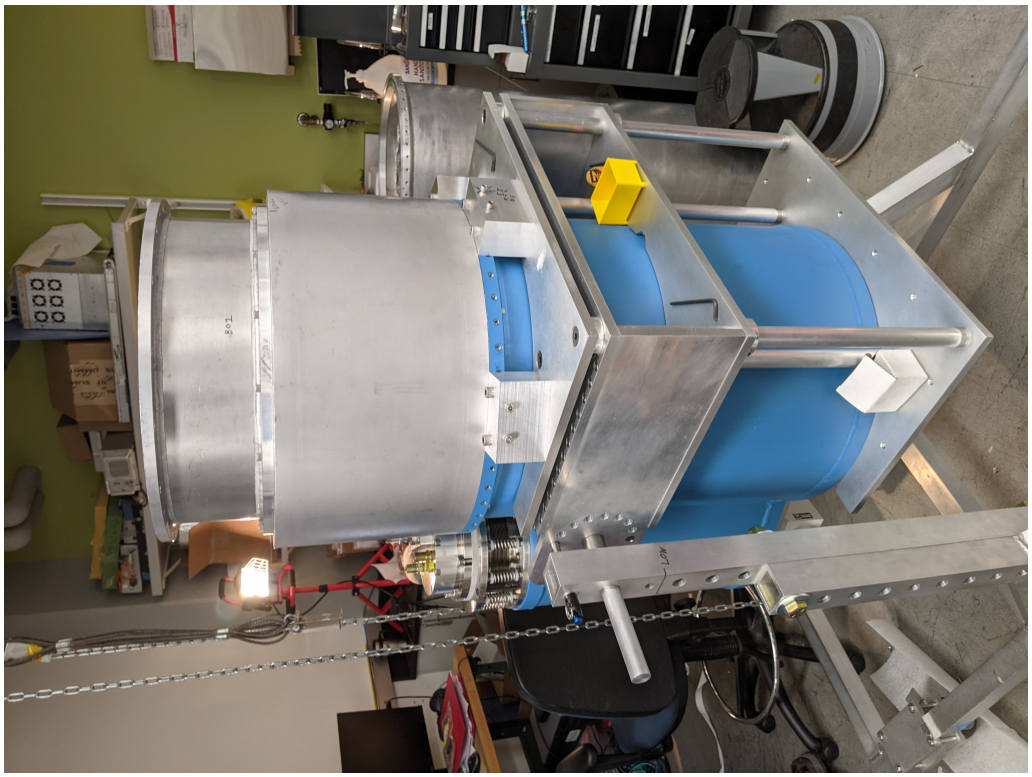

Figure 4.6: First full assembly of the short K0 cryostat.

The 300K vacuum interface was modified to accommodate a new RF front plate (fig. 4.7) that has 8 SMA connectors. The SMA connectors are connected to an 8-channel bundled Cri/oFlex flexible RF cables through copper coax cables internal to the 300K vacuum space. The Cri/oFlex cables are made by Delft circuits [4] and consist of 8 silver stripline channels enclosed in a polyimide (Kapton) as the dielectric and sandwiched by 2 conducting ground planes. The end of the Cri/oFlex cable is mechanically anchored at 300K using an aluminum bracket. The cable runs from 300K to 4K and is thermalized at 50K. The narrow form factor of the Cri/oFlex line was crucial because of the minimal clearance between adjacent thermal stages in the compact cryostat. This is in contrast to many cryogenic RF coax cables which often degrade in performance once they are bent into shape.

At the 4K stage, an additional 20 dB of attenuation per line is installed on the inputs to the amplifiers. The Cri/oFlex cable does not degrade the thermal performance of the 50K and 4K stages. This is in line with calculations performed using the online thermal load calculator provided by Delft circuits. For the cold amplification, we

[4] https://delft-circuits.com/cri-oflex-technology/core-technology/

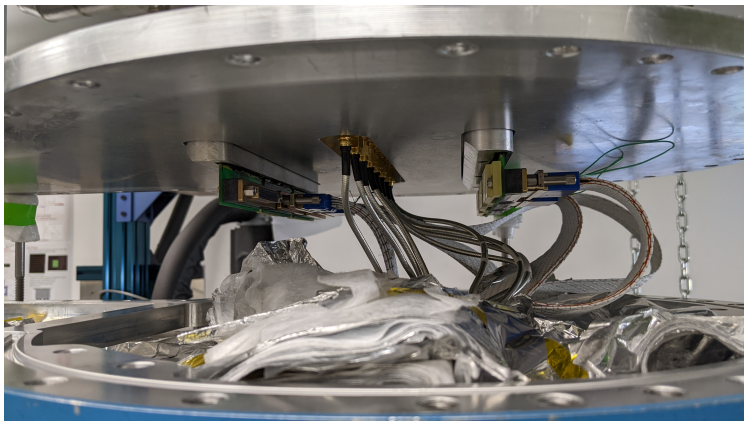

Figure 4.7: Modified 300K vacuum base plate in short K0 included a new RF front-plate that accommodates 8 SMA connectors.

use a set of 4 CIT-LF2 [5] Low Noise Amplifiers (LNAs) made by Cosmic Microwave Technology. These amplifiers have high gain across our entire readout band with a sufficiently low noise temperature previously measured to be about 5.2K in our ADR cyrostat. The amplifiers are housed within an aluminum box shown in fig. 4.8 that is mounted directly onto the 4K base plate next to the sorption fridge. The power dissipation of the 4 amplifiers raises the 4K stage temperature. This translates to a 20 mK increase in the UC stage temperature during dark measurements.

A second set of Cri/oFlex cables complete the RF path between 4K and the UC stage with an intermediate thermalization step at the 1K stage. The final set of 20dB attenuators are mounted directly to the SMA terminations of the Cri/oFlex lines and isothermal copper coaxial cables make the final connection between the focal plane unit and the flex cable. The attenuators are only placed on the transmit side of the RF chain. Figure 4.10 shows the TKID focal plane with the final RF cables installed. Figure 4.11 shows the final configuration of the focal plane with the RF shield enclosing all the cables.

[5] https://www.cosmicmicrowavetechnology.com/citlf2

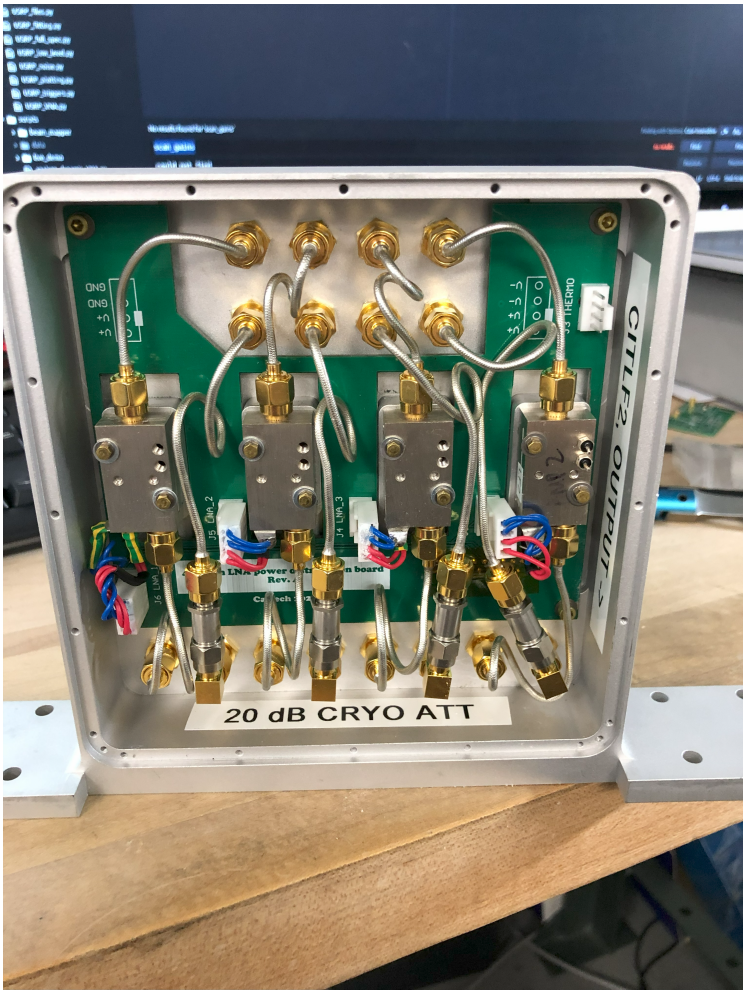

Figure 4.8: The amplifier box with all 4 CIT-LF2 low noise amplifiers and the power distribution board before installation onto the 4K base plate.

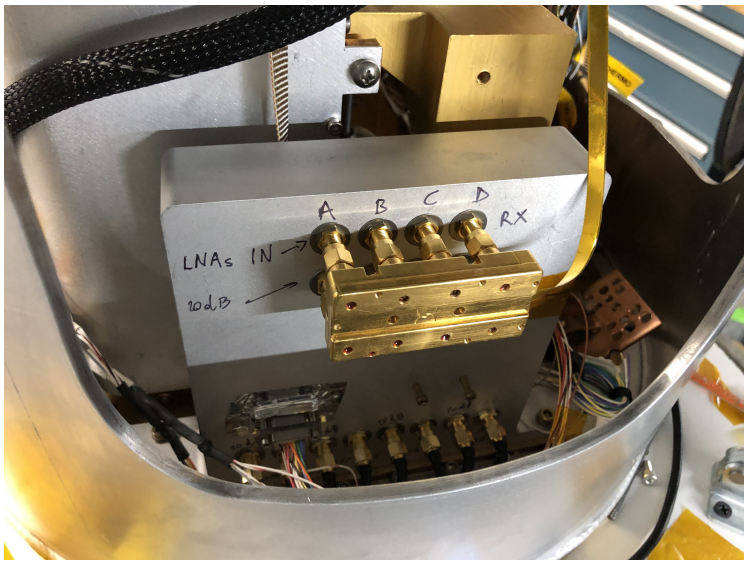

Figure 4.9: The amplifier box installed in the 4K fridge volume. The flex cable in view connects to the UC stage of the cryostat. The copper coax cables terminated at the base of the amplifier box connect the amplifiers to the first Cri/oFlex cable running between 300K and 4K.

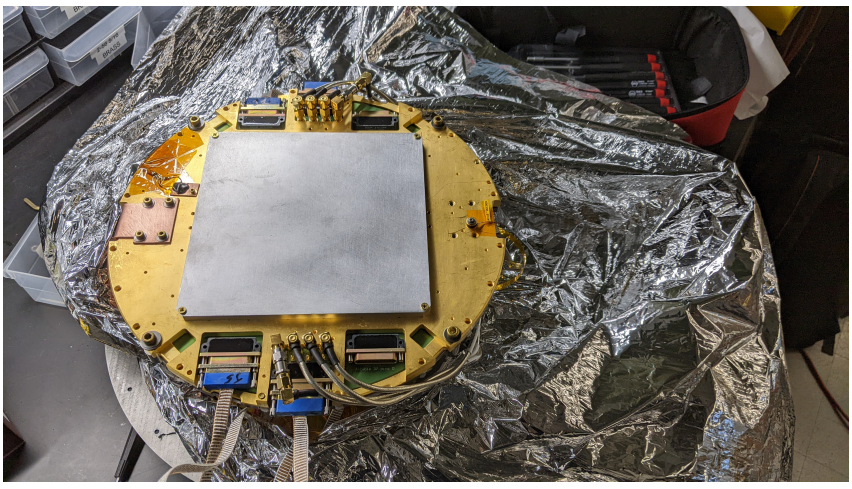

Figure 4.10: The TKID focal plane with the detectors covered and all RF cables installed. The Cri/oFlex cable is installed on the underside of the UC stage and is not visible in this image. The aluminized mylar shroud makes up the RF shield that encloses the 2K volume and the focal plane.

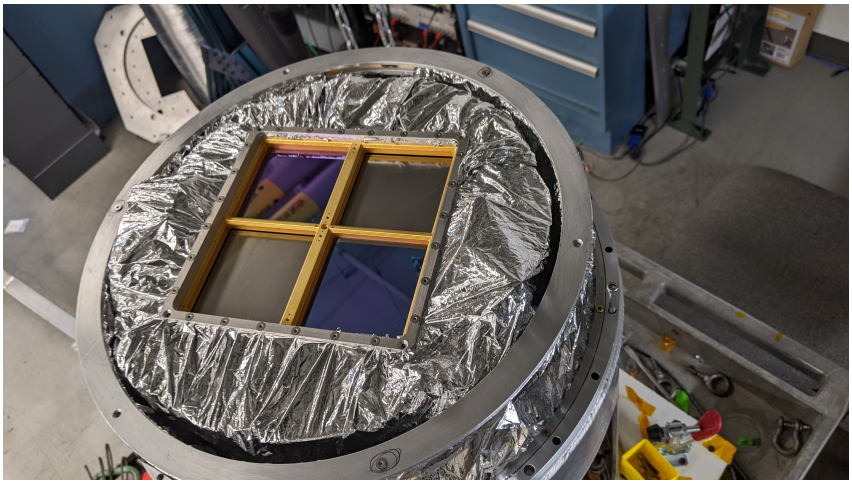

Figure 4.11: View of the focal plane with 2 tiles installed before installing the bandpass filter at 2K. The antennas on the wafer are back-illuminated through the silicon wafer and a quartz antireflection tile.

Chapter 5

DESIGN OF THE 150 GHZ TKID CAMERA

The prototype TKID devices achieved many of their prescribed goals. Both the waffle TKID devices and the 2x3 chips demonstrated the excellent noise performance needed to for CMB observations. The dark resonator arrays were instrumental in refining our fabrication process and developing new calibration tools. Additionally, we verified our optical design using the 2x3 chips and showed that TKIDs could be successfully coupled to planar phased array antennas. The design and development of the 150 GHz TKID tiles represents the final major milestone of this project. It is a significant scale up in the complexity of the design.

We developed 2 150 GHz tile designs, hereafter named the MLA and Ex-3 versions. As an endeavor, device design is not independent of fabrication. The design of the MLA version of the tile was designed in April 2020 during the Covid-19 pandemic. Because of the difficulty of procuring reticles for lithography on the Canon stepper as we initially planned as well as the inaccessibility of the stepper programming computer, we designed a version of the tile that could be fully fabricated using the Heidelberg laser writing sytem[1] to continue our fabrication efforts. A photograph of the MLA version of the tile is fig. 5.2. Unfortunately, the laser write system has a much lower resolution than the stepper system and could not reliably fabricate 1 micron wide inductors across the entire wafer greatly affecting the resonator yieldsection 6.1. The resolution also significantly affected the finest microstrip features on the antenna leading to anomalously low optical efficiency.

In summary, the changes in the design between the MLA version and the Ex-3 versions of the 150 GHz TKID tiles are:

- The pixel-to-pixel spacing was reduced from 8.4 mm to 8.16 mm. This restored antennas on the 4 corner pixels.
- The capacitor footprint on wafer changed from 0.516 mm x 2.4mm to 0.44 mm x 3.35 mm.

[1] https://heidelberg-instruments.com/product/mla150/

- The frequency schedule across the wafer in the MLA design was monotonic along the feedline as shown in fig. 5.3. In the Ex-3 design, polarization A and polarization B resonators were separated into 2 bands with a 25 MHz spacing. The 25 MHz gap is wide enough to discriminate between resonators corresponding to the two orthogonal polarization directions even under the highest optical loads encountered during laboratory characterization.

- The Ex-3 resonator design is compatible with 3 choices of bolometer leg length: [188 μm, 296 μm, 352 μm]. The baseline design is the 296 μm bolometer.

- On each row, the all the calibration heaters are wired out in series. In the MLA version, the heaters were only accessible in rows 2 – 7. In the Ex-3 design, all the rows have heater bias lines.

- In the MLA design, the resonators corresponding to the corner pixels were made into dark detectors. In the Ex-3 design all the resonators are connected to an antenna. However, we generate dark pixels during the capacitor trimming step by checking for unpaired resonators and isolating them from the antenna.

A single tile, shown in fig. 5.1 consists of an 8x8 array of dual polarization pixels. Each antenna is coupled to 2 bolometers: one for each polarization. All 128 detectors are coupled to a single feedline. We also maintain a number of calibration heaters to enable laboratory characterization.

In this chapter, we discuss the design of both the 150 GHz tile and the 150 GHz focal plane unit. I designed both the MLA and Ex-3 versions of the tile while Lorenzo Minutolo designed the focal plane PCB and readout.

Detector Simulations

A TKID resonator is too large to simulate monolithically. This is further complicated by the presence of different dielectrics at the capacitor in comparison to the inductor the inductor. To account for this, we instead separately simulate sections of the capacitor and inductor and assemble them as a Sonnet netlist[2]. Simulations include a section of the feedline in order to extract the resonance frequency and resonator parameters.

[2] `https://www.sonnetsoftware.com/products/sonnet-suites/ef-netlist.html`

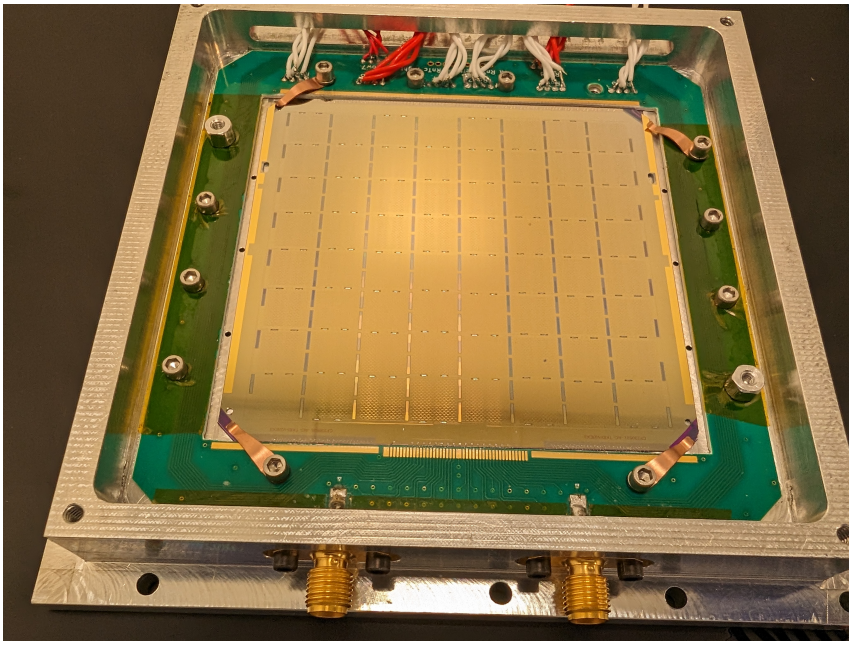

Figure 5.1: A single Ex-3-TKID tile installed in a wafer holder for dark testing at JPL. The SMA connectors are soldered onto an RF line on the PCB. The PCB also routes signals for biasing the heaters.

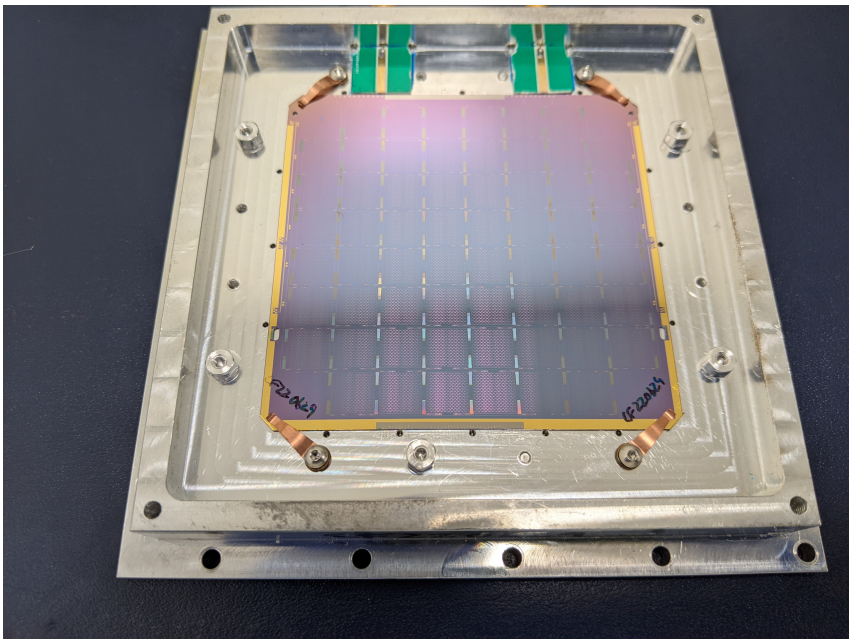

Figure 5.2: For comparison, a single MLA version 150 GHz TKID tile before dark testing at JPL. The corner pixels in the MLA version were dropped to allow for wider spacing between the pixels for the capacitors.

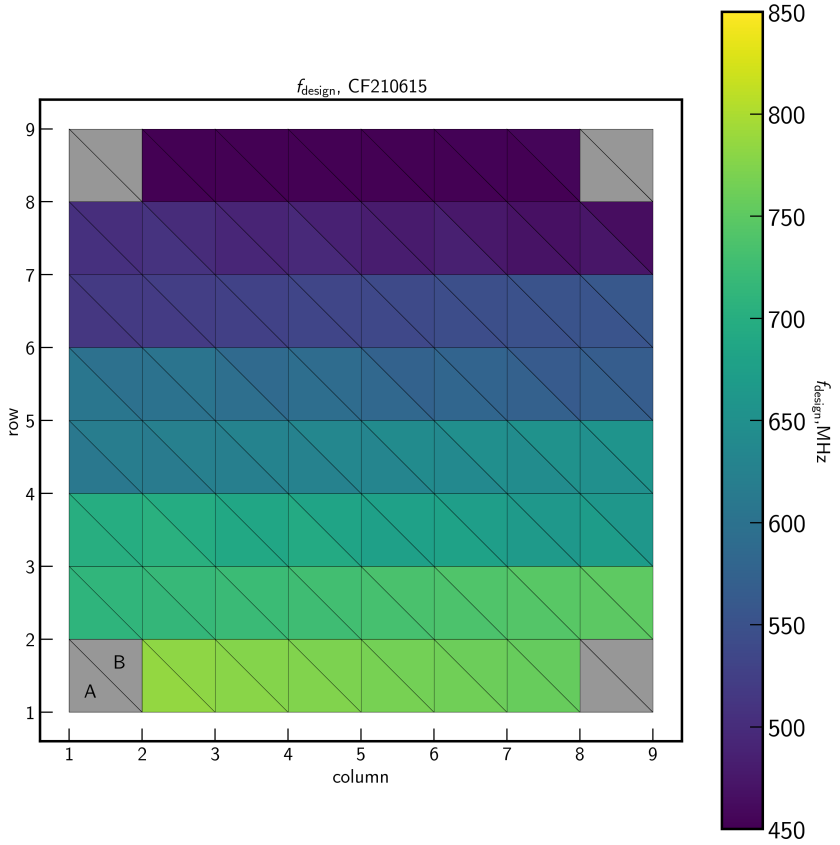

Figure 5.3: Design frequency schedule for a MLA 150 GHz TKID tile.

In Sonnet, we split the IDC into 50 finger sections. The largest IDC has 16 such sections. All the capacitors have the same footprint on the wafer because the ends of the capacitor are padded with single-sided finger stubs. We simulated the capacitor with [2,3,4,5,6,8,10,12,14,16] sections. The IDC consists of 2 micron wide fingers with 2 micron wide spacing between them. The fingers are 352 μm long on the main capacitor and 30 μm long on the coupling capacitors.

Layer	Material	Thickness [μm]	Properties
0	Air	500	Lossless
-	Nb	0.12	General Metal, 0.138 pH/sq surface inductance
1	SiO_2	0.3	Dielectric constant: 3.9, Lossless
-	Nb	0.12	General Metal, 0.138 pH/sq surface inductance
2	Si	500	Dielectric constant: 11.9, 1e-6 loss tangent
3	Air	1000	Lossless

Table 5.1: Dielectric stack used to simulate the capacitor.

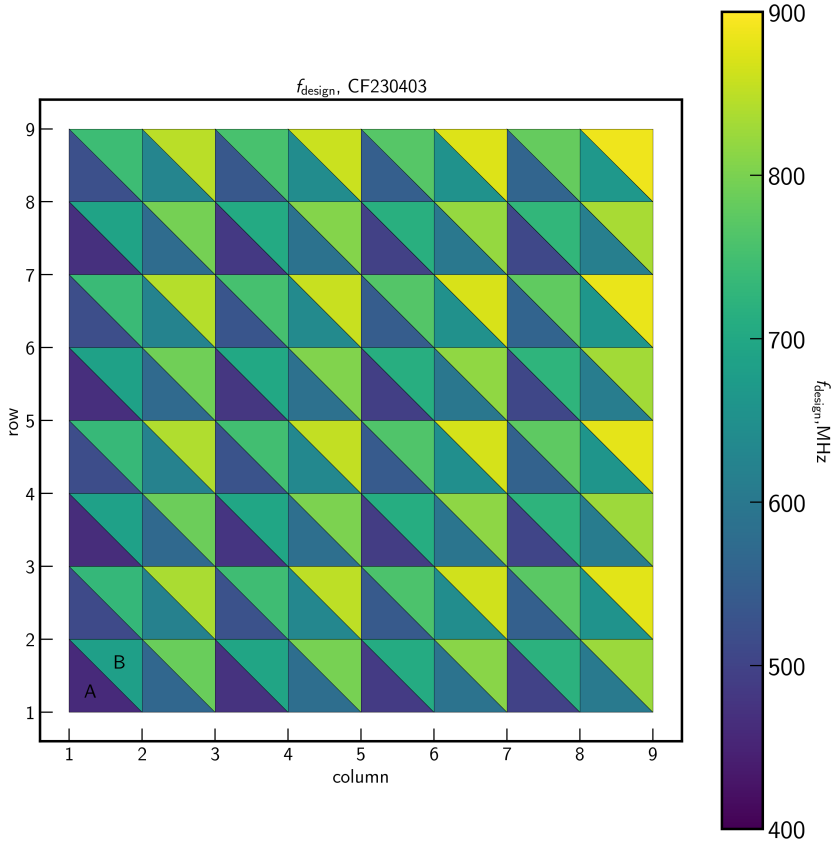

Figure 5.4: Design frequency schedule for an Ex-3 style 150 GHz TKID tile.

Capacitor Dielectric Stack

Inductor Dielectric Stack Only a single inductor design is used for all the resonators in the array. We therefore simulated an inductor on a bolometer island in the 100 MHz – 1200 MHz frequency range.

Layer	Material	Thickness [μm]	Properties
0	Air	500	Lossless
-	Nb	0.4	General Metal, 0.158 pH/sq surface inductance
-	Al	0.05	General Metal, 0.25 pH/sq surface inductance
-	Au	0.3	Resistivity 187.5 Ω·cm
1	Si_2N_3	0.3	Dielectric constant: 7.5, 1e-8 loss tangent
-	Nb	0.12	General Metal, 0.138 pH/sq surface inductance
2	SiO_2	0.3	Dielectric constant: 3.9, Lossless
3	Air	1000	Lossless

Table 5.2: Dielectric stack used to simulate the inductor on the bolometer.

The inductance as shown in fig. 5.5 has little variation across the entire frequency

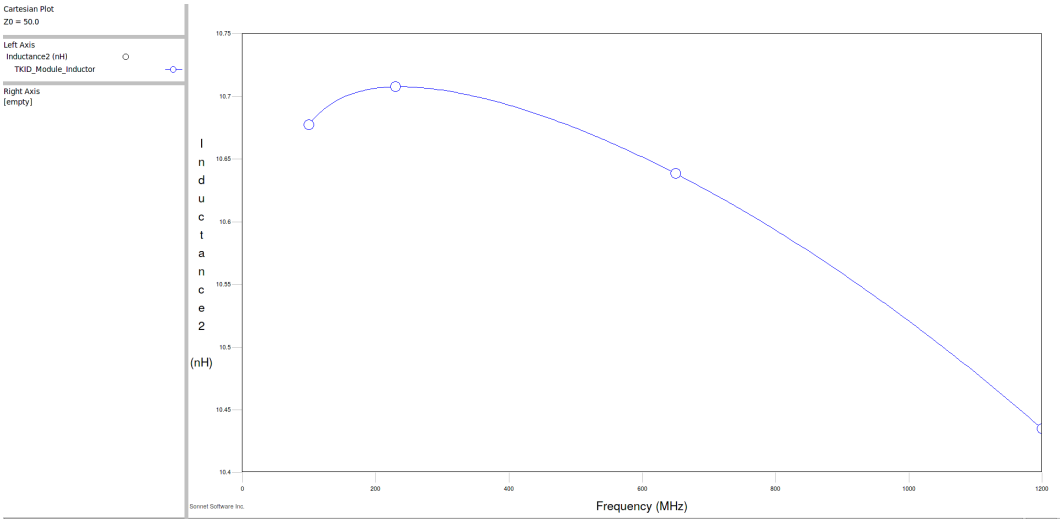

Figure 5.5: Simulated resonator inductance between 100 MHz and 1200 MHz. We conclude that all resonators on a tile. The variation in inductance between 400-900 MHz is less than

range we are considering. The frequency dependence of the IDC impedance will dominate the resonator placement. However, because of the presence of ground plane on the bolometer legs, the inductor has parasitic capacitance to GND of about 0.98 pF on each of its ports.

The capacitor is well modeled as a series capacitor and inductor. The capacitance has a small quadratic correction. In pF $C = 12.1626\ x + 2.2039\ x^2 + 1.3798$ with $N_0 = 800$ and $x = N/N_0$ where N is the number of fingers in the IDC.

The individual capacitor and bolometer simulations are assembled into a full resonator netlists and simulated over the entire frequency band (100 – 1200 MHz). However, this band is too wide to resolve the location of the resonator with the resolution of the simulation. We therefore perform repeated simulations while narrowing the simulation bandwidth eventually down to about 4 MHz in order to fit for the resonance and extract out the resonator parameters. The extracted S_{21} for the resonator simulation with 4 capacitor sections is shown in fig. 5.7. The dielectric loss added in the simulations lowers the internal quality factor of the resonator increasing its visibility in the simulation.

The resonator frequency f_r as a function of the number of IDC fingers N is well modeled by the relation

$$f_r = f_\alpha x^{-1/2} \left[1 + \alpha + \beta x + \epsilon/x\right]^{-1/2} . \tag{5.1}$$

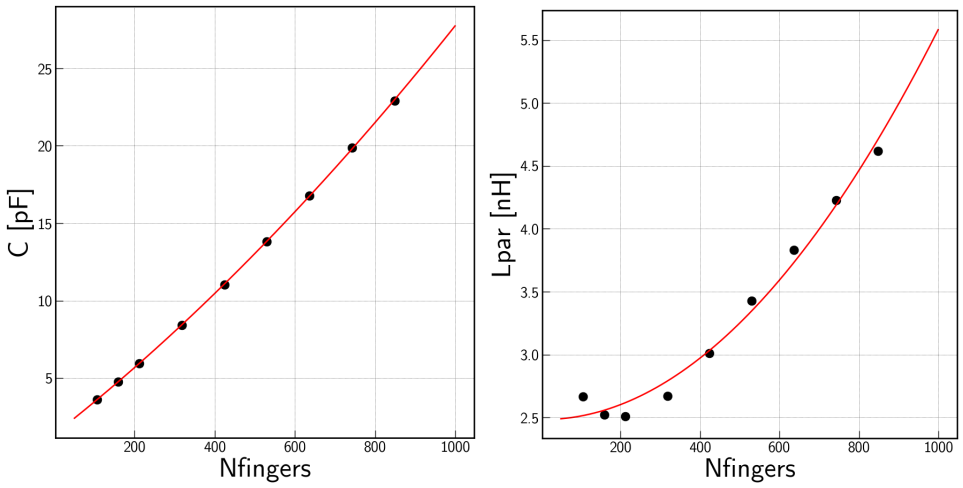

(a) (b)

Figure 5.6: Simulated capacitance and parasitic inductance of the IDC as a function of the number of fingers in the IDC. The extracted capacitance and inductance are the black circles. Quadratic polynomial fits to the data are given as the red curves.

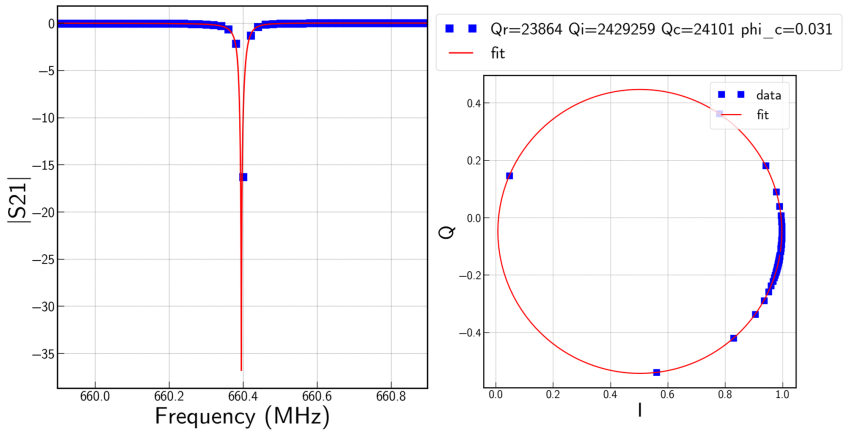

Figure 5.7: A fit to S_{21} extracted from a resonator netlist as a function of frequency. The best fit resonator parameters are given in the legend to the upper right. The simulation bandwidth was scaled down from 1.1 GHz to 4 MHz in order to resolve the resonance. Even so, only a few points lie well within the resonator bandwidth as evident from the I/Q circle.

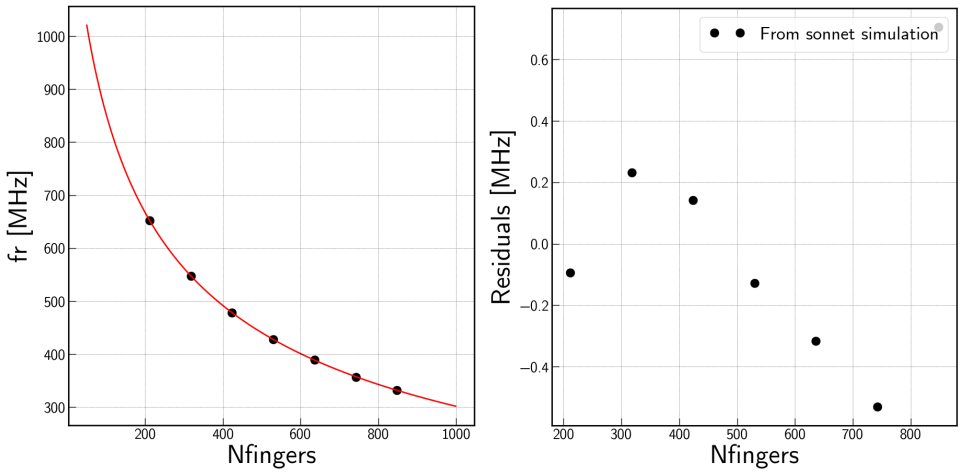

(a) (b)

Figure 5.8: A comparison of the simulated resonance frequencies to the model prediction. Left: Simulated resonance frequencies in black and a best fit curve using eq. (5.1). On the right are the best fit residuals. The residuals are not random but are much smaller than the spacing between adjacent resonators. We can therefore use this model to predict the resonance frequencies of the array.

This model was extracted from considering the IDC parameters extracted from the simulations. From the best fit shown in fig. 5.8, $f_\alpha = 478.6$MHz, $\alpha = 0.0924$, $\beta = 0.205$ and $\epsilon = 0.128$. With this model, the residuals have a std. deviation of less than 0.4 MHz, much smaller than the 3 MHz spacing between adjacent resonators. This equation is also easy to invert numerically to predict the number of fingers that correspond to a given frequency.

We are interested in bridging the simulated resonance properties with a circuit model based on all the elements in the resonator design. A simple resonator circuit model includes an inductance L, capacitor C and 2 identical coupling capacitors to the feedline and to ground C_c. We additionally account for the parasitic inductance of the capacitor, L_{series} and the excess capacitance to ground, C_{p1} on the feedline side and C_{p2} on the ground side of the capacitor. In such a model, the resonance frequency, f_r, and coupling quality factor are given by

$$\omega_r^2 = \left[(L + L_{\text{series}}) \left(C + C_{\text{par}} \right) \right]^{-1} \tag{5.2}$$

$$Q_c = \frac{2C}{\omega_r C_c^2 Z_0} \cdot \left(\frac{2C_c + C_{p1} + C_{p2}}{C_c + C_{p2}} \right)^2 \cdot \left(\frac{L + L_{\text{series}}}{L} \right)^2 \tag{5.3}$$

where $\omega_r = 2\pi f_r$ and $C_{par} = \left(C_c + C_{p2}\right) \left(C_c + C_{p1}\right) / \left(2C_c + C_{p1} + C_{p2}\right)$.

This circuit model however consistently underestimates the resonance frequency and overestimates the coupling quality factor. In the resonator design, we can account for this by scaling our circuit predictions by a multiplicative factor but this is a strong suggestion that we are not fully capturing the physics of the resonator in our on paper modeling.

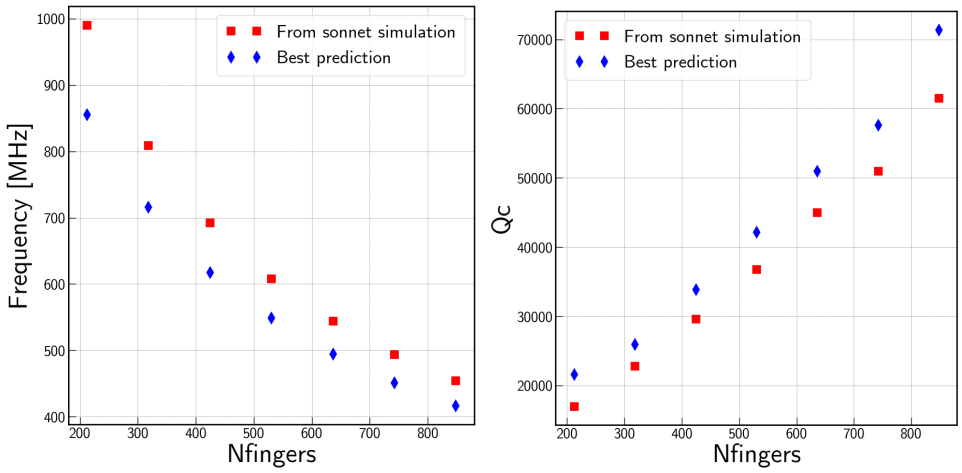

(a) (b)

Figure 5.9: Predicted resonance frequency and coupling quality factor (blue diamonds) from circuit models in comparison to the results from fitting the simulations in Sonnet. The circuit model underestimates the resonance frequency and overestimates the coupling quality factor.

A Novel Approach to Interpreting Resonator Simulations

In section 2.2, I detailed a consistent and unified approach to extracting resonator parameters from a circuit models. This approach lends itself naturally to interpreting simulations so as to better inform resonator design and generates intuition for understanding how resonator properties shift due to fabrication, line impedance mismatch, wire bond effects, and other effects.

The key observation, is that the resonator description is much simpler when expressed in the impedance parameters rather than the scattering parameters. In general, the impedance matrix (here denoted $\hat{Z}$) of a passive network is a function of 4 complex network functions of frequency: $[Z_a, Z_b, Y, \delta]$. We explicitly have

$$\hat{Z}(\omega) = \begin{pmatrix} \frac{1}{\delta}\left(Z_a(\omega) + \frac{1}{Y(\omega)}\right) & \frac{1}{Y(\omega)} \\ \frac{1}{Y(\omega)} & \delta\left(Z_b(\omega) + \frac{1}{Y(\omega)}\right) \end{pmatrix}. \tag{5.4}$$

δ is a parameter that is typically close to 1 and captures the degree to which the network being simulated is mismatched from the port impedances (here taken to be $Z_0 = 50\Omega$). In a circuit model, it is easy to extract δ. In simulations, if the loss is small and largely restricted to the resonator loss, we can estimate the value of δ as a function of frequency in either of 3 ways:

$$\delta = \left[\mathrm{Re}(\hat{Z}_{2,2})/\mathrm{Re}(\hat{Z}_{1,1})\right]^{1/2}, \tag{5.5}$$

$$= \left[\mathrm{Re}(\hat{Z}_{2,1})/\mathrm{Re}(\hat{Z}_{1,1})\right], \tag{5.6}$$

$$= \left[\mathrm{Re}(\hat{Z}_{2,2})/\mathrm{Re}(\hat{Z}_{2,1})\right]^{1/2}. \tag{5.7}$$

For the simulation set considered in chapter 5, the first approach works well. With δ in hand it is straightforward to extract out the remaining parameters. The full impedance parameters are given in fig. 5.10 as a function of frequency. Y is the only parameter that contains resonance features.

$$Y = 1/\hat{Z}_{2,1}, \tag{5.8}$$

$$Z_A = \hat{Z}_{1,1}\delta - \hat{Z}_{2,1}, \tag{5.9}$$

$$Z_b = \hat{Z}_{2,2}/\delta - \hat{Z}_{2,1}. \tag{5.10}$$

Z_a, Z_b, andδ can be combined by introducing two complex dimensionless functions: $\zeta = \delta + Z_a/Z_0$ and $\eta\,(\omega) = 1/\delta + Z_b/Z_0$. As we will see, the scattering parameters are concisely expressed in terms of ζ and η. Additionally, let $Z_{\mathrm{tot}} = Z_0\,[1/\zeta + 1/\eta]^{-1}$ be the total impedance looking out into the external circuit from the resonator.

The next step is to separate out the resonator filter function shown in fig. 5.11b from the slowly varying background admittance as $Y = \bar{Y} \cdot \mathcal{R}$ where $\mathcal{R}$ is the filter function. Here, we independently fit the real and imaginary parts of Y to the following rational functions:

$$\mathrm{Re}(Y) = \frac{p_2 f^2}{f^2 + q_1 f + q_0}, \tag{5.11}$$

$$\mathrm{Im}(Y) = \frac{r_3 f^3 + r_2 f^2 + r_1 f}{f^2 + q_1 f + q_0}, \tag{5.12}$$

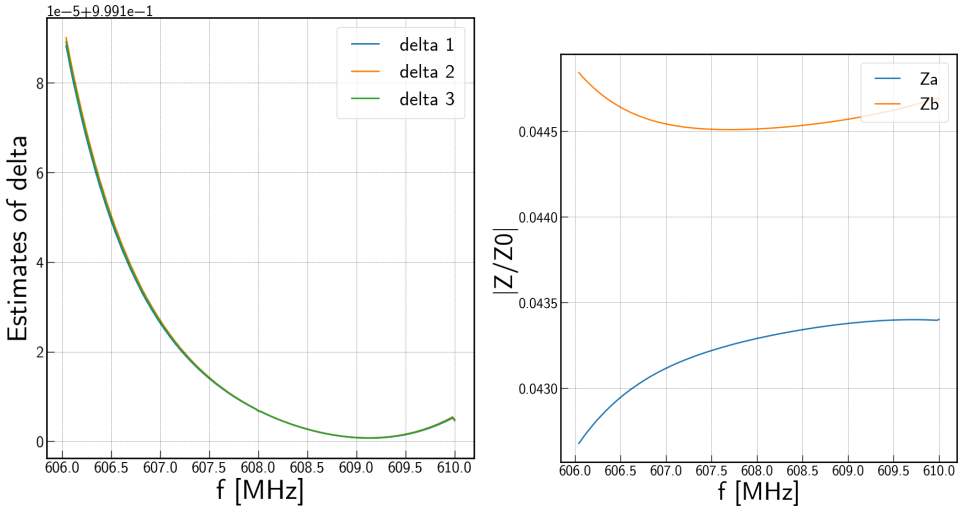

(a) (b)

Figure 5.10: Extracted impedance matrix parameters from the resonator simulation with 4 capacitor sections. Z_a and Z_b are purely imaginary. The 3 estimates of δ according to eq. (5.5) are largely consistent with each other. Importantly, Z_a, Z_b, δ show no resonance features.

to separate the 2 contributions $\bar{Y}$ and $\mathcal{R}$ as shown in fig. 5.11. Model fitting is not strictly necessary since we are only interested in the zero and pole frequencies of the resonator filter function. The smoothed admittance $\bar{Y} = (r_3/q_0) \cdot f$ can be extracted by applying a smoothing filter if the simulation has enough data points, or even from combining multiple simulations.

The resonator filter function is a model of only 3 parameters as given in eq. (2.21). It follows that We can predict S_{21} directly using equation eq. (2.18) as shown in fig. 5.12.

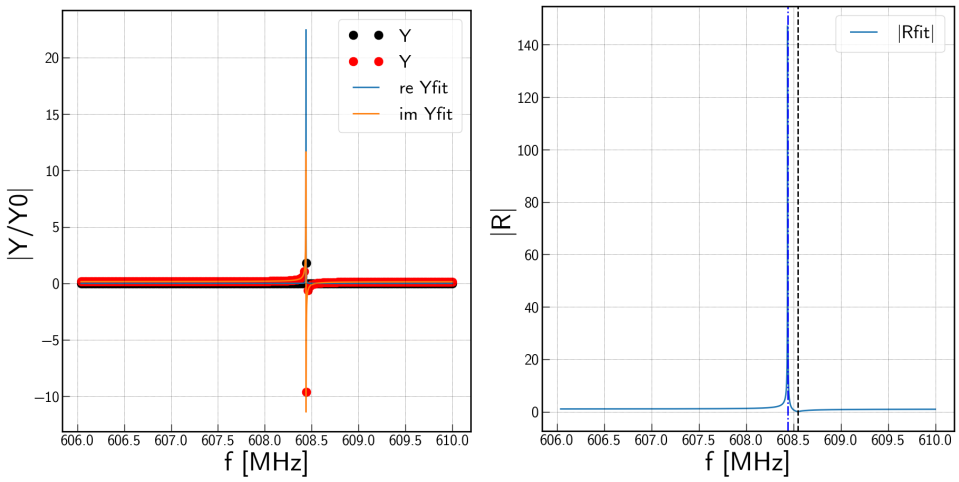

(a) (b)

Figure 5.11: A decomposition of the shunt admittance into a background and single pole component. (Left) Fit to the shunt admittance using the model detailed in eq. (5.11). (Right): The extracted single pole resonator filter. A single pole resonator filter can be modelled as a function of only 3 parameters.

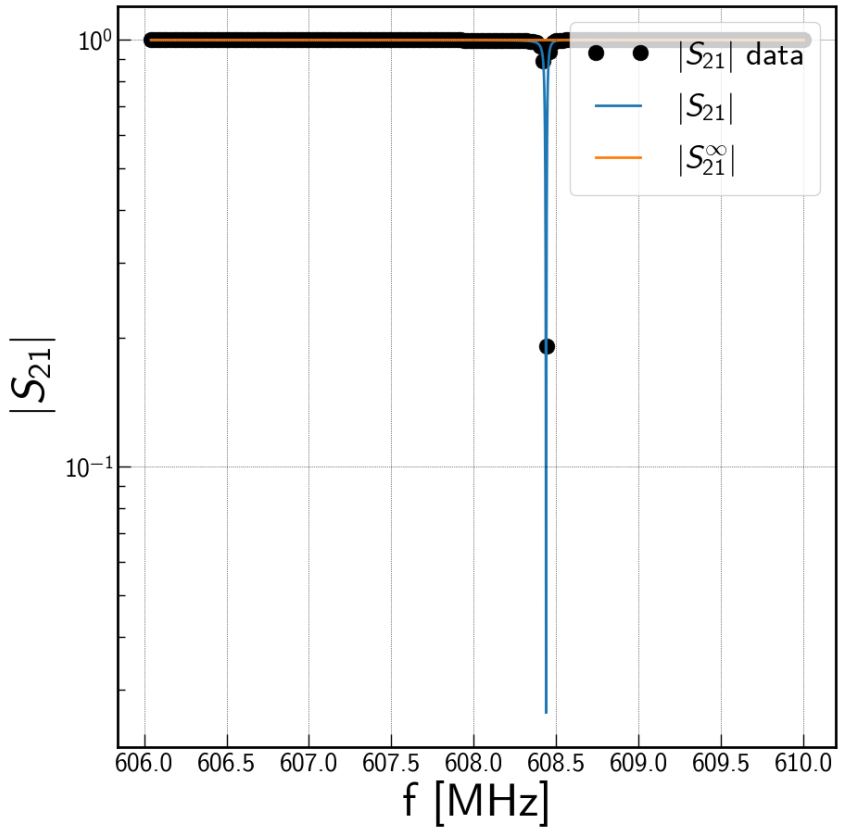

Figure 5.12: The predicted S_{21} from eq. (2.18) compared to S_{21} extracted from a resonator netlist as a function of frequency. This is the same resonator given in fig. 5.7.

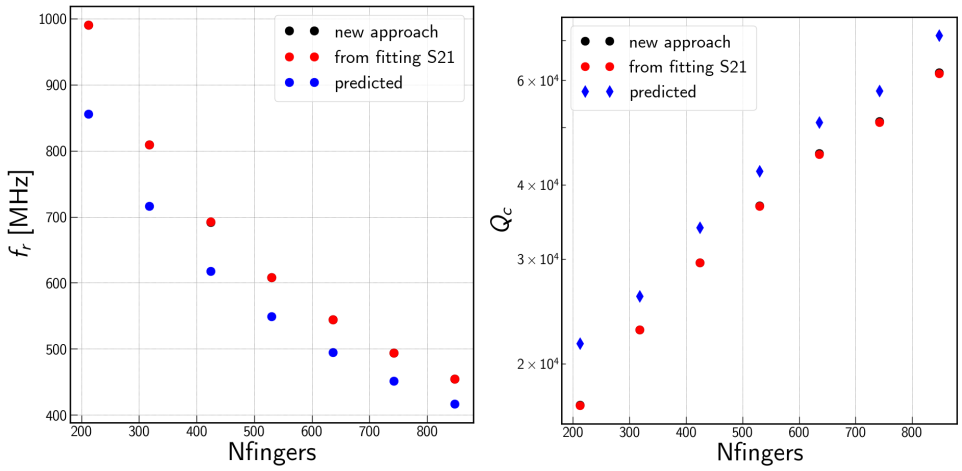

(a) (b)

Figure 5.13: Resonator parameters extracted from the impedance parameters (black circles) agree with the results of fitting S_{21} (in red). The blue data points are the results of a circuit model as detailed in chapter 5 and fig. 5.9.

5.1 Single Pixel Layout

We couple our TKIDs to a planar dual polarization slot array antenna designed and fabricated at Caltech/JPL (Ade, Aikin, Amiri, Barkats, Benton, Bischoff, Bock, Bonetti, et al., 2015; Kuo et al., 2008). This antenna does not require horns and other coupling optics. The wafer is back side illuminated through the silicon and the optical power couples to two co-located, orthogonally polarized 12x12 planar antenna array. Each slot sub-radiators is patterned in the superconducting niobium (Nb) ground plane. All slots of a given orientation are coherently combined through a microstrip summing tree to synthesize a single equivalent antenna for that polarization orientation. Power from each antenna is passed through an on-chip band-defining filter before being dissipated on a suspended bolometer island. We use a three-pole design for the filter, implemented using lumped element components instead of transmission line resonators which can suffer resonant frequency leaks.

Fig. 5.14 shows the layout of a single TKID pixel on the wafer. In order to maintain the tight packing of the antennas, the IDC tanks that set the resonance frequency of the resonators are long and narrow. The location of the bolometer also changes from above the antenna to below the antenna from column to column. This staggered placement allows heater bias lines to stitch through each row addresses every calibration heater (16 in total) on a single row of the wafer in series. This sacrifices our ability to address each bolometer independently, but allows us to do lab characterization assuming uniform resistor film properties across each row.

The staggered bolometer placement also allows for the placement of the IDCs from adjacent columns into the same spacing between the antennas. The gap between the two capacitors allows the 5 μm wide heater bias line to thread through and back till the end of the row. The microstrip lines from the antenna to the band filter run parallel to the capacitor via edge. From one of the two coupling capacitors, a short microstrip section connects to the feedline. A pair of 2 micron wide microstrip lines with 4 μm spacing run the length from the capacitor to the inductor. A final microstrip section connects a second coupling capacitor to GND through a large capacitor pad.

5.2 Focal Plane Unit

The Focal Plane Unit (FPU) is supported on thermally isolated V shaped carbon fiber supports mechanically anchored to the 350 mK Nb shield.

Copper Plate The OFHC copper plate provides the mechanical structure of the focal plane. It is the primary thermal mass of the focal plane. The center of the copper plate has 4 cutouts - one for each 4" detector tile. The edges of the cutouts have corrugations of specially designed grooves which depth and impedance chosen to suppress polarized reflections near the edge of the detector tile (Ade, Aikin, Amiri, Barkats, Benton, Bischoff, Bock, Bonetti, et al., 2015). The detectors are thermally sunk to the copper frame using hundreds of gold wirebonds along 3 of the 4 wafer edges. The gold bondpads on the detector tiles make direct contact with the silicon. A quartz anti-reflection (AR) tile, quarter wavelength thick is mounted on the illuminated side of the wafer and the antenna faces a niobium backshort at a quarter wavelength spacing away from the tile. The wafer and AR tile have a pin and a slot for precise alignment using pins on the focal plane. The slot allows for mechanical freedom to accommodate the differential thermal contraction of the copper during cool down without warping the detector tiles. Specially manufactured Beryllium-copper tile clips press the Si wafer and AR tile down against the copper plate preventing vertical motion of the wafer. The copper plate used in the TKID focal plane was obtained from spare focal plane parts from the *Keck Array*.

Focal Plane Distribution Board The focal plane distribution board interfaces all signals (both DC and RF) to and from the TKID tiles. The FPU distribution board shown in fig. 5.15 incorporates 6x 37-way micro-D connectors to complete the interface between the non-isothermal cables (J-cables) and the detector tiles. This

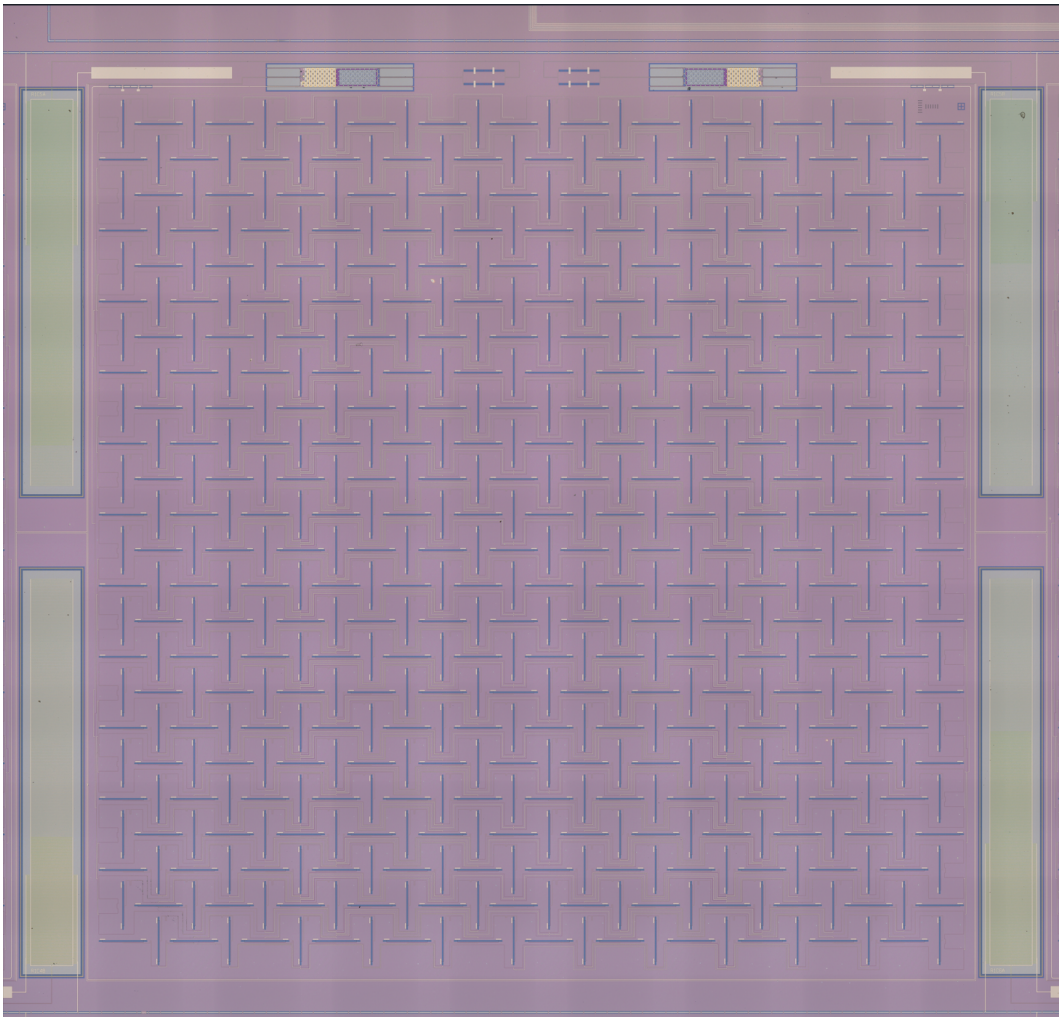

Figure 5.14: An image of the R1C5 pixel from the CF230725 Ex-3 wafer. The TKID bolometers measuring power from each polarization are located above the antenna. The bolometer position switches from above to below the antenna in each column to efficiently tile the wafer. The IDC tanks for each TKID resonator are located off the island and are slotted between adjacent antennas. The feedline and heater bias lines are in view at the top of the image. The features between the bolometers are the RF choke filters to reject direct stimulation pickup from the capacitors.

concept was maintained from the previous *Keck* design where the cables were used for the TDM readout of TES detectors. In our design, the connectors to distribute calibration signals to the heaters on each of the 4 detector tiles. The connectors on the board were repositioned to accomodate eight SMA connectors. The overall FPU footprint was left unchanged to accommodate a minimal deployment option to the field in which we would only carry a focal plane and the RF readout chain to install into a receiver already present at the South Pole. Note that the calibration infrastructure is only strictly necessary for lab measurements. On sky, no calibration signals will be applied to the detectors.

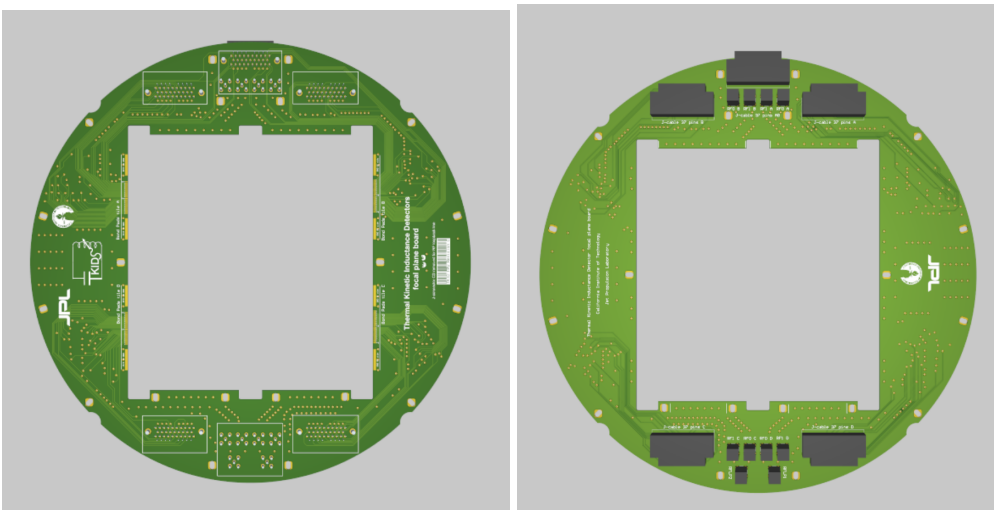

(a) (b)

Figure 5.15: 3D rendering of the FPU signal distribution board. On the left, the side pointing toward the cryostat is rendered. The soft Gold plated bondpands for the tile assembly are visible. On the right side the layer of the PCB that should have pointed to the sky is rendered. The black boxes on the panel are placeholders representing the mechanical clearances of the various connectors. We can note on this specific version the absence of one of the six micro-d. The connector removed specifically carried redundant diagnostic information used exclusively during the material characterization phase of the project. The micro-d connector has been replaced by two additional SMA RF connectors for loopback testing of the board.

Care was taken in the design of the distribution board to prevent cross-coupling between the RF and DC signal paths on the board. Each signal layer is interleaved with a double Copper weight ground plane, in a stripline geometry for the internal layers of the PCB. The calibration signals are routed entirely on the top layer. The PCB is made of standard Rogers Corporation (series 4000) material which is easily

procurable and was manufactured by PCBWay[3].

5.3 Fabrication, Inspection and Quality Control

The biggest challenges in developing TKIDs have been in fabrication. It is non-trivial to scale a design from a few prototype devices to a full working array. We will only detail the fabrication of the Ex-3 tiles in this section. These tiles were fabricated between March 2023 and January 2024. A summary of the processing steps is given in table 5.3

	Material/Function	Deposition	Etchant	Lithography System
1.	Low-stress Nitride	High temperature LPCVD	CHF_3, ICP-RIE	-
2.	Niobium Ground Plane	Sputtered	Etchback CHF_3/O_2 etch	Ex-3
3.	SiO_2 ILD	RF Sputtered	Etchback CHF_3/O_2 etch	MLA
4.	SiO_2 Via/Perimeter Oxide	RF Sputtered	-	MLA
5.	Gold Resistor	e-beam evaporated	Liftoff	Ex-3
6.	Aluminum Inductor	e-beam evaporated	Liftoff	Ex-3
7.	SiO_2 Al/Au PRO layer	RF Sputtered	-	MLA
8.	Niobium Capacitor/Microstrip	Sputtered	-	MLA
9.	Niobium Capacitor/Microstrip	-	Etchback CHF_3/O_2 etch	Ex-3
10.	FSN, Hole and Slot, dicelines	-	STS	MLA
11.	Titanium/Gold Frame	e-beam	Liftoff	MLA
12.	Capacitor Trimming	-	Etchback ICP-Cl etch	MLA
13.	Island Release	substrate	DRIE/XeF_2	MLA

Table 5.3: A summary of processing steps in the TKID fabrication.

All our device fabrication is done at the Micro Devices Laboratory (MDL) at the Jet Propulsion Laboratory (JPL). The TKID fabrication process was developed by Anthony Turner and Clifford Frez at JPL. I performed device inspections and rework both in the cleanroom at JPL and at the Kavli Nanoscience Institute (KNI) at Caltech. TKID devices are fabricated on 550μm thick high resistivity 4" Si wafers. We choose this thickness for optimal optical coupling since the antennas are back illuminated through the Si wafer. The wafers have a 40 nm thick oxide layer thermally grown layer on top. This oxide layer acts as a stop for the XeF_2 bolometer island release process. We deposit 300 nm thick Low Stress Silicon Nitride (LSN). The stress in the nitride is tuned to be low to ensure mechanical integrity of the bolometer thermal island.

The millimeter wave circuit of the antenna requires 4 films: a niobium ground plane, a SiO_2 interlayer dielectric (ILD), a microstrip niobium layer and a thin gold layer for a resistive termination to the antenna. We reuse these layers for the TKID resonator and feedline. Both the ground plane and the ILD are common between the resonators and the antenna. The capacitors, as well as all microstrip and coplanar

[3] `https://www.pcbway.com/`

waveguide (CPW) features for the resonators are patterned on the antenna microstrip layer. The only additional metal layer due to the TKID fabrication, is aluminum for the sensitive inductor. We prefer etch back of the Nb ground plane to a liftoff process. Liftoff often leaves metal flags during the etching process. These flags can be difficult to remove and are often tall enough to pierce through the ILD layer creating shorts between the ground plane and microstrip layers.

The photolithography for the TKID wafers is done using the 4" Ex-3 stepper. After the initial alignment marks and labels are placed, the Niobium is sputtered to define the ground plane is deposited and etched back in an inductively coupled plasma (ICP) Chloride etching. This step defines both the antenna ground plane slots and the opening for the later capacitor deposition step. This step also removes all the ground plane metal from the locations where the aluminum inductor will be patterned. The niobium ground plane is also etched away along the feedline for the CPW features. The Nb ground film defines the antenna slots, bandpass filter inductors, holes for bolometer release, and safety holes under the bond-pads along the edge of the wafer.

The etchback of the Nb ground plane exposes the silicon nitride layer underneath it. To mitigate Two Level System (TLS) noise in the resonator, it is necessary to remove amorphous dielectric where the electric field in the resonator is large. This is primarily in the interdigitated capacitors that determine the resonance frequency and set the coupling to the feedline and to ground. We therefore etch through the front side nitride (FSN) using Plasma Reactive Ion Etching (RIE) to expose the bare Si wafer in order to deposit metal and pattern the capacitor. The bare Si is also exposed along the perimeter of the wafer.

The microstrip layer of the antenna and the resonator feedline relies on a silicon dioxide interlayer dielectric (ILD). The ILD is deposited in two steps. This procedure was first developed for TES arrays, where it was initially noted that pin holes in the dielectric layer allowed shorts to develop between the ground plane and the microstrip layer. Shorts in the antenna lead to beam distortions while on the feedline, shorts to ground are catastrophic. An initial SiO_2 layer is sputtered over the ground plane before being polished and cleaned. The ILD thickness is measured and the wafer is returned into the sputter chamber to achieve the target thickness. The oxide is then patterned and etched back to reexpose the bare silicon. Before etching, the resist layer is reflowed by heating it on a hot plate. Reflowing the resist tapers the slope. The smoothed slope profile transfers to the oxide layers at the etch step

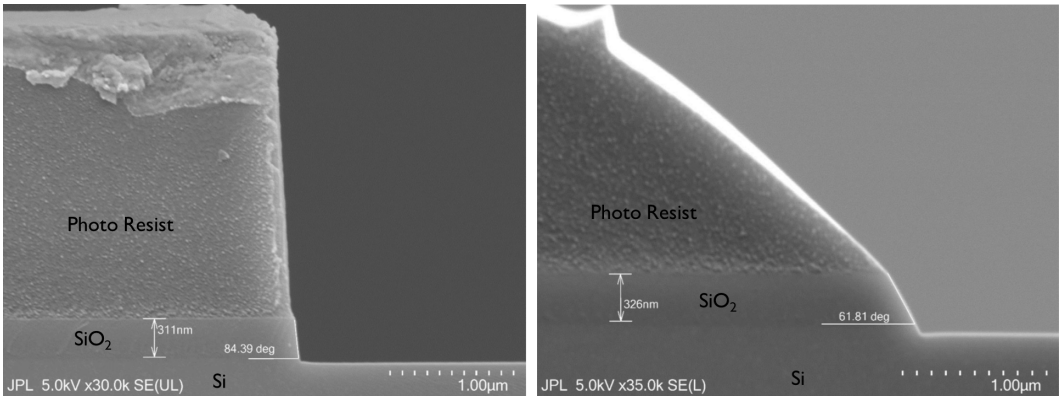

Figure 5.16: SEM images comparing the resist profile after an ICP etch without (left) and with reflow. The taper in the slope in the silicon dioxide is clear in the image to the right. The gentler slope translates to better step coverage once the niobium microstrip layer is deposited over the ILD.

leading to better step coverage when metal is deposited over the etched dielectric. Figure 5.16 shows a comparison of the impact of the reflow step on the taper in the dielectric after etching.

Since the TKID inductor is located on the bolometer island and not on the bare silicon, we will require microstrip interconnects between the inductor and the capacitor. The taper in the ILD at the via edge allows the microstrip interconnects to cover the step. To prevent shorts between this microstrip layer and the ground plane underneath close to the via edge, the boundary of the ground plane is pulled farther back away from the capacitor than both the FSN and the ILD. This ensures that there is always dielectric between metal features along the edge of the via. Figure 5.20 shows the relative placement of the ground plane, ILD and FSN edges in the wafer design. As an additional precaution, a perimeter oxide layer is sputtered along the edge of the via.

After the via protect step, we e-beam evaporate and pattern the aluminum inductor and then the gold meander and calibration heaters using liftoff. The aluminum pattern on wafer is complicated by the XeF_2 etch holes that allow etching the silicon underneath the bolometer membrane. This necessitates tight control of the inductor line width in the fabrication. In the initial design, our aluminum inductors were 1 μm wide – easily achievable using the Ex-3 system for photolithography. During the pandemic, the Ex-3 system was unavailable for more than a year. During this time, we switched to using the Heidelberg laser writing sytem[4] to continue our

[4] https://heidelberg-instruments.com/product/mla150/

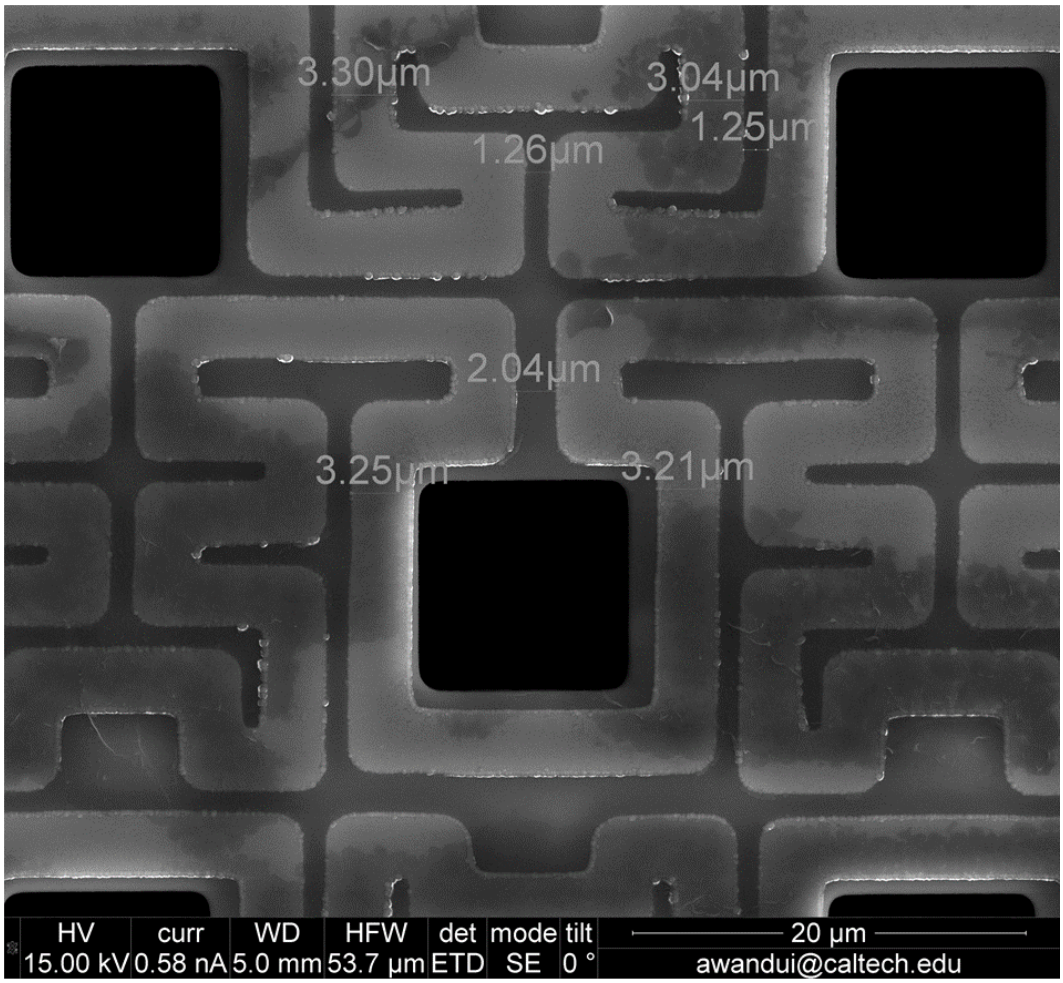

Figure 5.17: An SEM image of the TKID inductor. Image taken at KNI at *Caltech*. The variation in the line width around the XeF_2 release holes creates significant scatter in the resonator position after fabrication.

fabrication efforts. However, the laser writer has a much lower resolution than the stepper system and could not reliably fabricate 1 micron wide inductors. At the cost of detector responsivity, we switched to the wider 2 μm wide inductors. The 2 μm inductor is now the baseline design even with fabrication now mainly done on the Ex-3. The design reticle however, also holds a 1 μm wide inductor design if desired for future wafers as shown in fig. 5.18. The gold resistor meander and calibration heaters are e-beam deposited and patterned using liftoff following the aluminum step before the microstrip and capacitor features are laid down.

The capacitor patterning step is the most challenging step in our fabrication process. Fig. 5.19 shows a view of the entire capacitor situated in its via. This difficulty is due to the large via needed to expose the bare silicon. This via was defined in the

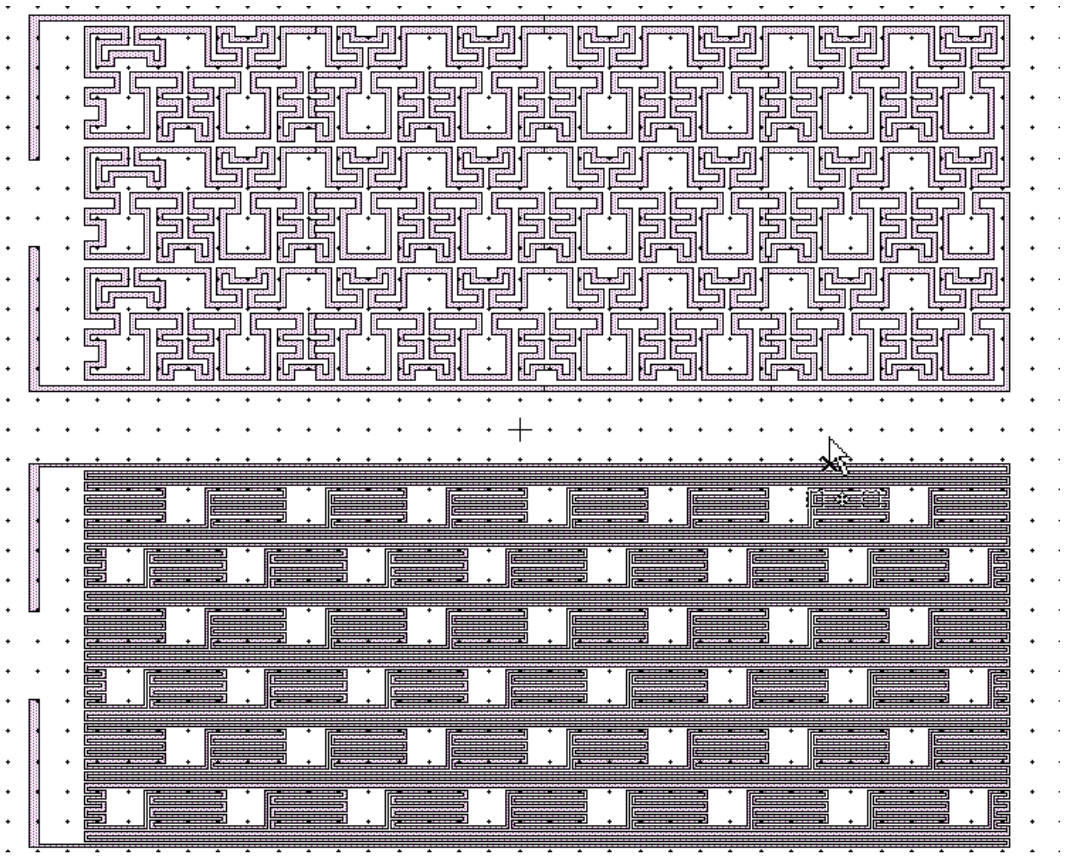

Figure 5.18: A comparison of the 1 micron and 2 micron inductor designs. Both inductors have the same footprint on the bolometer island. The design of the inductors is discussed in section

previous dielectric etch steps. The combined thickness of the ILD and FSN layers is about 600 nm. Even with resist reflow, many resonators developed Nb shorts along the via edge. In many cases, the Nb shorts were too small to be directly visible on an SEM but could the presence of Nb could be detected using Energy Dispersive Xray Spectroscopy (EDAX). At the end of the ILD etch, the exposed silicon surface along the via edge would develop microtrenches. This is likely due to decreased passivation of the resist polymer from top to bottom, or higher selectivity of the etch process to silicon. During subsequent metallization steps, Nb metal would be trapped in these pits providing a current path that bridges across parallel microstrip lines in close proximity crossing over the via edge. An example of a TKID device with a niobium short is shown in fig. 5.21. In the initial fabrication runs, more than 75% of the resonators on the wafer would not yield.

To remedy this problem, we added a Nb liftoff step before patterning the capacitor. A metal patch larger than the footprint of the capacitor but smaller than the size of

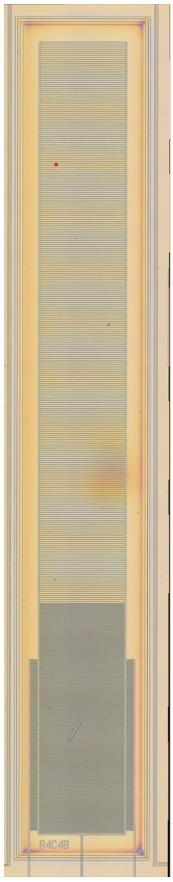

Figure 5.19: An image of the R4C4B capacitor tank situated in its via. The dark section of the IDC has interlaced fingers. The two coupling capacitors are also present. The microstrip lines at the bottom part of the image connect the capacitor to the feedline, inductor and GND, respectively.

the via would first be patterned and etched in a liftoff process. The key idea here is that the flagging left over by the liftoff process will no longer be located right at the via edge where it would be impossible to remove from the pits in the silicon surface. In a subsequent step, the Nb patches would be patterned and etched back to generate the capacitor fingers and trunk. As the excess metal is etched away, all the flags from the liftoff step would also be removed while the edge of the via was still protected. The antenna microstrip layer is patterned in the same step as the capacitor. For good step coverage at the via, we use 400 nm thick niobium.

In the final fabrication steps before releasing the bolometer islands, we first etch the FSN to define the bolometer area. After this, a perimeter gold area is deposited over the exposed Si along the wafer perimeter. During hybridization, gold wirebonds are placed along the perimeter to ensure good thermal contact between the wafer and the wafer holder. This has been a key determinant of instrument performance in

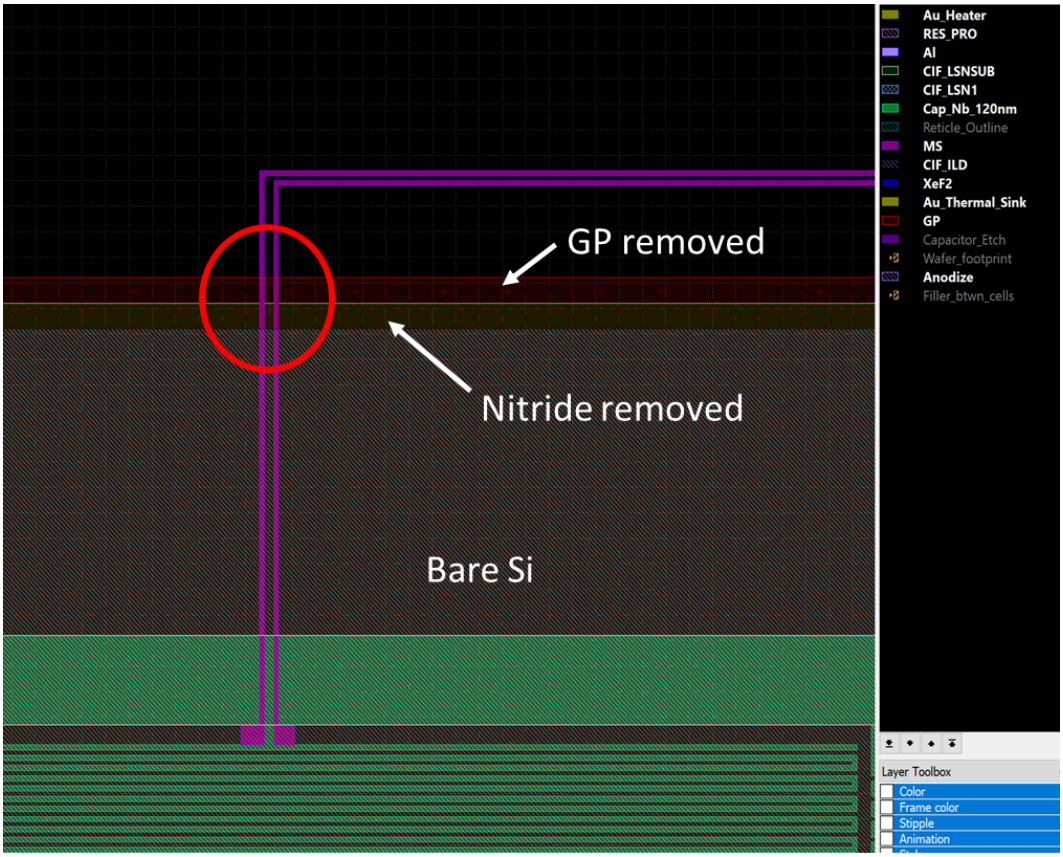

Figure 5.20: Layer arrangement at the edge of the via step in the TKID 150 GHz tile design. The purple pair of lines are microstrip interconnects between the capacitor and the inductor. The red oval highlights the location where shorts often developed during fabrication.

missions such as *Planck* (Planck HFI Core Team et al., 2011). Lastly, an STS Deep Reactive Ion Etch (DRIE) step is used to generate the pin and slot for mounting the tile onto the focal plane as well as defining the dice lines for the wafer.

Inspections and Quality Control

As already discussed, the fabrication requirements imposed by antenna coupling, TLS mitigation and bolometer membrane release make the TKID fabrication process complex. Each additional step in fabrication increases the risk on the wafer yield. This is especially true for TKIDs since the fabrication process is rapidly maturing but still in active development. Furthermore, once the bolometer island is released, only limited further processing is possible in order to fix defects.

In order to mitigate this risk, we require a tight feedback loop between fabrication and testing in order to identify and remedy defects as early as possible. The trade

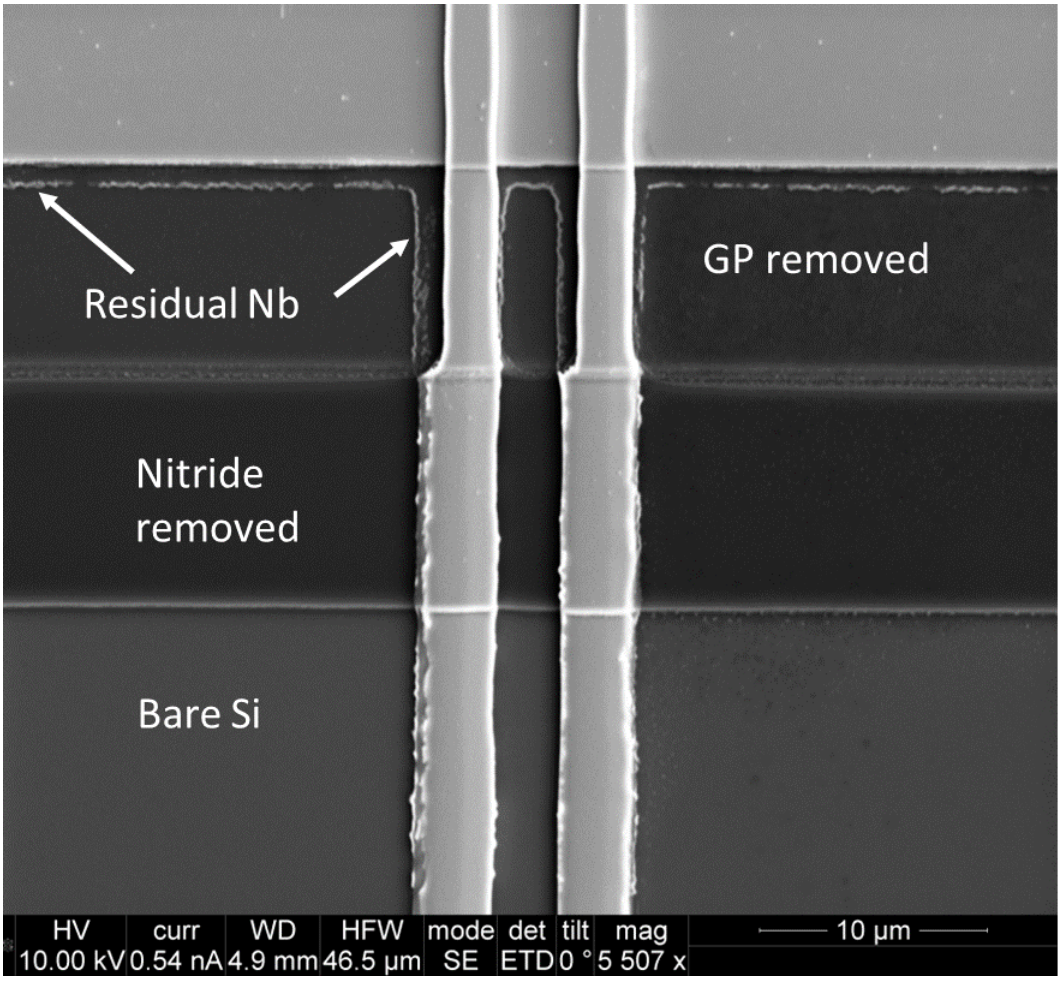

Figure 5.21: An SEM image of the via edge of a TKID resonator that did not yield. Image taken at KNI at *Caltech*. This SEM represents a rare case where the residual Nb along the via edge could be readily resolved without Xray spectroscopy.

off is a longer fabrication duration and an increased risk of wafer damage during intermediate handling.

The first set of inspection happens after the microstrip/capacitor patterning step but before the etching is done. The full wafer is imaged using the Keyence system in the MDL cleanroom. The inspection is done at a resolution of about 4 μm, high enough to visualize the spacing between the capacitor fingers. This is sufficient to identify defects in the antenna slots, capacitor, feedline and heater bias lines. 16 independent inspections are required to cover the full wafer and require about 4 hours of imaging time to complete. Figure 5.22 shows the upper left hand corner of the wafer labeled CF230725 during inspection. Each image is then visually scanned by two independent observers and all the possible defects are tabulated

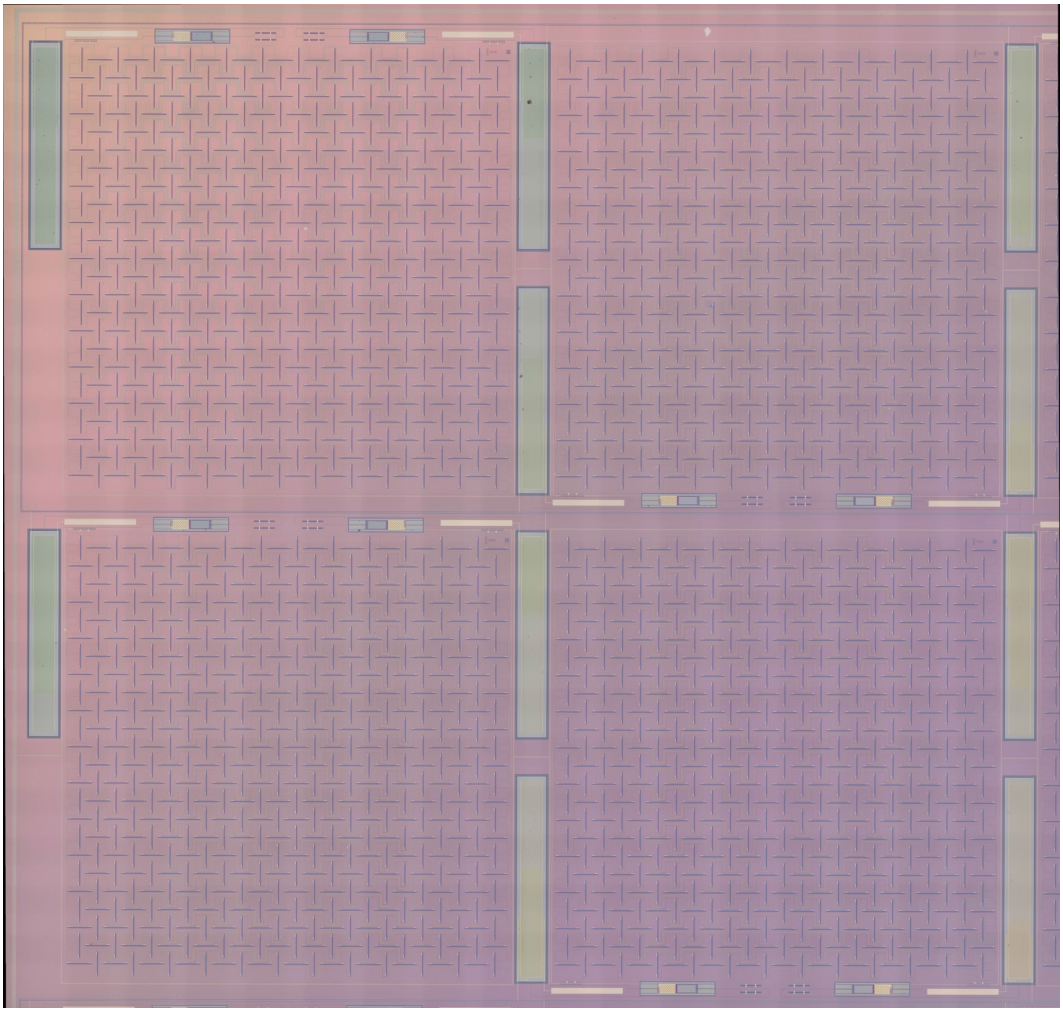

Figure 5.22: A view of 1/16th of the wafer during an intermediate inspection step.

and assessed for repair. It should be noted, that a number of defects that happen during earlier fabrication steps such as on the ground plane cannot be remedied even when identified at this stage. Lorenzo Minutolo developed a web based platform for quickly locating and recording defect locations.

Rectifiable defects are fixed on the MLA system using custom patterns. The fabrication then proceeds up to the STS step but before the bolometer islands are released. At this point, the wafer is diced and the wafer is hybridized for LED mapping in the JPL ADR cryostat. After wirebonding, the feedline and the heater lines are probed and checked for warm shorts to ground. This only diagnoses defects close to the edge of the line since the thin, long niobium traces are very resistive. Opens and shorts on the feedline are readily evident once the wafer is cold but can be difficult to localize on the wafer through warm probing. In section 5.3, we discuss Time

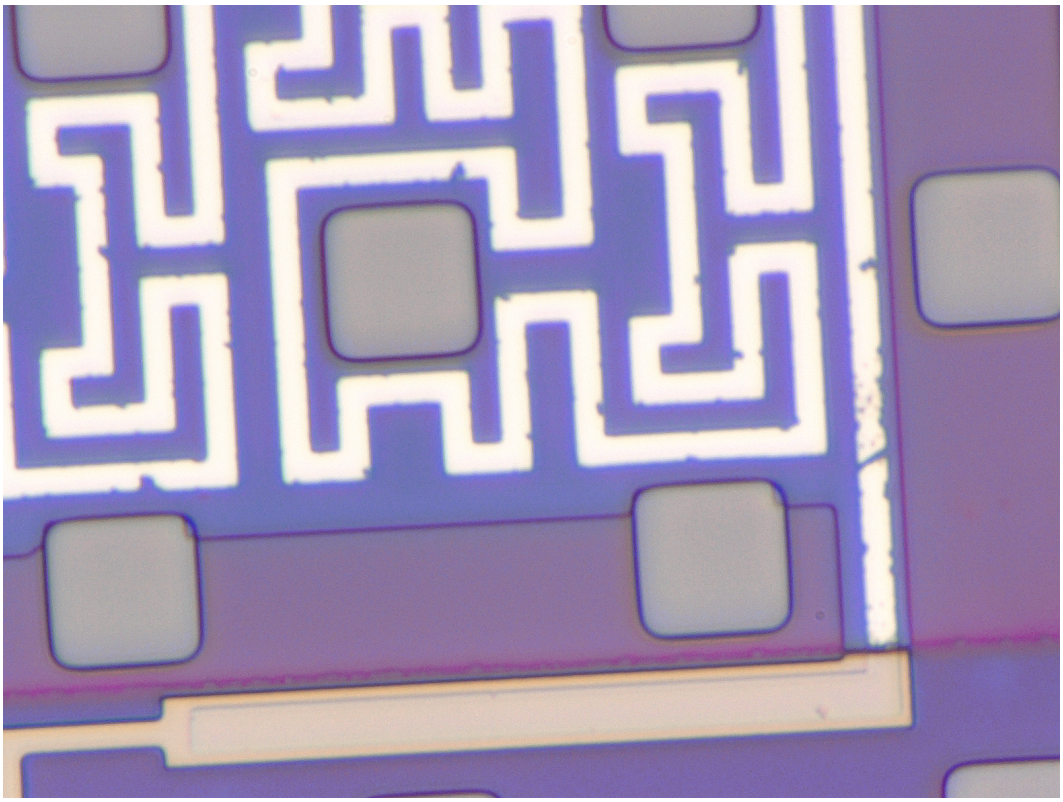

Figure 5.23: A line break across an inductor.

Domain Reflectometry (TDR) as an indispensable tool for identifying the type and resolving the physical location of defects along the line.

Resonators that did not yield as identified during the LED mapping are targets for further inspections. This often reveals more subtle defects such as the via shorts discussed previously or breaks in the inductor line as shown in fig. 5.23. However, it is often impractical to fix individual broken resonators. Rather, the inspections are used to further refine the fabrication process for future wafers.

After the first cooldown, a capacitor trimming layout is generated to adjust the locations of the resonators by trimming capacitor fingers to make the arrays more uniform in frequency spacing. The trimming layout is shot on the MLA and any final fixes to the wafer are performed before releasing the wafer. After release, the wafer either hybridized for dark testing in the JPL cryostat, or hybridized onto the focal plane for optical testing at Caltech.

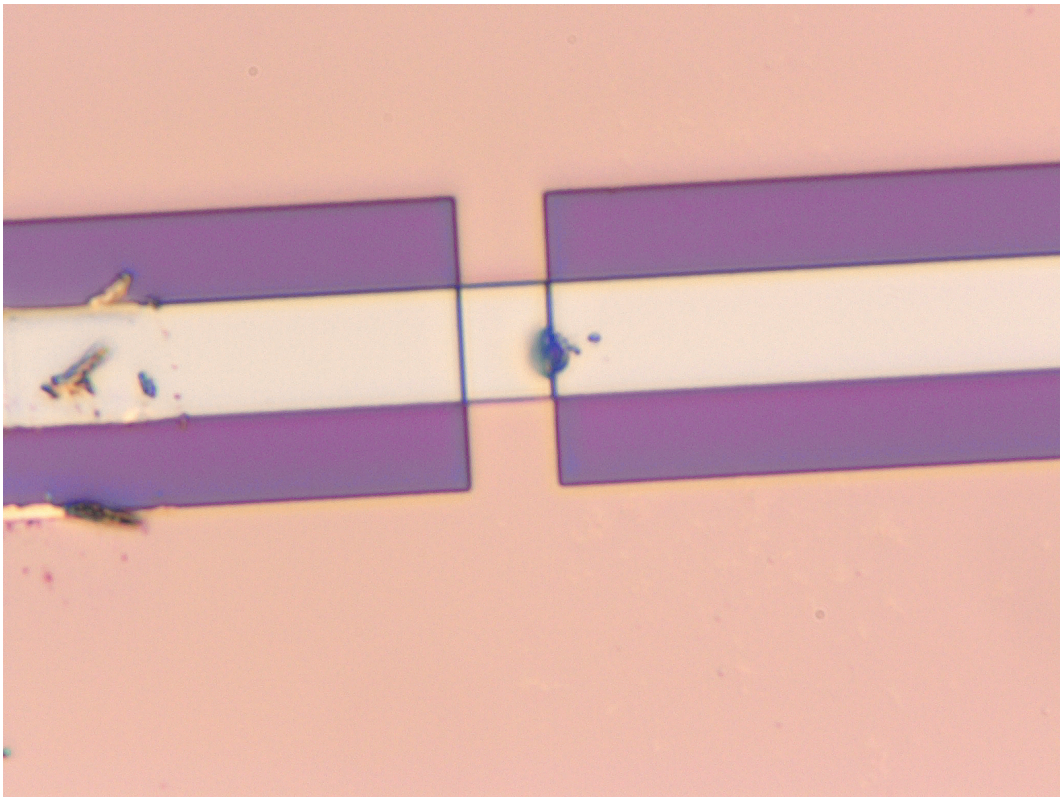

Figure 5.24: A defect on the feedline causing a short to GND.

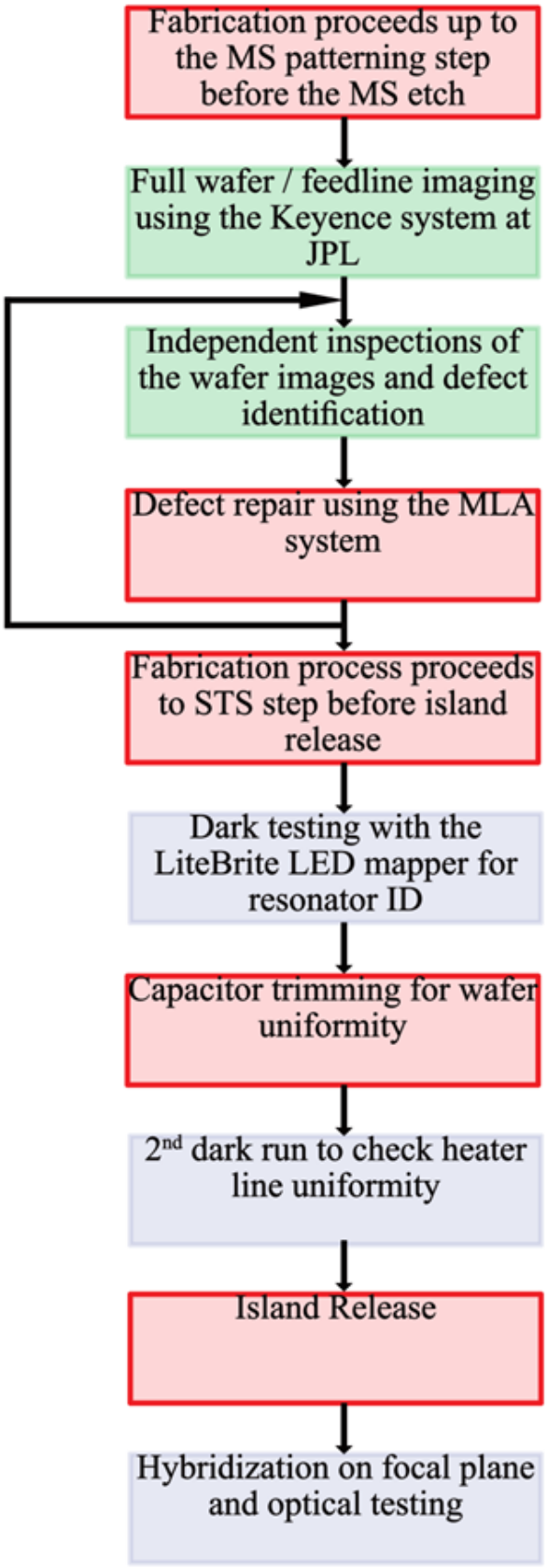

Figure 5.25: An overview of the steps involved in fabrication of TKID tiles.

Time Domain Reflectometry (TDR)

The total length of the 8 μm wide feedline on the tile is 0.854m. This makes the feedline difficult to inspect visually due to the duration of time needed to image the tile at high enough resolution to visualize defects. We, however, found that time domain reflectometry (TDR) is a reliable approach to localizing and identifying the nature of defects along the line. To do so, we make use of an already have a spare set of RF lines through the cryostat. All the attenuators and the cold amplifier were removed from the RF chain.

Time domain analysis was used to investigate a potential defects on the CF230402 tile, which showed low transmission on cooldown. Each of the lines was calibrated independently using a Short-Open-Load (SOL) calibration standard. At 3 K, the resistance to GND on both the RX and TX sides of the tile was open. Measurements were taken over the full frequency range of the Copper Mountain VNA [5] (20 kHz – 4.8GHz) using 54401 points.

The lowpass impulse measurement setup gives the most utility. This is done in reflection mode, which measures the reflection coefficient as a function of frequency. The impulse response is generated by convolving the input pulse with the transfer function relating the incident voltage and the reflected voltage. Lowpass mode is useful where the device under test (DUT) is expected to be transmissive down to DC. It also requires that the data points be linearly spaced with the stop frequency harmonically related to the start frequency. All of this is done automatically by the software. The DC value (which is not directly measured by a VNA) must be extrapolated. The negative frequency response is also taken to be the conjugate of the real frequency response to give a purely real time domain response. Because of this the lowpass measurement has better resolution for a given frequency span when compared to the bandpass response. Better yet, the time domain response contains information not only about the type of discontinuity that is present, but additionally, the type of impedance change that is present. The interpretation can be a bit tricky and subject to the resolution of the scan. An open in the line is a (near) unity positive peak while a short looks like a (near) unity negative peak. On the other hand, an inductive discontinuity looks like a small positive peak followed by an equal magnitude negative peak while a capacitive discontinuity looks like a small negative peak followed by a positive peak.

The lowpass impulse response over the 20 kHz – 1 GHz is summarized in fig. 5.26

[5] https://coppermountaintech.com/50-ohm-vnas/

for both the RX and TX ports. In the raw data, there is a large reflection at 2.8123 ns away from the TX port. This reflection exactly matches the one 8.1936 ns away from the RX port for a total length between reference planes of 11.0059 ns. The length of the RF line from the VNA to the RX port is 13.023 ns, and to the TX port is 13.063 ns.

After warming up the tile, the measured the distance from the RX and TX reference planes to the line open with the tile installed (but at room temperature) was found to be 0.7311 ns and 0.0689 ns, respectively. With the tile removed and the lines left open the distance to the open shifts down to 0.0422 ns and 0.7029 ns. We therefore conclude that the contribution from the PCB + wirebonds is 0.0282 ns and 0.0267 ns on the RX and TX sides, respectively. This gives a total tile delay of 10.2059 ns. We can expect to find the defect on the transmission line at about 27.5% of the way down the line from the TX port.

In follow up using a microscope system, we identified the open in the feedline between the capacitors for R7C6A and R8C5B; about 30.1% of the way down the feedline from the left bondpad. This matches the expected defect location with less than 5% difference. This defect was subsequently fixed and the wafer was tested. Such a case, exemplifies the utility of TDR as a diagnostic tool for identifying and classifying defects in dense superconducting arrays.

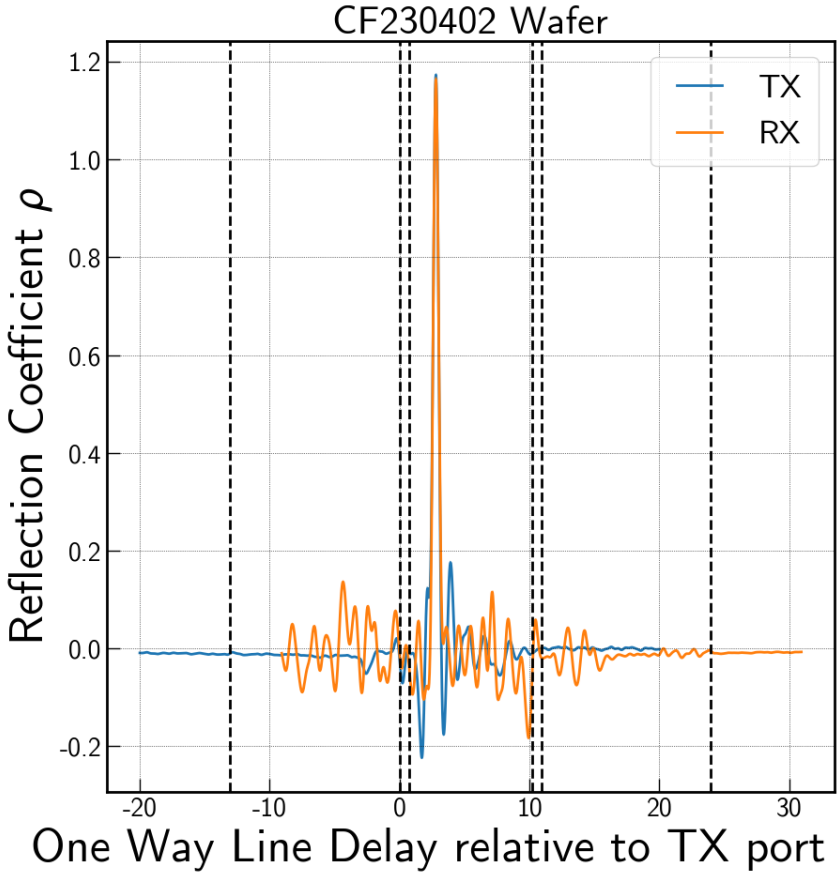

Figure 5.26: Low-pass impulse reflection coefficient matched between the RX and TX side. 0 ns is the reference plane at the TX port. In order from left - right, the vertical lines represent the VNA port, TX reference plane, left bondpad on tile, right bondpad on tile, RX reference plane and finally the VNA port.

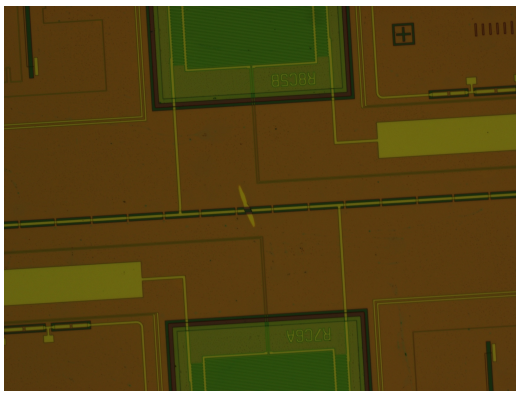

(a)

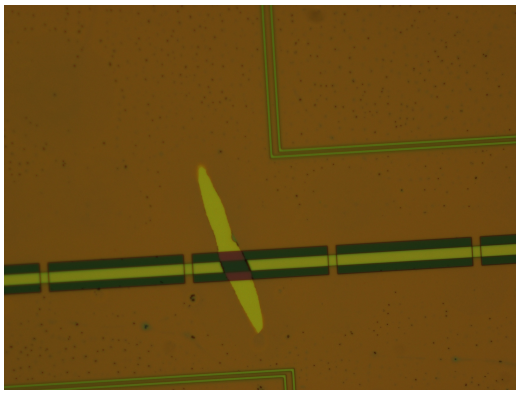

(b)

Figure 5.27: Location of the open on the feedline identified using an optical microscope after localization in a dedicated cooldown to perform Time Domain Reflectometry. This defect was easily fixed and the wafer was recovered and subsequently tested.

Chapter 6

LABORATORY CHARACTERIZATION OF THE 150 GHZ CAMERA

6.1 MLA Tiles: Wafer Yield and Uniformity

We fabricated a total of 16 MLA tiles of which 8 yielded and were LED mapped. The summary of the wafer yield is given in table 6.1.

Wafer ID	Detector Yield (128 total)	Pair Yield (64 total)
CF210430	65	10
CF210615	103	45
CF220629	29	1
CF220630	32	1
CF221020	70	15
CF230110	88	27
CF230111	86	28
CF230112	51	8

Table 6.1: A summary of the resonator yield across all MLA tiles. The low pair yield is due to defects in the inductor due to the limited resolution of the laser writer.

The resonators showed significant scatter away from design as shown in fig. 6.1. One way to proceed quantitatively is to consider the resonator frequencies as designed as defining a reference probability distribution. We can then compare the empirically derived measured distributions and assess how similar the two distributions are. One such test is the Kolmogorov-Smirnov (KS) test. Given a reference cumulative distribution function $F(x)$ and a measured distribution $F_n(x)$, the KS statistic, D_n is the largest absolute difference between the two distributions across all values of x.

$$D_n = \sup_x |F_n(x) - F(x)| \tag{6.1}$$

With a set threshold, $\alpha = 0.05$, the null hypothesis is rejected for all but the last three wafers fabricated (CF230110, CF230111, CF230112). The cumulative distribution functions for all yielded resonators are shown in fig. 6.2

In the MLA design, we were also interested in identifying significant systematic shifts in the resonator properties that could correlate with effects unaccounted for in

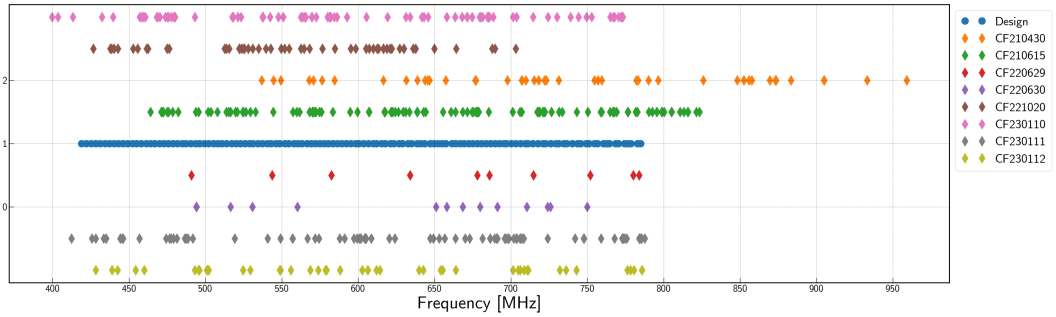

Figure 6.1: A comparison of the resonance frequency scatter between design and measurement.

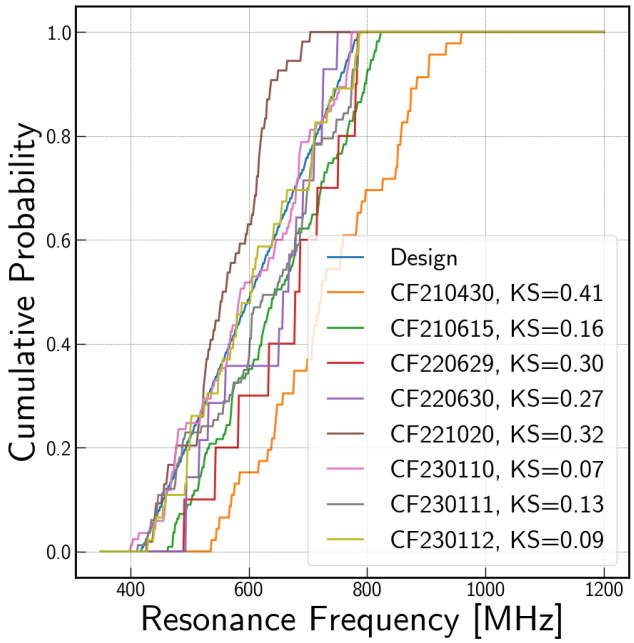

Figure 6.2: Cumulative distribution function of the resonator frequency locations for all 8 yielded wafers.

the design or point to repeatable fabrication defects. The frequency scatter, Q_i, Q_c and ϕ_c across all wafers are summarized in fig. 6.3.

6.2 Ex-3 Tiles: Wafer Yield and Uniformity

3 Ex-3 tiles yielded and were LED mapped. Both the total detector yield and the pair yield are much higher for the Ex-3 in comparison to the MLA version of the 150 GHz design (table 6.2).

Quantitatively, the KS test shows that the measured frequency distribution of the 3 yielded tiles is significantly different from design but are all consistent with each other (see figs. 6.4 and 6.5).

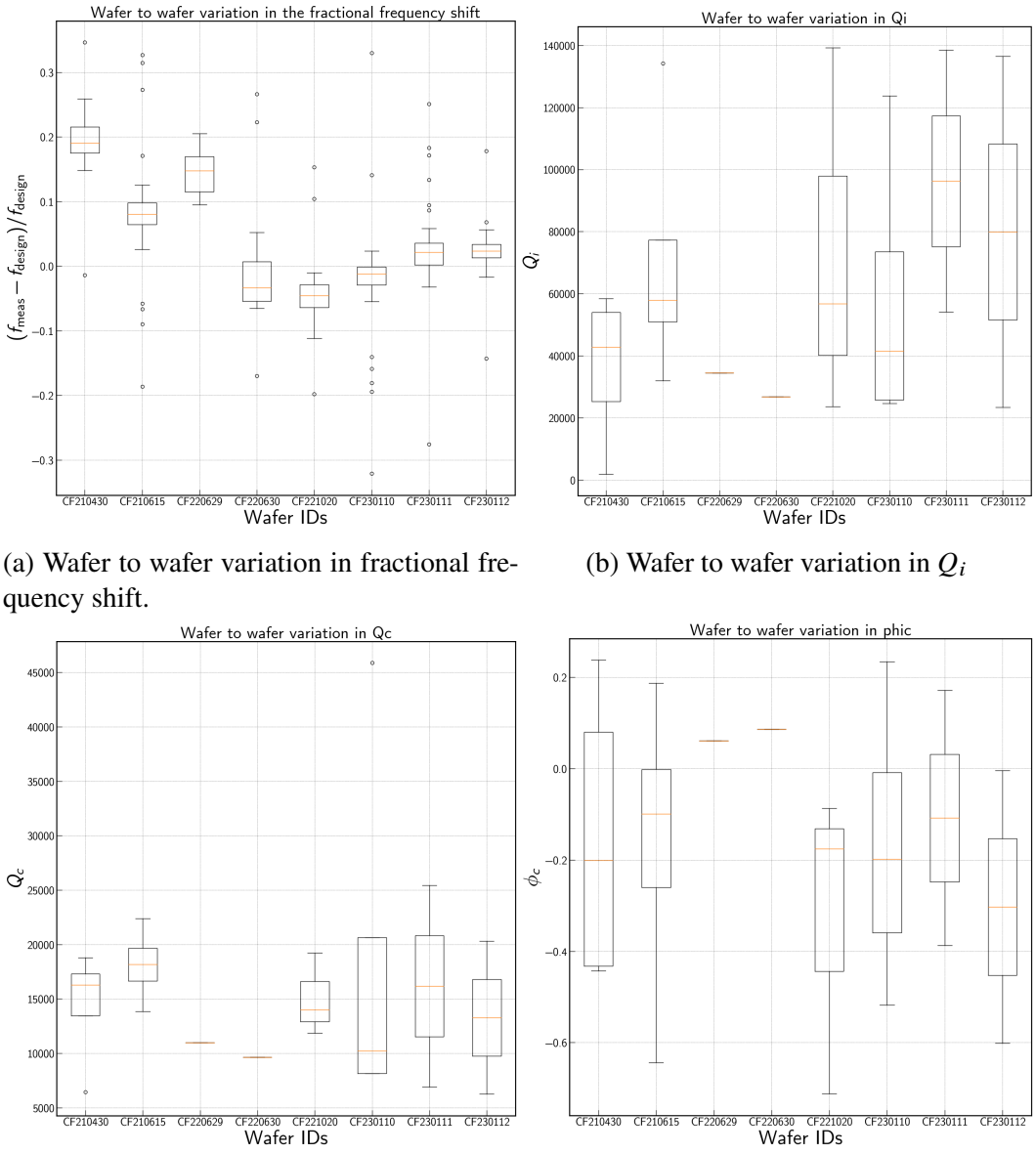

(a) Wafer to wafer variation in fractional frequency shift.

(b) Wafer to wafer variation in Q_i

(c) Wafer to wafer variation in Q_c.

(d) Wafer to wafer variation in ϕ_c.

Figure 6.3: Box plots summarizing resonator properties across all yielded MLA wafers. The red bar is the median and the box captures the first to 3rd quartile. Outliers are shown as single points.

Wafer ID	Detector Yield (128 total)	Pair Yield (64 total)
CF230403	107	39
CF230529	100	39
CF230531	87	32

Table 6.2: A summary of the resonator yield across all Ex-3 tiles. The low pair yield is due to defects in the inductor due to the limited resolution of the laser writer.

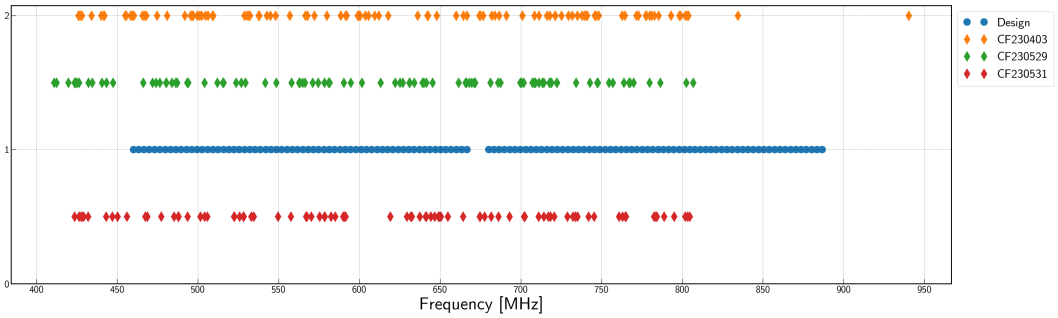

Figure 6.4: A comparison of the resonance frequency scatter between design and measurement for the Ex-3 tiles. All polarization A detectors are in the lower frequency band and all polarization B detectors are in the upper band. The gap is maintained but shifted with frequency scatter from fabrication.

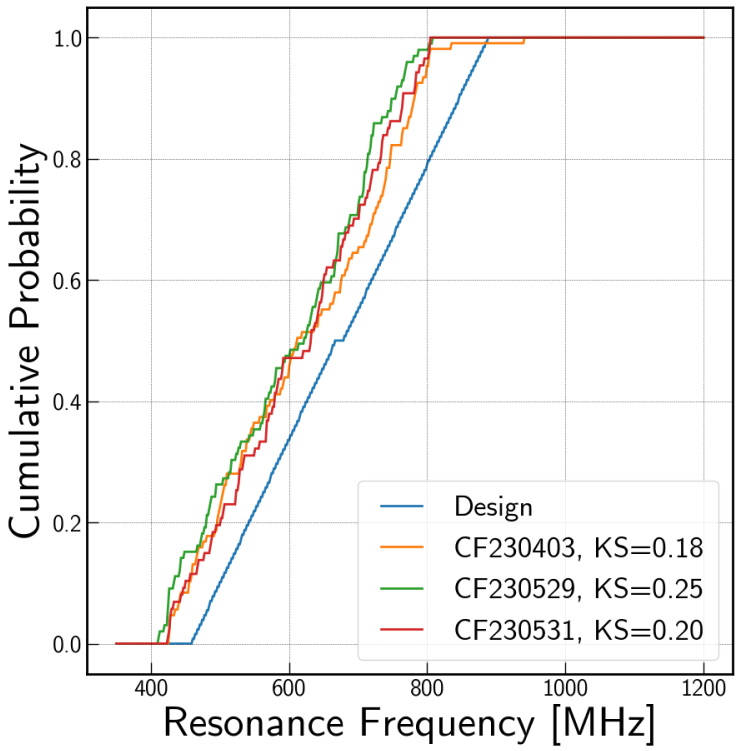

Figure 6.5: Cumulative distribution function of the resonator frequency locations for the 3 yielded Ex-3 tiles.

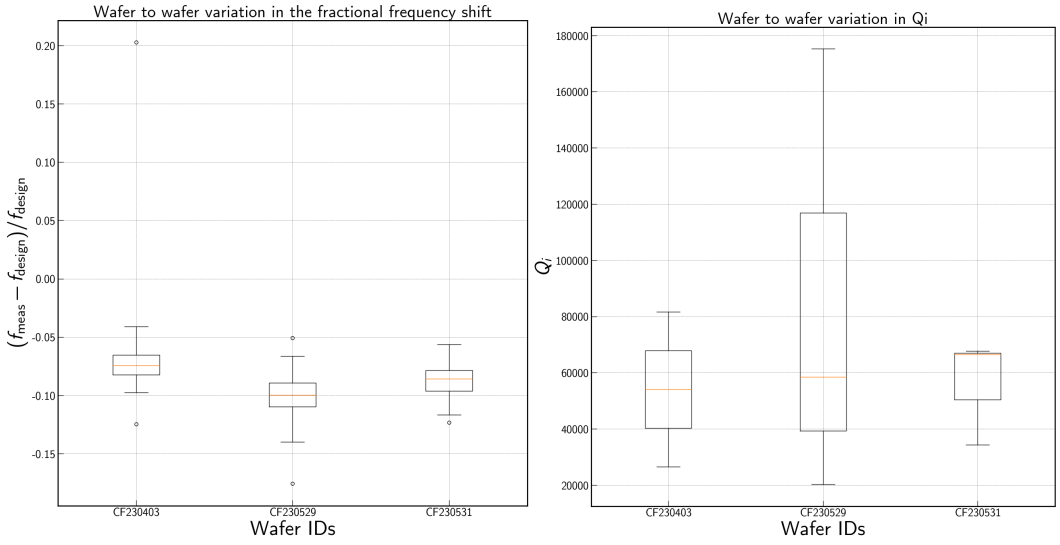

(a) Wafer to wafer variation in fractional frequency shift.

(b) Wafer to wafer variation in Q_i.

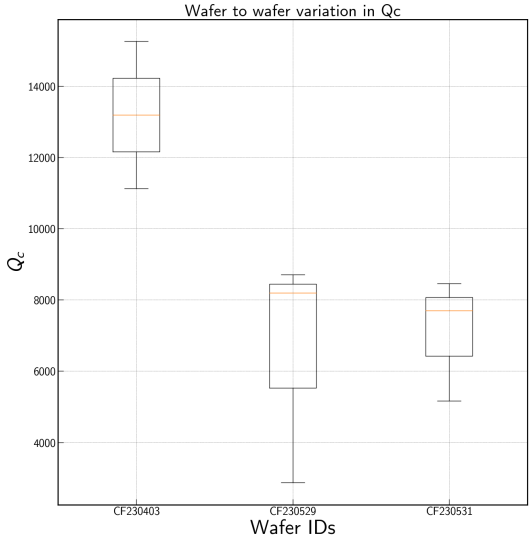

(c) Wafer to wafer variation in Q_c.

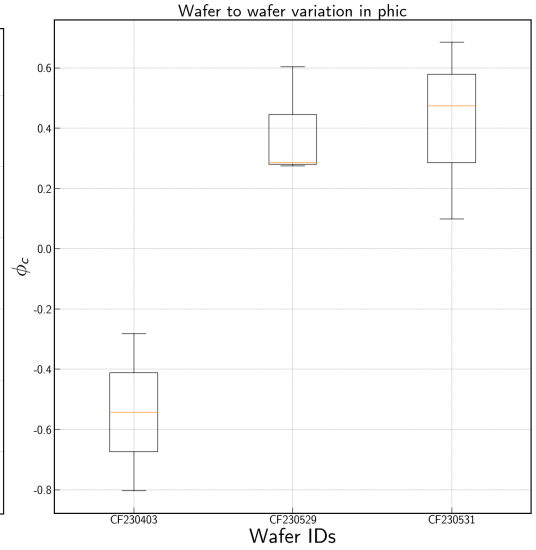

(d) Wafer to wafer variation in ϕ_c.

Figure 6.6: Box plots summarizing resonator properties across all yielded Ex-3 wafers. The red bar is the median and the box captures the first to 3rd quartile. Outliers are shown as single points

6.3 Resonator Characterization

This section summarizes the resonator properties across the entire wafer for three Ex-3 TKID tiles: CF230403, CF230529 and CF230531. Measured detector properties can deviate from design due to both unaccounted effects during the design as well as the fabrication process. During fabrication, variation in deposited metal or dielectric film thickness across the wafer or differences in etch rates can create dispersion in

the detector properties. To check for fabrication effects, we make wafer maps of the resonance frequency, and quality factors across the tile. A radial gradient in resonator frequency across the tile for example, would point to the effect of aluminum film thickness. The distribution of resonators that do not yield across the wafer is also informative. We naturally expect the defect density to be higher along the wafer edges than towards the wafer center. This greatly increases the probability that a resonator along the perimeter of the tile will be impacted and therefore fail to yield.

If the fabrication is consistent from tile to tile, we can assess design systematics by comparing resonator properties across multiple tiles. In design, since the inductor design is fixed, the resonance properties are a function of the properties of the main and coupling capacitances. The goal is to attribute for systematic deviations in resonance properties from their design values to other explanatory variables. We consider effects due to the design frequency, f_{design}, radial position on the wafer R, x and y coordinates of both the inductor and capacitor on the wafer, positioning of the bolometer relative to the antenna, and the location of the resonance along the feedline. The coordinate system on the tile is defined so that the direction of the bondpads is the $+Y$ direction.

In practice, wafer to wafer variation in properties as detailed in section 6.2 makes this procedure difficult. The results presented in this section are therefore largely qualitative rather than quantitative. Even so, we can clearly identify one systematic: the measured coupling quality factors (averaging at around 4000) were much lower than design for all the Ex-3 wafers. This will be accounted for in future resonator design work.

The resonator parameters $[f_r, Q_i, Q_c, \phi_c]$ discussed in the following section were measured at 90 mK in each case.

CF230403

The dispersion of the resonator properties across the CF230403 wafer are summarized in figs. 6.7 to 6.9. The fractional shift in the resonance frequency from design averages at about -7.4% with a few outliers. Both the fractional frequency shift and Q_i show dependence on the Y position of the resonator on the tile.

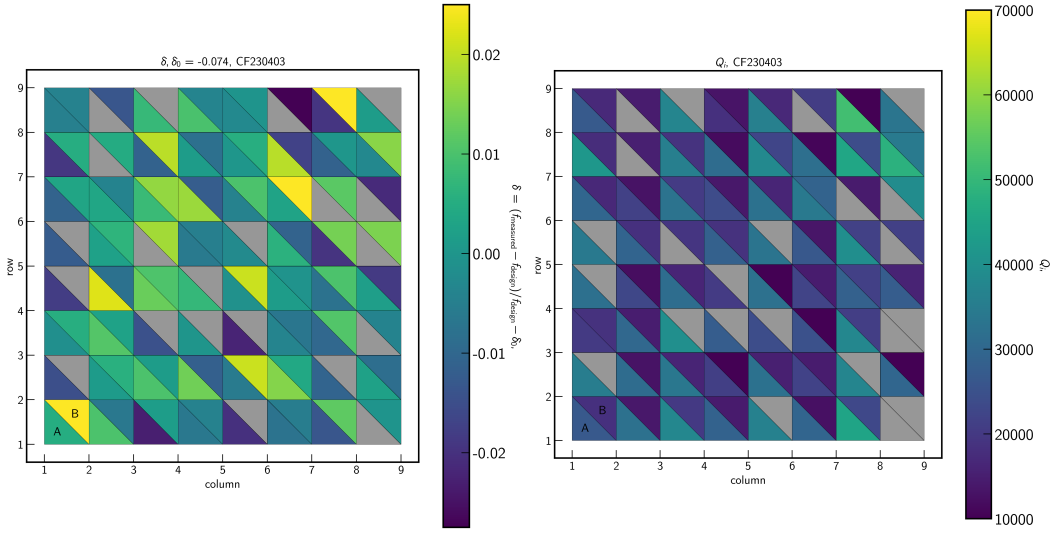

(a) $\delta = \frac{f_{\text{meas}} - f_{\text{design}}}{f_{\text{design}}}$ (b) Q_i

(c) Q_c (d) ϕ_c

Figure 6.7: Tile maps summarizing yield and resonator properties for the CF230403 tile. The wafer is organized in an 8x8 grid. The 2 triangles per square on the wafer grid represent the resonators coupled to the A and B polarizations respectively. Locations in grey represent resonators that failed to yield.

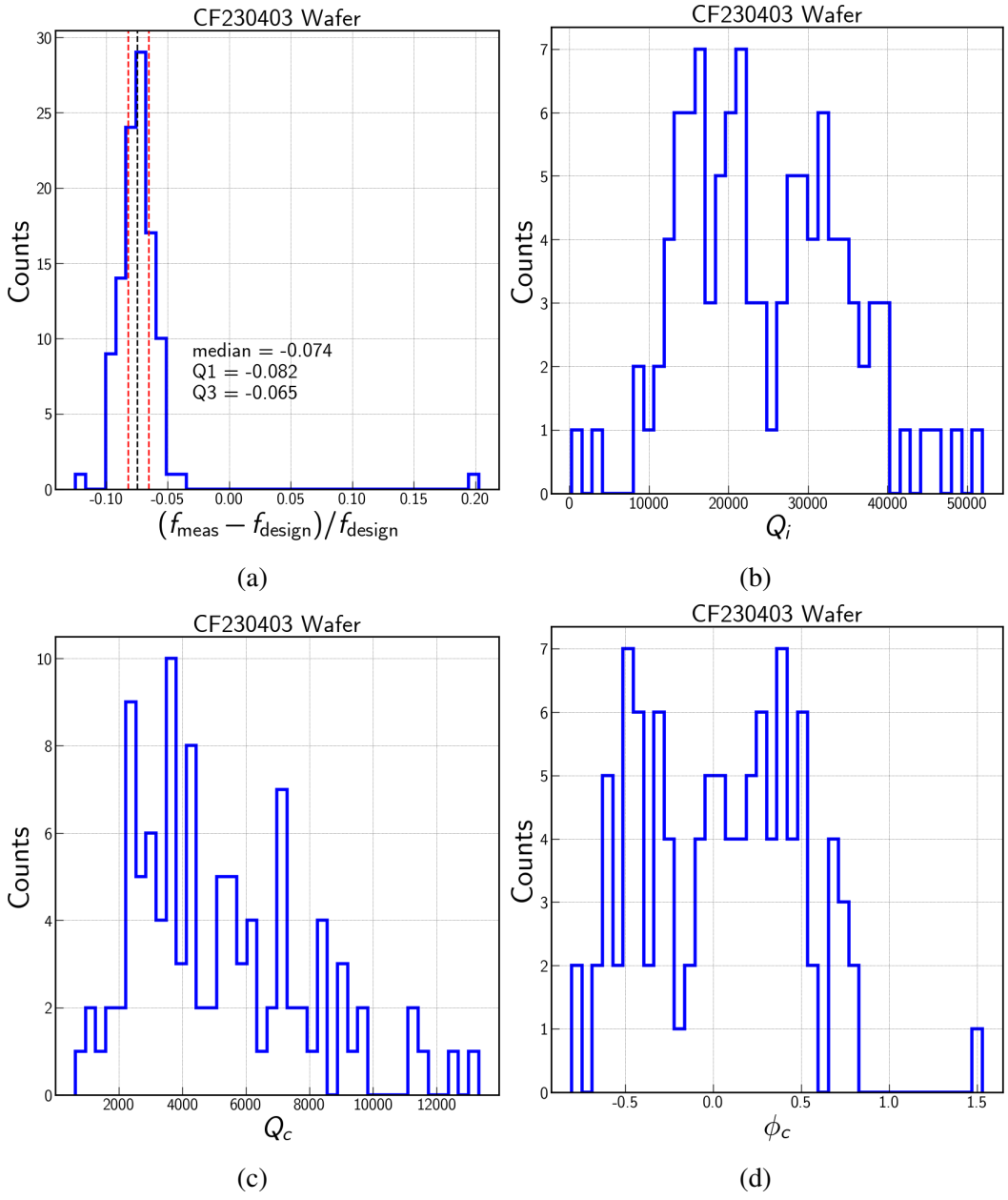

Figure 6.8: Summary histograms for the measured resonance parameters for the CF230403 tile.

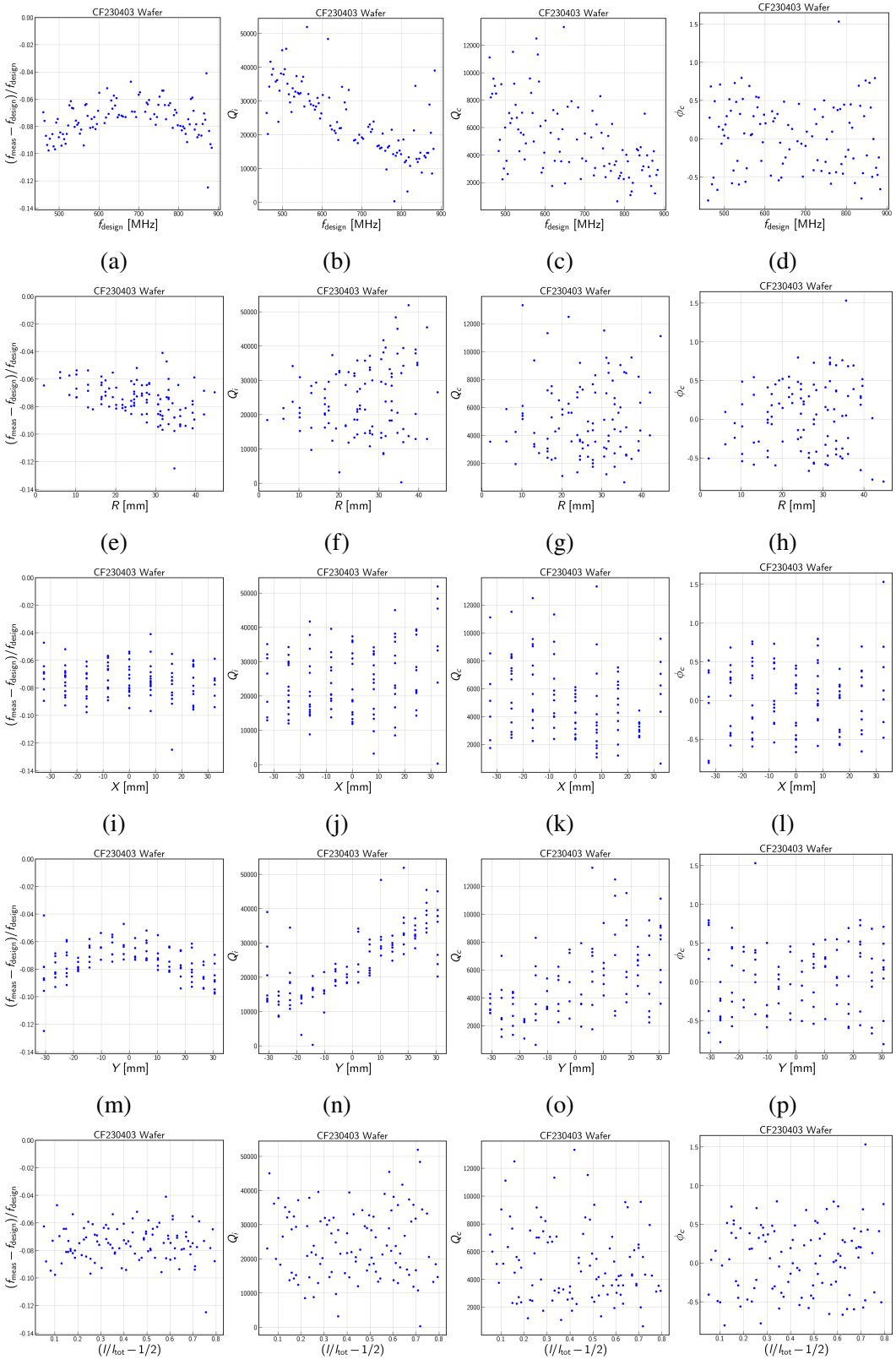

Figure 6.9: Systematic shifts in the resonator properties across the CF230403 tile. From right to left, the resonator parameters are $\delta f_r / f_r, Q_i, Q_c, \phi_c$. From top to bottom, these parameters are plotted against $f_{\text{design}}, R, X, Y$, and fractional distance from the midpoint of the feedline. The coordinates given reference the center point of the inductor on the wafer.

CF230529

The fractional shift in the resonance frequency from design on the CF230529 tile, averages at about -10.0% . This is consistent with CF230403. However, unlike the CF230403 wafer, the fractional frequency shift and Q_i show little if any dependence on the Y position of the resonator on the tile. This distinction is not yet understood. The dispersion of the resonator properties across the CF230529 wafer are summarized in figs. 6.10 to 6.12.

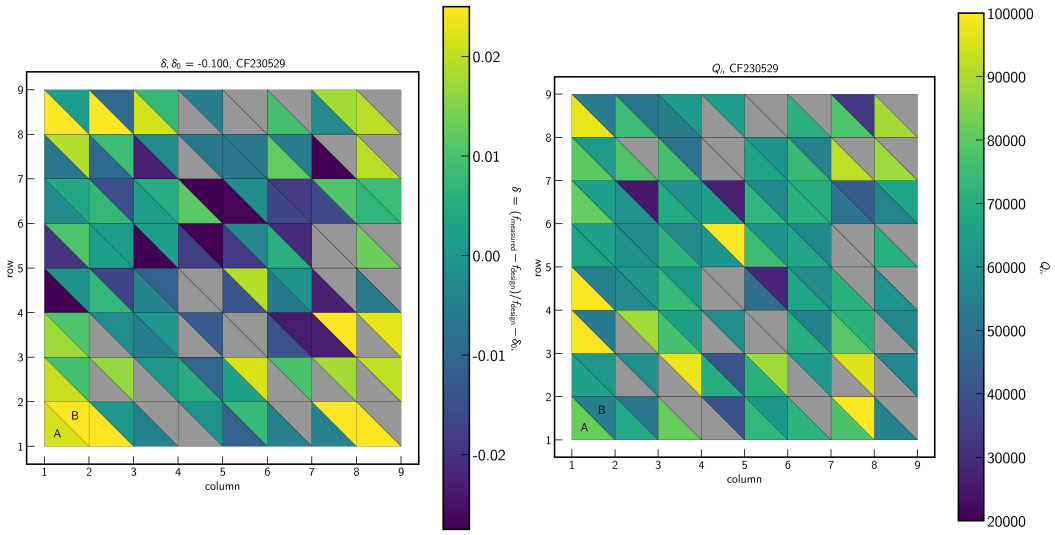

(a) $\delta = \frac{f_{\text{meas}} - f_{\text{design}}}{f_{\text{design}}}$

(b) Q_i

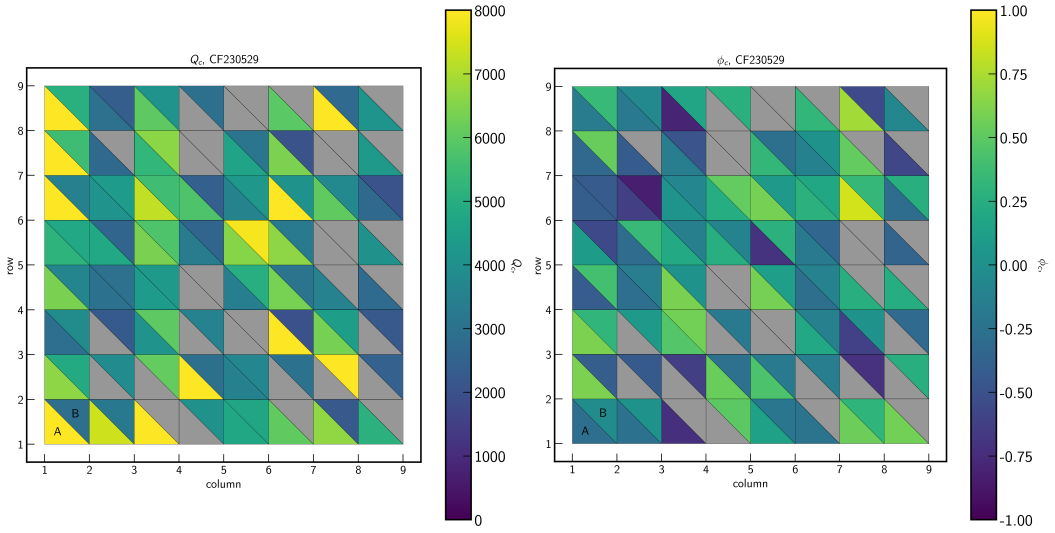

(c) Q_c

(d) ϕ_c

Figure 6.10: Tilemaps summarizing yield and resonator properties for the CF230529 tile. The wafer is organized in an 8x8 grid. The 2 triangles per square on the wafer grid represent the resonators coupled to the A and B polarizations respectively. Locations in grey represent resonators that failed to yield.

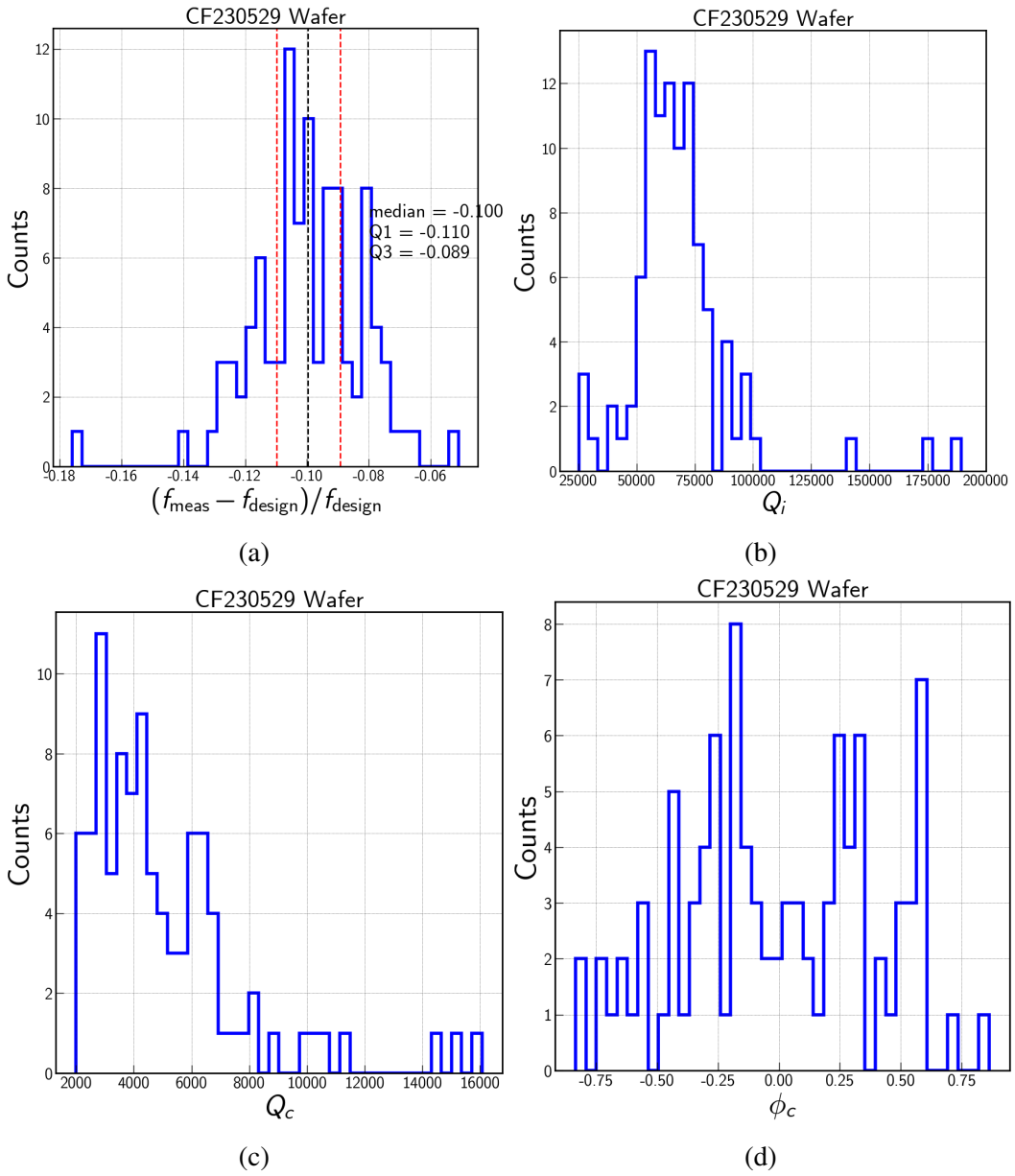

Figure 6.11: Histograms summarizing resonator properties for the CF230529 tile.

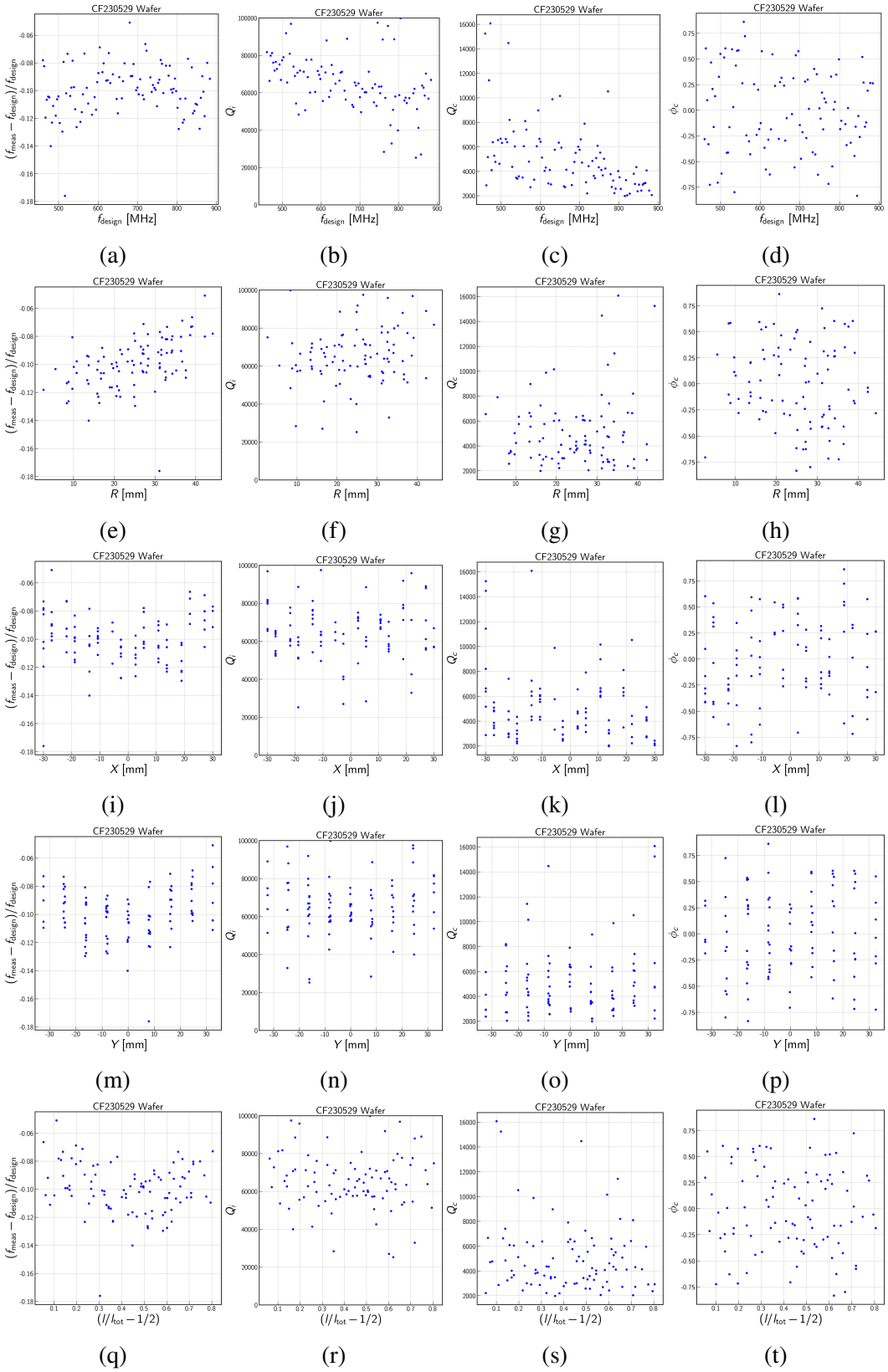

Figure 6.12: Systematic shifts in the resonator properties across the CF230529 tile. From right to left, the resonator parameters are $\delta f_r / f_r, Q_i, Q_c, \phi_c$. From top to bottom, these parameters are plotted against $f_{\text{design}}, R, X, Y$, and fractional distance from the midpoint of the feedline. The coordinates given reference the center point of the inductor on the wafer.

CF230531

Lastly, the dispersion of the resonator properties across the CF230531 wafer are summarized in figs. 6.13 to 6.15. The fractional shift in the resonance frequency from design averages at about -8.6% with a few outliers. The fractional frequency shift shows dependence on the X position of the resonator on the tile.

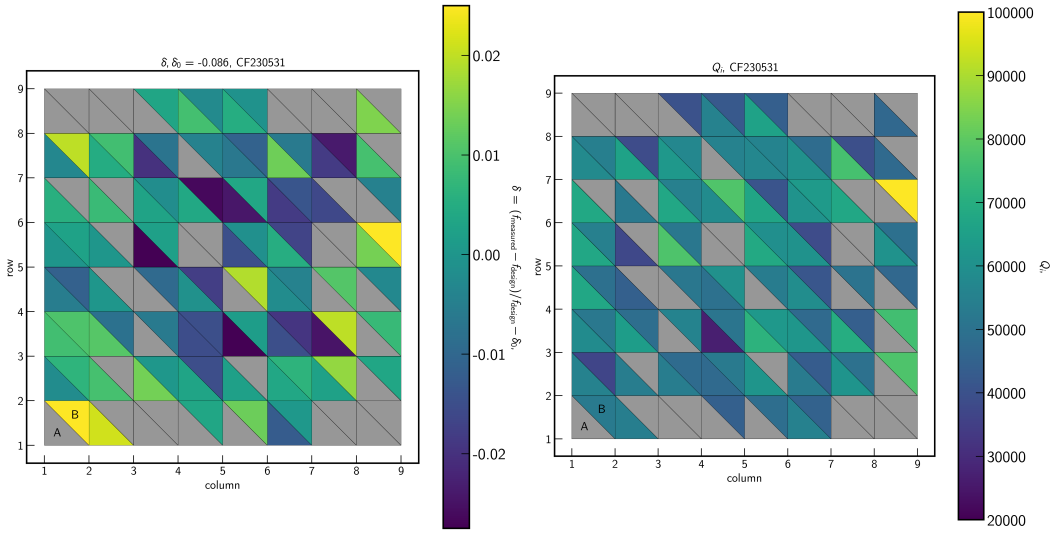

(a) $\delta = \frac{f_{\text{meas}} - f_{\text{design}}}{f_{\text{design}}}$

(b) Q_i

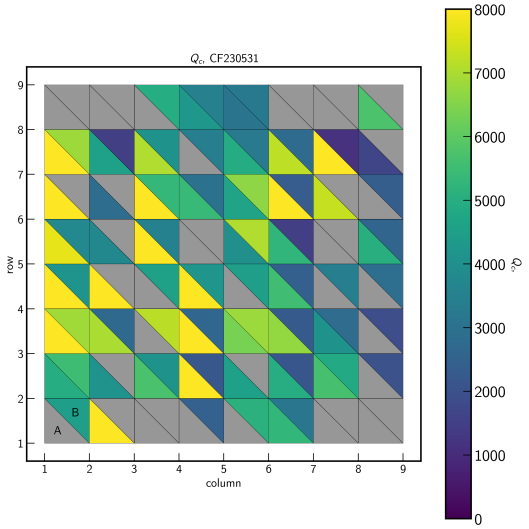

(c) Q_c

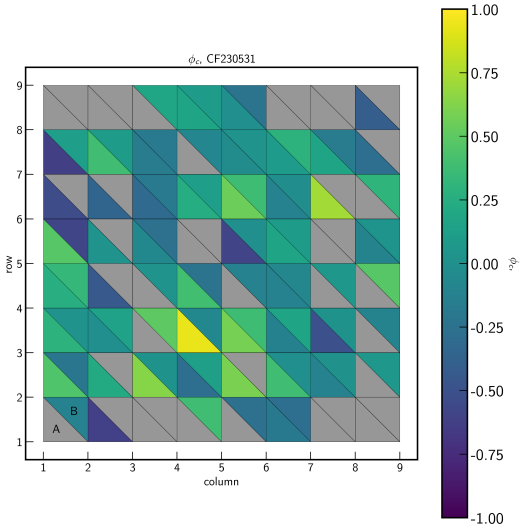

(d) ϕ_c

Figure 6.13: Tilemaps summarizing yield and resonator properties for the CF230531 tile. The wafer is organized in an 8x8 grid. The 2 triangles per square on the wafer grid represent the resonators coupled to the A and B polarizations respectively. Locations in grey represent resonators that failed to yield. The yield hits are largely concentrated along the edges of the wafer.

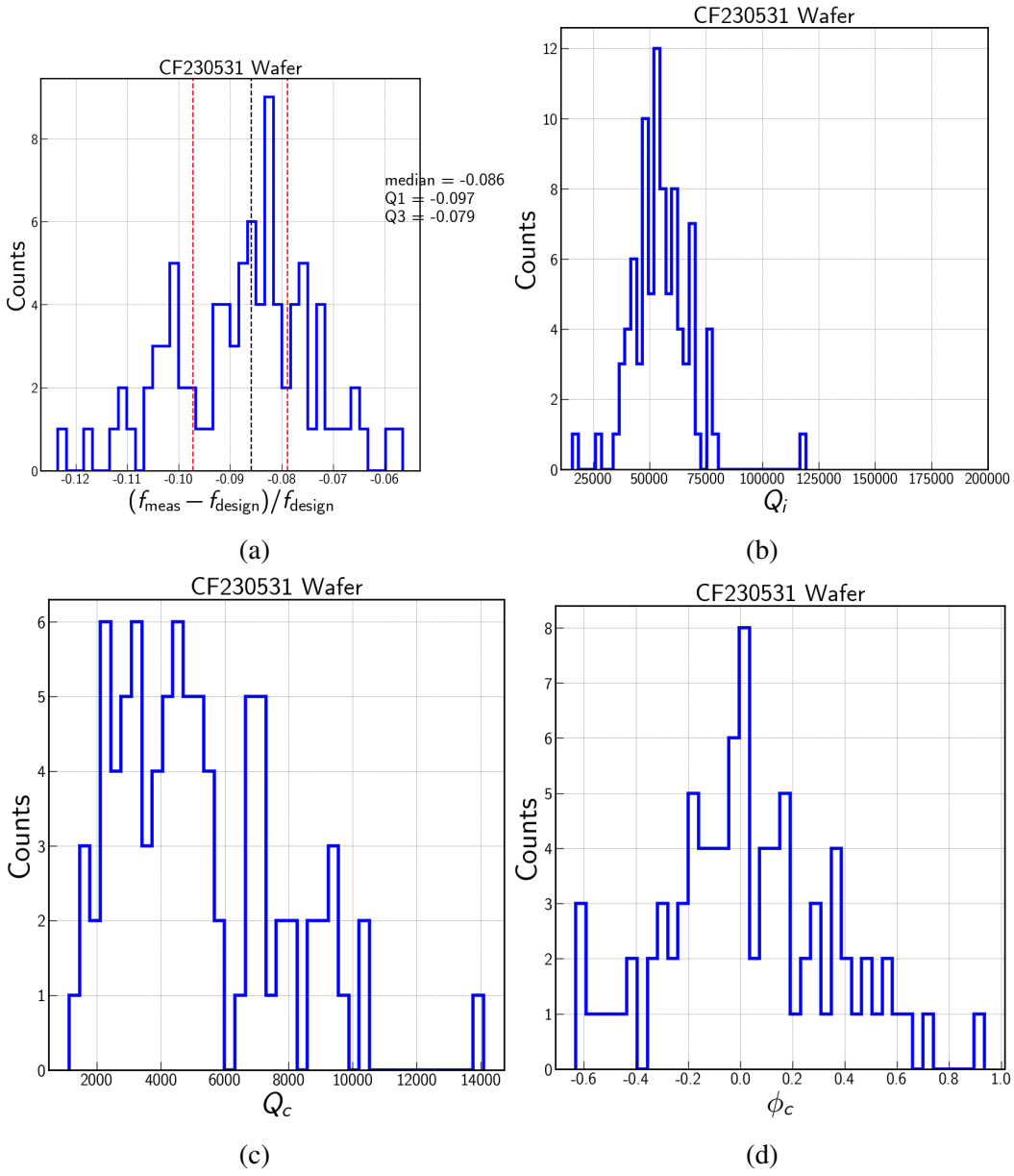

Figure 6.14: Histograms summarizing resonator properties for the CF230531 tile

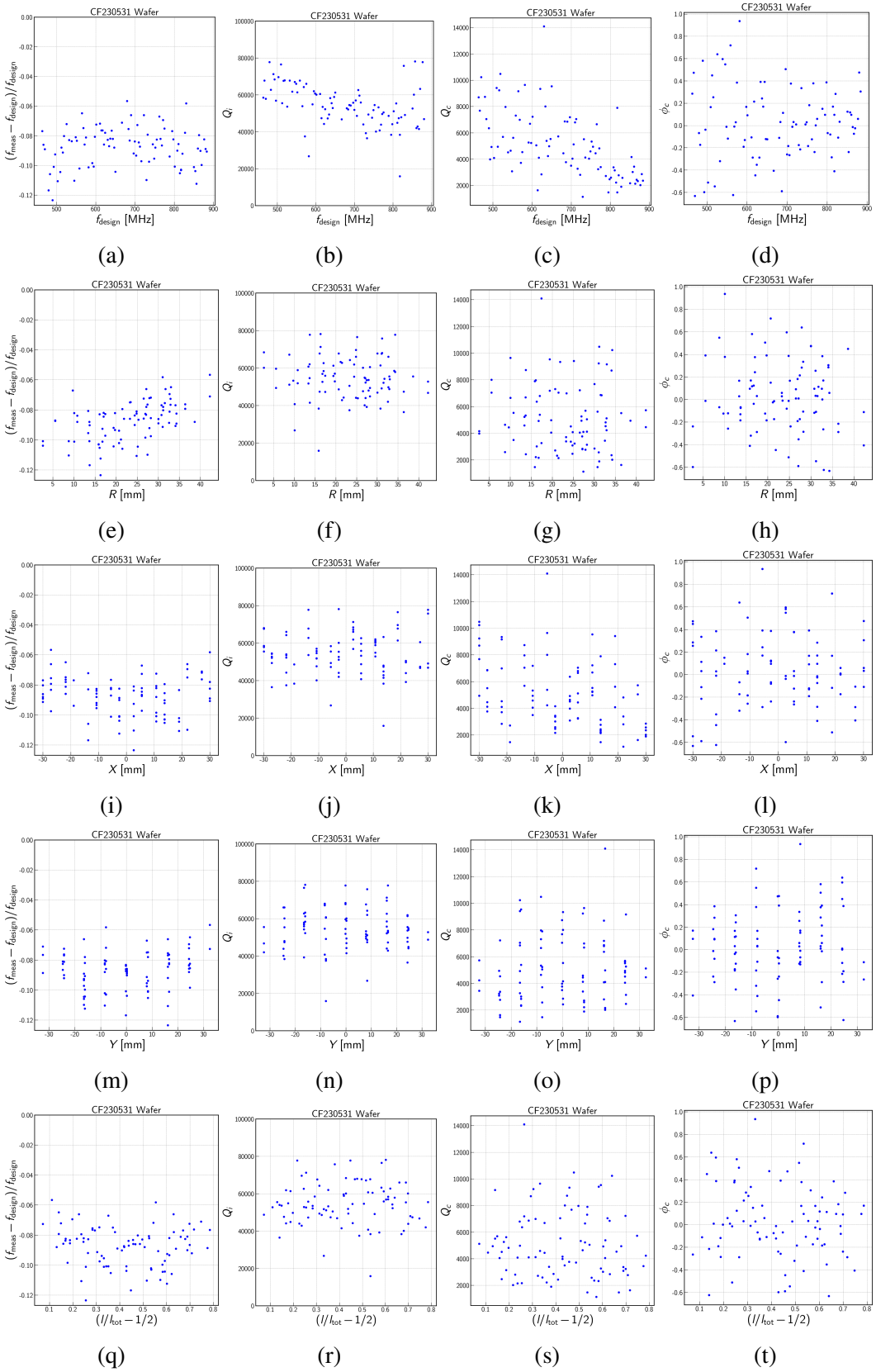

Figure 6.15: Systematic shifts in the resonator properties across the CF230531 tile. From right to left, the resonator parameters are $\delta f_r / f_r, Q_i, Q_c, \phi_c$. From top to bottom, these parameters are plotted against $f_{\text{design}}, R, X, Y$, and fractional distance from the midpoint of the feedline. The coordinates given reference the center point of the inductor on the wafer.

6.4 Resonator Trimming

On a TKID wafer with high multiplexing density, resonator collisions are a serious problem that can significantly limit the array yield. Resonance frequencies must inevitably be shifted from their design values due to variations in film thickness, superconducting film properties, or over-etch depth across the wafer. Resonator collisions occur when two resonators shift such that they overlap and are difficult to read out due to crosstalk section 2.11. A common approach to remedy this is to implement a successive round of design and fabrication to adjust the resonances to produce a wafer with a regular frequency spacing and minimal crosstalk. This is achieved by trimming fingers off the capacitor to adjust the resonance frequencies from their measured positions.

In TKIDs, this procedure is complicated by the temperature dependence of the resonator properties. Differences in T_c for example, cause adjacent resonators to shift by different amounts. The line crosstalk has non-trivial dependence on the measured temperature. To account for this, the resonances are measured at 250 mK both before and after the trimming procedure. This temperature was chosen because is the expected bath temperature of of the focal plane during field operation.

Trimming Strategy

In chapter 5, I presented a phenomenological model of the resonance frequency as a function of the number of fingers in the IDC. After fabrication, we only see a subset of the total number of resonances on the wafer. The parameters that set the resonance frequency as given in eq. (5.1), all shift from the design values. The new set of local variables is unknown. However, we can refit the measured noise data to obtain a new set of global fit parameters as shown in fig. 6.16. The fractional residuals on the fit are about 0.25%, much smaller than the design spacing between adjacent resonators. The new global variables are therefore a suitable reference for determining the trimming. Since $\alpha \ll \beta, \epsilon$, we drop it as a variable in the fitting. To illustrate this procedure, we consider the CF230531 wafer here.

According to this model, the fractional frequency shift δf_r as a function of δx given $x = N/N_0$, (N is the number of fingers and $N_0 = 800$ is a normalizing factor) is

$$\frac{\delta f_r}{f_r} = -\frac{\delta x}{2x}\frac{2\beta x + 1}{1 + \beta x + \epsilon/x}. \tag{6.2}$$

Because this relation only holds for small changes in the resonance frequency, we

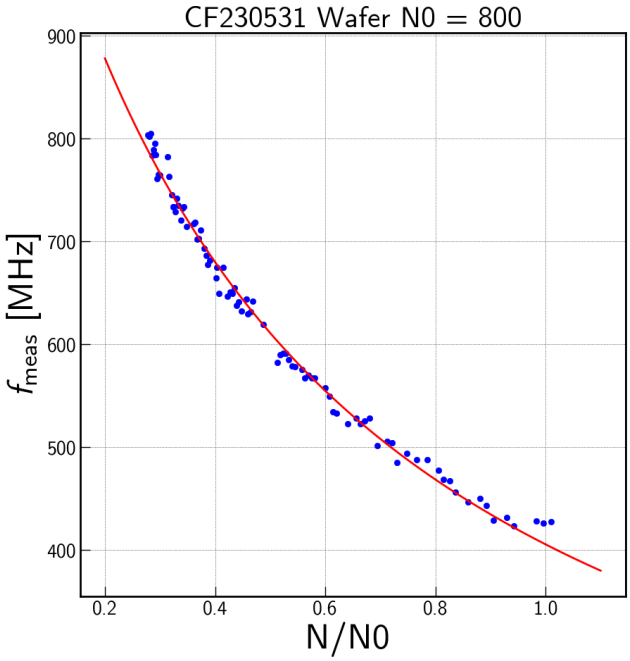

Figure 6.16: Measured resonance frequencies as a function of the number of fingers in the capacitor. The red curve is a fit of the resonance frequencies to the model eq. (5.1). The largest capacitors show the strongest deviation from this model.

aim to minimize the number of fingers to be trimmed. Since we can only remove capacitor fingers, the new frequency schedule must be strictly greater than or equal to the measured frequencies for the same measurement conditions. This condition is naturally satisfied by the convex hull of the distribution of the resonator frequencies after sorting and indexing in ascending order with frequency. The convex hull is piece-wise linear for all wafers considered. We additionally add a small offset of about 2 MHz to define a new frequency schedule. This is illustrated well in fig. 6.17. For the tiles considered, this procedure limits the percentage of the IDC that is trimmed to less than 10 % in the worst case (fig. 6.18).

Improvements to wafer uniformity for CF230531

The impact of trimming on the CF230531 wafer is visually evident as is reflected in the more uniform spacing across the readout bandwidth shown in fig. 6.21. More quantitatively of the trimming on the line crosstalk is summarized in the measured crosstalk as shown in fig. 6.19. As fig. 6.21, trimming is less successful for the highest frequency resonators in the array. This is to be expected since the number of fingers in the IDC decreases with increasing resonance frequency. The fractional change in capacitance is therefore much larger and unaccounted for effects in the

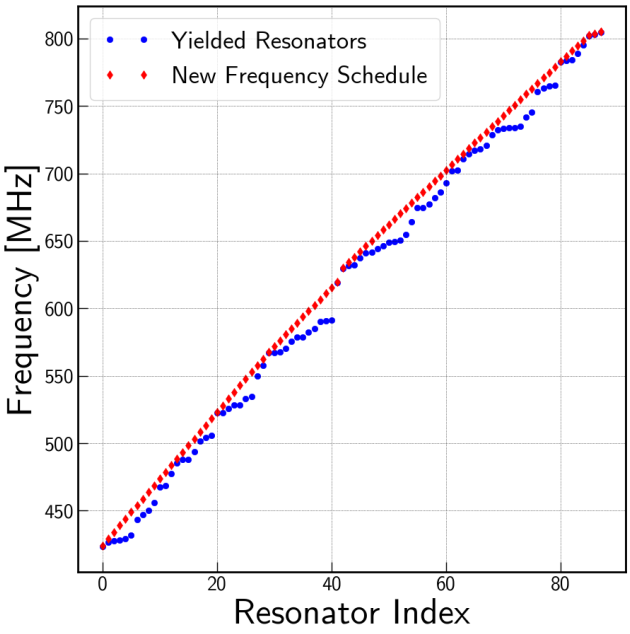

Figure 6.17: Measured resonance frequencies as a function of the resonator index sorted by frequency. The convex hull of this plot is used to determine the new frequency schedule. The gap in resonance frequencies at around index 40 preserves the larger gap between resonators reading out polarization A vs. B on the array.

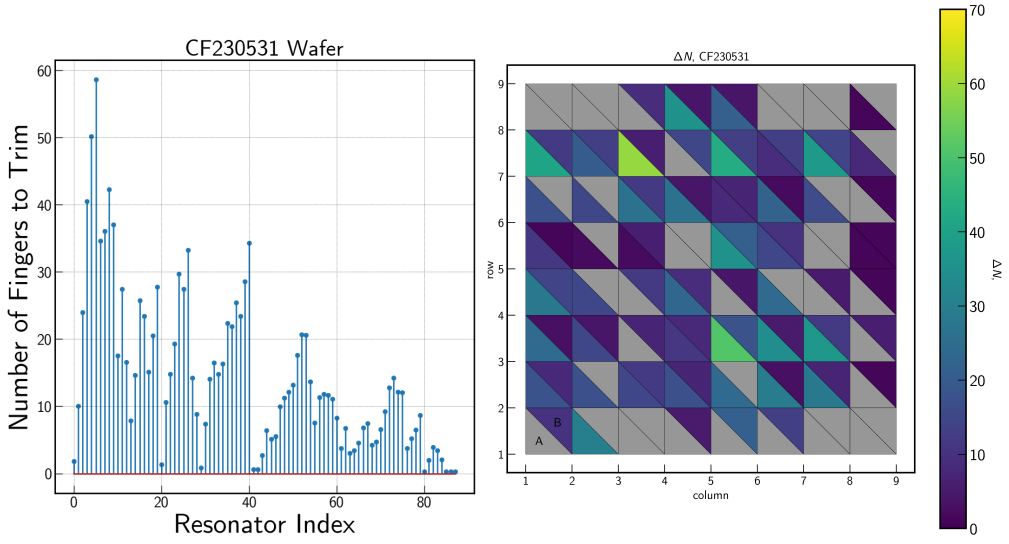

(a) (b)

Figure 6.18: A summary of the number of capacitor fingers to trim for the CF230531 wafer. (Left): Number of capacitor fingers to trim as a function of the resonator index. (Right): Distribution of the number of capacitor fingers to trim across the wafer.

resonator placement become more important.

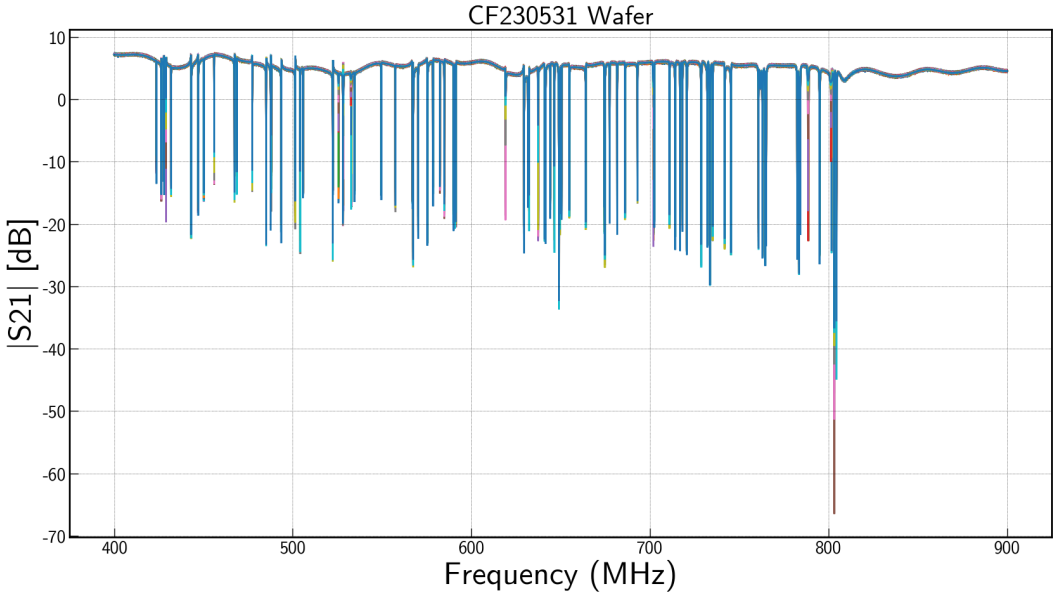

(a) Before Trimming

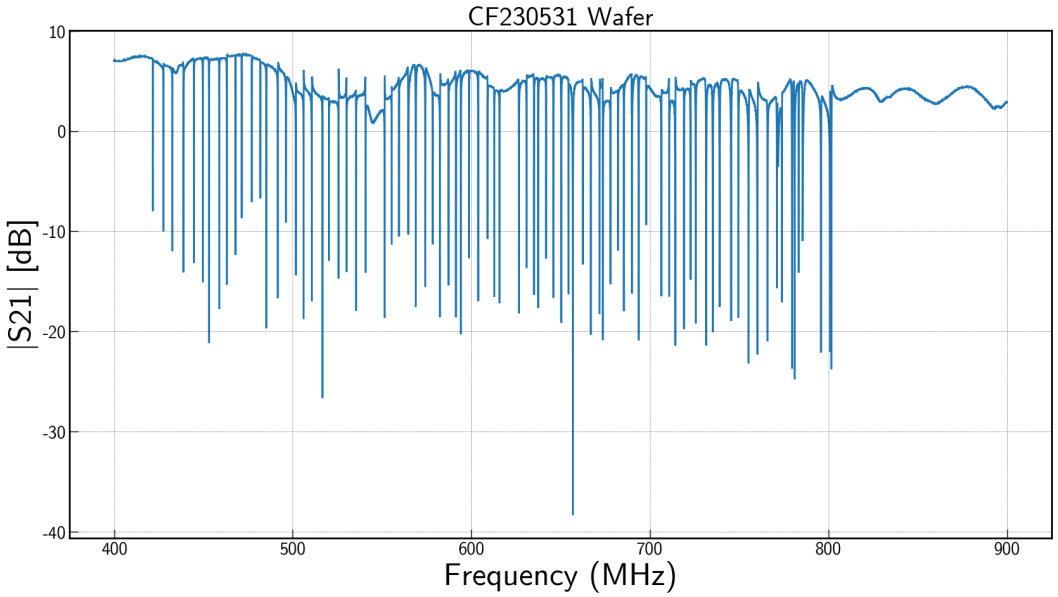

(b) After Trimming

Figure 6.19: Improvement in wafer uniformity through resonator trimming. The resonance frequencies are measured at 250 mK both before (fig. 6.19a) and after trimming (fig. 6.19b). The gap at 600 MHz in fig. 6.19a separates the resonators corresponding to polarization A vs. B on the wafer. This gap is preserved in fig. 6.19b but shifted up to about 630 MHz.

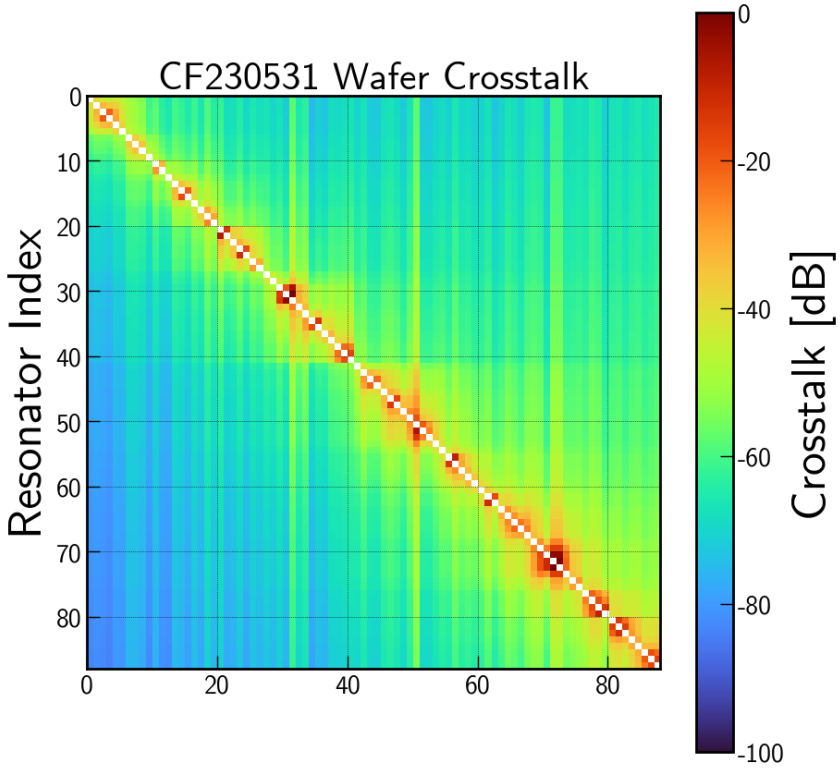

(a) Before Trimming

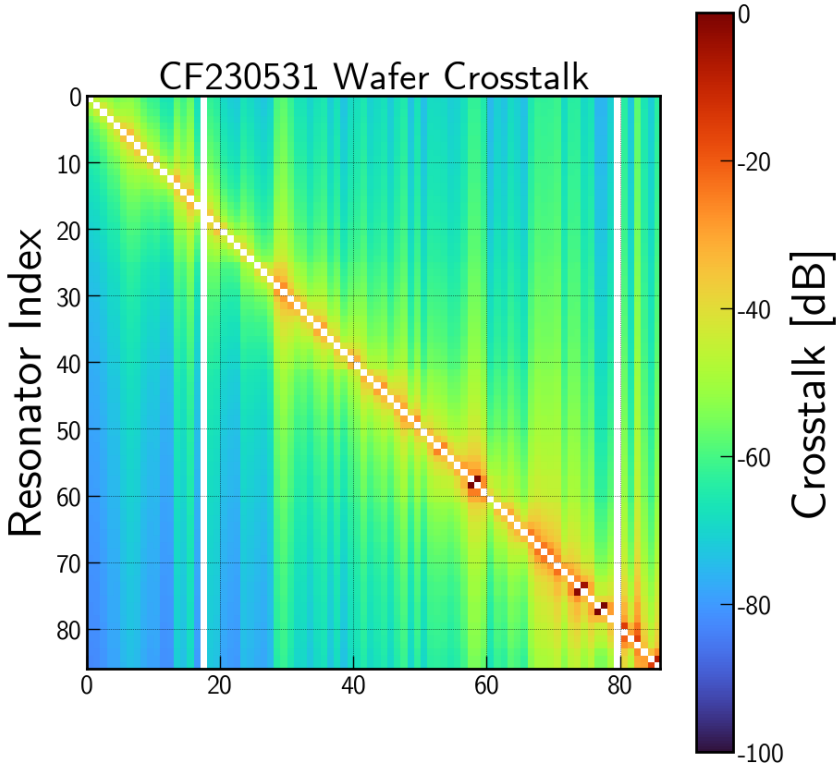

(b) Before Trimming

Figure 6.20: Reduction in line crosstalk through capacitor trimming.

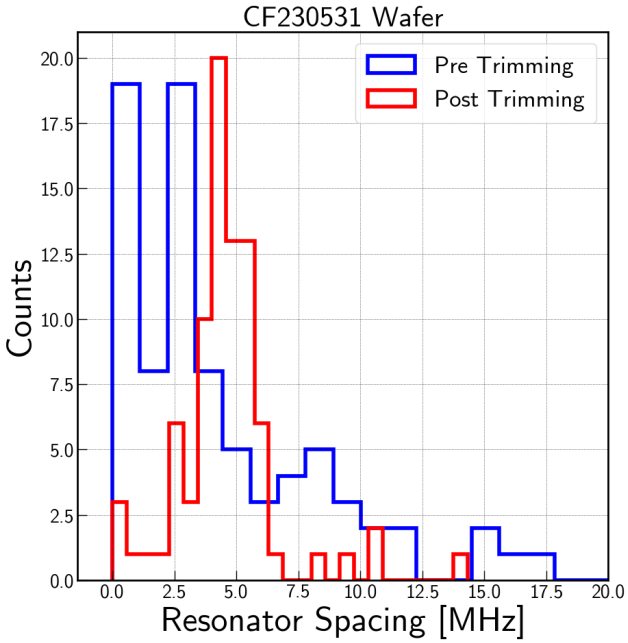

Figure 6.21: Significant reduction in resonator collisions through capacitor trimming.

Systematic Effects in Resonator Adjustment

As already detailed, capacitor trimming is indispensable in order to achieve highly uniform detector arrays as already detailed. A key challenge in our approach is the assumption that the number of fingers of the IDC only affects the resonance frequency and no other property of the resonator.

In reality, the parasitic inductance of the IDC, the coupling of the capacitor tank to ground, and the coupling to the transmission line all change with trimming. A more robust model of the IDC that can account for the dependence of all these factors is required. In appendix B, I develop a coupled transmission line model of the IDC accurate to the 2nd pole of the IDC. This model accounts for the effect of the single-sided capacitor section, which can be over half the total physical area of the capacitor on the wafer (see fig. 5.19). Its contribution had previously not been accounted for. Since this model was developed after all the wafer trimming discussed in this section was done, we currently cannot assess its efficacy experimentally. However, in future work, we aim to use this updated model to inform the capacitor trimming step. Figs. 6.22 and 6.23 for example, show that the acccuracy of targeting a particular frequency has dependence on both the number of fingers trimmed and the design frequency of the resonators.

An additional concern is the repeated processing of the wafer. This can potentially affect both the metal and dielectric properties between test runs. Further investigation is required in order to set limits on the drift in material properties with repeated reprocessing. On a more practical note, we established that careful cleaning of the bondpads between testing and reprocessing is crucial. Even small adhesions left by the wirebond feet, could lead to shadowing and subsequently improper removal of the metal during deposition steps.

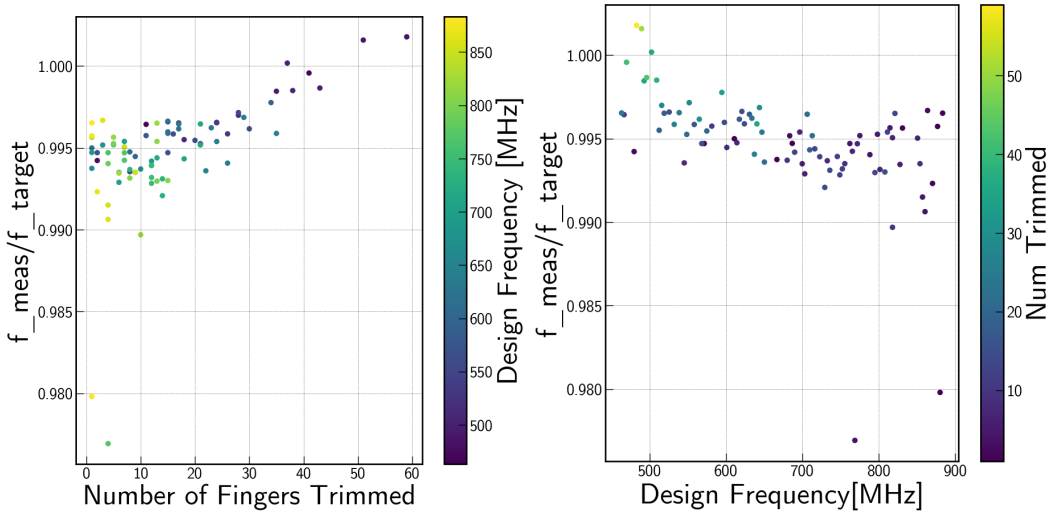

(a) (b)

Figure 6.22: (Left):Ratio of measured resonance frequency against target as a function of the number of capacitor fingers trimmed. (Right): Ratio of measured resonance frequency against target as a function of pre-trimmed design frequency.

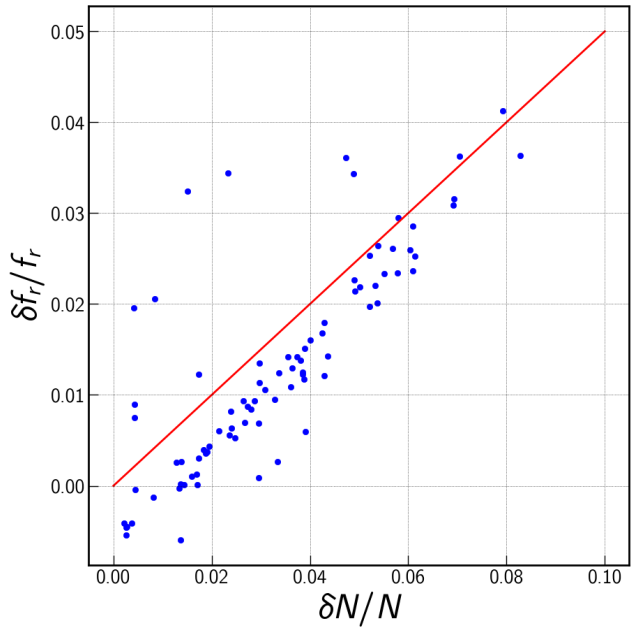

Figure 6.23: Fractional frequency shift as a function of the number of capacitor fingers trimmed. The red line with slope $1/2$ is the expected dependence assuming β, ϵ small. The negative intercept of the measured fractional frequency shift as well as the scatter shows that there are important systematic effects yet to be investigated.

6.5 Optical Testing

Measurements of CMB polarization require a careful characterization of the optical performance of the instrument. In this section, we detail a number of calibration measurements done in a laboratory setting. This is a significant challenge for CMB receivers since the detectors are optimized to work under the much lower expected loading during science observations. In the BICEP-*Keck* TES receivers, this challenge is overcome by using two TESes on a single bolometer island; an aluminum TES with a higher T_c for laboratory measurements and a titanium TES for on-sky measurements (Ade, Aikin, Amiri, Barkats, Benton, Bischoff, Bock, Bonetti, et al., 2015).

The TKID camera differs significantly from this approach. A single aluminum TKID resonator is optimized for on-sky measurements at about 5 pW of loading is also used to characterize the receiver in the laboratory setting. TKIDs are therefore significantly overcoupled under the high optical loading in lab settings. Overcoupled resonators are broad and have very high responsivity. Under the typical variation in the optical loading, the resonator shifts by many line widths. This makes traditional fixed tone readout (L. Minutolo, B. Steinbach, et al., 2019) ineffective.

We address this challenge by implementing a readout technique we refer to as fastchirp. Fastchirp readout is a two-step process. In the excitation step, we store energy in the resonators and then monitor the ringdown of the resonators in the listen step. We implemented this readout scheme using both the x300 and N321 software defined radios (SDR) platforms from Ettus Research [1] and the RFnOC framework [2]. We store a short buffer in the FPGA that represents a chirp waveform spanning the whole available RF band. A single fastchirp cycle is divided between a transmit (TX) and a receive (RX) phase. In the transmit phase we transmit the short buffer that is $\sim$ 10μs long. Each transmit phase is followed by a receive (RX) phase $\sim$ 100μs. Charging the resonator during TX requires the probe tone to have a significantly higher power that a fixed tone based readout. Each cycle is transmitted to a computer via optical fiber. The TX phases are discarded and multiple RX phases are synchronously accumulated to increase the signal to noise ratio. After taking an FFT, each of the peaks present in fig. 6.24a corresponds to the energy released by a resonator. Each peak is fit each with a complex Lorentian function to extract the resonant frequency. Each transform is a single frame and results in a sample per resonator. The resulting acquisition rate of the technique is, for a 250MHz complex base-band, around 1 k sample/s per device.

Near Field Beam Maps

Maxwell's equations are invariant under time reversal. We can therefore freely regard a receiving element as a transmitter. It is convenient to consider a telescope as illuminating the sky. The electromagnetic field pattern generated by the antenna is radiated outwards, modified by the telescope optics and finally propagate out into the environment. Artificial power sources placed at different locations in the beam pattern probe the sensitivity of the telescope as a function of the angular position and the polarization.

Near Field Beam Maps (NFBM) are taken close to the aperture plane of the detectors and are often the first check of the optical health of a receiver. Beams in the aperture plane are primarily sensitive to the phase of the electric field (K. Karkare, 2017). NFBM results often feedback into the detector and optics fabrication and design efforts. We measure the near field response of the detectors using a hot thermal source mounted onto a motorized XY stage at $\sim$ 12" above the focal plane. The ceramic thermal source is unpolarized and is chopped at a frequency of 17Hz using

[1] https://www.ettus.com/all-products/usrp-n321/

[2] https://kb.ettus.com/Getting_Started_with_RFNoC_Development

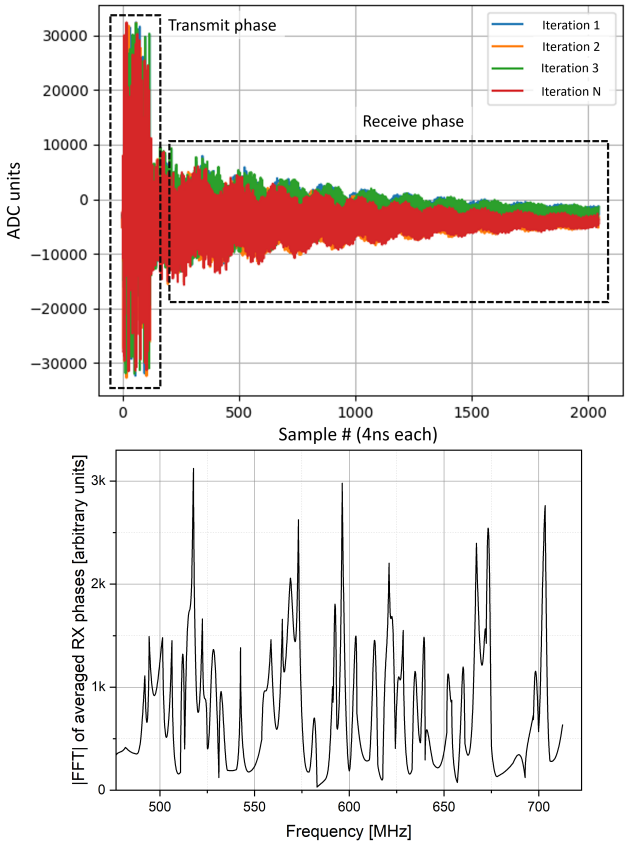

(a)

Figure 6.24: A summary of the fastchirp data acquisition and frequency extraction procedures. (Top): Real part of raw samples coming from a fastchirp acquisition. Each trace is an iteration of a fastchirp cycle. The fastchirp cycle is defined by a transmit (TX) phase, in which a chirp waveform is transmitted at high power across the whole available bandwidth (250MHz in this case), and a receive (RX) phase, where no signal is transmitted and the resonators' ringdown is observed. (Below): Fast chirp frame from the beam mapping pipeline this is with 500 avg and standard parameters. The black line in the plot is the magnitude of a FFT performed on 500 iteration of the RX phase described in section 6.5. The y axis is in arbitrary units because a scaler is used in the accumulation algorithm to avoid overflow. The falue of the scale and frequency with which it is applied are determined by the real-time nature of the acquisition. Each of the peaks visible in the plot corresponds to a resonator. By fitting the peak with a complex Lorentzian, we extract the resonator position.

a Thorlabs chopping wheel. This is a lock-in measurement to separate the signal from the large changing background. The XY-stage, enclosure for chop wheel, thermal source and mounting structure are all coated with Eccosorb HR10[3] in order to minimize reflections. The source therefore chops between ~ 500K and ambient temperature.

During data acquisition, the detector timestreams taken using fastchirp, the chop reference signal and the x,y encoder positions are. The chop reference signal is used to demodulate the detector timestreams to extract both the in-phase and quadrature signals. Typical beam maps are shown in fig. 6.25

We carried out a full NFBM campaign for the CF210615 wafer which had a post-trimming yield of 101 out of 128 devices. Among the 101 devices observed without loading, 9 had no optical responses, indicating defects in fabrication. 15 additional resonators overlapped with their neighbors and could not be reliably fit.

Optical Efficiency

The end-to-end optical efficiency is measured using aperture filling sources at 2 temperatures: 77K from a liquid nitrogen bath and 300K ambient temperature. In our frequency band, both sources are in the Rayleigh-Jeans limit.

For a single polarization single-mode detector, the difference in optical loading ΔP for a detector with spectrum $\eta(\nu)$ can be calculated from

$$\Delta P = \int_0^\infty \mathrm{d}\nu \eta(\nu) \frac{\nu^2 k_B \Delta T}{c^2} \cdot A\Omega = k_B \Delta T \int_0^\infty \mathrm{d}\nu \eta(\nu). \tag{6.3}$$

The second equality follows from $A\Omega = \lambda^2$ for a single-mode detector. Using the calibration heaters on the bolometer island, we can directly measure ΔP. ΔT = 300K−77K. Given $\mathrm{d}P/\mathrm{d}T \equiv \Delta P/\Delta T$ and known spectral bandwidth of the detectors $\Delta\nu$, the band averaged end-to-end optical efficiency $\bar{\eta}$ is given by

$$\bar{\eta} = \frac{\mathrm{d}P}{\mathrm{d}T} \frac{1}{k_B \Delta\nu} \tag{6.4}$$

Figure 6.26 details the procedure for extracting ΔP for TKID resonators. For the CF230403 Ex-3 tile, we measured the optical efficiency for 29 resonators. Corrected

[3] https://www.laird.com/sites/default/files/2018-11/RFP-DS-HR%20092815.pdf

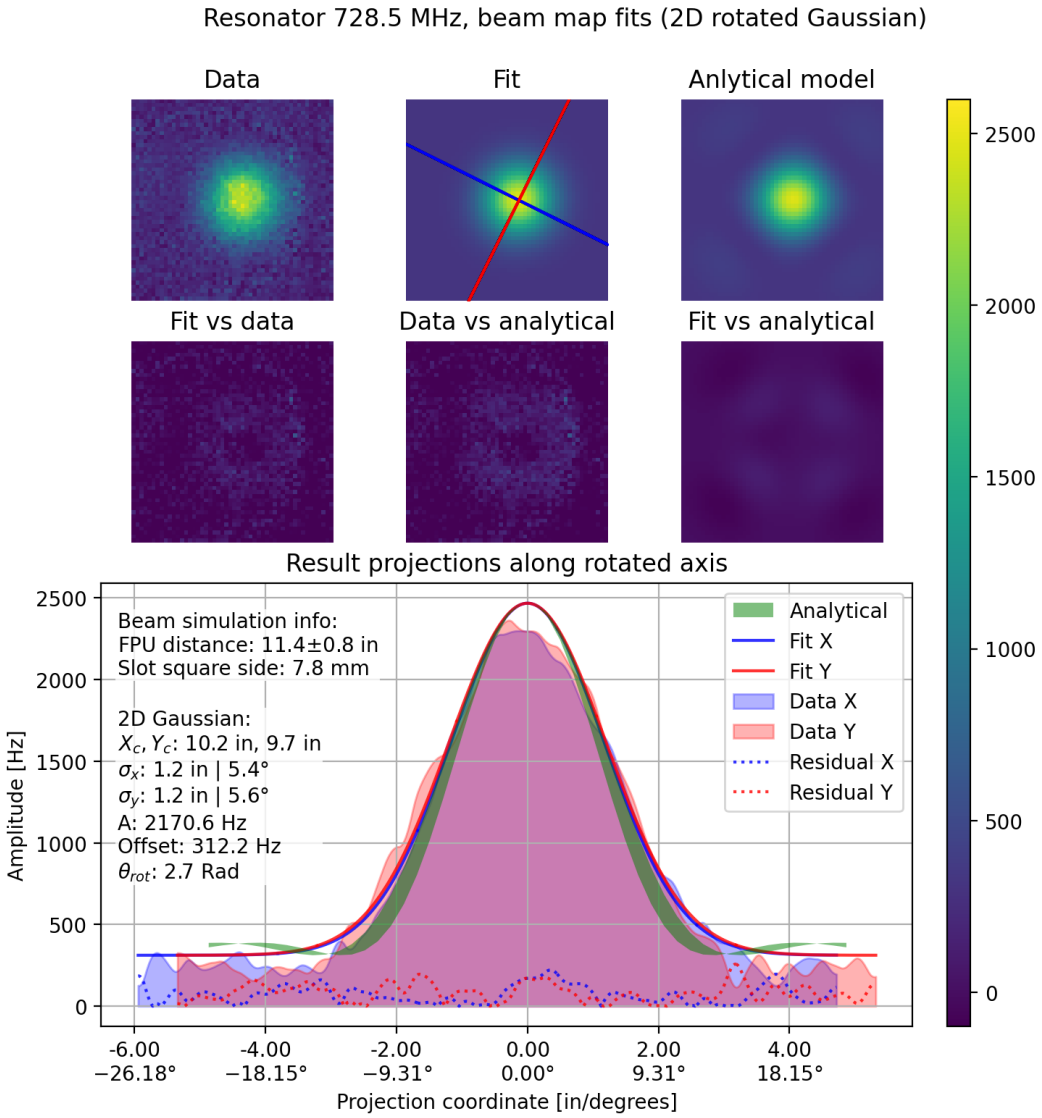

Figure 6.25: Typical near field beam map. Data taken on the CF210615 MLA tile. The 6 upper plots report the spatially binned data, a Gaussian fit, expected antenna beam pattern and the respective residuals. The colorbar gives the scale in Hz. The lower plot gives sections of the beam map along the 2 axes of the 2-D Gaussian. The X-axis is given in both inches and degrees. The projection from distance to angle is obtained from the geometry of the beam mapper.

for dark stimulation + wafer heating, the average optical efficiency is 44%. Due to fabrication defects that affect the heater bias lines, only 3 heater bias lines could be reliably operated.

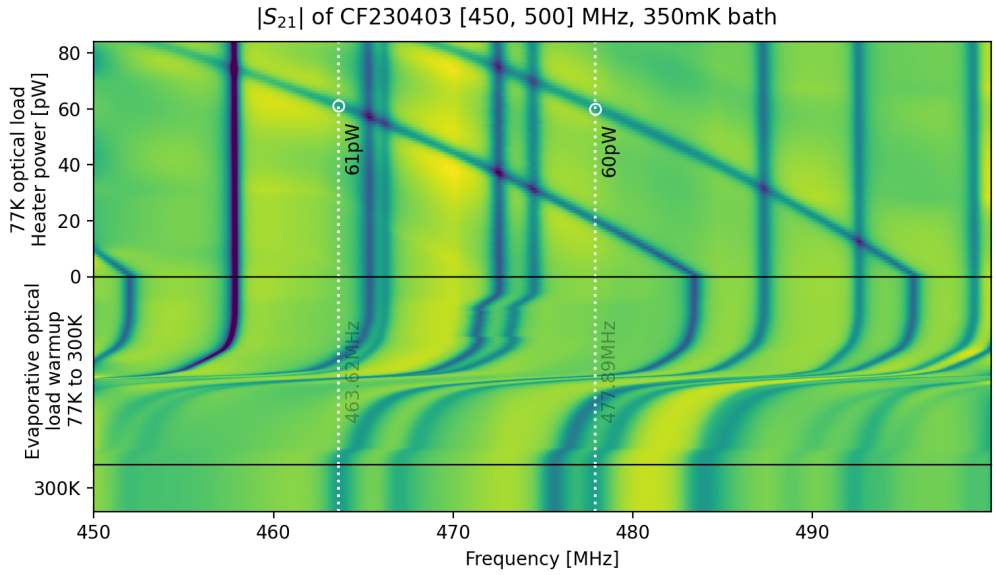

Figure 6.26: Stacked waterfall plots of a portion of the 450-500 MHz portion of the frequency band of the CF230403 Ex-3 wafer. The top half of the figure gives the resonance positions under a 77K optical load and with the heaters biased on a single line. The additional calibration power shifts the biased resonators across the band. In the bottom half of the figure, the liquid nitrogen load is allowed to cool evaporatively while the resonance frequencies are monitored under no heater bias. The increase in optical loading from 77K to 300K causes the resonator positions to shift. The coincidence in resonator position at 300K and at the 77K + bias condition is used to extract the optical efficiency.

Spectral Response

We measured detector spectra using a Martin-Puplett Fourier Transform Spectrometer (FTS) as shown in fig. 6.28 (Martin and Puplett, 1970). The FTS uses a polarized wired grid as a beam splitter. The FTS aperture is too small to fully fill the detector beam. The directional dependence of the input power can create a frequency dependent response in the detector. Even so, we can angle the FTS beam to ensure that it illuminates each detector through the center of the beam.

The input wire grid is right above the aperture, reflecting a single polarization to the horizon direction. The wire grid sits on a rotation stage with a goniometer which allows us to change pointing to cover different parts of the FPU. A second wire grid splits the reflected beam toward the two arms, each with a rooftop mirror at the

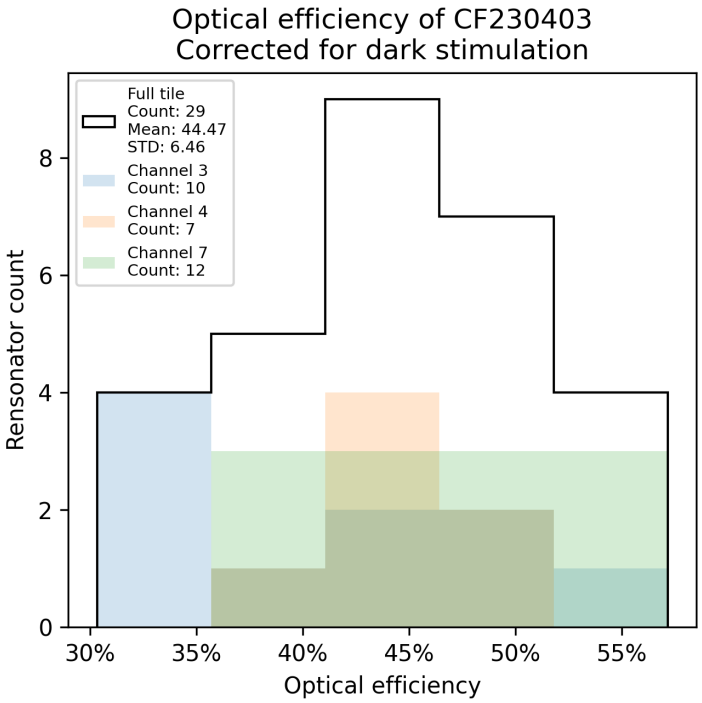

Figure 6.27: A histogram of the measured optical efficiencies for the CF230403 tile. The optical efficiencies were measured for only a fraction of the total number of yielded resonators due to fabrication defects that limited the number of operable heater bias lines.

end. One of the rooftop mirrors is fixed, while the other one is movable along the arm. The reflected beams recombine at the second pass of the beam splitter then illuminate a focusing parabolic mirror. The focused light from the mirror is again split into two beams; one terminates on Eccosorb HR-10 microwave absorber at ambient temperature, and the other on HR-10 held at 77 K in a container of LN2. The difference in temperature between the two sources leads to an interference pattern in the detector response when the path length is changed (Lesurf, 1990). A Fourier Transform of the time-order signal gives the detector's spectral response. In our data taking, we make the mirror move at 1.905mm/s and use the data of a full length of 230mm scan giving a frequency resolution of 0.65 GHz. The FTS sits on an x-y stage that mounts directly onto the 300K window of a *Keck* receiver. This 4 axis coupling scheme allows the FTS to be positioned above any detector on the focal plane and significantly mitigates the frequency dependence introduced by the partial beam filling. To take spectra of many devices at once the FTS is mounted at 45°with respect to the polarization axes of the detectors. Figure 6.29 shows sample FTS spectra and interferograms for 3 resonators on the CF230403 wafer.

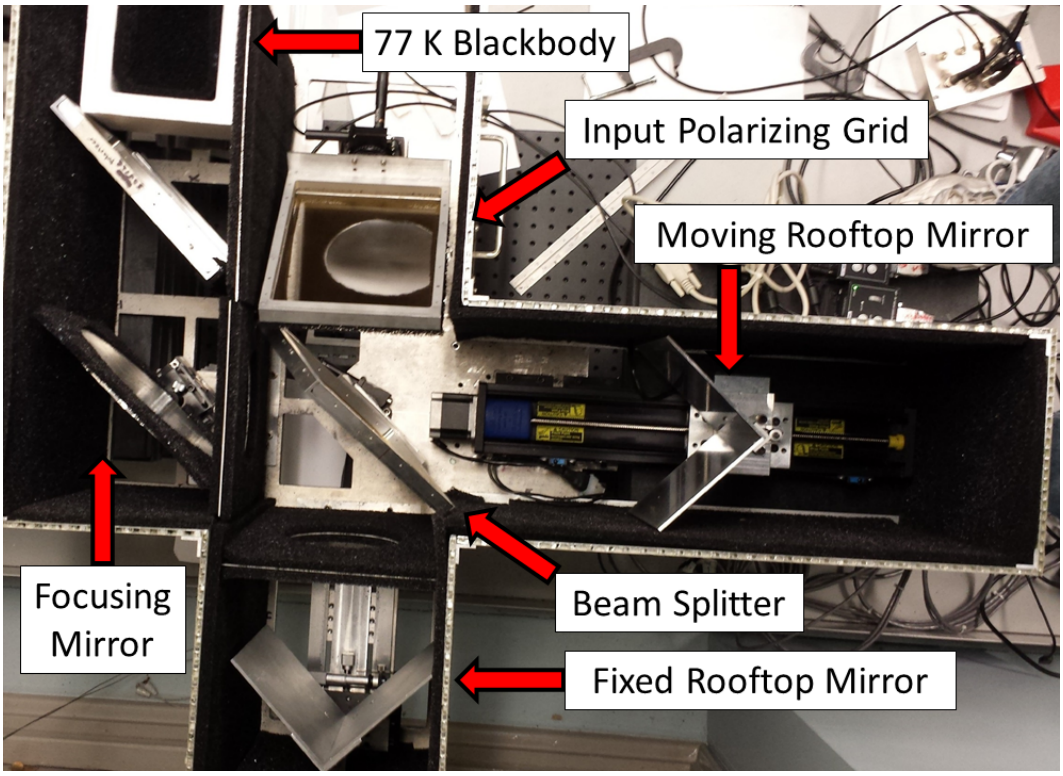

Figure 6.28: Martin-Puplett FTS in lab. In the time-reverse sense, the beam enters the FTS from below and is reflected into the interferometer with the input polarizing grid, is split into two polarizations with the beam splitter, travels different path lengths, is recombined, and terminates on either a 300 K blackbody (the ambient-temperature absorber-lined FTS wall to the left) or a 77 K blackbody (absorber soaked in LN2, held in a foam container), depending on the polarization state. The temperature difference between the two terminations determines the brightness of the modulated signal. Figure from K. S. Karkare et al., 2014.

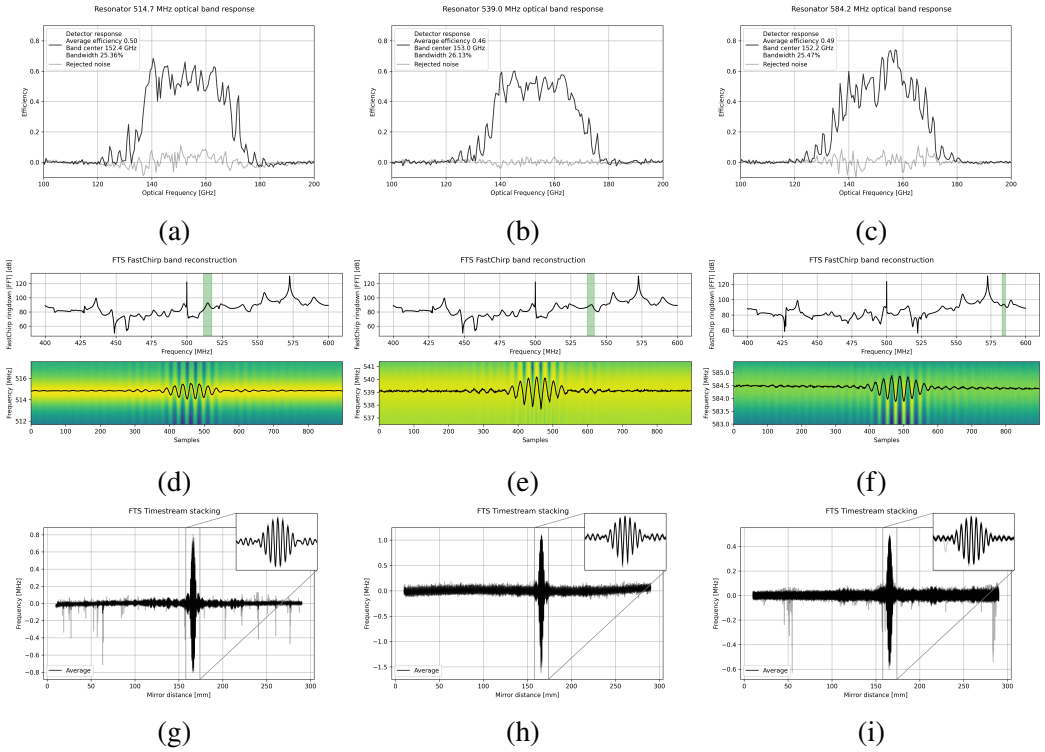

Figure 6.29: Spectral measurements of 3 resonators on the CF230403 tile. (Top) Measured spectra showing the band center and bandwidth consistent with the antenna design. The spectra are scaled by the measured band averaged optical efficiency. (Middle) FFT of averaged fastchirp cycles collected on a TKID array. The green bands on the plot represents the region considered for resonator fitting and is re-plotted below with the frequency is now given along the y-axis. (Bottom) Stacked interferograms used to generate the FTS spectra.

Chapter 7

CONCLUSIONS AND OUTLOOK

Using the NASA Technology Readiness criteria (see fig. 7.1) as a metric, through the scope of the work done at the Jet Propulsion Laboratory (JPL) and the California Institute of Technology, and presented in this thesis, TKIDs have matured from TRL 2 to just shy of TRL 6 - demonstration in a relevant environment. The research presented here shows that TKIDs can be used for not only CMB studies, but are suitable for precision cosmology and astrophysical measurements across the millimeter and submillimeter bands.

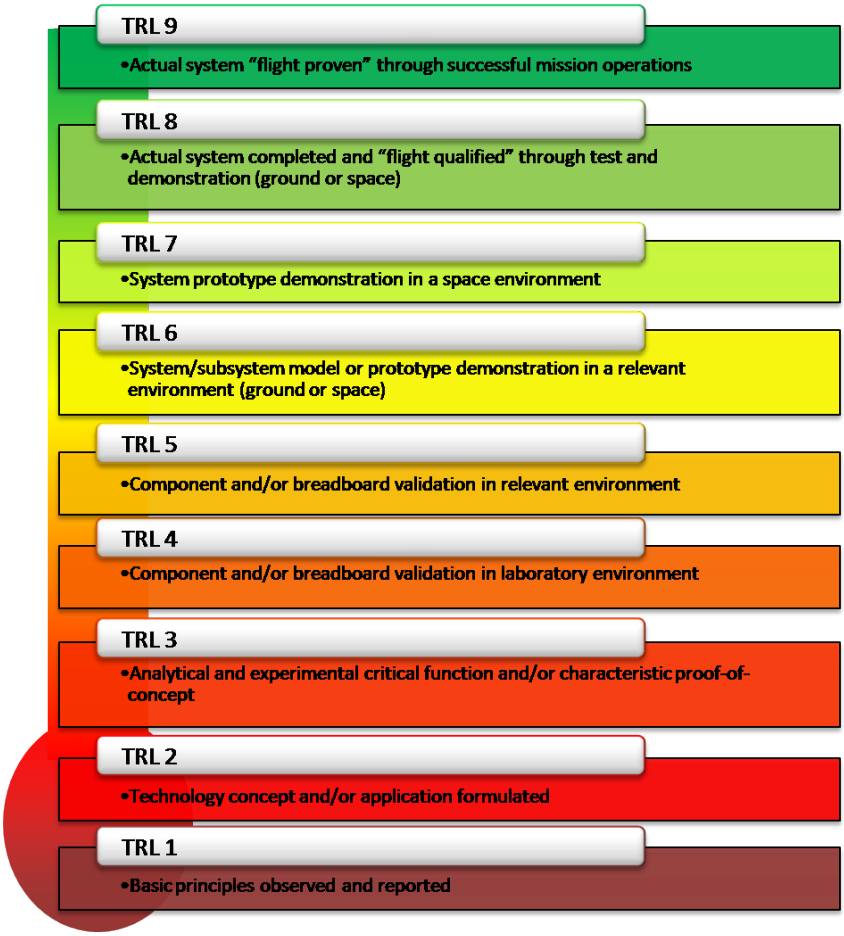

Figure 7.1: NASA Technology Readiness Levels for assessing the maturity of a particular technology.

TKIDs are complementary to exisiting TES and KID based platforms and have en-

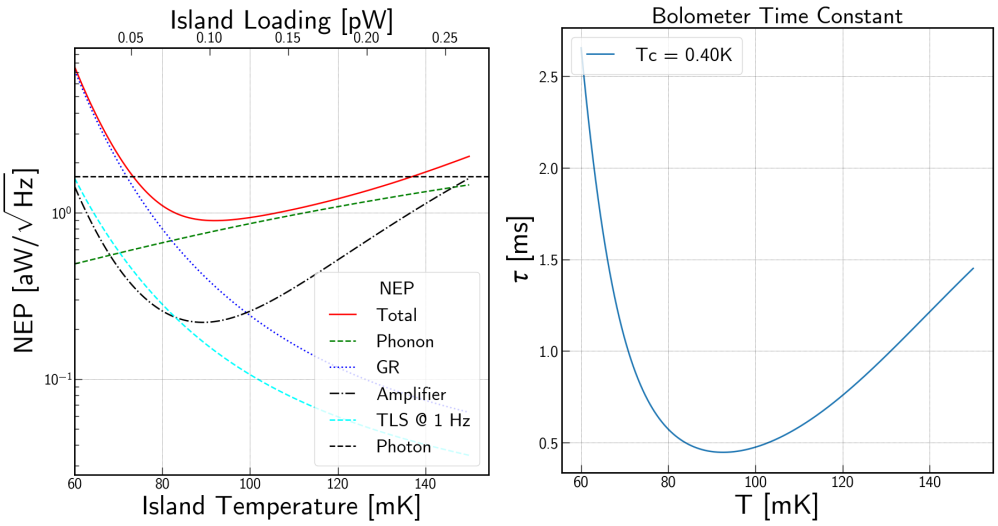

(a) (b)

Figure 7.2: Predicted noise (left) and time constant (right) of a WSi TKID suitable for CMB observations from space. The transition temperature of WSi is tunable by changing the concentration of Si during deposition. Here T_c = 0.4 K. WSi has a sheet resistance of about 40 Ω/sq in comparison with the modest sheet resistance of aluminum at 0.25 Ω/sq for a 50 nm thick film.

abled the development of new readout techniques such as fastchirp. TKIDs demonstrate effective TLS noise suppression strategies, phonon recycling approaches relevant to highly responsive KID devices and probe superconducting physics in the high temperature – high power regime even with amorphous dielectric present.

One promising direction for future work on TKIDs is to develop devices suitable for the low loading of space. Detectors on a space-borne CMB experiment will contend with power roughly two orders of magnitude lower than their ground-based counterparts. For background-limited operation both the phonon noise and the operating temperature will have to be reduced significantly. Such TKIDs will be designed to operate at ∼ 100 mK bath temperature. In order to maintain the detector time constants at suitable levels with much lower thermal conductance, the heat capacity of the island must also be reduced. This can be achieved by using superconductors with a large normal resistivity and therefore a large kinetic inductance fraction such as tungsten silicide (WSi). An initial analysis of the expected noise and detector time constant for such a TKID bolometer is given in fig. 7.2.

Strong negative electrothermal feedback with loop gains ∼ 10, has already been demonstrated using small TKID arrays. Negative ETF offers several advantages for

TKID operation. First, it linearizes the detector responsivity over a wide range of powers, eliminating gain compression and providing a calibration mechanism for determining the power on device. Additionally, under negative ETF, the thermal time constant can be significantly reduced. This is a requirement for applications requiring a faster detector response times such as in observations from space. Array-level readout exploiting feedback is yet to be demonstrated. The potential gains in linearity, responsivity, and time constants as well as the noise and stability requirements for dense arrays of TKID bolometers represent a unique opportunity to mature detector design and readout.

BIBLIOGRAPHY

Abazajian, Kevork N. et al. (2016). "CMB-s4 Science Book, First Edition". In: *arXiv e-prints*, arXiv:1610.02743, arXiv:1610.02743. DOI: 10.48550/arXiv.1610.02743. arXiv: 1610.02743 [astro-ph.CO].

Abitbol, Maximilian et al. (2018). "The EBEX Balloon-borne Experiment —detectors and Readout". In: *The Astrophysical Journal Supplement Series* 239.1, p. 8. DOI: 10.3847/1538-4365/aae436. URL: https://doi.org/10.3847%5C%2F1538-4365%5C%2Faae436.

Ade, P. A. R., Z. Ahmed, M. Amiri, A. J. Anderson, et al. (2021). "A Demonstration of Improved Constraints on Primordial Gravitational Waves With Delensing". In: *Phys. Rev. D* 103 (2), p. 022004. DOI: 10.1103/PhysRevD.103.022004. URL: https://link.aps.org/doi/10.1103/PhysRevD.103.022004.

Ade, P. A. R., Z. Ahmed, M. Amiri, D. Barkats, et al. (2021). "Improved Constraints on Primordial Gravitational Waves Using Planck, Wmap, and BICEP/Keck Observations Through the 2018 Observing Season". In: *prl* 127.15, 151301, p. 151301. DOI: 10.1103/PhysRevLett.127.151301. arXiv: 2110.00483 [astro-ph.CO].

Ade, P. A. R., R. W. Aikin, M. Amiri, D. Barkats, S. J. Benton, C. A. Bischoff, J. J. Bock, J. A. Bonetti, et al. (2015). "Antenna-coupled TES Bolometers Used In BICEP2, Keck Array, and SPIDER". In: *The Astrophysical Journal* 812.2, p. 176. DOI: 10.1088/0004-637x/812/2/176. URL: https://doi.org/10.1088%2F0004-637x%2F812%2F2%2F176.

Ade, P. A. R., R. W. Aikin, M. Amiri, D. Barkats, S. J. Benton, C. A. Bischoff, J. J. Bock, J. A. Brevik, et al. (2014). "BICEP2. II. Experiment and Three-year Data Set". In: *The Astrophysical Journal* 792.1, p. 62. DOI: 10.1088/0004-637x/792/1/62. URL: https://doi.org/10.1088%5C%2F0004-637x%5C%2F792%5C%2F1%5C%2F62.

Ade, P. A. R., R. W. Aikin, D. Barkats, et al. (2015). "BICEP2/Keck Array. IV. Optical Characterization and Performance of the BICEP2 AndKeck Array Experiments". In: *The Astrophysical Journal* 806.2, p. 206. DOI: 10.1088/0004-637x/806/2/206. URL: https://doi.org/10.1088%2F0004-637x%2F806%2F2%2F206.

Agrawal, Shubh et al. (2021). "Strong negative electrothermal feedback in thermal kinetic inductance detectors". In: *Journal of Applied Physics* 130.12, p. 124503. DOI: 10.1063/5.0064723. eprint: https://doi.org/10.1063/5.0064723. URL: https://doi.org/10.1063/5.0064723.

Arndt, M. et al. (2017). "Optimization of the Microwave Properties of the Kinetic-Inductance Bolometer (KIBO)". In: *IEEE Transactions on Applied Superconductivity* 27.4, pp. 1–5.

Bardeen, J., L. N. Cooper, and J. R. Schrieffer (1957). "Theory of Superconductivity". In: *Phys. Rev.* 108 (5), pp. 1175–1204. DOI: 10.1103/PhysRev.108.1175. URL: https://link.aps.org/doi/10.1103/PhysRev.108.1175.

Barends, R., J. J. A. Baselmans, et al. (2008). "Quasiparticle Relaxation In Optically Excited High-q Superconducting Resonators". In: *Phys. Rev. Lett.* 100 (25), p. 257002. DOI: 10.1103/PhysRevLett.100.257002. URL: https://link.aps.org/doi/10.1103/PhysRevLett.100.257002.

Barends, R., J. Wenner, et al. (2011). "Minimizing Quasiparticle Generation From Stray Infrared Light In Superconducting Quantum Circuits". In: *Applied Physics Letters* 99.11, p. 113507. DOI: 10.1063/1.3638063. eprint: https://doi.org/10.1063/1.3638063. URL: https://doi.org/10.1063/1.3638063.

Benson, B. A. et al. (2014). "SPT-3G: A Next-generation Cosmic Microwave Background Polarization Experiment on the South Pole Telescope". In: vol. 9153. DOI: 10.1117/12.2057305. URL: https://doi.org/10.1117/12.2057305.

Bergström, L. and A. Goobar (2006). *Cosmology and Particle Astrophysics*. Springer Praxis Books. Springer Berlin Heidelberg. ISBN: 9783540329244. URL: https://books.google.com/books?id=CQYu_sutWAoC.

Beyer, A. D. et al. (2010). "Characterizing Si_xN_y Absorbers and Support Beams for Far-infrared/submillimeter Transition-edge Sensors". In: *Millimeter, Submillimeter, and Far-infrared Detectors and Instrumentation for Astronomy V*. Ed. by Wayne S. Holland and Jonas Zmuidzinas. Vol. 7741. International Society for Optics and Photonics. SPIE, pp. 594–603. DOI: 10.1117/12.857885. URL: https://doi.org/10.1117/12.857885.

Bourrion, O. et al. (2016). "Nikel_amc: Readout Electronics for the NIKA2 Experiment". In: *Journal of Instrumentation* 11.11, P11001–P11001. DOI: 10.1088/1748-0221/11/11/p11001. URL: https://doi.org/10.1088%2F1748-0221%2F11%2F11%2Fp11001.

Bowden, M. et al. (2004). "Scientific Optimization of A Ground-based CMB Polarization Experiment". In: *Monthly Notices of the Royal Astronomical Society* 349.1, pp. 321–335. ISSN: 0035-8711. DOI: 10.1111/j.1365-2966.2004.07506.x. eprint: https://academic.oup.com/mnras/article-pdf/349/1/321/11182380/349-1-321.pdf. URL: https://doi.org/10.1111/j.1365-2966.2004.07506.x.

Burin, Alexander L., Shlomi Matityahu, and Moshe Schechter (2015). "Low-temperature $1/f$ Noise In Microwave Dielectric Constant of Amorphous Dielectrics In Josephson Qubits". In: *Phys. Rev. B* 92 (17), p. 174201. DOI: 10.1103/PhysRevB.92.174201. URL: https://link.aps.org/doi/10.1103/PhysRevB.92.174201.

Burnett, J, L Faoro, and T Lindström (2016). "Analysis of High Quality Superconducting Resonators: Consequences for Tls Properties In Amorphous Oxides". In: *Superconductor Science and Technology* 29.4, p. 044008. DOI: 10.1088/0953-

2048/29/4/044008. URL: https://doi.org/10.1088%5C%2F0953-2048%5C%2F29%5C%2F4%5C%2F044008.

Clarke, John and Alex I. Braginski (2005). *The Squid Handbook*. John Wiley & Sons, Ltd. ISBN: 9783527603640. DOI: 10.1002/3527603646.fmatter. eprint: https://onlinelibrary.wiley.com/doi/pdf/10.1002/3527603646.fmatter. URL: https://onlinelibrary.wiley.com/doi/abs/10.1002/3527603646.fmatter.

Corruccini, R.J. and J.J. Gniewek (1960). *Specific Heats and Enthalpies of Technical Solids At Low Temperatures. A Compilation From the Literature*. NBS Monograph 21. U.S. Government Printing Office, Washington, DC.

Cukierman, A. et al. (2020). "Microwave Multiplexing on the Keck Array". In: *Journal of Low Temperature Physics* 199.3, pp. 858–866. ISSN: 1573-7357. DOI: 10.1007/s10909-019-02296-2. URL: https://doi.org/10.1007/s10909-019-02296-2.

D'Addabbo, A. et al. (2014). "High-energy interactions in Kinetic Inductance Detectors arrays". In: *Proc. SPIE Int. Soc. Opt. Eng.* 9153, 91532Q. DOI: 10.1117/12.2056441. arXiv: 1505.01647 [astro-ph.IM].

Dabironezare, S. O. et al. (2018). "A Dual-band Focal Plane Array of Kinetic Inductance Bolometers Based on Frequency-selective Absorbers". In: *IEEE Transactions on Terahertz Science and Technology* 8.6, pp. 746–756.

Day, Peter K. et al. (2003). "A Broadband Superconducting Detector Suitable for Use In Large Arrays". In: *Nature* 425.6960, pp. 817–821. ISSN: 1476-4687. DOI: 10.1038/nature02037. URL: https://doi.org/10.1038/nature02037.

Deng, Chunqing, Martin Otto, and Adrian Lupascu (2013). "An Analysis Method for Transmission Measurements of Superconducting Resonators With Applications To Quantum-regime Dielectric-loss Measurements". In: *Journal of Applied Physics* 114.5, p. 054504. DOI: 10.1063/1.4817512. eprint: https://doi.org/10.1063/1.4817512. URL: https://doi.org/10.1063/1.4817512.

Dobbs, M. A. et al. (2012). "Frequency Multiplexed Superconducting Quantum Interference Device Readout of Large Bolometer Arrays for Cosmic Microwave Background Measurements". In: *Review of Scientific Instruments* 83.7, p. 073113. DOI: 10.1063/1.4737629. eprint: https://doi.org/10.1063/1.4737629. URL: https://doi.org/10.1063/1.4737629.

Dober, Bradley J. et al. (2014). "The Next-generation Blastpol Experiment". In: *Millimeter, Submillimeter, and Far-infrared Detectors and Instrumentation for Astronomy VII*. Ed. by Wayne S. Holland and Jonas Zmuidzinas. Vol. 9153. International Society for Optics and Photonics. SPIE, pp. 137–148. DOI: 10.1117/12.2054419. URL: https://doi.org/10.1117/12.2054419.

Doyle, S. et al. (2008). "Lumped Element Kinetic Inductance Detectors". In: *Journal of Low Temperature Physics* 151.1, pp. 530–536. ISSN: 1573-7357. DOI: 10.1007/s10909-007-9685-2. URL: https://doi.org/10.1007/s10909-007-9685-2.

Eliashberg, G M (1960). "Interactions Between Electrons and Lattice Vibrations In A Superconductor". In: *Soviet Physics - JETP (Engl. Transl.); (United States)* 11. URL: https://www.osti.gov/biblio/7354388.

Essinger-Hileman, Thomas et al. (2014). "Class: the Cosmology Large Angular Scale Surveyor". In: *Millimeter, Submillimeter, and Far-infrared Detectors and Instrumentation for Astronomy VII*. Ed. by Wayne S. Holland and Jonas Zmuidzinas. Vol. 9153. International Society for Optics and Photonics. SPIE, p. 91531I. DOI: 10.1117/12.2056701. URL: https://doi.org/10.1117/12.2056701.

Frossati, G et al. (1977). "Spectrum of Low-energy Dipolar States In Hydrated Vitreous Silica". In: *Journal of Physics C: Solid State Physics* 10.18, pp. L515–L519. DOI: 10.1088/0022-3719/10/18/004. URL: https://doi.org/10.1088%2F0022-3719%2F10%2F18%2F004.

Gao, J. et al. (2008). "Equivalence of the Effects on the Complex Conductivity of Superconductor Due To Temperature Change and External Pair Breaking". In: *Journal of Low Temperature Physics* 151.1-2, pp. 557–563. DOI: 10.1007/s10909-007-9688-z.

Gao, Jiansong (2008). "The Physics of Superconducting Microwave Resonators". PhD thesis. California Institute of Technology. URL: https://resolver.caltech.edu/CaltechETD:etd-06092008-235549.

Gao, Jiansong et al. (2008). "Experimental Evidence for A Surface Distribution of Two-level Systems In Superconducting Lithographed Microwave Resonators". In: *Applied Physics Letters* 92.15, p. 152505. DOI: 10.1063/1.2906373. eprint: https://doi.org/10.1063/1.2906373. URL: https://doi.org/10.1063/1.2906373.

Goldie, D J and S Withington (2012). "Non-equilibrium Superconductivity In Quantum-sensing Superconducting Resonators". In: *Superconductor Science and Technology* 26.1, p. 015004. DOI: 10.1088/0953-2048/26/1/015004. URL: https://doi.org/10.1088%5C%2F0953-2048%5C%2F26%5C%2F1%5C%2F015004.

Golwala, Sunil R. et al. (2012). "Status of Music, the Multiwavelength Sub/millimeter Inductance Camera". In: *Millimeter, Submillimeter, and Far-infrared Detectors and Instrumentation for Astronomy Vi*. Ed. by Wayne S. Holland. Vol. 8452. International Society for Optics and Photonics. SPIE, pp. 33–53. DOI: 10.1117/12.926055. URL: https://doi.org/10.1117/12.926055.

Gordon, Samuel et al. (2016). "An Open Source, Fpga-based Lekid Readout for Blast-tng: Pre-flight Results". In: *Journal of Astronomical Instrumentation* 05.04, p. 1641003. DOI: 10.1142/S2251171716410038. eprint: https://doi.

org/10.1142/S2251171716410038. URL: https://doi.org/10.1142/S2251171716410038.

Greenbaum, Anne, Ren-Cang Li, and Michael L. Overton (2020). "First-Order Perturbation Theory for Eigenvalues and Eigenvectors". In: *SIAM Review* 62.2, pp. 463–482. DOI: 10.1137/19M124784X. eprint: https://doi.org/10.1137/19M124784X. URL: https://doi.org/10.1137/19M124784X.

Henderson, S. W. et al. (2016). "Advanced ACTPOL Cryogenic Detector Arrays and Readout". In: *Journal of Low Temperature Physics* 184.3, pp. 772–779. ISSN: 1573-7357. DOI: 10.1007/s10909-016-1575-z. URL: https://doi.org/10.1007/s10909-016-1575-z.

Hoevers, H. F. C. et al. (2005). "Radiative Ballistic Phonon Transport In Silicon-nitride Membranes At Low Temperatures". In: *Applied Physics Letters* 86.25, p. 251903. ISSN: 0003-6951. DOI: 10.1063/1.1949269. eprint: https://pubs.aip.org/aip/apl/article-pdf/doi/10.1063/1.1949269/14002203/251903_1_online.pdf. URL: https://doi.org/10.1063/1.1949269.

Horowitz, Paul and Winfield Hill (2015). *The Art of Electronics; 3rd Ed.* Cambridge: Cambridge University Press. URL: https://cds.cern.ch/record/1981307.

Hu, Wayne and Takemi Okamoto (2002). "Mass Reconstruction With CMB Polarization". In: *Astrophys. J.* 574, pp. 566–574. DOI: 10.1086/341110. arXiv: astro-ph/0111606.

Hui, H. et al. (2016). "BICEP3 Focal Plane Design and Detector Performance". In: *Millimeter, Submillimeter, and Far-Infrared Detectors and Instrumentation for Astronomy VIII*. Ed. by Wayne S. Holland and Jonas Zmuidzinas. Vol. 9914. International Society for Optics and Photonics. SPIE, 99140T. DOI: 10.1117/12.2232986. URL: https://doi.org/10.1117/12.2232986.

Hui, Howard et al. (2018). "BICEP Array: A Multi-frequency Degree-scale CMB Polarimeter". In: *Millimeter, Submillimeter, and Far-infrared Detectors and Instrumentation for Astronomy IX*. Ed. by Jonas Zmuidzinas and Jian-Rong Gao. Vol. 10708. International Society for Optics and Photonics. SPIE, pp. 1–15. DOI: 10.1117/12.2311725. URL: https://doi.org/10.1117/12.2311725.

Irwin, K. D. and G. C. Hilton (2005). "Transition-edge Sensors". In: *Cryogenic Particle Detection*. Ed. by Claus E. Ascheron, Hans J. Koelsch, and Werner Skolaut. Heidelberg: Springer, Berlin, Heidelberg. Chap. 3, pp. 63–150.

Irwin, K. D., L. R. Vale, et al. (2002). "Time-division Squid Multiplexers". In: *AIP Conference Proceedings* 605.1, pp. 301–304. DOI: 10.1063/1.1457650. eprint: https://aip.scitation.org/doi/pdf/10.1063/1.1457650. URL: https://aip.scitation.org/doi/abs/10.1063/1.1457650.

Karkare, K. S. et al. (2014). "Keck Array and BICEP3: Spectral Characterization of 5000+ Detectors". In: *Millimeter, Submillimeter, and Far-infrared Detectors and Instrumentation for Astronomy VII*. Ed. by Wayne S. Holland and Jonas

Zmuidzinas. Vol. 9153. International Society for Optics and Photonics. SPIE, pp. 1027–1037. DOI: 10.1117/12.2056779. URL: https://doi.org/10.1117/12.2056779.

Karkare, Kirit (2017). "Multifrequency Beam Systematics and Measurements of B-mode Polarization With the BICEP/Keck Array Cosmic Microwave Background Experiments". PhD thesis. Harvard University. URL: https://dash.harvard.edu/handle/1/40046430.

Kermish, Zigmund D. et al. (2012). "The Polarbear Experiment". In: vol. 8452. DOI: 10.1117/12.926354. URL: https://doi.org/10.1117/12.926354.

Khalil, M. S. et al. (2012). "An Analysis Method for Asymmetric Resonator Transmission Applied To Superconducting Devices". In: *Journal of Applied Physics* 111.5, p. 054510. DOI: 10.1063/1.3692073. eprint: https://doi.org/10.1063/1.3692073. URL: https://doi.org/10.1063/1.3692073.

Kittel, C. and H. Kroemer (1980). *Thermal Physics*. W. H. Freeman. ISBN: 9780716710882.

Korte, Piet A. J. de et al. (2003). "Time-division Superconducting Quantum Interference Device Multiplexer for Transition-edge Sensors". In: *Review of Scientific Instruments* 74.8, pp. 3807–3815. DOI: 10.1063/1.1593809. eprint: https://doi.org/10.1063/1.1593809. URL: https://doi.org/10.1063/1.1593809.

Kovács, Attila et al. (2012). "Superspec: Design Concept and Circuit Simulations". In: *Millimeter, Submillimeter, and Far-infrared Detectors and Instrumentation for Astronomy Vi*. Ed. by Wayne S. Holland. Vol. 8452. International Society for Optics and Photonics. SPIE, pp. 748–757. DOI: 10.1117/12.927160. URL: https://doi.org/10.1117/12.927160.

Kuo, C. L. et al. (2008). "Antenna-coupled TES Bolometer Arrays for CMB Polarimetry". In: *Millimeter and Submillimeter Detectors and Instrumentation for Astronomy IV*. Ed. by William D. Duncan et al. Vol. 7020. International Society for Optics and Photonics. SPIE, pp. 415–428. DOI: 10.1117/12.788588. URL: https://doi.org/10.1117/12.788588.

Lesurf, J.C.G. (1990). *Millimetre-wave Optics, Devices and Systems*. Taylor & Francis. ISBN: 9780852741290. URL: https://books.google.com/books?id=IHJ509_Bf8AC.

Lindeman, M. A. (2014). "Resonator-bolometer Theory, Microwave Read Out, and Kinetic Inductance Bolometers". In: *Journal of Applied Physics* 116.2, p. 024506. DOI: 10.1063/1.4890018.

Liu, X. et al. (2017). "Cryogenic Led Pixel-to-frequency Mapper for Kinetic Inductance Detector Arrays". In: *Journal of Applied Physics* 122.3, p. 034502. ISSN: 0021-8979. DOI: 10.1063/1.4994170. eprint: https://pubs.aip.org/aip/jap/article-pdf/doi/10.1063/1.4994170/15196695/034502_1_online.pdf. URL: https://doi.org/10.1063/1.4994170.

Martin, D. H. and E. Puplett (1970). "Polarised Interferometric Spectrometry for the Millimeter and Submillimeter Spectrum." In: *Infrared Physics* 10, pp. 105–109. DOI: 10.1016/0020-0891(70)90006-0.

Mates, J. A. B. et al. (2019). "Crosstalk in microwave SQUID multiplexers". In: *Applied Physics Letters* 115.20, p. 202601. ISSN: 0003-6951. DOI: 10.1063/1.5116573. eprint: https://pubs.aip.org/aip/apl/article-pdf/doi/10.1063/1.5116573/14528879/202601_1_online.pdf. URL: https://doi.org/10.1063/1.5116573.

Mather, John C. (1982). "Bolometer Noise: Nonequilibrium Theory". In: *Applied Optics* 21.

– (1984). "Bolometers: Ultimate Sensitivity, Optimization, and Amplifier Coupling". In: *Applied Optics* 23.

Mattis, D. C. and J. Bardeen (1958). "Theory of the Anomalous Skin Effect In Normal and Superconducting Metals". In: *Phys. Rev.* 111 (2), pp. 412–417. DOI: 10.1103/PhysRev.111.412. URL: https://link.aps.org/doi/10.1103/PhysRev.111.412.

Mauskopf, P. D. (2018). "Transition Edge Sensors and Kinetic Inductance Detectors In Astronomical Instruments". In: *Publications of the Astronomical Society of the Pacific* 130.990, p. 082001. DOI: 10.1088/1538-3873/aabaf0. URL: https://doi.org/10.1088%5C%2F1538-3873%5C%2Faabaf0.

Mazin, B. A. et al. (2013). "Arcons: A 2024 Pixel Optical Through Near-ir Cryogenic Imaging Spectrophotometer". In: *Publications of the Astronomical Society of the Pacific* 125.933, pp. 1348–1361. DOI: 10.1086/674013. URL: https://doi.org/10.1086%5C%2F674013.

McCarrick, H. et al. (2014). "Horn-coupled, Commercially-fabricated Aluminum Lumped-element Kinetic Inductance Detectors for Millimeter Wavelengths". In: *Review of Scientific Instruments* 85.12, p. 123117. DOI: 10.1063/1.4903855. eprint: https://doi.org/10.1063/1.4903855. URL: https://doi.org/10.1063/1.4903855.

McKenney, Christopher M. et al. (2012). "Design Considerations for A Background Limited 350 Micron Pixel Array Using Lumped Element Superconducting Microresonators". In: *Millimeter, Submillimeter, and Far-infrared Detectors and Instrumentation for Astronomy Vi*. Ed. by Wayne S. Holland. Vol. 8452. International Society for Optics and Photonics. SPIE, pp. 220–229. DOI: 10.1117/12.925759. URL: https://doi.org/10.1117/12.925759.

Minutolo, L. (2024). "Thermal Kinetic Inductance Detector (tkids) Camera: A Pathfinder Mm-wave Polarimeter". Thesis. California Institute of Technology.

Minutolo, L., C. Frez, et al. (2021). "Thermal Kinetic Inductance Detectors Camera: System Level Design, Strategy and Performance Forecast". In: *IEEE Transactions on Applied Superconductivity* 31.5, pp. 1–4. DOI: 10.1109/TASC.2021.3069732.

Minutolo, L., B. Steinbach, et al. (2019). "A Flexible GPU-accelerated Radio-frequency Readout for Superconducting Detectors". In: *IEEE Transactions on Applied Superconductivity* 29.5, pp. 1–5. ISSN: 1051-8223. DOI: 10.1109/TASC.2019.2912027.

Minutolo, Lorenzo (2019). *GPU SDR*. https://github.com/nasa/GPU_SDR.

Monfardini, A. et al. (2011). "A Dual-band Millimeter-wave Kinetic Inductance Camera for the IRAM 30 M Telescope". In: *The Astrophysical Journal Supplement Series* 194.2, p. 24. DOI: 10.1088/0067-0049/194/2/24. URL: https://doi.org/10.1088%2F0067-0049%2F194%2F2%2F24.

Pajot, F. et al. (2010). "Planck Pre-launch Status: HFI Ground Calibration". In: *Astronomy & Astrophysics* 520, A10. DOI: 10.1051/0004-6361/200913203. URL: https://doi.org/10.1051/0004-6361/200913203.

Patel, A. et al. (2013). "Fabrication of Mkids for the Microspec Spectrometer". In: *IEEE Transactions on Applied Superconductivity* 23.3, pp. 2400404–2400404.

Peebles, P. J. E. (1993). *Principles of Physical Cosmology*. DOI: 10.1515/9780691206721.

Phillips, W A (1987). "Two-level States In Glasses". In: *Reports on Progress in Physics* 50.12, pp. 1657–1708. DOI: 10.1088/0034-4885/50/12/003. URL: https://doi.org/10.1088%2F0034-4885%2F50%2F12%2F003.

Phillips, William A. (Ed.) (1981). *Amorphous Solids, Low-temperature Properties*. Springer-Verlag Berlin Heidelberg. DOI: 10.1007/978-3-642-81534-8.

Planck Collaboration, Adam, R., Ade, P. A. R., Aghanim, N., Alves, M. I. R., et al. (2016). "Planck 2015 Results - X. Diffuse Component Separation: Foreground Maps". In: *Astronomy and Astrophysics* 594, A10. DOI: 10.1051/0004-6361/201525967. URL: https://doi.org/10.1051/0004-6361/201525967.

Planck Collaboration, Adam, R., Ade, P. A. R., Aghanim, N., Arnaud, M., et al. (2016). "Planck 2015 Results - VII. High Frequency Instrument Data Processing: Time-ordered Information and Beams". In: *Astronomy & Astrophysics* 594, A7. DOI: 10.1051/0004-6361/201525844. URL: https://doi.org/10.1051/0004-6361/201525844.

Planck Collaboration, Aghanim, N., et al. (2020). "Planck 2018 Results - Vi. Cosmological Parameters". In: *Astronomy and Astrophysics* 641, A6. DOI: 10.1051/0004-6361/201833910. URL: https://doi.org/10.1051/0004-6361/201833910.

Planck HFI Core Team et al. (2011). "Planck Early Results. IV. First Assessment of the High Frequency Instrument In-flight Performance". In: *Astronomy and Astrophysics* 536, A4. DOI: 10.1051/0004-6361/201116487. URL: https://doi.org/10.1051/0004-6361/201116487.

Pozar, David M (2005). *Microwave Engineering; 3rd Ed.* Hoboken, NJ: Wiley.

Quaranta, O. et al. (2013). "X-ray Photon Detection Using Superconducting Resonators In Thermal Quasi-equilibrium". In: *Superconductor Science and Technology* 26.10, p. 105021.

Ramanayaka, A. N., B. Sarabi, and K. D. Osborn (2015). "Evidence for Universal Relationship Between the Measured 1/f Permittivity Noise and Loss Tangent Created By Tunneling Atoms". In: *arXiv e-prints*, arXiv:1507.06043, arXiv:1507.06043. arXiv: 1507.06043 [cond-mat.supr-con].

Richards, P. L. (1994). "Bolometers for Infrared and Millimeter Waves". In: *American Institute of Physics* 76. DOI: 10.1063/1.357128. URL: http://dx.doi.org/10.1063/1.357128.

Rostem, K., P. J. de Visser, and E. J. Wollack (2018). "Enhanced Quasiparticle Lifetime In A Superconductor By Selective Blocking of Recombination Phonons With A Phononic Crystal". In: *Phys. Rev. B* 98 (1), p. 014522. DOI: 10.1103/PhysRevB.98.014522. URL: https://link.aps.org/doi/10.1103/PhysRevB.98.014522.

Sauvageau, J. E. and D. G. McDonald (1989). "Superconducting Kinetic Inductance Bolometer". In: *IEEE Transactions on Magnetics* 25.2, pp. 1331–1334.

Seki, S. and H. Hasegawa (1981). "Cross-tie Slow-wave Coplanar Waveguide on Semi-insulating Gaas Substrates". In: *Electronics Letters* 17, p. 940. DOI: 10.1049/el:19810657.

Semenov, A.V. et al. (2020). "Effect of Microwaves on Superconductors for Kinetic Inductance Detection and Parametric Amplification". In: *Phys. Rev. Appl.* 13 (2), p. 024079. DOI: 10.1103/PhysRevApplied.13.024079. URL: https://link.aps.org/doi/10.1103/PhysRevApplied.13.024079.

Shu, S. et al. (2018). "Increased Multiplexing of Superconducting Microresonator Arrays By Post-characterization Adaptation of the On-chip Capacitors". In: *Applied Physics Letters* 113.8, p. 082603. ISSN: 0003-6951. DOI: 10.1063/1.5040968. eprint: https://pubs.aip.org/aip/apl/article-pdf/doi/10.1063/1.5040968/14515923/082603_1_online.pdf. URL: https://doi.org/10.1063/1.5040968.

Steinbach, B. A. et al. (2018). "Thermal Kinetic Inductance Detectors for Ground-based Millimeter-wave Cosmology". In: *Journal of Low Temperature Physics* 193.3, pp. 88–95. ISSN: 1573-7357. DOI: 10.1007/s10909-018-2016-y. URL: https://doi.org/10.1007/s10909-018-2016-y.

Swenson, L. J. et al. (2013). "Operation of A Titanium Nitride Superconducting Microresonator Detector In the Nonlinear Regime". In: *Journal of Applied Physics* 113.10, p. 104501. DOI: 10.1063/1.4794808. eprint: https://doi.org/10.1063/1.4794808. URL: https://doi.org/10.1063/1.4794808.

Tanabashi, M. et al. (2018). "Review of Particle Physics". In: *Phys. Rev. D* 98 (3), p. 030001. DOI: 10.1103/PhysRevD.98.030001. URL: https://link.aps.org/doi/10.1103/PhysRevD.98.030001.

Thomas, C N, S Withington, and D J Goldie (2015). "Electrothermal Model of Kinetic Inductance Detectors". In: *Superconductor Science and Technology* 28.4, p. 045012. DOI: 10.1088/0953-2048/28/4/045012. URL: https://dx.doi.org/10.1088/0953-2048/28/4/045012.

Timofeev, A. V. et al. (2013). "Submillimeter-wave Kinetic Inductance Bolometers on Free-standing Nanomembranes". In: *Superconductor Science and Technology* 27.2, p. 025002.

Tinkham, Michael. (1996). *Introduction To Superconductivity*. McGraw-Hill New York. ISBN: 0070648778.

Ulbricht, Gerhard et al. (2015). "Highly Multiplexible Thermal Kinetic Inductance Detectors for X-ray Imaging Spectroscopy". In: *Applied Physics Letters* 106.25, p. 251103. DOI: 10.1063/1.4923096. eprint: https://doi.org/10.1063/1.4923096. URL: https://doi.org/10.1063/1.4923096.

van Rantwijk, J. et al. (2016). "Multiplexed Readout for 1000-pixel Arrays of Microwave Kinetic Inductance Detectors". In: *IEEE Transactions on Microwave Theory and Techniques* 64.6, pp. 1876–1883.

Visser, P. J. de et al. (2014). "Evidence of A Nonequilibrium Distribution of Quasiparticles In the Microwave Response of A Superconducting Aluminum Resonator". In: *Phys. Rev. Lett.* 112 (4), p. 047004. DOI: 10.1103/PhysRevLett.112.047004. URL: https://link.aps.org/doi/10.1103/PhysRevLett.112.047004.

Visser, Pieter J. de et al. (2021). "Phonon-Trapping-Enhanced Energy Resolution in Superconducting Single-Photon Detectors". In: *Physical Review Applied* 16 (3), p. 034051. DOI: 10.1103/PhysRevApplied.16.034051. URL: https://link.aps.org/doi/10.1103/PhysRevApplied.16.034051.

Wandui, Albert et al. (2020). "Thermal kinetic inductance detectors for millimeter-wave detection". In: *Journal of Applied Physics* 128.4, p. 044508. DOI: 10.1063/5.0002413. eprint: https://doi.org/10.1063/5.0002413. URL: https://doi.org/10.1063/5.0002413.

Wandui, Albert K. et al. (2020). "Antenna-coupled thermal kinetic inductance detectors for ground-based millimeter-wave cosmology". In: *Millimeter, Submillimeter, and Far-Infrared Detectors and Instrumentation for Astronomy X*. Ed. by Jonas Zmuidzinas and Jian-Rong Gao. Vol. 11453. International Society for Optics and Photonics. SPIE, 114531E. DOI: 10.1117/12.2563373. URL: https://doi.org/10.1117/12.2563373.

Wang, G. et al. (2010). "Thermal Properties of Silicon Nitride Beams Below 1 Kelvin". In: *AIP Conference Proceedings* 1219.1, pp. 75–82. DOI: 10.1063/1.3402336. eprint: https://aip.scitation.org/doi/pdf/10.1063/1.3402336. URL: https://aip.scitation.org/doi/abs/10.1063/1.3402336.

Wernis, R. A. (2013). "Characterizing A Resonator Bolometer Array". Senior Thesis. California Institute of Technology. URL: https://resolver.caltech.edu/CaltechTHESIS:05312013-022124797.

Wilson, C. M. and D. E. Prober (2004). "Quasiparticle Number Fluctuations In Superconductors". In: *Phys. Rev. B* 69 (9), p. 094524. DOI: 10.1103/PhysRevB.69.094524. URL: https://link.aps.org/doi/10.1103/PhysRevB.69.094524.

Withington, S. et al. (2017). "Thermal Elastic-wave Attenuation In Low-dimensional Sinx Bars At Low Temperatures". In: *Journal of Applied Physics* 122.5, p. 054504. DOI: 10.1063/1.4997466. eprint: https://doi.org/10.1063/1.4997466. URL: https://doi.org/10.1063/1.4997466.

Wu, Wai Ling Kimmy (2015). "BICEP3 and CMB-S4 : Current and Future CMB Polarization Experiments To Probe Fundamental Physics". PhD thesis. Stanford University. URL: https://searchworks.stanford.edu/view/11391830.

Yoon, Jae Woong, Myoung Jin Jung, et al. (2012). "Analytic Theory of the Resonance Properties of Metallic Nanoslit Arrays". In: *IEEE Journal of Quantum Electronics* 48.7, pp. 852–861. DOI: 10.1109/JQE.2012.2192914.

Yoon, Jae Woong and Robert Magnusson (2013). "Fano Resonance Formula for Lossy Two-port Systems". In: *Opt. Express* 21.15, pp. 17751–17759. DOI: 10.1364/OE.21.017751. URL: https://opg.optica.org/oe/abstract.cfm?URI=oe-21-15-17751.

Zmuidzinas, Jonas (2003). "Thermal Noise and Correlations In Photon Detection". In: *Appl. Opt.* 42.25, pp. 4989–5008. DOI: 10.1364/AO.42.004989. URL: https://opg.optica.org/ao/abstract.cfm?URI=ao-42-25-4989.

– (2012). "Superconducting Microresonators: Physics and Applications". In: *Annual Review of Condensed Matter Physics* 3.1, pp. 169–214. DOI: 10.1146/annurev-conmatphys-020911-125022. eprint: https://doi.org/10.1146/annurev-conmatphys-020911-125022. URL: https://doi.org/10.1146/annurev-conmatphys-020911-125022.

Appendix A

CALCULATING THE NOISE EQUIVALENT TEMPERATURE (NET)

Given an observing site, let the transmission of the atmosphere at the frequency ν be $\mathcal{T}(\nu)$. We consider a telescope observing the sky at Zenith angle ZA using detectors with normalized detector response $S(\nu)$. The total optical load on a detector measuring a single polarization across the frequency band is a sum of 3 contributions: the CMB loading, the atmospheric loading and the instrument contribution.

$$Q_{\text{total}} = Q_{\text{CMB}} + Q_{\text{atm}} + Q_{\text{inst}}. \tag{A.1}$$

Each of these terms are

$$Q_{\text{CMB}} = \frac{1}{2} A\Omega \int_{\text{band}} \mathrm{d}\nu\, \eta(\nu) B\left(\nu, T_{\text{CMB}}\right) \left[1 - \frac{1 - \mathcal{T}(\nu)}{\sin(\text{ZA})}\right] \cdot S(\nu), \tag{A.2}$$

$$Q_{\text{atm}} = \frac{1}{2} A\Omega \int_{\text{band}} \mathrm{d}\nu\, \eta(\nu) B\left(\nu, T_{\text{atm}(\nu)}\right) \frac{1 - \mathcal{T}(\nu)}{\sin(\text{ZA})} \cdot S(\nu), \tag{A.3}$$

$$Q_{\text{inst}} = \frac{1}{2} A\Omega \int_{\text{band}} \mathrm{d}\nu\, \eta(\nu) S(\nu) \frac{2\nu^2 k_B T_{\text{inst}}}{c^2}. \tag{A.4}$$

$B(\nu, T)$ is the blackbody spectral flux per unit solid angle per unit frequency at absolute temperature T and $\eta(\nu)$ is the total optical efficiency of the telescope. The atmosphere is often characterized using its Rayleigh Jeans temperature

$$T_{rj}(\nu) = [1 - \mathcal{T}(\nu)] \cdot T_{\text{atm}}(\nu). \tag{A.5}$$

For a single-moded detector, $A\Omega = \lambda^2$. The total loading on a single polarization detector is $Q_{\text{total}} = Q_{\text{CMB}} + Q_{\text{atm}} + Q_{\text{inst}}$. The photon flux incident on the detector obeys Bose-Einstein statistics that is the variance on the number of photons in a single spectral and spatial mode, $\left\langle \Delta N^2 \right\rangle = N\,(1 + N)$, where N is the photon arrival rate per spectral bandwidth. This allows us to derive the expected variance

in photon power integrated over the observing band for one polarization, the photon Noise Equivalent Power NEP_γ as

$$\mathrm{NEP}_\gamma^2 = \int_{\mathrm{band}} \mathrm{d}\nu \left[2h\nu \frac{\mathrm{d}Q_{\mathrm{tot}}}{\mathrm{d}\nu} + 2\left(\frac{\mathrm{d}Q_{\mathrm{tot}}}{\mathrm{d}\nu}\right)^2 \right], \tag{A.6}$$

$$\approx 2h\langle\nu\rangle Q_{\mathrm{tot}} + 2\frac{Q_{\mathrm{tot}}^2}{\Delta\nu}. \tag{A.7}$$

where

$$\langle\nu\rangle = \frac{\int_{\mathrm{band}} \mathrm{d}\nu\nu S(\nu)}{\int_{\mathrm{band}} \mathrm{d}\nu S(\nu)} \tag{A.8}$$

is the bandcenter and

$$\Delta\nu = \frac{\left[\int_{\mathrm{band}} \mathrm{d}\nu\nu S(\nu)\right]^2}{\int_{\mathrm{band}} \mathrm{d}\nu S^2(\nu)} \tag{A.9}$$

is the bandwidth.

From CMB studies, the instrument sensitivity is typically quoted as a Noise Equivalent Temperature, $\mathrm{NET}_{\mathrm{CMB}}$, to bridge experiment and theory since the power spectra are defined in temperature units. The NEP is given in power per unit bandwidth while the NET is in $\mathrm{K}\sqrt{s}$. Since 1 Hz of bandwidth corresponds to 1/2 second of integration time, this accounts for the $\sqrt{2}$ factor in the definition of the NET:

$$\mathrm{NET}_{\mathrm{CMB}} = \frac{\mathrm{NEP}_{\mathrm{tot}}}{\sqrt{2}\frac{\mathrm{d}Q_{\mathrm{CMB}}}{\mathrm{d}T}} \tag{A.10}$$

Appendix B

A TRANSMISSION LINE MODEL OF THE FULL TKID CAPACITOR

In independent simulations of the double-sided and single-sided sections of the capacitors, the simulations surprisingly indicated that the double-sided and single-sided sections had almost identical inductance matrices even though the capacitance matrices are quite disimilar. Here we account for the impact of the additional inductance from the single-sided sections has on the resonator properties.

To simulate the capacitor over a broad frequency range, we modelled the capacitor as a coupled line simulation as shown in fig. B.1. The box is large (6000um x 6000 um) and most of the silicon dielectric (500 um thick) is covered by a Niobium ground plane. The ILD layer is made of silicon dioxide and is 0.3 um thick. In order to accurately extract out the coupled transmission line parameters the ports 1 and 2 are located on the same side of the capacitor tank. The spacing between the edge of the IDC and the ground plane is 96 um matching the current design. The DC frequency response is of interest, so we use two separate frequency sweeps: one adaptive between 100 – 6000 MHz and the second, linear between 0 and 6000 MHz in 200 MHz steps.

From the simulation, we can extract the coupled transmission line matrices. Ignoring the R and G parameters we will only focus on the inductance and capacitance matrices. Referencing the extracted parameters at 500 MHz we find that

Double-sided IDC

$$\hat{L} = \begin{bmatrix} 1.054 & 8.375 \times 10^{-2} \\ 8.375 \times 10^{-2} & 1.050 \end{bmatrix} \times 10^{-6}\ \mathrm{H} \cdot \mathrm{m}^{-1} \tag{B.1}$$

$$\hat{C} = \begin{bmatrix} 3.139 & -3.036 \\ -3.036 & 3.139 \end{bmatrix} \times 10^{-9}\mathrm{F}\ \cdot \mathrm{m}^{-1} \tag{B.2}$$

The even and odd mode impedances are$Z_e = 105\ \Omega$, $Z_o = 12.5\ \Omega$, respectively with even and odd refractive indices $n_e = 3.25$, $n_o = 23.16$, respectively. The line impedances vary very little ($\sim 2\%$) over the entire frequency range simulated (0 – 6 GHz) but there is quite a bit of velocity dispersion. This is not unexpected since

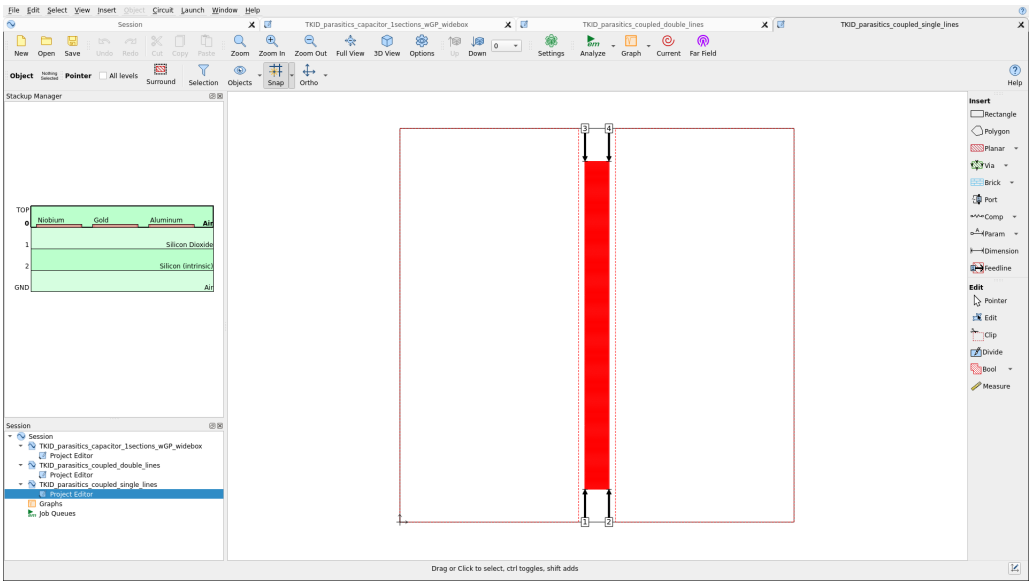

Figure B.1: A coupled line simulation of the TKID IDC. The simulation is 6000 μm long and includes the ground plane in proximity as is similar to the design on wafer.

the propagating modes are not Transverse Electromagnetic Modes (TEM). Figure 2. shows a comparison of the extracted Y_{21} from the simulation with the model developed using the parameters extracted at 500 MHz.

Single-sided IDC

In comparison, the extracted inductance and capacitance matrices for the single sided capacitor are given by

$$\hat{L} = \begin{bmatrix} 1.053 & 8.503 \times 10^{-2} \\ 8.503 \times 10^{-2} & 1.053 \end{bmatrix} \times 10^{-6}\ \mathrm{H \cdot m^{-1}}, \tag{B.3}$$

$$\hat{C} = \begin{bmatrix} 2.548 & -7.613 \times 10^{-1} \\ -7.613 \times 10^{-1} & 1.016 \end{bmatrix} \times 10^{-10}\ \mathrm{F \cdot m^{-1}}. \tag{B.4}$$

The capacitance per unit length for the single-sided lines are much smaller than the double-sided case by about 2 orders of magnitude. The inductance per unit length is quite comparable.

We can model the full capacitor by terminating two identical coupled transmission line sections of length l with two un-identical but coupled transmission line sections of length $l_t - l$, where the total length of the capacitor is fixed at l_t. The entire

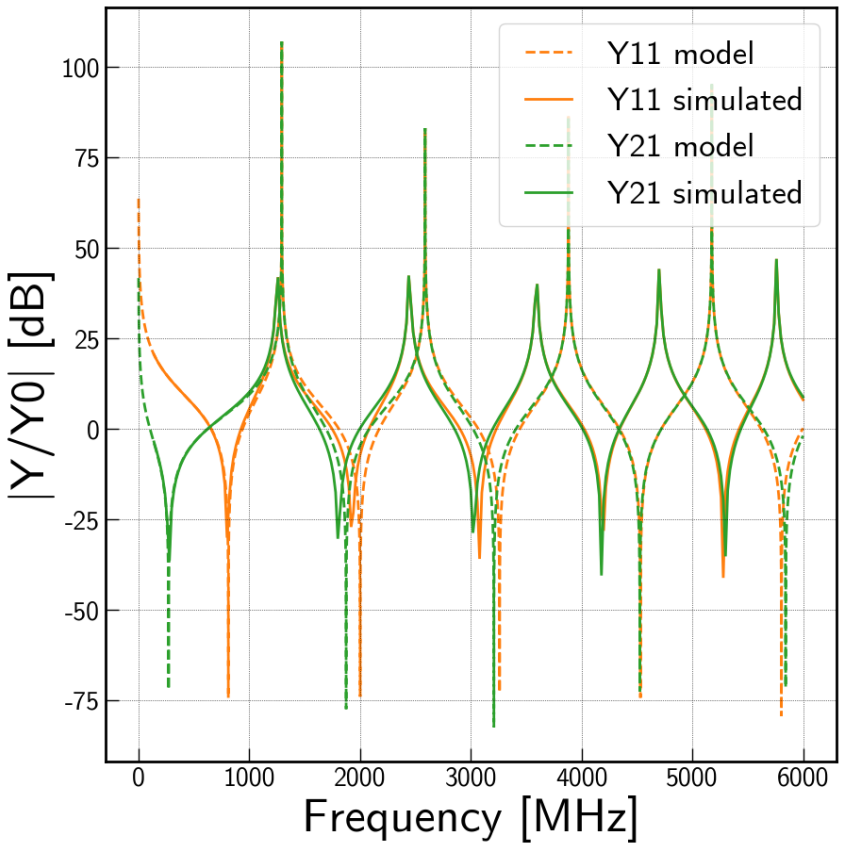

Figure B.2: The extracted Y parameters from the simulation shown in fig. B.1 are well matched by a coupled line model using the even and odd parameters extracted at 500 MHz up to about 1200 MHz.

capacitor is then terminated by capacitances to ground since the end of the capacitor is left open. The two transmission lines are labelled by subscripts 1 and 2.

Let $\vec{V}(z) = \begin{bmatrix} V_1(z) \\ V_2(z) \end{bmatrix}$ and $\vec{I}(z) = \begin{bmatrix} I_1(z) \\ I_2(z) \end{bmatrix}$. The voltage and current along the line evolve according to the coupled transmission line equations

$$\frac{\partial \vec{V}}{\partial z} = -\begin{bmatrix} L_1 & L_m \\ L_m & L_2 \end{bmatrix} \frac{\partial \vec{I}}{\partial t}, \tag{B.5}$$

$$\frac{\partial \vec{I}}{\partial z} = -\begin{bmatrix} C_1 & -C_m \\ -C_m & C_2 \end{bmatrix} \frac{\partial \vec{V}}{\partial t}. \tag{B.6}$$

In Fourier space (w.r.t. time), the voltage and current vectors evolve according to the coupled TL equations:

$$\frac{\mathrm{d}}{\mathrm{d}z}\begin{bmatrix}\vec{V}(z)\\ \vec{I}(z)\end{bmatrix} = -j\omega\begin{bmatrix}0 & \hat{L}\\ \hat{C} & 0\end{bmatrix}\cdot\begin{bmatrix}\vec{V}(z)\\ \vec{I}(z)\end{bmatrix}. \tag{B.7}$$

The identical coupled transmission line section, where $L_1 = L_2 = L, C_1 = C_2 = C$, has an exact solution. Starting from our coupled TL equation

$$\frac{\mathrm{d}}{\mathrm{d}z}\begin{bmatrix}\vec{V}(z)\\ \vec{I}(z)\end{bmatrix} = -j\omega\hat{H}\cdot\begin{bmatrix}\vec{V}(z)\\ \vec{I}(z)\end{bmatrix}, \tag{B.8}$$

the solution to these 4 coupled equations can be written concisely in terms of the 4x4 propagator matrix $\hat{K}(z) = e^{-j\omega\hat{H}z}$, that gives the voltage and current at any point along the coupled lines, given the voltage and current at the start of the lines.

$$\begin{bmatrix}\vec{V}(z)\\ \vec{I}(z)\end{bmatrix} = \hat{K}(z)\cdot\begin{bmatrix}\vec{V}(0)\\ \vec{I}(0)\end{bmatrix}. \tag{B.9}$$

In block matrix form, the propagator can be expressed as

$$\hat{K}(z) = \begin{bmatrix}\cos\mathcal{B}z & -j\mathcal{Z}\sin\mathcal{B}z\\ -j\mathcal{Z}^{-1}\sin\mathcal{B}z & \cos\mathcal{B}z\end{bmatrix}, \tag{B.10}$$

where $\omega\hat{L} = \mathcal{Z}\mathcal{B}$ and $\omega\hat{C} = \mathcal{B}\mathcal{Z}^{-1}$ with $[\mathcal{B}, \mathcal{Z}] = 0$. This is a generalization of the 2x2 ABCD matrix of a single transmission line. Note that all the 2x2 matrices are symmetric since the inductance and capacitance matrices are symmetric. The uncoupled line impedance and wave number are $Z_0 = \sqrt{L/C}$ and $\beta_s = \omega\sqrt{L\cdot C}$, respectively.

We can also write out the inverse propagator, $\hat{G}(z)$ such that $\hat{G}\cdot\hat{K} = \hat{K}\cdot\hat{G} = \hat{I}$,

$$\hat{G}(z) = \begin{bmatrix}\cos\mathcal{B}z & j\mathcal{Z}\sin\mathcal{B}z\\ j\mathcal{Z}^{-1}\sin\mathcal{B}z & \cos\mathcal{B}z\end{bmatrix}. \tag{B.11}$$

Using the propagator and the extracted inductance and capacitance per unit length, we can figure out the exact voltage and current in the capacitor at the end of the double-sided capacitor section. $\mathcal{B}, \mathcal{Z}$ can be diagonalized simultaneously using the matrix

$$\hat{Q} = \frac{1}{\sqrt{2}} \begin{bmatrix} 1 & 1 \\ 1 & -1 \end{bmatrix}. \tag{B.12}$$

Even though there is no exact analytical solution for coupled non-identical TLs, the numerical solution is quite accessible. We do not have an exact solution, we can tackle the problem quite successfully using perturbation theory to build on our existing solution for the identical coupled lines. This problem simplifies further when we note that $\hat{L}_{1,1} \sim \hat{L}_{2,2}$ for the single-sided capacitor. Therefore only the capacitances per unit length are mismatched! With this, let $\hat{C} = \hat{C}_0 + \epsilon\, \hat{C}_1$ where

$$\hat{C} = \begin{bmatrix} C_1 & -C_m \\ -C_m & C_2 \end{bmatrix}, \tag{B.13}$$

is the full capacitance matrix.

We take $\epsilon = (C_1 - C_2)/(C_1 + C_2)$ and $C_0 = (C_1 + C_2)/2$ so that

$$\hat{C}_0 = \begin{bmatrix} C_0 & -C_m \\ -C_m & C_0 \end{bmatrix}. \tag{B.14}$$

is the symmetrized capacitance matrix

and

$$\hat{C}_1 = C_0 \begin{bmatrix} 1 & 0 \\ 0 & -1 \end{bmatrix}. \tag{B.15}$$

is the perturbation to the capacitance.

Our goal is now to compute the first order term in the perturbative expansion of the propagator $\hat{K}(z) = \hat{K}_0(z) + \epsilon\, \hat{K}_1(z) + \cdots$. This procedure should feel familiar (echo time-independent perturbation theory in QM). The approach will be exactly the same, except that in this case, our propagator is not a Hermitian matrix. To simplify, we will switch to a basis that diagonalizes the unperturbed solution by defining $V_\pm(z) = (V_1 \pm V_2)/\sqrt{2}, I_\pm(z) = (I_1 \pm I_2)/\sqrt{2}$.

In the diagonal basis, $\hat{K}_0(z) = \mathrm{diag}\left(e^{j\beta_+ z}, e^{-j\beta_+ z}, e^{j\beta_- z}, e^{-j\beta_- z}\right)$. The matrices wave number and impedance matrices are $\mathcal{B} = \mathrm{diag}\,(\beta_+, \beta_-)\,, \mathcal{Z} = \mathrm{diag}\,(Z_+, Z_-)$, where

$$Z_{\pm} = \sqrt{\frac{L \pm L_m}{C_0 \mp C_m}}, \tag{B.16}$$

$$Z_0 = \sqrt{L/C_0}. \tag{B.17}$$

$$\beta_{\pm} = \omega\sqrt{(L \pm L_m)\,(C_0 \mp C_m)}, \tag{B.18}$$

$$\beta_s = \omega\sqrt{L \cdot C_0}. \tag{B.19}$$

We want to compute the expansion $\hat{K}(z) = e^{-j\omega(\hat{H}_0+\epsilon\hat{H}_1)z} = \hat{K}_0(z)+\epsilon\,\hat{K}_1(z)+\cdots$. Since the matrices $\hat{H}_0, \hat{H}_1$ do not commute, the expansion of the matrix exponent is non-trivial (see the Zassenhaus formula). The easiest path is to consider the perturbation to the eigenvalues, and the right and left eigenvectors of the propagator matrix.

We directly apply the results of perturbation theory applied to general eigenvalues and eigenvectors (Greenbaum et al., 2020). Simply quoting, if $\hat{H}_0$ with a simple eigenvalue λ_0 corresponding to right eigenvector x_0 and left eigenvector y_0. $\left(\hat{H}_0 x_0 = \lambda_0 x_0, y_0^{\dagger}\hat{H}_0 = \lambda_0 y_0^{\dagger}\right)$. To first order the eigenvalue can be written as

$$\lambda(\epsilon) = \lambda_0 + \epsilon\; y_0^{\dagger} \cdot \hat{H}_1 \cdot x_0 \tag{B.20}$$

.

Similarly, given the matrix of right eigenvectors $X = [x_0, X_j]$ and that of left eigenvectors $Y = [y_0, Y_j]$ and B_j is the diagonal matrix of all eigenvalues that differ from λ_0, let $S = X_j \cdot \left(B_j - \lambda_0 \hat{I}_3\right)^{-1} Y_j^{\dagger}$, then

$$x(\epsilon) = x_0 - \epsilon\; S \cdot \hat{H}_1 \cdot x_0, \tag{B.21}$$

$$y(\epsilon) = y_0 - \epsilon\; y_0^{\dagger} \cdot \hat{H}_1 \cdot S. \tag{B.22}$$

In our case, we find that to first order, the eigenvalue perturbation is zero. Therefore our propagator can be expanded as $\hat{K}(z) \approx (X_0 + \epsilon X_1) \cdot e^{-j\omega H_0 z} \cdot (Y_0 + \epsilon Y_1)^{\dagger}$ so that

$$\hat{K}(z) \;=\; \hat{K}_0(z) + \;\epsilon\; \left[Y_1^{\dagger} \cdot X_0 \cdot \hat{K}_0(z) \;+\; \hat{K}_0(z) \cdot Y_0^{\dagger} \cdot X_1\right] + O(\epsilon^2). \tag{B.23}$$

In block matrix form (and using the subscript $_s$ to reference the single-sided capacitor)

$$\hat{K}_0(z) = \begin{bmatrix} \hat{A}_s & \hat{B}_s \\ \hat{C}_s & \hat{D}_s \end{bmatrix}, \tag{B.24}$$

$$\hat{K}_1(z) = \begin{bmatrix} \delta\hat{A}_s & \delta\hat{B}_s \\ \delta\hat{C}_s & \delta\hat{A}_s^T \end{bmatrix}. \tag{B.25}$$

and the perturbation to the inverse propagator is

$$\hat{G}_1(z) = \begin{bmatrix} \delta\hat{A}_s & -\delta\hat{B}_s \\ -\delta\hat{C}_s & \delta\hat{A}_s^T \end{bmatrix}. \tag{B.26}$$

This ensures that $\hat{G} \cdot \hat{K} = \hat{K} \cdot \hat{G} = \hat{I} \; = \; \hat{I} \; + \; O(\epsilon^2)$.

The transmission line is passive so the network has to be reciprocal. This imposes constraints on the possible form of the perturbed propagator. Reciprocity requires that $\delta\hat{B}_s, \delta\hat{C}_s$ are symmetric. Additionally, the following matrix equations hold:

$$\hat{A}_s \cdot \hat{D}_s \; - \; \hat{B}_s \cdot \hat{C}_s \; = \; \hat{I}, \tag{B.27}$$

$$\hat{A}_s \cdot \delta\hat{A}_s \; + \; \delta\hat{A}_s \cdot \hat{A}_s \; = \; \delta\hat{B}_s \cdot \hat{C}_s \; + \; \hat{B}_s \cdot \delta\hat{C}_s, \tag{B.28}$$

$$\hat{B}_s \cdot \delta\hat{D}_s \; + \; \delta\hat{B}_s \cdot \hat{D}_s \; = \; \delta\hat{A}_s \cdot \hat{B}_s \; + \; \hat{A}_s \cdot \delta\hat{B}_s, \tag{B.29}$$

$$\hat{C}_s \cdot \delta\hat{A}_s \; + \; \delta\hat{C}_s \cdot \hat{A}_s \; = \; \delta\hat{D}_s \cdot \hat{C}_s \; + \; \hat{D}_s \cdot \delta\hat{C}_s. \tag{B.30}$$

Explicitly in the diagonal basis,

$$\delta\hat{A}_s(z) = -\frac{\beta_s}{\beta_+^2 - \beta_-^2} \frac{\cos(\beta_+ z) - \cos(\beta_- z)}{Z_0} \begin{bmatrix} 0 & Z_+\beta_+ \\ Z_-\beta_- & 0 \end{bmatrix}, \tag{B.31}$$

$$\delta\hat{B}_s(z) = \frac{-j\beta_s}{\beta_+^2 - \beta_-^2} \frac{\beta_+ \sin(\beta_- z) - \beta_- \sin(\beta_+ z)}{Z_0} \begin{bmatrix} 0 & Z_+Z_- \\ Z_+Z_- & 0 \end{bmatrix}, \tag{B.32}$$

$$\delta\hat{C}_s(z) = \frac{j\beta_s}{\beta_+^2 - \beta_-^2} \frac{\beta_+ \sin(\beta_+ z) - \beta_- \sin(\beta_- z)}{Z_0} \begin{bmatrix} 0 & 1 \\ 1 & 0 \end{bmatrix}. \tag{B.33}$$

Each of the perturbation matrices is purely off-diagonal and mixes the even and odd modes propagating down the capacitor.

From this point, we only need to rearrange the elements of the propagator in order to construct the 4x4 admittance matrix of the single-sided section of the capacitor. We have to reverse the direction of the current due to the change in convention between admittance parameters and ABCD parameters. The expression looks a little messy, but it is all here, accurate to 2nd order

$$\begin{bmatrix} \vec{I}(l) \\ -\vec{I}(l_t - l) \end{bmatrix} = \left(\hat{Y}_s + \epsilon\, \delta\hat{Y}_s\right) \cdot \begin{bmatrix} \vec{V}(l) \\ \vec{V}(l_t - l) \end{bmatrix}. \tag{B.34}$$

where

$$\hat{Y}_s \;=\; \begin{bmatrix} -\hat{B}_s^{-1} \cdot \hat{A}_s & \hat{B}_s^{-1} \\ \hat{B}_s^{-1} & -\hat{D}_s \cdot \hat{B}_s^{-1} \end{bmatrix}, \tag{B.35}$$

and

$$\delta\hat{Y}_s \;=\; \begin{bmatrix} \hat{B}_s^{-1} \cdot \delta\hat{B}_s \cdot \hat{B}_s \cdot \hat{A}_s - \hat{B}_s^{-1} \cdot \delta\hat{A}_s & \hat{B}_s^{-1} \cdot \delta\hat{B}_s \cdot \hat{B}_s^{-1} \\ \{\delta\hat{A}_s, \hat{B}_s^{-1} \cdot \hat{A}_s\} - \hat{A}_s \cdot \hat{B}_s^{-1} \cdot \delta\hat{B}_s \cdot \hat{B}_s^{-1} \cdot \hat{A}_s - \delta\hat{C}_s & \hat{A}_s \cdot \hat{B}_s^{-1} \cdot \delta\hat{B}_s \cdot \hat{B}_s - \delta\hat{A}_s^T \cdot \hat{B}_s^{-1} \end{bmatrix}. \tag{B.36}$$

The final improvement to our solution is to symmetrize the admittance matrix. This removes some additional 2nd order differences in our perturbative expansion leading to the quite good agreement between the numerical solution and the perturbative expansion as shown in fig. B.3. shows a comparison of the numerical solution with the perturbative solution for the single-sided capacitor with the parameters listed above.

Assembling the full capacitor

We can cascade our two solutions to solve for the voltage and current everywhere along the capacitor. The double-sided and single-sided capacitor sections have the same inductance matrix but different capacitance matrices. To distinguish them, we use subscript d for the double-sided capacitor in contrast with subscript s for the single sided. In terms of the propagators,

$$\begin{bmatrix} \vec{V}(l_t) \\ \vec{I}(l_t) \end{bmatrix} = \hat{K}_s(l_t - l) \cdot \hat{K}_d(l) \begin{bmatrix} \vec{V}(0) \\ \vec{I}(0) \end{bmatrix}. \tag{B.37}$$

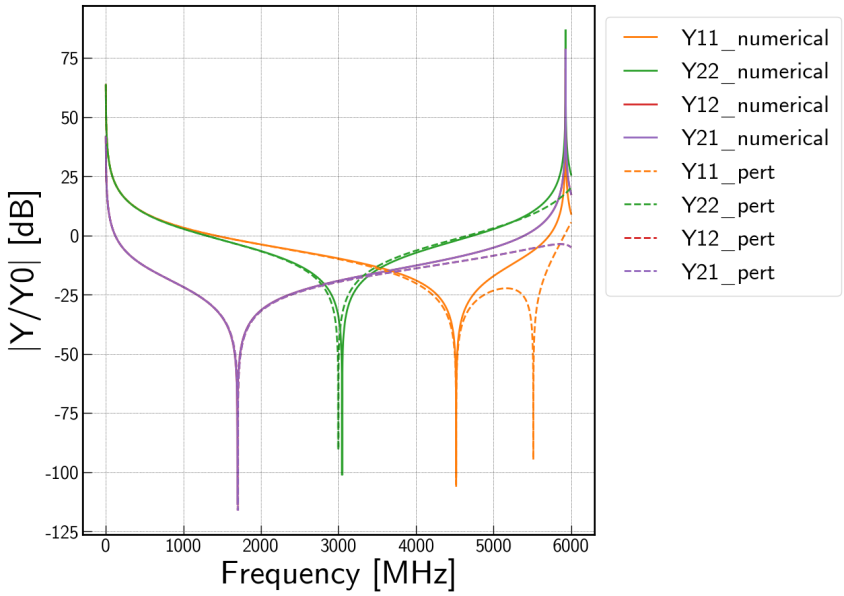

Figure B.3: The first order perturbative solution to the nonidentical coupled lines reduces the first pole and the first zero of all the admittance parameters. This gives accuracy well up to about 4.8 GHz.

To get us closer to the final answer, we express the propagators as ABCD matrices

$$\begin{bmatrix} \vec{V}(l_t) \\ \vec{I}(l_t) \end{bmatrix} = \begin{bmatrix} \hat{A}_s + \epsilon\,\delta\hat{A}_s & \hat{B}_s + \epsilon\,\delta\hat{B}_s \\ \hat{C}_s + \epsilon\,\delta\hat{C}_s & \hat{D}_s + \epsilon\,\delta\hat{D}_s \end{bmatrix} \cdot \begin{bmatrix} \hat{A}_d & \hat{B}_d \\ \hat{C}_d & \hat{D}_d \end{bmatrix} \cdot \begin{bmatrix} \vec{V}(0) \\ \vec{I}(0) \end{bmatrix}. \tag{B.38}$$

The final piece that is needed is to terminate the end of the capacitor with load capacitances to ground, $\hat{C}_L = \text{diag}\,(C_{L1}, C_{L2})$ so that $\vec{I}(l_t) = \hat{Y}_L\vec{V}(l_t) = j\omega\hat{C}_L\vec{V}(l_t)$. This gives the 2x2 admittance matrix of our full capacitor from the equation below

$$\vec{I}(0) = -\left(\hat{Y}_L \cdot \hat{B}_{\text{full}} + \hat{D}_{\text{full}}\right)^{-1} \cdot \left(\hat{Y}_L \cdot \hat{A}_{\text{full}} + \hat{C}_{\text{full}}\right) \cdot \vec{V}(0). \tag{B.39}$$

To make progress, we are mostly interested in the low frequency behavior of our capacitor. We can Taylor expand the network terms in powers of ω. It is easiest to backtrack and expand the ABCD parameters first:

$$\begin{bmatrix} \vec{V}(l_t) \\ \vec{I}(l_t) \end{bmatrix} = \begin{bmatrix} \hat{I} - \omega^2\hat{L}_T \cdot \hat{C}_A & -j\omega\hat{L}_T \\ -j\omega\hat{C}_T & \hat{I} - \omega^2\hat{L}_T \cdot \hat{C}_D \end{bmatrix} \cdot \begin{bmatrix} \vec{V}(0) \\ \vec{I}(0) \end{bmatrix}. \tag{B.40}$$

$\hat{L}_T = \hat{L}\cdot l_t$ gives the total inductance. $\hat{C}_T = \left(\hat{C}_s + \epsilon\,\hat{C}_1\right)(l_t - l) + \hat{C}_d \cdot l$ gives the total capacitance. $\hat{C}_A = \frac{4}{\pi^2}\left(\hat{C}_T\left(1 - \frac{l}{2l_t}\right) + \frac{1}{2}\hat{C}_d\,(l_t - l)\right)$ and $\hat{C}_D = \frac{4}{\pi^2}\left(\hat{C}_T\left(\frac{l}{2l_t}\right) - \frac{1}{2}\hat{C}_d\,(l_t - l)\right)$

so that $\hat{C}_A + \hat{C}_D = \frac{4}{\pi^2}\hat{C}_T$.

Coming back to the 2x2 admittance matrix of the capacitor,

$$\hat{Y} = \left[\hat{I} - \omega^2\left(\hat{C}_D + \hat{C}_L\right)\cdot\hat{L}_T\right]^{-1}\cdot\left[j\omega\left(\hat{C}_T + \hat{C}_L\right)\right]. \tag{B.41}$$

The first piece of $\hat{Y}$ gives the first 2 poles of the capacitor and the remaining piece gives the first zero. As expected, the first zero is at $\omega = 0$ and is given by the total capacitor and the load capacitance to GND. The first zero and pole describe the capacitor up to 1 GHz.

Things are much clearer using the impedance matrix.

$$\hat{Z}(s = j\omega) = \frac{1}{s}\left(\hat{C}_T + \hat{C}_L\right)^{-1} + s\left(\hat{C}_T + \hat{C}_L\right)^{-1}\cdot\left(\hat{C}_D + \hat{C}_L\right)\cdot\hat{L}_T. \tag{B.42}$$

The impedance of the capacitor splits into 2 separate impedance matrices. This allows us to construct the full impedance model by connecting 2 smaller 2 port networks in series (not in cascade).

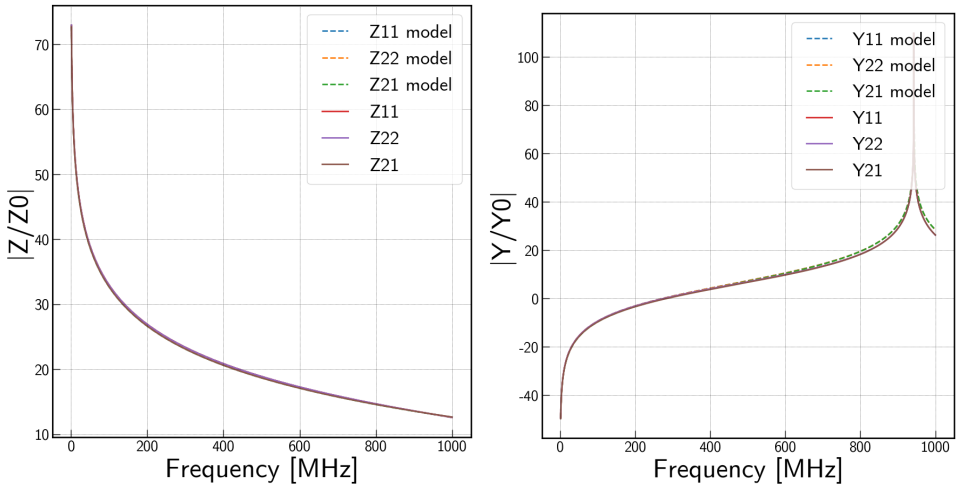

(a) (b)

Figure B.4: The numerical solution to the capacitor impedance agrees well with the perturbative model everywhere within the design band. Impedance parameters of the capacitor are given on the left while the admittance parameters are on the right.

In conclusion, a transmission line model of our IDC capacitor is accurate across the entire design band and reflects the relationship between the IDC capacitance, coupling to ground and the parasitic inductance in the structure. This approach can

be extended to higher frequencies to model harmonics of the fundamental resonance mode.